Exploration of the proxiOME of large subunit ribosomal proteins reveals Acl1 and Bcl1 as cooperating dedicated chaperones of Rpl1

Sébastien Favre[1], Benjamin Pillet[1], Fabiana Burchert[2,†], Devanarayanan Siva Sankar[1,†], Alfonso Méndez-Godoy[1], Jörn Dengjel[1], Gert Bange[2,3], and Dieter Kressler[1,*]

[1] Department of Biology, University of Fribourg, 1700 Fribourg, Switzerland

[2] Center for Synthetic Microbiology (SYNMIKRO) and Department of Chemistry, Philipps-University Marburg, 35043 Marburg, Germany

[3] Max Planck Institute for Terrestrial Microbiology, Molecular Physiology of Microbes, 35043 Marburg, Germany

[*]To whom correspondence should be addressed. Tel: +41 26 300 86 45; Fax: +41 26 300 97 41; Email: dieter.kressler@unifr.ch

[†]Fabiana Burchert and Devanarayanan Siva Sankar contributed equally to this work.

Present address: Devanarayanan Siva Sankar, Global Health Institute, Swiss Federal Institute of Technology Lausanne (EPFL), 1015 Lausanne, Switzerland

ABSTRACT

The eukaryotic ribosome consists of four ribosomal RNAs (rRNAs) and around 80 ribosomal proteins (r-proteins). Most r-proteins, due to their extensive interactions with rRNA, contain highly basic regions, which can predispose them to aggregation prior to their assembly. Accordingly, dedicated chaperones (DCs) and importins have been shown to play a crucial role in safeguarding newly synthesized r-proteins until their incorporation into pre-ribosomal particles. However, only relatively few DCs and interactions with importins have so far been identified for the 79 r-proteins in *Saccharomyces cerevisiae*. Here, we systematically explored the physical proximities of all r-proteins of the large 60S subunit by TurboID-based proximity labelling. This approach revealed importins and potential novel DCs within the proxiOME of several r-proteins. We provide evidence for a direct interaction of Kap119/Nmd5 with the r-protein Rpl30 (eL30), of Kap121/Pse1 with Rpl38 (eL38), and of Kap114 with both Rpl6 (eL6) and Rpl40 (eL40). Notably, the two previously uncharacterized proteins Acl1 (Ycr051w) and Bcl1 (Ynl035c) were found in the proxiOME of the universally conserved Rpl1 (uL1). While Acl1 appears to be a fungi-specific protein, the human orthologue of Bcl1, WDR89, was found in the proxiOME of the human Rpl1 orthologue RPL10A, suggesting that Bcl1 carries out an evolutionarily conserved function. We show that both Acl1 and Bcl1 are direct interaction partners of Rpl1 and that they have the capacity to form a trimeric complex with Rpl1 in vitro. We also report the crystal structure of a minimal Acl1-Rpl1 complex, which reveals how the ankyrin repeats of Acl1 interact with the second domain of Rpl1. Moreover, we have performed a detailed mutational analysis, based on the Acl1-Rpl1 crystal structure and the predicted Bcl1-Rpl1 structure, to verify the relevance of the interaction-mediating surfaces on Rpl1 and Acl1. In vivo, concomitant absence of Acl1 and Bcl1 leads to a synergistic growth defect and affects the subunit-joining capacity of the produced 60S subunits, presumably due to the reduced incorporation of Rpl1 into nuclear pre-60S subunits. Interestingly, both Acl1 and Bcl1 contain a functional nuclear localization signal (NLS) at their C-terminal extremity. While the exact mechanism of Acl1 import remains to be established, we show that the NLS of Bcl1 corresponds to a Kap104-interacting PY-NLS. Notably, only simultaneous absence of both NLSs abolishes the nuclear accumulation of Acl1 and Bcl1, suggesting that they can be co-imported into the nucleus as a trimeric Acl1-Rpl1-Bcl1 complex. Taken together, our data indicate that Acl1 and Bcl1 may function as cooperating DCs of Rpl1 that assure the safe nuclear transfer and efficient loading of Rpl1 onto pre-60S subunits. In addition, and besides permitting the identification of DCs and importins, our TurboID-based proximity labelling screen also proved to be highly suitable for the visualization of both transient and stable neighbourhoods of r-proteins on pre-60S and mature 60S subunits, altogether making this data set a rich resource for studying many potentially exciting physical proximities of large subunit r-proteins along their entire life cycle.

INTRODUCTION

Protein synthesis is an essential process accomplished by ribosomes in all organisms; accordingly, ribosomes of all three domains of life share a conserved functional core (1). As their overall structure and composition are quite well conserved among eukaryotes, functional and structural studies of the eukaryotic ribosome and its assembly process were and are still often carried out in the budding yeast *Saccharomyces cerevisiae* (*S. cerevisiae*), notably due to the experimental amenability of this unicellular organism. In eukaryotes, translating 80S ribosomes consist of two asymmetric subunits, referred to as the small 40S (SSU) and large 60S (LSU) ribosomal subunit. In *S. cerevisiae*, the SSU contains 33 ribosomal proteins (r-proteins) and the 18S ribosomal RNA (rRNA), whereas the LSU is composed of 46 r-proteins and three rRNAs, the 5S, 5.8S, and 25S rRNA (1,2). In order to maintain the cellular amounts of this macromolecular nanomachine, yeast cells in exponential growth phase need to produce approximately 2,000 functional ribosomes per minute (3). This task represents a major challenge, not only to coordinate the production of the ribosomal components but also for their well-orchestrated assembly. Ribosome assembly alone requires more than 200 assembly factors (AFs) and around 80 small nucleolar RNAs (snoRNAs) to provide accuracy and speed to this multistep process, during which the r-proteins get sequentially incorporated into pre-ribosomal particles as the precursor rRNAs (pre-rRNAs) are progressively processed into mature rRNAs and, at the same time, folded into their final conformation (2,4-8).

Most r-proteins, owing to their capacity to interact with rRNA, contain highly basic regions. In unassembled r-proteins, these highly basic regions are prone to engage in non-specific interactions with polyanions, such as cytoplasmic tRNAs, which can result in r-protein aggregation (9). Accordingly, an excess of unassembled r-proteins, in certain cases even of an individual r-protein, can lead to r-protein aggregation and elicit a proteostatic collapse (10-14). To limit the detrimental effects of unassembled r-proteins while still producing sufficient amounts of new r-proteins to meet the actual demand of ribosome assembly, cells possess several general as well as highly specific regulation and protection mechanisms. First, the production of r-proteins is already coordinated at the transcriptional level as the synthesis of all r-protein gene (RPG) mRNAs is driven by only three distinct types of co-regulated promoters, which probably most notably differ by their diverging dependence on the TORC1-controlled transcriptional activators Ifh1 and Sfp1, thereby ensuring the provision of roughly equal amounts of each RPG mRNA in different growth conditions and, hence, at different rates of ribosome assembly (15-19). Second, cells continuously monitor the levels of free r-proteins and respond to their excess presence by two general regulatory mechanisms, the ERISQ (excess ribosomal protein quality control) pathway and a stress response pathway, termed RASTR (ribosome assembly stress response) or RPAS (ribosomal protein assembly stress) (10,12,13,16). The ERISQ pathway selectively eliminates free r-proteins and, thus, enables cells to readily cope with a moderate excess of unassembled r-proteins. To do so, the nucle(ol)ar E3 ubiquitin ligase Tom1 ubiquitinates excess free r-proteins on sites that are only

accessible in their unassembled, unprotected state, thereby channelling its target r-proteins to degradation by the proteasome (10,11,20). The adaptive RASTR or RPAS stress response is activated by the aggregation of excess free r-proteins, which leads to the sequestration of Ifh1 and chaperones in these aggregates and, thereby, to a downregulation of Ifh1-dependent RPG transcription and the upregulation of Hsf1 target genes, altogether lowering the proteostatic burden by decreasing the amounts of newly synthesized r-proteins and by bolstering the cellular protein folding and degradation capacity (12,13,16). Third, while the above mechanisms operate to regulate r-protein expression at the transcriptional level and to degrade excess unassembled r-proteins that have accumulated in the nuclear compartment, the two ribosome-associated chaperone systems, the ribosome-associated complex (RAC)-Ssb chaperone triad and the nascent polypeptide-associated complex (NAC) (21-24), cooperate during translation of RPG mRNAs to prevent the aggregation of many newly synthesized r-proteins (25). Fourth, most r-proteins associate with pre-ribosomal particles in the nucle(ol)us and the high rate of ribosome assembly relies on their rapid nuclear accumulation (26,27); accordingly, studies in mammalian cells have shown that the nuclear import of r-proteins largely depends, despite their (mostly) small size, on active, importin-mediated transport (9,28). As importins also prevent the aggregation of r-proteins, likely by recognizing and shielding the exposed rRNA-binding regions of free r-proteins, they appear to exhibit a dual function as transport receptors and chaperones (9,29). In yeast, import of r-proteins has been suggested to be mainly mediated by the importin-β Kap123 (30). In support of this, selective ribosome profiling revealed that Kap123 has the capacity to co-translationally associate with seven r-proteins, whereas, out of the remaining ten importins (nine importin-βs and the importin-α Kap60/Srp1), only Kap104 exhibited co-translational recognition of one r-protein (31). However, thorough experimental proof, pinpointing both the NLS and the responsible importin, for the selective import of a given r-protein by a distinct importin has only been reported in very few cases (32,33), presumably also owing to a partial redundancy among importins, the potential presence of multiple NLSs in an r-protein, and the NLS not necessarily having to correspond to a short linear sequence (30,34,35).

Besides the above-mentioned, mostly general regulation, protection, and import mechanisms, several r-proteins rely on tailor-made solutions in order to be furnished in adequate amounts and in an unproblematic, assembly-competent form. In the case of two r-proteins, Rpl40 (eL40) and Rps31 (eS31), their initial production as fusion proteins (Ubi1/2 and Ubi3) bearing an N-terminal ubiquitin moiety, which is cleaved off prior to their incorporation into pre-ribosomal particles, is necessary to ensure their efficient production (36-40), suggesting that the fused ubiquitin may fulfil the function of a *cis*-acting chaperone. Notably, several r-proteins have been shown to be transiently associated with a selective binding partner; as these ensure, albeit by different means and by employing different folds for specific r-protein recognition, the soluble expression, nuclear transport, and/or efficient assembly of their r-protein clients, they are collectively referred to as dedicated chaperones (DCs) of r-proteins (41,42). Up

to now, eight bona fide DCs that beneficially act on nine different r-proteins have been identified (42-45), with one of these, Syo1, being able to simultaneously interact with the r-proteins Rpl5 (uL18) and Rpl11 (uL5) (46). By doing so, the transport adaptor Syo1 not only enables the Kap104-mediated co-import of Rpl5 and Rpl11 but also their subsequent assembly with the 5S rRNA into an assembly-competent 5S ribonucleoprotein (RNP) precursor (46-48). Interestingly, six of the eight DCs, namely Rrb1, Acl4, Syo1, Sqt1, Tsr4, and Yar1, have the capacity to co-translationally capture, almost exclusively by recognizing an N-terminally located binding site, the r-protein Rpl3 (uL3), Rpl4 (uL4), Rpl5, Rpl10 (uL16), Rps2 (uS5), and Rps3 (uS3), respectively (34,41,44,45), indicating that such an early encounter may in many instances be crucial for an optimal protection and/or folding of the r-protein client. In contrast, the DCs Bcp1 and Tsr2 have been suggested to only associate with Rpl23 (uL14) and Rps26 (eS26), respectively, once the r-protein has entered the nucleus, where they would act, by releasing Rpl23 and Rps26 from redundant import receptors and mediating their safe transfer to the pre-ribosomal assembly site, as nuclear escortins (43,49). Finally, and in line with the necessity for a tight regulation of the abundance of unassembled r-proteins, the expression levels of several r-proteins are fine-tuned through autoregulatory feedback mechanisms. Some r-proteins, when excessively present, bind to their own (pre-)mRNA and thereby, for example, repress its translation, inhibit its splicing, and/or promote its degradation (50-56). In the case of Rpl3 and Rpl4, their excess presence indirectly downregulates *RPL3* or *RPL4* mRNA levels by reducing the availability of Rrb1 and Acl4 to bind in a timely manner to nascent Rpl3 and Rpl4, respectively, and thereby enabling instead the recruitment of a regulatory machinery consisting of the NAC and the Caf130-associated Ccr4-Not complex (14). Strikingly, deregulated expression of Rpl3 and/or Rpl4 in cells lacking Tom1 leads to their massive aggregation, a perturbation of overall proteostasis, and lethality, underscoring the importance of the ERISQ pathway and the DCs Rrb1 and Acl4 for protecting cells from the potentially detrimental effects of their surplus production (14).

We have a long-standing interest in understanding how r-proteins safely reach their site of pre-ribosomal incorporation. With the primary aim of identifying novel DCs, we have performed a TurboID-based proximity labelling screen with all *S. cerevisiae* LSU r-proteins. Despite the relatively short 1-h duration of induced r-protein expression and biotinylation, chosen to preferentially capture transient interactions of r-proteins prior to their assembly into pre-ribosomal particles, this approach nevertheless permits, as illustrated for selected examples, a spatiotemporal resolution of r-protein neighbourhoods on successive pre-60S particles. More importantly, and as aimed for, our large-scale proximity labelling screen has proven to be well suited for the detection of transient interactions of unassembled r-proteins. Besides unveiling potential interactions with distinct importins, which we confirmed in the case of four r-proteins by yeast two-hybrid (Y2H) assays, our approach also allowed to uncover established and potential DCs among the enriched proteins. In this study, we have focused on two previously uncharacterized, non-essential proteins, Acl1 (Ycr051w) and Bcl1 (Ynl035c), which could be identified in the proxiOME of the universally conserved Rpl1 (uL1). Our genetic, cell

biological, biochemical, and structural data indicate that the ankyrin repeat-containing Acl1 and the predicted WD-repeat β-propeller protein Bcl1 likely function as cooperating DCs that contribute to the safe and efficient transfer of Rpl1 to its assembly site on nucleolar pre-60S subunits. While Acl1 appears to be a fungi-specific protein, proximity labelling with human RPL10A, the orthologous protein of Rpl1, in the human HeLa cell line uncovered WDR89, the likely human orthologue of Bcl1, as an RPL10A-proximal protein, suggesting that Bcl1 carries out an evolutionarily conserved function as a DC of uL1.

MATERIALS AND METHODS

Plasmids

All recombinant DNA techniques were according to established procedures using *Escherichia coli* DH5α for cloning and plasmid propagation. All cloned DNA fragments generated by PCR amplification were verified by sequencing. More information on the plasmids, which are listed in the Supplementary file 1, is available upon request.

Yeast genetics

The *S. cerevisiae* strains used in this study are listed in Supplementary file 2 and are, unless otherwise specified, derived from W303 (57). Deletion disruption as well as C-terminal tagging at the genomic locus was performed as described (58,59). The preparation of media, yeast transformation, and genetic manipulations were done according to established procedures.

TurboID-based proximity labelling assay in yeast

The wild-type strain YDK11-5A (60) was transformed with centromeric plasmids (*LEU2* marker) expressing the TurboID-fused bait proteins under the control of the copper-inducible *CUP1* promoter. Transformed cells were grown in exponential phase to an OD_{600} of around 0.5 at 30°C in 100 ml of synthetic complete medium containing 2% glucose as carbon source and lacking leucine (SC-Leu) that was prepared with copper-free yeast nitrogen base (FORMEDIUM). Expression of the tagged proteins from the *CUP1* promoter was induced by addition of copper sulphate to a final concentration of 500 µM. Simultaneously, biotin (Sigma-Aldrich, St. Louis, MO, USA), from a freshly prepared 100 mM stock solution in dimethyl sulfoxide, was added to a final concentration of 500 µM. Then, cells were grown for an additional hour, harvested by centrifugation at 4000 rpm for 5 min at 4°C, and washed once with 50 mL of ice-cold nanopure water and once with 1 mL of ice-cold lysis buffer (LB: 50 mM Tris-HCl (pH 7.5), 150 mM NaCl, 1.5 mM $MgCl_2$, 0.1% SDS, and 1% Triton X-100) containing 1 mM PMSF. Pelleted cells were rapidly frozen in liquid nitrogen and stored at -80°C. Prior to their lysis, cells were resuspended in 400 µL lysis buffer containing 0.5% sodium deoxycholate and 1 mM PMSF (LB-P/D). After addition of glass beads, cells were lysed with a Precellys 24 homogenizer (Bertin Technologies, Montigny-le-Bretonneux, France) set at 5000 rpm for three 30 s lysis cycles alternating with 30 s breaks at 4°C. The resulting lysates were transferred to a new 1.5 mL tube. The remaining beads were rinsed with an additional 200 µL of LB-P/D, which were combined with the initial lysate after short vortexing. Cell lysates were centrifuged for 10 min at 13,500 rpm at 4°C and supernatants transferred into a new 1.5 mL tube. Total protein concentration was measured using the Pierce™ BCA Protein Assay Kit (Thermo Scientific, Waltham, MA, USA) with a BioTek 800 TS microplate reader. 2 mg of total protein in a final volume of 800 µL of LB-P/D was added to the equivalent of 100 µL of Pierce™ High-Capacity Streptavidin Agarose Resin (Thermo Scientific) slurry, which had been incubated in 1 mL of LB containing 3% of freshly added BSA for 1 h at RT and washed four times with

1 mL of LB. For affinity purification of biotinylated proteins, lysates were incubated for 1 h on a rotating wheel at RT. Then, beads were washed once with 1 mL of wash buffer (50 mM Tris-HCl (pH 7.5), 2% SDS), five times with 1 mL LB, and five times with 1 mL ABC buffer (100 mM ammonium bicarbonate (pH 8.2)). Purified proteins were eluted from the beads by addition of 30 µL 3x SDS sample buffer containing 10 mM biotin and 20 mM dithiothreitol (DTT) and incubation for 10 min at 75°C. This step was repeated a second time, and the two eluates were combined and stored at -20°C. The denatured proteins were incubated for 10 min at 75°C with 1 µL of 100 mM DTT in a thermoshaker set at 1000 rpm, followed by a 10 min incubation in the dark at RT with 1 µL of 550 mM iodoacetamide (IAA). Then, the proteins were separated on NuPAGE 4-12 % Bis-Tris gels (Invitrogen, Carlsbad, CA, USA) in NuPAGE 1x MES SDS running buffer (Novex) for a total of 12 min at 200 V. Then, the gels were incubated in fixing solution (40% methanol, 7% acetic acid) for 1 h, stained by a 5-min incubation in Brilliant Blue G Colloidal Coomassie (Sigma-Aldrich), rinsed for 5 min in rinsing solution (25% methanol, 5% acetic acid), destained three consecutive times for 40 min with destaining solution (25% methanol), and washed for 3x 5 min in nanopure water. Each lane was cut from the slot to the migration front into three gel pieces of equal lengths (fractions), which were cut into smaller pieces. From this point on, each fraction was individually treated in HPLC-graded solutions and in low protein-binding tubes (Sarstedt). The fractions were washed three times by alternating 10-min incubations in 100-150 µL ABC buffer and 100-150 µL ethanol in a thermoshaker, set at 1000 rpm, at RT. Proteins were digested in-gel by an overnight incubation at 37°C in 120 µL ABC buffer containing 1 µg Sequencing Grade Modified Trypsin (Promega Madison, WI, USA). Proteolytic digestion was quenched by addition of 50 µL of 2% trifluoroacetic acid (TFA) and incubation of 10 min at RT in a thermoshaker set at 1000 rpm. The supernatant was transferred into a new tube and the remaining gel pieces were incubated in 100-150 µL of ethanol for 10 min, again at RT and at 1000 rpm. Then, the ethanol was combined with the first supernatant. The ethanol incubation and transfer were repeated a second time. The organic solvent of the combined supernatants was evaporated by using a SpeedVac. 200 µL of buffer A (0.1% formic acid) was added to the remaining volume and the samples centrifuged for 10 min at 13 krpm were loaded on C18 StageTips (61), which were beforehand equilibrated with 50 µL of buffer B (80% acetonitrile, 0.1 % formic acid) and washed twice with 50 µL of buffer A. After loading the samples, the StageTips were washed with 100 µL of buffer A. The samples were eluted with 50 µL of buffer B. The elution solvent was completely evaporated using a SpeedVac and the remaining peptides were resuspended first by addition of 3 µL of buffer A* (3% acetonitrile, 0.3% TFA) and vortexing and then 17 µL of buffer A*/A (30% buffer A*/70% buffer A). The samples were vortexed, quickly centrifuged, and stored at -80°C.

Mass spectrometry-based proteomic analysis

LC-MS/MS measurements were performed on a Q Exactive HF-X (Thermo Scientific) coupled to an EASY-nLC 1200 nanoflow-HPLC (Thermo Scientific). HPLC-column tips (fused silica) with 75 µm

inner diameter were self-packed with ReproSil-Pur 120 C18-AQ, 1.9 µm particle size (Dr. Maisch GmbH, Ammerbuch, Germany) to a length of 20 cm. Samples were directly applied onto the column without a pre-column. A gradient of A (0.1% formic acid in H_2O) and B (0.1% formic acid in 80% acetonitrile in H_2O) with increasing organic proportion was used for peptide separation (loading of sample with 0% B; separation ramp: from 5-30% B within 85 min). The flow rate was 250 nL/min and for sample application, it was 600 nL/min. The mass spectrometer was operated in the data-dependent mode and switched automatically between MS (max. of 1 x 10^6 ions) and MS/MS. Each MS scan was followed by a maximum of ten MS/MS scans using a normalized collision energy of 25% and a target value of 1000. Parent ions with a charge state form z = 1 and unassigned charge states were excluded for fragmentation. The mass range for MS was m/z = 370-1750. The resolution for MS was set to 70,000 and for MS/MS to 17,500. MS parameters were as follows: spray voltage 2.3 kV, no sheath and auxiliary gas flow, ion-transfer tube temperature 250°C.

The MS raw data files were analysed with the MaxQuant software package version 1.6.2.10 (62) for peak detection, generation of peak lists of mass-error-corrected peptides, and database searches. The UniProt *Saccharomyces cerevisiae* database (version March 2016), additionally including common contaminants, trypsin, TurboID, and GFP, was used as reference. Carbamidomethylcysteine was set as fixed modification and protein aminoterminal acetylation, oxidation of methionine, and biotin were set as variable modifications. Four missed cleavages were allowed, enzyme specificity was Trypsin/P, and the MS/MS tolerance was set to 20 ppm. Peptide lists were further used by MaxQuant to identify and relatively quantify proteins using the following parameters: peptide and protein false discovery rates, based on a forward-reverse database, were set to 0.01, minimum peptide length was set to seven, and minimum number of unique peptides for identification and quantification of proteins was set to one. The 'match-between-run' option (0.7 min) was used.

For quantification, missing iBAQ (intensity-based absolute quantification) values in the two control purifications from cells expressing either the GFP-TurboID or the NLSGFP-TurboID for the C-terminal tag bait controls or the TurboID-GFP or the NLS-TurboID-GFP for the N-terminal bait controls were imputed in Perseus (63). For normalization of intensities in each independent purification, iBAQ values were divided by the median iBAQ value, derived from all nonzero values, of the respective purification. To calculate the enrichment of a given protein compared to its average abundance in the two control purifications, the normalized iBAQ values were log2-transformed and those of the control purifications were subtracted from the ones of each respective bait purification. In the case of the TurboID series with the DC baits, the enrichment of a given protein was calculated compared to its median abundance in the two control purifications and the remaining DC purifications, except for the Acl1 and Bcl1 TurboID assays where these two were reciprocally excluded. For graphical presentation, the normalized iBAQ value (log10 scale) of each protein detected in the bait purification was plotted against its relative abundance (log2-transformed enrichment) compared to the control purifications. For the bar graph representation, the log2-transformed enrichment of a given protein in the indicated TurboID assays is

represented by bars, while its median normalized log2-transformed enrichment across the different TurboID assays is shown as a dotted line.

MiniTurbo-based proximity labelling in HeLa cells

The DNA sequence coding for the *Homo sapiens* RPL10A protein was PCR-amplified from plasmid pADH111-HsRPL10A (pDK10427), generated by cloning the PCR-amplified *RPL10A* coding sequence (template pNTI194 (Addgene plasmid #84266)) into the *Nde*I/*Bam*HI-restricted plasmid pADH111-LTV1 (pDK3331), and cloned by Gibson assembly (NEB, M5510A) between the *Nhe*I and *Pst*I restriction sites of the lentiviral donor vector pSKP-32, a pCW57.1-derived plasmid bearing the MND-Blasticidin resistance cassette instead of the hPGK-Puromycin resistance cassette (64), to generate plasmid pDS79 containing the *RPL10A* gene under the transcriptional control of a doxycycline-inducible promoter and fused at its 3' end to sequences encoding the V5 tag, the miniTurbo (MT) biotin ligase, and the HA tag. As controls, pSKP-32 plasmids encoding HA-MT-V5-EGFP (pDS48) and EGFP-V5-MT-HA-NLS (pDS82), respectively, were constructed. Replication-defective lentiviral particles were produced as previously described (65) by co-transfecting, using the JetPRIME transfection reagent (Polyplus, 114-75), the above lentiviral donor plasmids with packaging and envelope expressing plasmids psPAX2 (Addgene plasmid #12260) and pMD2.G (Addgene plasmid #12259) into HEK293T cells seeded the night before. Transfection medium was changed 12 h post transfection, and lentiviral supernatants were harvested 24 h later, filter-sterilized through 0.2 µm syringe filters, supplemented with 8 µg/ml polybrene (Sigma-Aldrich, H9268), and stored in aliquots at -80°C. These lentiviral particles expressing the different fusion constructs were, at different viral dilutions (1:2 to 1:100) prepared in Dulbecco's Modified Eagle Medium (DMEM, PAN-Biotech, P04-04510) containing 8 µg/ml polybrene, used to infect HeLa cells (ATCC CCL-2), which had been validated by genotyping (Microsynth) and negatively tested for mycoplasma. HeLa cells were grown in a humidified incubator in DMEM supplemented with 10% Fetal Bovine Serum (FBS, Biowest, S181B-500) and 1% penicillin-streptomycin (PAN-Biotech, P06-07100) at 37°C and 5% CO_2. Infected cells were selected 24 h post infection in medium (DMEM, 10% FBS, and 1% penicillin-streptomycin) containing 4 µg/ml Blasticidin (InvivoGen, ant-bl-1) until selection was complete. Selected cells were tested by Western blotting using anti-HA antibodies (mouse monoclonal anti-HA antibody (6E2); Cell Signaling, #2367) to assess expression of the HA-tagged fusion proteins and to determine the optimal viral dilution. For the proximity-labelling experiment, HeLa cells (two 15 cm dishes per replicate) were infected in three experimental replicates with the lentiviral particles expressing the RPL10A-V5-MT-HA fusion protein and the HA-MT-V5-EGFP and EGFP-V5-MT-HA-NLS control fusion proteins. Expression was induced with 2 mg/ml doxycycline for 24 h and biotinylation by incubation in the presence of 400 µM biotin for 90 min. Then, cells were washed five times with ice-cold PBS, scraped, harvested by centrifugation at 3000 rpm for 2 min, snap frozen in liquid nitrogen, and stored at -80ºC.

Cell pellets were lysed in 1.2 mL of modified RIPA buffer (50 mM Tris-HCl (pH 7.5), 150 mM NaCl, 1 mM EDTA, 1 mM EGTA, 1% Triton X-100, 0.5% sodium deoxycholate, and 0.1% SDS), containing Benzonase (1:5000 dilution), cOmplete™, EDTA-free Protease Inhibitor Cocktail (Roche, 05-056-489-001), and 1 mM PMSF, by a 30-min incubation on ice with periodical vortexing (four times 15 s). Then, cell lysates were clarified by centrifugation at 14,000 rpm for 10 min at 4ºC and transferred to a new tube. Total protein concentration in the clarified cell extracts was determined with the Pierce™ BCA Protein Assay Kit (Thermo Scientific, 23225) using a microplate reader (BioTek 800 TS). For affinity purification of biotinylated proteins, 100 µL of Pierce™ High Capacity Streptavidin Agarose Resin (Thermo Scientific, 20361) slurry, corresponding to 50 µL of settled beads, were washed twice with modified RIPA buffer L (lacking sodium deoxycholate, SDS, protease inhibitors, and PMSF), and equal amounts of proteins (3.5 mg) in a total volume of 1.3 mL were incubated with the washed beads for 90 min on a rotating wheel at RT. After binding, beads were washed five times with the modified RIPA buffer, three times with a HEPES buffer (50 mM HEPES-KOH (pH 8), 100 mM KCl, 2 mM EDTA, 0.1% Triton X-100, and 10% glycerol), and two times with the ABC buffer (100 mM ammonium bicarbonate (pH 8.2).

Bound proteins were processed by a filter-aided sample preparation (FASP) protocol (66). After the last wash, biotinylated proteins bound to the streptavidin beads were denatured with 8 M urea in a 50 mM Tris-HCl (pH 8) buffer containing 1 mM DTT for 5 min at RT. The denatured proteins and the beads were transferred to a 10 kDa molecular weight cut-off filter centrifugal unit (Vivacon 500, 10,000 MWCO; Sartorius, VN01H02), followed by reduction with 1 mM DTT and alkylation with 5.5 mM iodoacetamide for 10 min in the dark at RT. The samples were centrifuged at 10,000 x g for 30 min and then washed three times with 50 mM Tris-HCl (pH 8) buffer with the same centrifugation conditions. On-filter digestion of proteins was performed overnight at 37°C in a thermoshaker set to 550 rpm in 200 µL 50 mM Tris-HCl (pH 8) buffer containing 1.5 µg Sequencing Grade Modified Trypsin (Promega, V5113). Tryptic peptides were eluted by centrifugation, purified over C18 StageTips, and analysed by LC-MS/MS as described above.

The MS raw data files were analysed with the MaxQuant software package version 1.6.2.10 (62), using the UniProt *Homo sapiens* database (version 2016), additionally including common contaminants, trypsin, miniTurbo, and GFP, as reference. Perseus (software version 1.6.2.3) (63) was used for further data analysis. For quantification, missing iBAQ values in the control purifications from cells expressing either the HA-MT-V5-EGFP or the EGFP-V5-MT-HA-NLS bait were imputed in Perseus.

For normalization of intensities in each independent purification, iBAQ values were divided by the median iBAQ value, derived from all nonzero values, of the respective purification. Then, the average of the median-normalized iBAQ values obtained for the three experimental RPL10A bait replicates, excluding the missing values (Not a Number (NaN) values), and the six experimental control replicates were calculated. To calculate the enrichment of a given protein compared to its average abundance in the control purifications, the normalized, averaged iBAQ values were log2 transformed and those of the

control purifications were subtracted from the ones of the RPL10A bait purification. For graphical representation, the normalized, averaged iBAQ value (log10 scale) of each protein detected in the RPL10A bait purification was plotted against its relative abundance (log2-transformed enrichment compared to the control purifications).

Yeast two-hybrid (Y2H) interaction assay

The Y2H reporter strain PJ69-4A (67) was co-transformed with two plasmids expressing the bait protein fused to the Gal4 DNA-binding domain (G4BD, *TRP1*) and the prey protein fused to the Gal4 activation domain (G4AD, *LEU2*). Transformed cells were selected on synthetic complete plates lacking leucine and tryptophan (SC-LT). The protein-protein interactions were documented by spotting representative transformants in 10-fold serial dilution steps onto SC-LT, SC-His-Leu-Trp (SC-HLT, *HIS3* reporter), and SC-Ade-Leu-Trp (SC-ALT, *ADE2* reporter) plates, which were incubated for 3 days at 30°C. Growth on SC-HLT plates is indicative of a weak/moderate interaction, whereas only relatively strong interactions also permit growth on SC-ALT plates.

In vitro binding assays

For in vitro binding assays between binary combinations of full-length or truncated variants of Acl1, Bcl1, and Rpl1, the two proteins were co-expressed from pETDuet-1 (Novagen) in Rosetta(DE3) (Novagen) *E. coli* cells. Cells were grown in 200 mL of lysogeny broth (LB) medium containing ampicillin and chloramphenicol at 37°C and protein expression was induced at an $OD_{600\ nm}$ of around 0.6 to 0.8 by the addition of IPTG to a final concentration of 0.5 mM. After 5 h of growth at 23°C, cells were harvested and stored at -80°C. Cells were resuspended in 25 mL lysis buffer (50 mM Tris-HCl pH 7.5, 200 mM NaCl, 1.5 mM MgCl2, 5% glycerol) and lysed with a M-110L Microfluidizer (Microfluidics). The lysate (30 mL volume) was adjusted by the addition of 300 µL 10% NP-40 to 0.1% NP-40 (note that from here onwards all buffers contained 0.1% NP-40). An aliquot of 50 µL of total extract (sample T) was taken and mixed with 50 µL of 6x SDS sample buffer. The total extract was then centrifuged at 4°C for 20 min at 14,000 rpm. The soluble extract was transferred to a 50 mL Falcon tube and, as above, an aliquot of 50 µL of soluble extract (sample S) was taken and mixed with 50 µL of 6x SDS sample buffer. The insoluble pellet fraction (sample P) was resuspended in 3 mL of lysis buffer and 5 µL thereof were mixed with 45 µL of lysis buffer and 50 µL of 6x SDS sample buffer. The soluble extract (30 mL) was adjusted to 15 mM imidazole by adding 180 µL 2.5 M imidazole pH 8. Upon addition of 250 µL of Ni-NTA Agarose slurry (Qiagen), samples were incubated for 2 h on a turning wheel at 4°C. Then, the Ni-NTA Agarose beads were pelleted by centrifugation at 4°C for 2 min at 1800 rpm, resuspended in 2 mL of lysis buffer, and transferred to a 2 mL Eppendorf tube.

The Ni-NTA Agarose beads were first washed five times with 1 mL of lysis buffer containing 15 mM imidazole and then two times for 5 min, by rotation on a turning wheel at 4°C, with 1 mL lysis buffer containing 50 mM imidazole. Elution of bound proteins was carried out by incubation of the Ni-NTA Agarose beads with 1 mL of lysis buffer containing 500 mM imidazole for 5 min on a turning

wheel at 4°C. The eluate (sample E) was transferred to a 1.5 mL Eppendorf tube and 50 µL thereof were mixed with 50 µL of 6x SDS sample buffer. Protein samples (5 µL of samples T, P, S, and E) were separated on Bolt 4-12% Bis-Tris Plus 15-well gels (Invitrogen), run in Bolt 1x MES SDS running buffer, and subsequently stained with Brilliant Blue G Colloidal Coomassie (Sigma). For Western analysis, appropriate dilutions of the above samples were separated on Bolt 4-12% Bis-Tris Plus 15-well gels, run in 1x MES SDS running buffer, and proteins were subsequently blotted onto nitrocellulose membranes (GE Healthcare).

For purification of the trimeric Acl1-Rpl1-Bcl1 complex, Rpl1 and either C-terminally Flag-tagged Acl1 or untagged Acl1 (negative control purification) were co-expressed from pETDuet-1 and C-terminally $(His)_6$-tagged Bcl1.N366 was expressed from pET-24d. Rosetta(DE3) cells were co-transformed with the two plasmids and grown in 600 mL of LB medium containing ampicillin, kanamycin, and chloramphenicol. The co-expressed proteins were purified by a two-step affinity purification approach, first via Ni-NTA and then via anti-FLAG agarose beads. The Ni-NTA purification was done as described above, but bound proteins were eluted two consecutive times with 500 µL of lysis buffer containing 500 mM imidazole for 5 min on a turning wheel at 4°C. An aliquot of 50 µL of the first imidazole eluate (sample E1) was mixed with 50 µL of 6x SDS sample buffer. Then, the two eluates were combined and incubated for 2 h with 30 µL of Anti-FLAG M2 Affinity Gel slurry (Sigma-Aldrich). Subsequently, the bead-containing solution was transferred to Mobicol "Classic" columns (Mo Bi Tec), and beads were washed three consecutive times with 1 mL of lysis buffer. Bound proteins were eluted with 50 µL of lysis buffer containing 454 µg/mL 1xFLAG peptide (Sigma-Aldrich) for 30 min on a turning wheel 4°C. The entire FLAG eluate (~50 µL) was mixed with 50 µL of 6x SDS sample buffer (sample E2). 5 µl of eluate samples E1 and E2 were, as described above, separated on gels and analysed by Coomassie staining and Western blotting.

Fluorescence microscopy

To assess their subcellular localization, proteins were tagged with yeast codon-optimized mNeonGreen (referred to as ymNeonGreen or ymNG) ((68); Allele Biotechnology, San Diego, USA) or a single (yEGFP) or triple yeast-enhanced GFP (3xyEGFP) (69) and expressed, as indicated in the figure legends, either from the genomic locus or from plasmids under the control of their cognate promoter or the *ADH1* promoter. The nucleolar marker protein Nop58-yEmCherry was either expressed from its genomic locus or from plasmid under the control of its cognate promoter. Transformed cells were grown in the indicated liquid media at 30°C and inspected in exponential growth phase. Live yeast cells were imaged by fluorescence microscopy using a VisiScope CSU-W1 spinning disk confocal microscope (Visitron Systems GmbH, Puchheim, Germany). The ImageJ software was used to process the images.

Sucrose gradient analysis and fractionation

Cell extracts for polysome profile analyses were prepared as previously described (70) and eight A_{260} units were layered onto 10-50% sucrose gradients that were centrifuged at 39,000 rpm in a TH-641

swinging bucket rotor (Thermo Scientific) at 4°C for 2 h 45 min. Sucrose gradients were analysed using an ISCO UA-6 system with continuous monitoring at A_{254}. For the fractionation experiments, five A_{260} units were subjected to sucrose gradient centrifugation and 20 fractions of around 500 µL were collected and processed as described (60). Precipitated proteins were resuspended in 50 µL 3x SDS sample buffer and 5 µL each fraction was separated on NuPAGE 4-12% Bis-Tris 26-well gels (Novex), run in 1x MES running buffer, and subsequently analysed by Western blotting. As an input control, 0.05 A_{260} units of total cell extract was run alongside the fractions.

Preparation of total yeast protein extracts and Western analysis

Total yeast protein extracts were prepared as previously described (71). Western blot analysis was carried out according to standard protocols. The following primary antibodies were used in this study: anti-Rpl1 (1:5000; obtained from the laboratory of J. de la Cruz, University of Sevilla, Sevilla, Spain (72)), anti-Rpl4 (1:10,000; L. Lindahl, University of Baltimore, Baltimore, USA), anti-Rps3 (1:15,000; M. Seedorf (73)), mouse monoclonal anti-FLAG (1:2000 - 1:10,000; Sigma), anti-His_6 (1:500; Roche). Secondary goat anti-mouse or anti-rabbit horseradish peroxidase-conjugated antibodies (Bio-Rad, Hercules, USA) were used at a dilution of 1:10,000. For detection of TAP-tagged proteins, the peroxidase anti-peroxidase (PAP) Soluble Complex antibody produced in rabbit (Sigma-Aldrich) was used at a dilution of 1:20,000. Immobilized protein-antibody complexes were visualized by using enhanced chemiluminescence detection kits (WesternBright Quantum and Sirius; Advansta, San Jose, USA) and a Fusion FX7 Edge imaging system (Vilber, Germany). Images were processed with ImageJ (74) or the Evolution-Capt Software (Vilber). Intensities of Rpl1 and Rpl4 signals in sucrose gradient fractions were quantified using the Evolution-Capt Software for the two experimental replicates (n=2). The normalized abundance of Rpl1 and Rpl4 in the individual fractions was calculated by dividing their signal intensity in each fraction by their average signal intensity in two polysomal fractions (fractions 13 and 14). The normalized Rpl1/Rpl4 ratios of each fraction were calculated and plotted on the y-axis against the corresponding fraction number on the x-axis.

Protein expression and purification for X-ray crystallography

For the expression and purification of the Rpl1(63-158)-Acl1.N127 complex, *E. coli* BL21(DE3) cells (Novagen) were transformed with pDK9667 (pETDuet-1/RPL1B(63-158)-$(His)_6$--ACL1.N127) and plated on LB agar containing 100 µg/mL ampicillin. Following overnight incubation at 37°C, expression cultures were inoculated directly from the plate. Protein production was carried out in LB medium containing 100 µg/mL ampicillin under auto-induction conditions (1% (w/v) D(+)-lactose-monohydrate). The cultures were incubated for 16 h at 30°C with shaking at 180 rpm. Cells were harvested by centrifugation (4000 rpm, 15 min, 4°C; Fiberlite F9-6 x 1000 LEX fixed angle rotor (Thermo Scientific)) using a Sorvall LYNX 6000 centrifuge (Thermo Scientific) and resuspended in 20 mL of buffer A (20 mM HEPES (pH 8.0), 250 mM NaCl, 20 mM $MgCl_2$, 20 mM KCl, 40 mM imidazole). Cell lysis was performed using a M-110L Microfluidizer (Microfluidics) and the lysate was

clarified by high-speed centrifugation (20,000 rpm, 20 min, 4°C; LYNX A27-8 x 50 fixed angle rotor (Thermo Scientific)) using a Sorvall LYNX 6000 centrifuge. Protein purification was then accomplished in a two-step process via immobilized metal ion affinity chromatography (IMAC) with nickel-nitrilotriacetic acid (Ni-NTA) followed by size exclusion chromatography (SEC): The clarified lysate was first applied to a 5 mL HisTrap Fast Flow column (Cytiva). Immobilized target proteins were washed with ten column volumes (CV) of buffer A and eluted with seven CV of buffer B (20 mM HEPES (pH 8.0), 250 mM NaCl, 20 mM $MgCl_2$, 20 mM KCl, 500 mM imidazole). The Rpl1(63-158)-Acl1.N127 complex was then further purified by SEC using a HiLoad 16/600 Superdex 200 column (Cytiva) equilibrated with SEC buffer (20 mM HEPES (pH 7.5), 200 mM NaCl, 20 mM $MgCl_2$, 20 mM KCl). Finally, peak fractions containing the Rpl1(63-158)-Acl1.N127 complex, as verified by Coomassie-stained SDS-PAGE, were pooled and concentrated.

Crystallization and structure determination

Crystallization screens were performed by the sitting drop method in MRC 2-well crystallization plates (SWISSCI) at 20°C, with 0.5 µL drops composed of protein and precipitant solutions mixed in 1:1 and 1:2 ratios. Precipitation solutions were acquired commercially (NeXtal JCSG Core Suite I-IV, each comprising 96 crystallization conditions). The Rpl1(63-158)-Acl1.N127 complex crystallized at a concentration of 39 mg/mL within four weeks in 0.2 mM ammonium acetate, 0.1 mM sodium citrate (pH 5.6), and 30% (w/v) PEG 4000.

Prior to data collection, crystals were flash-frozen in liquid nitrogen employing a cryo-solution that consisted of mother liquor supplemented with 20% (v/v) glycerol. X-ray diffraction data were collected under cryogenic conditions at the European Synchrotron Radiation Facility (ESRF; Grenoble, France) beamline ID30A-3. Data were processed with XDS and scaled with XSCALE (75). The structure was determined by molecular replacement with Phaser (76), manually built in Coot (77), and refined with PHENIX (78). The search models for the Rpl1(63-158)-Acl1.N127 complex were the X-ray structure of the synthetic E3_5 DARPin L86A mutant (PDB: 4J7W; (79)) and the structure model of *S. cerevisiae* Rpl1b (AF-P0CX44-F1) predicted by AlphaFold (80-82).

Analysis of experimental and predicted structures

Analysis and image preparation of three-dimensional structures, downloaded from the PDB archive or predicted with AlphaFold-Multimer or AlphaFold3 (80,81,83), were carried out with the ChimeraX (84,85) software.

Identification of orthologous proteins and sequence alignments

Orthologous proteins of *S. cerevisiae* Acl1 (UniProt: P25631) were found using the defaults settings of the BLAST function of the UniProtKB (86), which also indicates the phylogenetic tree (e.g., kingdom, subkingdom, phylum, and subphylum) of the identified orthologous proteins. Multiple sequence alignments of orthologous proteins were independently generated for subkingdoms, phyla, or subphyla

in the ClustalW output format with T-Coffee using the default settings of the EBI website interface (87). According to the Alliance of Genome Resources (https://www.alliancegenome.org; Version: 8.2.0), *H. sapiens* WDR89 (UniProt: Q96FK6) is the orthologous protein of *S. cerevisiae* Bcl1 (UniProt: P53962).

Determination of co-translational capturing by qRT-PCR

Co-translational association of Acl1-TAP, Bcl1-TAP, TAP-Bcp1, Bcp1-TAP, TAP-Rrb1, and Acl4-TAP with nascent r-proteins was assessed by IgG-Sepharose pull-down and real-time quantitative reverse transcription PCR (real-time qRT-PCR) as previously described (41,44) with the following modifications: (i) after the last wash, the beads were resuspended in 200 µL of lysis buffer-PC containing 1 mM of DTT; then, 2 µL of RiboLock and 5 µL of home-made TEV protease were added and the samples were incubated overnight on a rotating wheel at 4°C; (ii) for RNA isolation, 50 µL of total cell extracts were diluted with 150 µL of lysis buffer, and RNA was purified from total extracts and TEV eluates using the Quick-RNA Microprep Kit (Zymo Research) and eluted in 15 µL of RNase/DNase free water; then, purified total RNAs were diluted to 5 ng/µL and the volume of the TEV-eluate RNA extracts was increased to 120 µL.

The following oligonucleotide pairs were used for the specific amplification of DNA fragments, corresponding to the *RPL1A/B*, *RPL3*, *RPL4*, and *RPL23A/B* mRNAs, from the input cDNAs: RPL1A/B-forward: 5'-ACCCCAGTTTCTCACAACGA-3', RPL1A/B-reverse: 5'-GCAACAGCCAAACACAAGA-3' (amplicon size 98 base pairs (bp)), RPL3-forward: 5'-ACTCCACCAGTTGTCGTTGTTGGT-3', RPL3-reverse: 5'-TGTTCAGCCCAGACGGTGGTC-3' (amplicon size 86 bp), RPL4-forward: 5'-ACCTCCGCTGAATCCTGGGG T-3', RPL4-reverse: 5'-ACCGGTACCACCACCACCAA-3' (amplicon size 72 bp), RPL23-forward: 5'-AGGGTAAGCCAGAATTGAGAAA-3', RPL23-reverse: 5'-ACACCGTCTCTTCTTCTCCAAG-3' (amplicon size 82 bp)

RESULTS

Establishing the proxiOME of LSU r-proteins by TurboID-based proximity labelling

DCs transiently interact with free r-proteins before these get incorporated into pre-ribosomal subunits and then become integral components of the long-lived mature ribosomal subunits. Accordingly, it has turned out to be challenging and laborious to efficiently identify DCs in classical affinity purifications of their tagged r-protein clients (34,44,88). With the aim of facilitating the identification of new potential DCs, we considered harnessing the beneficial characteristics of the TurboID-based proximity labelling approach (Figure 1A). TurboID is a promiscuous, highly efficient biotin protein ligase derived from the *Escherichia coli* BirA protein (89). Biotin protein ligases convert biotin into a reactive biotinoyl-5'-AMP (bioAMP) intermediate, which is bound with lower affinity by promiscuous variants, such as BioID or TurboID, than by wild-type BirA (89-91), thereby leading to the formation of a bioAMP concentration gradient around these enzyme variants (92). The released bioAMP then reacts with surface-exposed primary amines, i.e., mostly the ε-amino group of lysine residues, of proximal proteins; thus, not only leading to the covalent biotinylation of the enzyme-fused bait protein but also of neighbouring proteins that are situated within a certain radius, up to ~10 nm in the case of BioID (93), around the promiscuous biotin protein ligase (92). However, the actual labelling radius depends on a number of different parameters, such as the used biotin protein ligase variant and its activity in a given subcellular compartment, the labelling time, the intracellular concentration of biotin, the half-life of the reactive bioAMP, and the duration of the proximity between the enzyme-fused bait protein and its protein neighbourhood(s). Compared to the first-generation BioID variant, which requires long labelling times (up to 24 h) and shows optimal activity at 37ºC (89,91,93), TurboID exhibits much faster labelling kinetics, yielding almost the same extent of protein biotinylation in 10 min as BioID in 18 h after biotin addition (89). Importantly, TurboID also displays high activity at 30ºC; thus, permitting to successfully implement the TurboID-based proximity labelling approach in yeast (89,94-96). After the in vivo proximity labelling and cell lysis, the biotinylated proteins, i.e., the enzyme-fused bait protein and its proximal proteins as well as any non-specifically labelled proteins (background of non-proximal biotinylated proteins that is specific for the cellular compartment(s) where the enzyme-fused bait protein is present) and the four endogenously Bpl1-biotinylated proteins (Acc1/Hfa1, Arc1, Dur12, and Pyc1/Pyc2 (93,96)), can be efficiently purified with streptavidin-coupled beads under stringent conditions and, subsequently, identified and quantified by liquid chromatography-tandem mass spectrometry (LC-MS/MS) (Figure 1A; see Materials and Methods). As our main goal was to identify new DCs, which are expected to only transiently interact with newly synthesized r-proteins until these get incorporated into pre-ribosomal particles (42), we decided to express the TurboID-fused r-proteins from a centromeric plasmid under the control of the copper-inducible *CUP1* promoter in exponentially growing wild-type cells for 1 h. In this setting, expression and biotinylation can be simultaneously induced by simply adding copper and biotin to the culture medium. To minimize as much as possible

persistent biotinylation arising prior induction from the continuous low-level expression of the TurboID-tagged bait r-proteins, due to basal activation of the *CUP1* promoter by low copper concentrations in the standard culture media, and from the utilization of endogenous biotin, which could lead to a disproportionately high labelling of the long-lived r-protein neighbourhoods on mature 60S subunits, we cultured cells in synthetic complete medium prepared with copper-free yeast nitrogen base.

By employing this approach, we have already shown in a previous study that Rrb1 is strongly enriched and highly abundant in the streptavidin pull-down of cells expressing the C-terminally TurboID-tagged Rpl3 bait (95), indicating that our TurboID-based proximity labelling approach should in principle be well suited for the identification of new candidate DCs. Therefore, and initially focusing on the LSU r-proteins, we decided to directly perform TurboID assays with all 46 LSU r-proteins. Since 35 of the 46 different LSU r-proteins are encoded by two paralogous genes (referred to as the A and B copy), yielding identical or nearly identical r-proteins (denoted by an a or b after the r-protein name), we selected in almost all cases the paralogous r-protein whose absence was shown to be lethal or to confer the stronger growth defect (97), which largely correlates with their higher estimated abundance (98), as bait for the assay. Considering that five of the eight established DCs have been shown to recognize the N-terminal extremity of their r-protein client (32,41,44-46,99), we chose, reasoning that an N-terminally fused TurboID moiety might potentially affect the capacity of an r-protein bait to interact with its prospective DC, to first conduct the TurboID-based proximity labelling screen with the C-terminally TurboID-tagged LSU r-proteins. Nevertheless, and in order to maximize the discovery of novel DCs, we also analysed in a second series the proxiOMEs of the N-terminally TurboID-tagged LSU r-proteins. As Rpl40 (eL40) is naturally expressed from the paralogous *UBI1*/*UBI2* genes as identical fusion proteins (Ubi1/2) containing an N-terminal ubiquitin moiety (36), which enhances the stable expression of Rpl40 and is rapidly, normally prior to the incorporation of Rpl40 into cytoplasmic pre-60S particles, removed from the Ubi1/2 precursors (38,39,100,101), we performed the proximity labelling with the Ubi1-TurboID and the TurboID-Rpl40a baits. By doing so, the natural context of ubiquitin release from the Ubi1 precursor is preserved for the Ubi1-TurboID bait, whereas the generation of Rpl40 lacking the N-terminal TurboID moiety is avoided by directly fusing the TurboID to the N-terminal end of Rpl40. In each independent experimental set of the screen with the C-terminally TurboID-tagged LSU r-proteins, consisting for practical reasons of maximally nine different r-protein baits, we included Rpl3-TurboID as an internal quality control in order to validate the successful realization of the multi-step experiment. As most r-proteins exhibit a transient nuclear localization, we used two different C-terminally TurboID-tagged yEGFP fusion proteins, the mainly cytoplasmic yEGFP-TurboID and the nuclear NLS-yEGFP-TurboID (Supplementary Figure S2A), as controls for determining the non-specific background labelling in the two cellular compartments containing unassembled and (pre-)ribosome-incorporated r-proteins. To calculate the specific enrichment of the purified proteins detected upon induced expression of a given TurboID-tagged r-protein, we divided the normalized abundance intensity (intensity-based absolute quantification (iBAQ) values) of each protein

by its averaged normalized iBAQ abundance intensity, with prior imputation of missing values, in the two control purifications (see Materials and Methods). For graphical representation, we plotted the normalized iBAQ abundance (y-axis) of each protein detected in the streptavidin pull-down from cells expressing a given TurboID-tagged bait r-protein against its specific enrichment (x-axis); thus, displaying strongly enriched and highly abundant proteins in the upper right zone of these plots (see for example Figure 1B). For the screen with the N-terminally TurboID-tagged r-proteins, we used in each independent experimental set TurboID-Rpl1b as the positive control, which enriches the novel DC Acl1 as well as several AFs that are in the proximity of Rpl1 on successive pre-60S particles (see below and Figure 3A), and the mainly cytoplasmic TurboID-yEGFP and nuclear NLS-TurboID-yEGFP fusion proteins as background controls (Supplementary Figure S2A). Having at disposal eight and six experimental replicates of the Rpl3-TurboID and the TurboID-Rpl1b experiment, respectively, enabled us to evaluate the reproducibility of our TurboID-based proximity labelling approach. Importantly, both the DC and the same set of enriched AFs and r-proteins could be detected at similar enrichment in all replicates of the Rpl3-TurboID or the TurboID-Rpl1b assays (Figure 1C and Supplementary Figure S10A). Given the high reproducibility and relatively low enrichment variability, we considered it fully sufficient to perform the TurboID assays of all LSU r-proteins in single replicates, even more so because we utilized this approach as a large-scale screen to identify candidate interactors and select promising ones for further validation. On the other hand, the highly reproducible replicates encouraged us to confidently explore and evaluate, on the basis of the Rpl3-TurboID and TurboID-Rpl1b proxiOMEs, whether our TurboID-based proximity labelling approach was also suitable for the identification of r-protein neighbourhoods on pre-60S particles and mature 60S subunits (see below). To display the enormous amount of generated data in an easily accessible manner, the r-protein baits as well as the prominently enriched proteins, mainly corresponding to AFs and r-proteins, are labelled with their protein names in the graphical representations of the complete TurboID data set of all N- and C-terminally TurboID-tagged LSU r-proteins (Supplementary Figure S1).

As judged by the iBAQ abundance of the fused TurboID in the streptavidin pull-downs of biotinylated proteins, all TurboID-tagged bait r-proteins were expressed at comparable levels after copper induction for 1 h. In line with their efficient expression, almost all bait r-proteins could be detected by the MS analysis and were found to be substantially enriched in their proximity labelling assays (Supplementary Figure S1). In three cases (Rpl29, Rpl40a, and Rpl41b bait), only the TurboID moiety but not the fused r-protein could be detected in the analysis of non-biotinylated peptides generated by trypsin cleavage, which was used for the identification and quantification of proteins. Rpl41 (eL41) is the shortest yeast r-protein, it is made up of 25 amino acids and contains a total of 17 Arg and Lys residues; thus, digestion with trypsin does not yield any peptides that can be identified and quantified by MS analysis. In the case of Rpl29 (eL29), which consists of 59 amino acids and contains 13 Lys and four Arg residues, it is less clear why it could not be detected as trypsin digestion should in theory yield two unique peptides that are not excluded by the applied minimum peptide length parameter,

which was set to seven residues. However, the enrichment of Rpl29 could be detected by the specific identification of peptides containing the biotin modification in the Rpl29 TurboID assays. The identical Rpl40a and Rpl40b are only 52 residues long and contain 10 Lys and six Arg residues. Therefore, and not unexpectedly, non-biotinylated Rpl40 peptides could neither be detected in the MS analysis of the streptavidin pull-downs from cells expressing the Ubi1-TurboID nor the TurboID-Rpl40a bait. However, one Rpl40 peptide containing a biotinylated Lys residue (Lys12 in Rpl40 sequence) could be identified in the TurboID assay of the Ubi1-TurboID bait. Finally, Rpl42 (eL42), consisting of 106 amino acids and containing 23 Lys and eight Arg residues, could only be detected in the TurboID assay performed with the Rpl42a-TurboID bait, but not when TurboID-Rpl42a was used as the bait.

TurboID-based proximity labelling reveals neighbourhoods of r-proteins on pre-ribosomal particles

It is important to mention that we have not experimentally assessed the capacity of the TurboID-tagged r-proteins to get incorporated into pre-60S particles and mature 60S subunits. However, the identification of AFs or r-proteins that are known, based on the available cryo-EM and X-ray structures of pre-60S and mature 60S subunits, to be in the neighbourhood of a given TurboID-tagged r-protein can be used as a proxy for its successful incorporation. A closer inspection of the Rpl3-TurboID bait proxiOME revealed that, besides its DC Rrb1, several known early-associating (Dbp9, Loc1, Mak11, Nog1, Rlp24, Rrp15, Spb4, and Ssf1/2) and late-associating (Reh1 and Rei1) pre-60S AFs were reproducibly and quite specifically enriched (Figure 1B, C, and Supplementary Figure S3), indicating that the Rpl3-TurboID fusion protein gets efficiently incorporated into early nucleolar pre-60S particles and remains associated with pre-60S particles along their entire maturation path. In line with this, Rpl3-TurboID, when expressed from a centromeric plasmid under the transcriptional control of its cognate promoter, complemented the absence of endogenous Rpl3 reasonably well on synthetic growth medium (Supplementary Figure S2B). Importantly, and in support of the observed proximity labelling being due to a true physical proximity, most of these highly enriched AFs are indeed located in close proximity of the C-terminus of Rpl3, from which the TurboID moiety emerges at the LSU surface, on pre-60S particles. Five of the early-associating AFs (Mak11, Nog1, Rlp24, Rrp15, and Ssf1) could be visualized in the cryo-EM structure of the early nucleolar state 2 pre-60S particle (102), purified via the Nsa1 and Nop2 baits, and parts of Nog1, Rlp24, Rrp15, and Ssf1 are in immediate vicinity of Rpl3's C-terminal end, while the β-propeller domain of Mak11 is located behind the Rpl3-proximal regions of Nog1 and Rlp24 (Figure 1D). The extent of Nog1's proximity becomes even more apparent on the late nucleolar state E1 pre-60S intermediate (Figure 1E), where two additional α-helices within the C-terminal region of Nog1 can for the first time be seen in atomic models of pre-60S cryo-EM structures (103). In the case of Spb4, which likely associates with intermediate nucleolar pre-60S particles (state D) and can be visualized both on state D and the late nucleolar state E pre-60S particles (103-105), its only partially resolved C-terminal extension projects from the LSU surface and thereby gets into proximity of the

TurboID moiety attached to Rpl3's C-terminal end (Figure 1E; (103)). On the cytoplasmic state I pre-60S intermediate, purified via the Lsg1-TAP bait, the C-terminal end of Rei1 plunges deep into the polypeptide exit tunnel (PET), and the preceding Rei1 segments meander across the solvent-side surface of the LSU, leaving the unmodelled N-terminal part of Rei1 (residues 1-144) in close proximity of Rpl3's C-terminal end (Figure 1G; (101)). In subsequent snapshots of cytoplasmic, Lsg1-purified pre-60S subunits (states II-VI), Rei1 has been replaced by Reh1; however, the atomic model of Reh1 is limited to its C-terminal region that is inserted into the PET. Notably, the cryo-EM maps contain additional density that corresponds to the N-terminal parts of Rei1 and Reh1 in direct contact with the AF Tif6 (101). In support of this, AlphaFold3 predictions revealed that the highly conserved C2H2-type zinc finger domain located at the N-terminal end of Rei1 (residues 1-45) and Reh1 (residues 1-44) has the capacity to interact with Tif6. Importantly, superposition of the AlphaFold models with the cryo-EM structures of Rei1- or Reh1-bound pre-60S subunits indicated that these predicted interactions between Tif6 and Rei1 or Reh1 could in principle also occur on pre-60S subunits (Supplementary Figure S4D) (83). In line with these in silico analyses, Y2H assays revealed a quite robust interaction of the N-terminal 66 residues of Rei1 (N66 construct; i.e., starting at the N-terminus and ending at residue 66) or the N-terminal 62 residues of Reh1 (N62 construct) with full-length Tif6 (Supplementary Figure S4E) (83). Tif6, however, which is in close proximity of Rpl3's C-terminal end almost throughout the entire pre-60S maturation path, could only be detected via one non-biotinylated peptide in one of the eight experimental replicates of the TurboID assays with the Rpl3-TurboID bait. At first glance, this non-enrichment of Tif6 seems surprising, but it can easily be explained by the fact that Tif6 contains only two lysine residues (K18 and K93), with the K18 side chain engaging in a backbone hydrogen bond at the interior and only the K93 side chain being surface-exposed and in reasonable proximity of Rpl3' C-terminal end; thus, limiting the identification of this long-lasting pre-60S neighbourhood by our biotinylation-dependent proximity labelling approach. Similarly, while the directly interacting Rpl3 neighbour Rpl24 (eL24), which gets incorporated into early cytoplasmic pre-60S particles upon Drg1-mediated release of the closely related AF Rlp24 (106-108), was reproducibly enriched, the Rpl3-proximal Rpl23 (from early nucleolar (state B/state 2) pre-60S particles onwards) showed a similarly low enrichment as non-proximal r-proteins (Figure 1B, C, and Supplementary Figure S4C). Based on the inspection of pre-60S, mature 60S, and 80S structures, this non-enrichment is likely due to Rpl23 being efficiently shielded from the bioAMP cloud that is generated around the TurboID moiety fused to Rpl3's C-terminal end by Rpl3, Rlp24/Rpl24, Nog1, Tif6, and helix H95 as well as by engaging in two intersubunit bridges (Figure 1D, E, and Supplementary Figure S4A and B).

While the specific enrichment of the above-mentioned AFs can be readily explained by their immediate proximity to Rpl3's C-terminal end in the available pre-60S cryo-EM structures, the TurboID assays with the Rpl3-TurboID bait also indicated potential proximities with the reproducibly and highly enriched AFs Dbp9 and Loc1 (Figure 1B, C, and Supplementary Figure S3). The DEAD-box RNA helicase Dbp9 is a substoichiometric component of primordial and early nucleolar pre-60S

particles but is not visible in the cryo-EM structures of early nucleolar, Nsa1-defined pre-60S particles (state 2 and states A, B, and C; (102,104,109,110)); however, as Dbp9 and Rpl3 are functionally connected by a synthetic lethal relationship and as crosslinking MS revealed a potentially direct interaction between Dbp9 and the Rpl3-proximal r-protein Rpl9 (uL6) (111,112), the observed enrichment of Dbp9 in the Rpl3-TurboID assay likely reflects a true physical proximity. In further support of this possibility, the proximity labelling with N-terminally TurboID-tagged Rlp24 also revealed a substantial enrichment of Dbp9 (Supplementary Figures S1 and S3); notably, the C-terminal end of Rpl3 and the N-terminal end of the adjacent Rlp24 project in a similar direction from the pre-60S surface (104). In the case of Loc1, the available cryo-EM structures of pre-60S particles do not offer a straightforward explanation for its suggested proximity to Rpl3's C-terminal end. Loc1 is already substantially enriched in early and/or intermediate nucleolar pre-60S particles sequentially purified via the Nsa1 and Ytm1 baits (110), but a reasonable portion of Loc1 only starts to be visible in late nucleolar state E pre-60S particles purified via the Spb4 bait (103,105). On these state E pre-60S particles, the modelled Loc1 segments are located on the opposite side of Rpl3; however, it cannot be excluded that parts of Loc1, especially its lysine-rich C-terminal region (residues 149-204), which is not resolved in the state E pre-60S particles and projects away from the pre-60S surface, could be within the radius of the bioAMP cloud generated by the TurboID moiety emanating from Rpl3's C-terminus on earlier pre-60S particles. In this respect, it is worth mentioning that the middle part of Loc1 (modelled residues 74-148 in state E1 pre-60S structure) is located nearby the base of the L1 stalk (103). Notably, the entire L1 stalk is still highly flexible in early nucleolar pre-60S particles (until state C) before it gets temporarily fixed in a pre-mature conformation on the late nucleolar state E pre-60S intermediates and finally, upon a large structural reorientation involving rotation of its base and occurring at the transition from the nucleolus to the nucleoplasm on the successive state NE1 pre-60S intermediate where the L1 stalk is again flexible and unresolved, gets accommodated in its typical mature-like conformation on the nucleoplasmic state NE2 pre-60S intermediate (103,104,113). Intriguingly, Rpl2 (uL2) is, after the Rpl3 bait protein, the most enriched r-protein in the Rpl3-TurboID assays (Figure 1B and C). Rpl2 can for the first time be visualized on the state NE1 pre-60S intermediate (103); at this maturation stage, on subsequent pre-60S particles, and on the mature LSU, Rpl2 appears, however, to be too far away from Rpl3's C-terminus to explain its substantial enrichment. The visible incorporation of Rpl2, i.e., of its central, well-structured part (residues 25-200), and the neighbouring Rpl43 (eL43) is enabled by and/or coincides with the release of several AFs, including Loc1, Rrp17, Noc2, Noc3 and Spb4, which is part of the major compositional and structural rearrangements occurring during the transition from the late nucleolar state E to the early nucleoplasmic state NE1/NE2 pre-60S particles (103,113). On the state E2 pre-60S intermediate, where the rRNA-binding sites of the central Rpl2 part within folding domains II and III are occluded by Noc2 and Noc3, respectively, the unresolved rRNA region encompassing helices H65 to H71, which contains the main rRNA-binding sites (H66 and H68) of Rpl2 and participates in intersubunit bridges on mature 80S ribosomes (114), emanates next to the N-terminal

part of Rrp17's long, surface-exposed α-helix from the surface (Supplementary Figure S4A). We speculate that Rpl2 could already be associated, likely via its extensive interactions with rRNA helices H66 and H68, with the state E2 and/or during the transition to the state NE1 pre-60S intermediate. In this scenario, by being associated with this unresolved and, thus, presumably flexible rRNA region, Rpl2 would get into close enough proximity of Rpl3's C-terminus to account for its observed enrichment in the TurboID assays.

In support of the suitability of the TurboID-based proximity labelling approach for the detection of r-protein neighbourhoods on pre-60S particles, the single data set TurboID assays revealed transient proximities of LSU r-proteins with directly adjacent AFs that can also be observed in pre-60S cryo-EM structures. Nsa1, for example, was most highly enriched in the proximity labelling assays of the C-terminally TurboID-tagged Rpl26 (uL24) and the N-terminally TurboID-tagged Rpl35 (uL29), respectively (Supplementary Figure S5A, left panel); these two r-proteins are in close vicinity of Nsa1 within early nucleolar pre-60S particles (state 2 and states A to D) (102,104), in both cases positioning the fused TurboID moiety on the pre-60S surface in reasonable proximity of Nsa1 (Supplementary Figure S5A, right panel). Rrp1, another member of the four-component Nsa1 module, was found to be most strongly enriched in the assays with the N-terminally TurboID-tagged Rpl4, Rpl7 (uL30), and Rpl18 (eL18) baits (Supplementary Figure S5C, upper panel). These three r-proteins are in immediate proximity and even in direct contact with Rrp1 from the earliest structurally characterized pre-60S assembly intermediate (the so-called Noc1-Noc2 RNP), on which Rrp1 can, contrary to Nsa1, already be visualized, until the state D pre-60S intermediate, from which the Nsa1 module gets, presumably concertedly, released by the AAA-ATPase Rix7 (102,104,109,115). While the N-terminal 14 residues of Rpl18 are not resolved in the cryo-EM structures of these early nucleolar pre-60S intermediates, the surface-exposed N-termini of Rpl4 and Rpl7 are directly adjacent to Rrp1 (Supplementary Figure S5C, lower panel). Nmd3 and Lsg1 were prominently enriched in the TurboID assays performed with C-terminally TurboID-tagged Rpl40 and N-terminally TurboID-tagged Rpl10 (Supplementary Figure S5B, left panels), two r-proteins that only get assembled during the cytoplasmic pre-60S maturation phase and can first be visualized on the state III and state IV pre-60S intermediate, respectively (101); thus, recapitulating their observed proximities on late cytoplasmic pre-60S intermediates purified via the Lsg1-TAP bait (Supplementary Figure S5B, right panel). Intriguingly, Yvh1, which could only be visualized on the state I and state II pre-60S intermediates and, thus, prior to the visible incorporation of Rpl40 and Rpl10 (101), was also substantially enriched in these Rpl40 and Rpl10 TurboID assays (Supplementary Figure S5D, upper panel), suggesting that Yvh1 is nevertheless simultaneously present with Rpl40 and/or Rpl10 on cytoplasmic pre-60S intermediates. Accordingly, the order of cytoplasmic maturation events might be less hierarchical than deduced from the cryo-EM snapshots of consecutive Lsg1-purified pre-60S intermediates (101). In agreement with this possibility, cryo-EM structures of late cytoplasmic pre-60S intermediates purified via the Nmd3-TAP bait from cells treated with the Drg1 inhibitor diazaborine revealed the simultaneous presence of Yvh1 and Rpl40 on pre-Lsg1 (PL) and

Lsg1-engaged (LE) pre-60S particles and of Yvh1, Rpl40, and Rpl10 on the Rpl10-inserted (RI) pre-60S particle (Supplementary Figure S5D, lower panel) (116). However, it cannot be excluded that the partial inhibition of Drg1 or the fused TurboID moiety, especially in the case of Rpl40, could delay the release of Yvh1. Finally, and as briefly outlined later on, the TurboID assays with Rpl1, especially the ones with N-terminally TurboID-tagged Rpl1 performed in six biological replicates, revealed transient proximities of Rpl1 to distinct AFs on consecutive pre-60S intermediates as well as its longer-lasting proximities to r-proteins on mature 60S and assembled 80S ribosomes (Figure 3A and Supplementary Figure S10A).

We conclude that a rather specific and substantial enrichment of a given AF is a strong indication for its immediate proximity to the TurboID-tagged LSU r-protein bait on pre-60S particles. Moreover, it appears that our TurboID-based proximity labelling approach quite selectively highlights the neighbouring proteins (AFs and r-proteins) of LSU r-proteins that are most proximal to the fused TurboID enzyme on pre-60S intermediates and mature 60S subunits.

TurboID-based proximity labelling is suitable to identify DCs of r-proteins

To fully assess the suitability of our TurboID-based proximity labelling approach for the identification of DCs, we also performed TurboID assays with N- and C-terminally TurboID-tagged Rps2, Rps3, and Rps26. Six of the eight known DCs, namely Rrb1, Syo1, Bcp1, Tsr4, Yar1, and Tsr2, could be well detected and were substantially enriched in one of the two or both TurboID assays of their respective r-protein client Rpl3, Rpl5, Rpl23b, Rps2, Rps3, and Rps26a (Figure 1B, C, and Supplementary Figure S6). On the other hand, our TurboID-based proximity labelling screen would not have enabled the identification of Acl4 and Sqt1 as candidate DCs of Rpl4 and Rpl10, respectively. While Acl4 could not be detected in the assay with the C-terminally TurboID-tagged Rpl4a bait, it was present at relatively low abundance and weakly enriched in the streptavidin pull-down of cells expressing N-terminally TurboID-tagged Rpl4a. However, as Acl4 was, if at all, only detected at low intensity via few peptides across all LSU r-protein TurboID assays and not always present in the control purifications of the different experimental series, increasing the variability and, thus, potentially resulting in a randomly distributed low-level enrichment, its enrichment was not sufficiently prominent or specific to unequivocally infer a true positive proximity to Rpl4 (Supplementary Figure S7). This weak enrichment was surprising as N-terminally TAP-tagged Rpl4a gets efficiently incorporated into mature 60S subunits and enables the co-purification of Acl4 (34). Moreover, by recognizing and embracing Rpl4's long internal loop (residues 44-113) via its concave surface (20,34), Acl4 is closely connected to Rpl4's globular domain and, thus, expected to be in close enough proximity of the N-terminally fused TurboID moiety for the biotinylation of its surface-exposed lysine residues to occur. Rpl4's globular domain is followed by an around 100-residue-long, eukaryote-specific C-terminal extension that spans across more than half the width (~14 nm) of the solvent-side surface on mature 60S subunits (34,88,114), indicating that the C-terminally fused TurboID might be too far away from Acl4 to enable its

biotinylation. In line with this possibility, performing the TurboID assay with C-terminally TurboID-tagged Rpl4 lacking its C-terminal extension (Rpl4a.N264-TurboID construct) resulted in a pronounced enrichment of Acl4 (Supplementary Figure S6J). Sqt1, which accommodates residues 2-15 of Rpl10 on the negatively charged top surface of its WD-repeat β-propeller domain (41), was not detected in any of the LSU r-protein TurboIDs. According to this mode of interaction, the TurboID moiety fused to Rpl10's C-terminal end, which is separated from the universally conserved uL16 core by an around 50-residue-long, eukaryote-specific C-terminal extension, might be too far away and/or too flexibly attached to enclose Sqt1 in a well-defined bioAMP cloud. The N-terminally fused TurboID, however, should in principle be appropriately positioned to enable biotinylation of at least some of the 18, mostly surface-exposed, lysine residues of Sqt1. While Y2H assays did not provide evidence for a negative impact of an N-terminally located Gal4 DNA-binding domain (G4BD) on the interaction between Rpl10 and Sqt1 (Supplementary Figure S2C), we cannot rule out, as Sqt1 was shown to exhibit a twofold higher affinity for an N-terminal Rpl10 peptide lacking the initiator methionine in vitro (41), that endogenously expressed Rpl10, whose co-translational capturing would, moreover, not be perturbed by the presence of an N-terminally fused TurboID moiety, is preferentially recognized and bound by the available Sqt1 in vivo. The equilibrium might be further shifted towards the recognition of untagged Rpl10 as the N-terminally fused TurboID could lower the efficiency of co-translational Rpl10 capturing by Sqt1 (41). In the case of Rpl3, whose N-terminal 15 residues are sufficient to mediate a robust Y2H interaction and are predicted to interact with the top surface of Rrb1's seven-bladed WD-repeat β-propeller (Supplementary Figure S2D) (41), the N-terminal location of the G4BD abolished the Y2H interaction with Rrb1 (Supplementary Figure S2C); thus, offering a plausible explanation for the non-enrichment of Rrb1 in the proximity labelling assay with N-terminally TurboID-tagged Rpl3. Similarly, and in line with the much lower and less specific enrichment of Syo1 in the TurboID assay with the TurboID-Rpl5 bait, the Y2H interaction between Rpl5 and Syo1, which accommodates residues 2-20 of Rpl5 within an extended groove on its inner α-solenoid surface (46), was markedly reduced when the Rpl5 bait contained the G4BD at its N-terminal end (Supplementary Figure S2C). Finally, the TurboID assays with Rpl11, the second binding partner of Syo1 and the 5S rRNA (46,47), revealed some enrichment of Syo1 with the C-terminally TurboID-tagged Rpl11 bait (Supplementary Figure S6E).

To reciprocally explore the suitability of the TurboID-based proximity labelling approach for the detection of the r-protein clients of DCs and, if possible, to gain further insight into the mode of operation of the different DCs, we also performed TurboID assays with all eight N- and C-terminally TurboID-tagged DCs. In these two experimental series, we calculated the enrichment of each protein detected in the TurboID assay of a given DC by dividing its normalized iBAQ intensity by the median value of its normalized iBAQ intensities, with prior imputation of missing values, in the two control TurboIDs and the TurboIDs of the remaining seven DCs. Except for the TurboID assay with the C-

terminally TurboID-tagged Syo1, which only yielded a relatively low enrichment of Rpl5, all other TurboID assays resulted in a prominent and specific enrichment of the respective r-protein client (Supplementary Figure S8). However, Rpl11 was only very weakly enriched, while nevertheless being the most abundant r-protein, in the TurboID of the Syo1-TurboID bait, but not at all enriched in the assay with N-terminally TurboID-tagged Syo1 (Supplementary Figure S8C). The reason for this is unclear, especially in the case of the C-terminally fused TurboID moiety, which is, according to the structures of Syo1-containing complexes from the thermophilic filamentous ascomycete *Chaetomium thermophilum*, expected to be in close proximity of Rpl11 (47,48). Considering that Syo1 is not essential and that its tandem affinity purification co-enriches less Rpl11 than Rpl5 (46), the Syo1-enabled import of Rpl5 and Rpl11 is dispensable for the assembly and pre-60S incorporation of the 5S RNP and may not obligatorily involve the co-import of Rpl11, raising the possibility that Syo1, which is intimately functionally connected to Rpl5 by synthetic lethality and reciprocal dosage rescue (46), primarily acts, at least in *S. cerevisiae*, as a transport adaptor and DC of Rpl5. In line with the importin Kap104 mediating the nuclear import of Syo1, by recognizing, most likely in a co-translational manner (31), its N-terminally located PY-NLS (46), Kap104 was specifically, albeit relatively weakly, enriched in the TurboID of the Syo1-TurboID bait (Supplementary Figure S8C). Overall, and as expected for selective binding partners of individual r-proteins, the TurboID-based proximity labelling assays with DC baits only identified a limited number of specifically and highly enriched proteins. Conspicuously, however, almost all DC TurboIDs revealed a specific enrichment of at least one AF or r-protein, indicating that DCs are transiently associated with pre-ribosomal particles to coordinate the transfer of their r-protein client to its binding site. For example, the Rrb1 TurboIDs enriched, albeit to different extents, several members of the Npa1 complex (Supplementary Figure S8A) (117,118), which is part of the primordial pre-60S particle and functionally connected to Rpl3 by synthetic lethal relationships (110,111,117,119,120). The AF Mak16, whose close proximity to Rpl4 can already be observed on the Noc1-Noc2 RNP (115), was highly abundant and strongly enriched in both Acl4 TurboIDs (Supplementary Figure S8B). The two AFs Rpf2 and Rrs1, which are part of the hexameric 5S RNP precursor (5S rRNA, Rpl5, Rpl11, Rpf2, Rrs1, and Syo1) and required for the incorporation of the 5S RNP into pre-60S particles (48,121), were noticeably enriched in the Syo1 TurboIDs (Supplementary Figure S8C). The Rpf2-Rrs1 heterodimer is already associated with early nucleolar pre-60S particles, but can only be visualized in the cryo-EM structure of the early nucleoplasmic, Nog2-purified pre-60S intermediate, where it anchors the 5S RNP in its rotated, immature conformation (104,109,110,121-124). Thus, the observed enrichment of Rpf2 and Rrs1 in the Syo1 TurboIDs could either be evidence for the in vivo existence of the hexameric 5S RNP precursor in *S. cerevisiae*, which could so far, unlike in *C. thermophilum*, not be experimentally observed under normal growth conditions (46,48), or could alternatively indicate that Syo1 is present during the transfer of the 5S RNP to and/or the completion of 5S RNP assembly at its initial binding site, mainly consisting of the pre-bound Rpf2-Rrs1 complex, on nucleolar pre-60S particles. In line with the transient association of Sqt1 with late cytoplasmic pre-60S

subunits for coordinating the stable incorporation of Rpl10 with the Lsg1-mediated release of Nmd3 (41,125,126), Nmd3 was prominently enriched in the proximity labelling assay with N-terminally TurboID-tagged Sqt1, while a moderate enrichment of Lsg1 could be observed with both Sqt1 baits (Supplementary Figure S8D). Notably, Bcp1 exhibited a more multifaceted proxiOME than the other seven DCs (Supplementary Figure S8E). On the one hand, the two AFs Rlp24 and Mak11, which are in direct contact with or, respectively, in close proximity of Rpl23 (Figure 1D), were enriched, strongly suggesting that Bcp1 is transiently associated with early nucleolar pre-60S particles at the time of Rpl23 incorporation. Additionally, the Bcp1 proxiOME also included an already validated binding partner of Rpl23 (Rkm1) and two potential direct interactors of Bcp1 (Kap60/Srp1 and Mss4). The SET domain-containing methyltransferase Rkm1, which is responsible for dimethylation of lysine residues K106 and K110 of Rpl23 but dispensable for optimal growth of yeast cells (127-129), was shown to form a binary complex with Rpl23, but not with Bcp1, and a trimeric complex with Rpl23 and Bcp1 in vitro (129). Moreover, co-immunoprecipitation experiments have indicated an Rpl23-dependent interaction between Bcp1 and Rkm1 (129); thus, our proximity labelling data, showing an enrichment of Rkm1 in both the Rpl23 and Bcp1 TurboIDs (Supplementary Figures S6F and S8E), provide further evidence for the in vivo occurrence of the trimeric Bcp1-Rpl23-Rkm1 complex. Bcp1 contains two predicted classical NLS regions (130), the first (residues 11-20) within its N-terminal extension and the second (residues 219-234) within an internal loop. According to AlphaFold3 predictions, positively charged side chains of the first and second NLS region interact in a canonical manner with the minor and major NLS-binding site (131), respectively, of the importin-α Kap60 (Supplementary Figure S9A, left panels), suggesting that the transport adaptor Kap60, in conjunction with the importin-β Kap95, mediates the nuclear import of Bcp1. Mss4 is an essential phosphatidylinositol-4-phosphate 5-kinase that almost exclusively localizes to the plasma membrane (132,133). Moreover, the C-terminally GFP-tagged Mss4-1 mutant protein, bearing the D127N and L393P substitutions, was shown to almost exclusively accumulate in the nucleus at the non-permissive temperature. Notably, while absence of Kap123 abrogated the nuclear accumulation and conferred a cytoplasmic localization, overexpression of Bcp1 fully restored the plasma membrane localization of Mss4-1-GFP (133). This data was, by also considering the finding that a temperature-sensitive *bcp1* allele (F241S) conferred a pre-60S export defect, interpreted as Bcp1 being responsible for nuclear export of Mss4 (133). In line with their physical proximity suggested by the Bcp1 TurboID assays, AlphaFold3 predicted with good confidence the formation of a Bcp1-Mss4 complex (Supplementary Figure S9A, right panels). According to this model, Bcp1 interacts with the first subdomain (residues 376-555) of the phosphatidylinositol phosphate kinase (PIPK) domain (residues 376-756) as well as with a segment (residues 335-357) that precedes the first PIPK subdomain and notably encompasses part of the NLS region of Mss4. Consistent with this predicted mode of interaction, an Mss4 variant (residues 332-565) consisting essentially of the N-terminally extended first PIPK subdomain showed a robust Y2H interaction with full-length Bcp1

(Supplementary Figure S9B). Moreover, as an Mss4 variant (residues 371-565) comprising only the first PIPK subdomain exhibited a reduced Y2H interaction, it appears that both predicted Bcp1-binding surfaces of Mss4 are necessary for an optimal interaction. Interestingly, in the structure model of the Bcp1-Mss4 complex, Bcp1's internal loop, whose first negatively charged residues are predicted to contact a positively charged surface on the first PIPK subdomain, and the NLS region of Mss4 are not in a configuration that would grant access to their respective importin, thereby providing a plausible explanation for how the Bcp1-Mss4 interaction would prevent the nuclear entry of Mss4. Since Bcp1 binding is predicted to efficiently shield all prominent positively charged surfaces of Mss4 (Supplementary Figure S9C), it is likely that Bcp1 also ensures the safe transfer of Mss4 to the plasma membrane, a scenario that is fully compatible with the previously reported cell biological and genetic data (133).

We conclude that despite certain limitations, such as the distance between the fused TurboID moiety and the interacting DC, the requirement for a native context of N-terminally located DC-binding sites on r-proteins, and a potentially limited number of surface-accessible lysine residues on the predominantly negatively charged surface of DCs, our TurboID-based proximity labelling screen should be a valid approach to unveil hitherto unidentified DCs and other transient interaction partners, including importins (see below), of r-proteins. Moreover, as revealed by the identification of distinct AFs and/or r-proteins in the TurboID-based proximity labelling assays of DCs, a common feature of DCs appears to be their transient association with pre-ribosomal particles in order to facilitate the coordinated incorporation of their r-protein clients.

The r-protein proxiOMEs also unveil potential interactions with importins

Interestingly, several LSU r-protein TurboIDs showed a noticeable enrichment of distinct importins (Figure 2A-D, left panels; see also Supplementary Figure S1). Here, we focused on obtaining evidence in support of a physical interaction between three of these importins, namely Kap114, Kap119 (also called Nmd5), and Kap121 (also called Pse1), and their potential cargo r-proteins Rpl6 (eL6) and Rpl40, Rpl30 (eL30), and Rpl38 (eL38), respectively. To this end, we first performed AlphaFold predictions, initially with AlphaFold-Multimer and then with AlphaFold3 (83,134), revealing that in each case almost the entire LSU r-protein is expected to be accommodated on the inner surface of the importin (Figure 2A-D, middle panels, and data not shown). In line with both termini of Rpl30 being predicted to be surface exposed, Kap119 was enriched with both the N- and C-terminally TurboID-tagged Rpl30 bait (Figure 2B and Supplementary Figure S1). In the case of Rpl30 and Rpl40, their interaction with Kap119 and, respectively, Kap114 was predicted to also occur in the presence of GTP-bound Gsp1 (the *S. cerevisiae* counterpart of the mammalian GTPase Ran (135-138)) (Figure 2D and data not shown), whose binding to importin-βs is generally sufficient to dissociate the bound import cargo in the nucleus (139-143), but may as well, as also observed in the case of Kap114 and Kap119 (144-150), only result in incomplete cargo release in vitro and/or be coupled to cargo transfer to specific chaperones or the

cognate nuclear interaction site (reviewed in (151)). To provide first experimental evidence for a direct interaction between the above importins and r-proteins, we next performed Y2H assays. Since our well-functioning Y2H system, optimised for high specificity by expressing the bait and prey (as G4BD and Gal4 activation domain (G4AD) fusion proteins, respectively) from monocopy plasmids under the transcriptional control of the *ADH1* promoter, relies on the detection of interactions that occur at the promoters (*GAL1* and *GAL2*, respectively) of the *HIS3* and *ADE2* reporter genes in the nucleus, it will likely fail, due to the rapid binding of the highly abundant GTP-loaded Gsp1 (152), to reveal RanGTP-sensitive interactions between importin-βs and their r-protein import cargo. According to available co-structures, Gsp1 and Ran interact in their GTP-bound state with the four N-terminal HEAT repeats of all importins in a conserved manner, but they also engage in additional importin-specific contacts that centre mainly around HEAT repeats 7 and 8 or may even involve the four C-terminal HEAT repeats (149,151,153). On the other hand, and not unsurprisingly, the observed cargo binding modes of the different importin-βs are quite diverse. However, importin-βs mostly employ the HEAT repeats, as well as interspersed loop regions, that succeed the N-terminal RanGTP-binding site to accommodate, often via negatively charged surfaces and hydrophobic pockets, linear sequences and/or folded domains within their inner concave surface (143,149,151,153-159). We therefore reasoned that it should be possible, by progressively deleting the N-terminal RanGTP-binding site and, if necessary, adjacent HEAT repeats, to obtain importin-β variants with abolished or, at least, sufficiently reduced RanGTP-binding capacity that can be successfully employed in the classical nuclear Y2H system. In line with this, we have previously shown that the Kap121.302C variant (302C construct; i.e., starting at residue 302 and extending to the C-terminal end), which lacks HEAT repeats 1 to 7 and thus almost all RanGTP-interacting residues (143,153), engages in a productive Y2H interaction with its r-protein import cargo Rps2 (33). To control that the full-length importin-β versions, when fused to the G4AD at their C-terminal end, have the capacity to form Y2H interactions, we assessed their interaction with the N-terminally G4BD-tagged Gsp1.Q71L mutant variant, which is the *S. cerevisiae* equivalent of the GTPase-deficient human Ran(Q69L) (160,161). These Y2H assays revealed that Gsp1.Q71L interacts strongly with Kap121 but only relatively weakly with Kap114 and Kap119 (Figure 2A-C, lower right panels), which may reflect the previously reported lower affinities of Kap114 and Kap119 for Gsp1.Q71L in vitro (152). On the other hand, and as expected, the Kap121, Kap119, and Kap114 variants lacking part of or the complete N-terminal RanGTP-binding site no longer exhibited a Y2H interaction with Gsp1.Q71L (Figure 2A-C, lower right panels). In line with the predicted Rpl38-binding region comprising almost exclusively residues of HEAT repeats 8 to 16, the Kap121.302C variant, fused at its C-terminus to the G4AD, showed a robust Y2H interaction with C-terminally G4BD-tagged Rpl38 (Figure 2A, upper right panel). Conversely, no interaction between full-length Kap121 and Rpl38 could be observed, altogether suggesting that Rpl38 likely represents and import cargo of Kap121. Similarly, while not interacting with full-length Kap119, C-terminally G4BD-tagged Rpl30 showed a

strong Y2H interaction with the Kap119.289C (starting after the predicted HEAT repeat 6) and Kap119.328C (beginning shortly before the predicted second α-helix of HEAT repeat 7) variants (Figure 2B, upper right panel), which lack the predicted N-terminal binding site (HEAT repeats 1 to 3) of GTP-bound Gsp1 (data not shown), but apparently contain all necessary elements for the efficient accommodation of Rpl30. For the Y2H assays with Kap114, we generated N-terminal deletion variants that lack partially (Kap114.75C; deletion of HEAT repeats 1 and 2) or completely (Kap114.159C; deletion of HEAT repeats 1 to 4) the N-terminal binding site (HEAT repeats 1 to 4) of GTP-bound Gsp1 (149). Consistent with Rpl6 being predicted to extensively and almost exclusively contact Kap114 from HEAT repeat 5 onwards, N-terminally G4BD-tagged Rpl6 engaged in a robust Y2H interaction with the C-terminally G4AD-tagged Kap114.75C and Kap114.159C variants (Figure 2C, upper right panel). On the other hand, Rpl6 did not show a Y2H interaction with full-length Kap114, indicating that Rpl6 could be an import cargo of Kap114. In support of this notion, a previous study detected Rpl6 via numerous peptides in MS analyses of Kap114 affinity purifications from the post-ribosomal supernatant of yeast cytosol (147). Interestingly, the C-terminally G4BD-tagged Ubi1, i.e., Rpl40a-G4BD due to the rapid proteolytic removal of the ubiquitin moiety from the ubiquitin-Rpl40a precursor protein Ubi1 (36,39), only interacted with full-length Kap114 but not with the two N-terminal deletion variants (Figure 2D, right panel), suggesting that the formation of a productive Y2H interaction between Rpl40 and Kap114 may depend on the binding of endogenous GTP-loaded Gsp1. Considering that Rpl40 gets only incorporated into pre-60S subunits in the cytoplasm and that one of the yeast importin-βs, Kap122 (also called Pdr6), has previously been shown to function as a biportin, i.e., a bidirectional transport receptor (100,101,116,153,162), it appears reasonable to speculate that Kap114, when associated with GTP-loaded Gsp1, could be responsible for the export of any Rpl40 that has inadvertently entered the nucleus in order to prevent its premature incorporation into pre-60S particles.

We conclude that our TurboID-based proximity labelling approach is also suitable to reveal transient interactions of r-proteins with distinct importins. However, as Kap123 and Kap121, suggested to be the main and partially redundant transport receptors for import of r-proteins (30), were not noticeably enriched, except for Kap123 with both Rpl8 (eL8) baits, in the TurboIDs of their supposed r-protein cargos (30,31,33,43,49) (Supplementary Figure S1), we suspect that not all importins form sufficiently long-lived interactions with their r-protein cargos to warrant their identification by TurboID-based proximity labelling. Notably, and in contrast to the predominant recognition of short linear sequences by Kap121 and Kap123 (143,151,157,163,164), the four LSU r-proteins that enabled the TurboID-based identification of distinct importins are predicted to be almost entirely accommodated by the respective importin. This, together with their presumably not too short-lived association with the importins, may point to a necessity for being chaperoned by these importins and/or to a coupling of their release with the transfer to their pre-ribosomal binding site. Clearly, future experiments are required to address the in vivo relevance of the here unveiled interactions between the importins Kap114,

Kap119, and Kap121 and their potential cargo r-proteins Rpl6 and Rpl40, Rpl30, and Rpl38, respectively.

Identification of Acl1 and Bcl1 as potential interaction partners of Rpl1

The proximity labelling assays with N- and C-terminally TurboID-tagged Rpl1b enriched several r-proteins and AFs as well as the previously uncharacterized protein Ycr051w (Figure 3A and Supplementary Figure S10A), which we have named Acl1 for Ankyrin repeat chaperone of Rpl1 (see below). In support of a highly specific biotinylation of proximal proteins by the two Rpl1b baits, both assays revealed a strong enrichment of the AF Nop2, whose globular domain is in direct contact with the concave surface of the L1 stalk on the late nucleolar state E pre-60S particles (103) (Supplementary Figure S10B), and of the LSU r-protein Rpl13 (eL13), which is, especially its lysine-rich C-terminal region (residues 165-199), in proximity of the N- and C-terminal end of Rpl1 once the L1 stalk has moved from its pre-mature position in the state E pre-60S particles to its mature-like position on nucleoplasmic (from state NE2 onwards) pre-60S particles (113) (Supplementary Figure S10C-H). The long-lasting proximity between Rpl1 and Rpl13, from nucleoplasmic pre-60S particles to mature 60S subunits, likely accounts for the strong enrichment and the high abundance of Rpl13 in the streptavidin pull-downs of cells expressing TurboID-tagged Rpl1b. Moreover, the proximity labelling with N-terminally TurboID-tagged Rpl1b highlighted proximities with additional AFs that sequentially occur on successive pre-ribosomal particles. For example, parts of Loc1 (modelled residues 74-148 in state E1/E2 pre-60S structures) are located near the base of the L1 stalk on late nucleolar pre-60S particles (103) (Supplementary Figure S10B), and, notably, the lysine-rich C-terminal region of Loc1 (residues 149-204), which is not visible in the cryo-EM structures of state E pre-60S particles, very likely emanates from the last modelled residue towards the upper part of the L1 stalk and is therefore expected to get into the bioAMP cloud around the Rpl1-fused TurboID. On nucleoplasmic pre-60S particles purified via the Nog2 bait, in which the 5S RNP (composed of the 5S rRNA, Rpl5 and Rpl11) is stably bound in a rotated, pre-mature orientation (124,165,166), the 5S RNP-anchoring Rpf2-Rrs1 heterodimer is facing the L1 stalk (Supplementary Figure S10D), whose tip region including the bound Rpl1 is, however, not resolved in the cryo-EM structures, indicating that the L1 stalk still exhibits some flexibility at this assembly stage. On the subsequent Rix1-Rea1 pre-60S particle (113), the HEAT repeat domain of Sda1 contacts both the L1 stalk, with parts of Sda1 being directly adjacent to Rpl1, and the almost mature 5S RNP-containing central protuberance (CP), while its non-resolved C-terminal extension (residues 516-767) projects away from the pre-60S surface in an area that is surrounded by Rpl1 and Rpl5 (Supplementary Figure S10E). From this maturation stage onwards, with the 5S RNP being in its mature conformation, Rpl5 is in proximity of Rpl1 (Supplementary Figure S10E-H); however, the N- and C-terminal end of Rpl1 do not point in direction of Rpl5 on NPC-trapped pre-60S and mature 60S subunits (167,168), which agrees with the relatively low enrichment of Rpl5 in the Rpl1b TurboIDs. Rpl42 can first be visualized on the late nuclear (LN) pre-60S intermediate (116),

where it is located in proximity of the partially resolved L1 stalk. In structures with an atomic model of Rpl1 (e.g., NPC-trapped pre-60S), the N-terminal end of Rpl1 is in very close proximity of the surface-exposed β-strand domain of Rpl42 (Supplementary Figure S10F-H). However, Rpl42 could only be identified in two of the six TurboID-Rpl1b replicates, likely because trypsin digestion of Rpl42 only yields very few peptides that are suitable for LC-MS/MS analysis. Finally, Rps25 faces the rRNA side of the L1 stalk on the 80S ribosome (167) (Supplementary Figure S10H), and its lysine-rich N-terminal extension, which is not resolved in the crystal structure of the 80S ribosome, could potentially come into close proximity of Rpl1.

Notably, both Rpl1 TurboIDs revealed a strong enrichment and a relatively high abundance of Acl1 (Figure 3A), a protein of hitherto unknown function, suggesting that Acl1 could be a direct interaction partner, possibly a DC, of Rpl1. To obtain further indications that would reinforce this possibility, we first compared the features of Acl1 with the ones of the already established DCs. Acl1 is a relatively small protein consisting of 222 amino acids, and its N-terminal part (residues 1-126) is predicted to contain four ankyrin repeats (80,81,169) (AlphaFold model AF-P25631-F1-v4; see also Figure 5B), which are expected to serve as a scaffold for mediating a protein-protein interaction (PPI). In this respect, Acl1 is highly similar to Yar1, the DC of Rps3 (170). Yar1 also contains four N-terminal ankyrin repeats, and these were shown to mediate the interaction with the N-terminal α-helix of Rps3 (32,99). Moreover, Acl1's calculated isoelectric point (pI) of 4.25 is similar to the average pI (4.26; range 3.87-4.83) of all eight known DCs. Finally, comparative analysis of gene expression profiles, using the SPELL search engine on the *Saccharomyces* Genome Database (SGD) website (171,172), indicates that *ACL1* is transcriptionally co-regulated with genes belonging to the largely overlapping rRNA and ribosome biosynthesis (RRB) and ribosome biogenesis (RiBi) regulons (173,174). In line with the nuclear pre-60S assembly stage of Rpl1 (103,113,175), Acl1-GFP, as indicated by a high-throughput localization study (176), accumulates in the nucleus but also displays some cytoplasmic localization; such a dual steady-state localization has been previously observed for the DCs Acl4, Bcp1, and Syo1 (34,46,88,133). Contrary to most known DCs (see SGD website and (42)), Acl1 does not have a clearly identifiable human orthologue, moreover, our database searches only revealed clear orthologues in the fungi kingdom, suggesting that Acl1 is likely a fungi-specific protein (see below and Supplementary Figure S11). According to systematic analyses of gene deletion phenotypes (see SGD website and (177)), *ACL1* is a non-essential gene whose absence is not annotated to confer any severe growth defects. Furthermore, only very few potential physical and genetic interactions, mainly derived from high-throughput studies, have been reported for Acl1 (see SGD website). Notably, however, a large-scale screen for genetic interactions identified a weak negative genetic interaction (SGA score -0.167) between the Δ*rpl1a* and Δ*acl1* null mutants (178). Based on the strong enrichment of Acl1 in the Rpl1b TurboID assays and the above-mentioned supportive indications, we considered Acl1 as a promising candidate DC for the basic Rpl1 (pI 10.38) and, thus, selected it for further analysis. To validate the

proximal relationship between Rpl1 and Acl1 and, at the same time, explore the proxiOME of Acl1, we first performed the reciprocal proximity labelling assays with both N- and C-terminally TurboID-tagged Acl1 (Figure 3B). Not unexpectedly and like most known DCs (Supplementary Figure S8), Acl1 exhibits a very limited proximal network. In strong support of their close proximity and suggestive of a direct physical interaction, Rpl1 was the most abundant of the few substantially enriched proteins in both Acl1 TurboID assays. Besides Rpl1, only the uncharacterized Ynl035c, which we have named Bcl1 for Beta-propeller chaperone of Rpl1 (see below), was noticeably enriched in both assays, especially in the one of the N-terminally TurboID-tagged Acl1 bait. A closer inspection of the Rpl1b TurboID assays revealed that Bcl1 could also be detected among the enriched proteins, albeit only in four of the six experimental replicates and at relatively low abundance, in the proximity labelling with the N-terminally TurboID-tagged Rpl1b bait, raising the possibility that Bcl1 could be a direct interactor of Rpl1 or Acl1. Bcl1 is an acidic protein (pI 5.09) of 389 amino acids, which is predicted to fold into a typical seven-bladed WD-repeat β-propeller (residues 1-322) that is followed by a largely unstructured C-terminal extension (AlphaFold model AF-P53962-F1-v4; see also Figure 7B). In this respect, Bcl1 is similar to the known DCs Rrb1 and Sqt1, which mainly consist of a predicted seven-bladed or an experimentally-determined eight-bladed WD-repeat β-propeller that mediates the interaction with the N-terminal residues of Rpl3 or Rpl10 (41), and may likely engage in a PPI via its WD-repeat domain (179). According to database searches (e.g., OrthoDB (180)), Bcl1 is conserved throughout eukaryotes and has a predicted human orthologue called WDR89. *BCL1* is a non-essential gene, and no pronounced phenotypes have been observed for Δ*bcl1* null mutant cells in large-scale surveys (see SGD website). Comparative analysis of gene expression profiles performed with the SPELL search engine on the SGD website reveals that the transcriptional co-regulation of *BCL1* with genes belonging to the RRB and RiBi regulons is less pronounced than in the case of *ACL1*, nevertheless several AF-encoding genes exhibit an expression profile that is similar to the one of *BCL1*. So far, only very few potential physical interactions have been reported for Bcl1 and these as well as its genetic interaction network, which is almost exclusively based on high-throughput data, do not provide any indications for a function in ribosome biogenesis that could be related to Rpl1. Finally, Bcl1-GFP, as indicated by a high-throughput study (176), exhibits nuclear localization.

Acl1 is a direct interaction partner of Rpl1 and is involved in LSU biogenesis

As Bcl1 was only detected and, moreover, only moderately enriched in the proximity labelling assays with N-terminally TurboID-tagged Rpl1b, we first focused our efforts on obtaining further insight into the physical and functional interaction between Acl1 and Rpl1. To obtain evidence for a direct physical interaction, we first conducted Y2H assays between all possible combinations of N- and C-terminally G4BD- and G4AD-tagged Rpl1b and Acl1. For all but one combination (G4BD-Acl1 with G4AD-Rpl1b), we observed very strong or relatively strong Y2H interactions as indicated by the extent of growth, enabled by activation of the *HIS3* and *ADE2* reporter genes, on plates lacking histidine or

adenine as well as by the white or only light red colony colour (Figure 4A). To corroborate the Y2H data and to obtain definite evidence for their direct interaction, we co-expressed C-terminally $(His)_6$-tagged Rpl1b and C-terminally Flag-tagged Acl1 in *E. coli* and subsequently purified the Rpl1b-$(His)_6$ bait by Ni-NTA affinity purification. Analysis of the binding assay by SDS-PAGE and Coomassie staining as well as by Western blotting revealed an efficient and specific co-purification of Acl1-Flag with Rpl1b-$(His)_6$ (Figure 4B). When co-expressed with non-tagged Rpl1b, the recovery of Acl1-Flag in the imidazole eluate was, however, strongly reduced, showing that the observed substantial enrichment of Acl1-Flag with the Rpl1b-$(His)_6$ bait was not due to its non-specific binding to the Ni-NTA agarose beads. We conclude that Acl1 is a direct interaction partner of Rpl1.

Next, we wished to gain insight into the functional relevance of Acl1 as an interaction partner of Rpl1. As haploid Δ*acl1* null mutant strains, generated *de novo* by deletion disruption of one *ACL1* copy in the diploid W303 background and subsequent tetrad dissection, did not display any clearly discernible growth defect on YPD plates at different incubation temperatures (Figure 4C), we assessed whether the absence of Acl1 would have an effect on growth when Rpl1 is present in lower amounts. The essential and universally conserved r-protein Rpl1 is encoded by two paralogous genes, *RPL1A* and *RPL1B*, as proteins (Rpl1a and Rpl1b) with identical amino acid sequence (72). In agreement with the higher *RPL1B* mRNA levels and the higher cellular abundance of Rpl1b (72,98,181), Δ*rpl1b* null mutant cells exhibited a strong slow-growth (sg) phenotype, which was especially pronounced at 37ºC, while Δ*rpl1a* null mutant cells did not show any obvious growth defect (Figure 4C), confirming the previously observed growth phenotypes of these null mutant strains in the same (W303) or a different genetic background (72,97,181). Analysis of the growth characteristics of spore clones derived from tetratype tetrads, obtained by crossing Δ*rpl1a* with Δ*acl1* null mutant strains and subsequent sporulation of the heterozygous diploid strains, revealed that Δ*acl1*/Δ*rpl1a* double mutants exhibited a synthetic growth defect at all tested temperatures (Figure 4C); thus, validating the negative genetic interaction previously indicated by a large-scale genetic interaction study (178). Moreover, absence of Acl1 aggravated the growth defect of the Δ*rpl1b* null mutant to an extent that Δ*acl1*/Δ*rpl1b* double mutant cells were only barely growing (Figure 4C). These genetic findings indicate that Acl1 becomes functionally relevant when Rpl1 is present in lower amounts, presumably owing to its contribution as a direct interaction partner to the provisioning of assembly-competent Rpl1. To evaluate the impact of the absence of Acl1 on ribosome biogenesis, both in the presence and absence of Rpl1a, we analysed the polysome profiles of wild-type, Δ*acl1*, Δ*rpl1a*, and Δ*acl1*/Δ*rpl1a* cells originating from the same tetratype tetrad (Figure 4D). While the polysome profiles of wild-type and Δ*rpl1a* cells were almost indistinguishable, absence of Acl1 resulted in a slight increase in free 40S subunits and a faintly perceptible appearance of half-mers (Figure 4D, see also Figure 10B), which consist of mRNAs that are associated with one or multiple translating 80S ribosomes and a 43S pre-initiation complex awaiting subunit joining (182). Notably, Δ*acl1*/Δ*rpl1a* double mutant cells showed a clearly noticeable accumulation of free 40S subunits and of half-mers that was accompanied by an overall decrease in

polysome content (Figure 4D). However, the size of the 60S peak was not reduced, but rather appeared to be slightly increased, indicating a defect in pre-60S export and/or subunit joining. In line with this, previous studies have shown that pre-60S subunits lacking Rpl1 are inefficiently exported from the nucleus and that the exported 60S subunits are less competent for subunit joining (175,181). Additionally, we also examined the subcellular localization and (pre-)ribosome association of genomically expressed Acl1 that was fused at its C-terminal end to a yeast codon-optimized mNeonGreen (ymNeonGreen) or, respectively, the TAP tag. Fluorescence microscopy revealed that Acl1-ymNeonGreen localized almost exclusively to the nucleus, where it was predominantly located, as also judged by the co-localization with the nucleolar marker protein Nop58-yEmCherry, in the nucleoplasm (Figure 4E). In line with the Acl1 TurboID assays not highlighting close proximities with known AFs or other r-proteins besides Rpl1 (Figure 3B), sucrose gradient fractionation and subsequent Western blot analysis revealed that Acl1-TAP was exclusively present in the soluble fractions (Figure 4F), altogether indicating that Acl1 is, if at all, only very transiently associated with pre-60S particles. We conclude that Acl1 contributes to the biogenesis of 60S subunits as a transient interaction partner of free Rpl1. Considering their robust interaction, it seems probable that Acl1 could already bind to Rpl1 in the cytoplasm and get transported together with Rpl1 to the nucleus, where it would dissociate from assembly-competent Rpl1 prior to or during the incorporation of Rpl1 into nucleolar pre-60S particles.

Acl1 interacts via its ankyrin repeat domain with the second domain of Rpl1

To gain insight into their mode of interaction, we decided to first map the respective interaction-mediating regions by Y2H assays, expecting that this information should also help to obtain minimal Rpl1-Acl1 complexes that are amenable to structure determination by X-ray crystallography. As we started this endeavour before the creation of the AlphaFold Protein Structure Database or the availability of AlphaFold-Multimer to predict the structures of protein complexes (80,81,134), we based the design of our constructs on available Rpl1 structures (mainly the one of Rpl1 in the cryo-EM structure of the Rix1-Rea1 pre-60S particle and the one of human RPL10A in the cryo-EM structure of the cytoplasmic state C pre-60S particle (113,183)) and, in the case of Acl1, on multiple sequence alignments (T-Coffee (87)) and secondary structure predictions (PSIPRED (184)). Notably, Rpl1 mainly consists of two separate structural domains (Figure 5A, lower panel). The first domain (D1) is formed both by N- (approximately from residue 6 to 37) and C-terminal (approximately from residue 165 to 217) primary sequence segments, whereas the second domain (D2) is exclusively formed by an internal primary sequence segment (approximately from residue 64 to 153). To map the Acl1-binding surface on Rpl1, we therefore performed Y2H assays with N-terminal, C-terminal, and internal deletion variants as well as with internal fragments of Rpl1, all C-terminally fused to the G4BD (for the complete Y2H mapping data set, see Supplementary Figure S12A). These mapping experiments revealed that the second domain of Rpl1 is both sufficient and required for the interaction with C-terminally G4AD-tagged full-length

Acl1 and that a short segment within D2 (residues 85-104) contains the relevant interaction-mediating residues (Figure 5A, upper panel). The Y2H assays with N- and C-terminal deletion variants of Acl1 showed that the N-terminal 127 residues, essentially containing the four predicted ankyrin repeats (Figure 5B, lower panel), correspond to the minimal fragment mediating full interaction with full-length Rpl1 (Figure 5B, upper panel; for the complete Y2H mapping data set, see Supplementary Figure S12B). Further Y2H assays revealed that the minimal Rpl1 fragments (residues 63-158, 63-104, and 85-104) exhibiting a strong interaction with full-length Acl1 still interacted equally well with the C-terminally truncated Acl1.N127 variant (Figure 5C). In agreement with these Y2H results, the D2-containing Rpl1b fragment (residues 63-158) and C-terminally Flag-tagged Acl1.N127 formed, when co-expressed in *E. coli* and purified via the C-terminally $(His)_6$-tagged Rpl1b bait by Ni-NTA affinity purification, a seemingly stoichiometric complex in vitro, as indicated by the similar intensity of the two Coomassie-stained bands (Figure 5D).

Next, we aimed to exploit the efficient in vitro production of this minimal complex to illuminate the molecular details of the Rpl1-Acl1 interaction by X-ray crystallography. To this end, we co-expressed Rpl1b(63-158)-$(His)_6$ and untagged Acl1.N127 in *E. coli* and purified the complex by Ni-affinity chromatography followed by size exclusion chromatography and subjected the purified complex to crystallisation screens. Gratifyingly, diffracting crystals were obtained and the co-structure of Rpl1b (residues 64-151) and Acl1 (residues 2-127) could be solved at 2.6 Å by molecular replacement (Figure 6A; see Materials and Methods and Supplementary Table S1). Analysis of the electrostatic surface properties revealed that the negatively charged ankyrin repeat surface accommodates the complementary, positively charged surface of Rpl1 (Figure 6B and Supplementary Figure S13A). Accordingly, the interaction interface is primarily established by salt bridges and hydrogen bonding networks (Figure 6C). In good agreement with the Y2H mapping data (Figure 5A), the five Rpl1 residues involved in the interaction, i.e., Asn94, Lys95, Lys97, Lys98, and Lys101, cluster within a short segment (residues 94-101) of the D2 domain (Figure 6A and C); moreover, these residues are conserved in Rpl1 orthologues from metazoans, plants, and other fungi (Supplementary Figure S13D). Notably, an Rpl1 segment (residues 98-105) containing the interaction-mediating residues Lys98 and Lys101 is in direct contact with the tip of the L1 stalk (rRNA residues 2481-2486 that are part of the bulge connecting 25S rRNA helices H78 and H77) both on state E pre-60S particles and mature 60S subunits (103,185) (Supplementary Figure S13B and C), indicating that Acl1 and the L1 stalk interact in a mutually exclusive manner with the D2 domain of Rpl1. On Acl1, the residues involved in the interaction are located on the one hand at the end of the first α-helix (Asp11 and Tyr47) or within the short loop connecting the first and second α-helix (Glu79 and Glu114) of each ankyrin repeat, and, on the other hand, within the β-turn at the end of the long repeat-connecting loops (Asp34, Asp68, Asp70, and Asp72), in both cases aligned in-line to jointly form the Rpl1-binding interface along the concave inner, groove-like surface of the ankyrin repeat domain (Figure 6A and D). Moreover, residue Asn4,

which is situated before the first α-helix, contributes by hydrogen bonding to the interaction with Rpl1 residue Asn94 (Figure 6C). According to BLAST searches and multiple sequence alignments, most of the nine interaction-mediating residues are identical or highly similar in predicted Acl1-like proteins of the Fungi kingdom, especially in those belonging to the Dikarya subkingdom (Supplementary Figure S11), suggesting that all fungal Acl1 homologues likely fulfil a conserved function as Rpl1-binding proteins. To get an idea of the importance of the above residues for the mutual interaction, we first individually substituted the five Rpl1 residues by alanine or aspartate and the nine Acl1 residues by alanine or lysine and assessed the effects of these amino acid exchanges on the interaction by Y2H assays. Of the individual alanine substitutions in Rpl1, only the N94A and the K98A exchange had a major impact and, respectively, either strongly reduced or completely abolished the Y2H interaction with Acl1 (Figure 6E). Moreover, the K95A exchange resulted in a visibly weaker Y2H interaction, while the K97A and the K101A exchange only slightly, if at all, affected the interaction capacity of Rpl1. As expected, the charge reversal substitutions had a more drastic effect, leading to a complete loss (K95D and K97D) or a substantial weakening (K101D) of the Y2H interaction. However, replacing the carboxamide of Asn94 by a carboxyl group (N94D exchange) did not much more weaken the Y2H interaction than the N94A exchange. Finally, simultaneous alanine substitution of two neighbouring Rpl1 residues (i.e., N94A/K95A, K95A/K97A, and K97A/K101A), whose individual alanine substitution still permitted a reduced or almost full interaction, respectively, abolished the Y2H interaction with Acl1, indicating that these Rpl1 residues synergistically contribute to the interaction with Acl1. In line with the importance of Rpl1 residues Asn94 and Lys98 for the interaction, alanine substitution of the contacting Acl1 residues Asp34 and Asp68, respectively, eliminated the Y2H interaction (Figure 6F, left panel). Moreover, while the N4A, D11A, and E114A exchanges had almost no effect, the Y47A, D70A, D72A, and E79A exchanges affected, albeit to slightly different extents, the interaction capacity of Acl1. Consistent with this, introducing the positively charged lysine at these positions (Y47K, D70K, D72K, and E79K exchanges) abolished the Y2H interaction (Figure 6F, middle panel). However, this radical charge insertion or reversal did not observably (N4K and D11K) or completely (E114K) reduce the interaction capacity of these Acl1 variants, indicating that Glu114 and, especially, Asn4 and Asp11 are less important interaction determinants. Their contribution to Rpl1 binding became, however, apparent when assessing the effects of simultaneous amino acid substitutions. While the N4A/D11A, N4A/E114A, and D11A/E114A exchanges already resulted in a visibly weaker Y2H interaction, Acl1 variants bearing the analogous lysine substitutions or their triple alanine substitution only barely (N4K/D11K) or no longer (N4K/E114K, D11K/E114K, and N4A/D11A/E114A) interacted with Rpl1 (Figure 6F, middle and right panels). Moreover, combining the N4A, D11A, and E114A substitutions with the Y47A or the E79A substitution, which on their own still permitted Acl1 to engage in a productive but reduced Y2H interaction with Rpl1, completely abolished the interaction capacity of Acl1 (Figure 6F, right panel). Likewise, introducing the double Y47A/E79A exchange or reducing the negative charge within the second β-turn by the simultaneous

D70A/D72A exchange also eliminated the Y2H interaction between Acl1 and Rpl1. To sum up, all Rpl1 and Acl1 residues that are prominently involved in the mutual interaction according to the crystal structure also contribute, albeit to different degrees, to the interaction in the Y2H assays, thus providing experimental support for the validity of the structurally visualized mode of interaction. Remarkably, our experimentally derived co-structure is practically congruent with the predicted structure model, indicating that AlphaFold3 can apparently predict co-structures of ankyrin repeat domains and their protein binding partners with good accuracy (Supplementary Figure S13E).

The conserved Bcl1 interacts via its WD40 β-propeller with Rpl1

As our homology and database searches, combined with sequence analyses and AlphaFold-Multimer predictions to evaluate the conservation of the above-determined interaction-mediating residues and the mode of mutual interaction, failed to identify clear eukaryotic Acl1 orthologues beyond the Fungi kingdom, Acl1 is likely a fungi-specific Rpl1-binding protein. Intrigued by this possibility as the majority of the known DCs are conserved throughout eukaryotes (42-44,186), we performed proximity labelling in HeLa cells with the human Rpl1 orthologue RPL10A (see Materials and Methods), fused at its C-terminus to the promiscuous miniTurbo biotin ligase variant (89), to explore the proxiOME of RPL10A in an unbiased manner and, if possible, identify its elusive, evolutionarily conserved binding partner. Enriched and abundantly detected proteins included nucleolin (NUCL), a resident of the dense fibrillar component of the nucleolus, nucleophosmin (NPM1), the scaffold protein of the granular component of the nucleolus, the early-acting AFs NOL8 (yeast Nop8) and URB1 (Npa1/Urb1), and several components of nucleolar and nucleoplasmic pre-60S particles, such as SURF6 (Rrp14), RRP1B (Rrp1), DDX18 (Has1), EBP2 (Ebp2), FTSJ3 (Spb1), LLPH (Ybl028c), CCDC86 (Cgr1), and NOP53 (Nop53) (187-193) (Figure 7A). Notably, and as observed in the TurboID assay with C-terminally TurboID-tagged Rpl1 (Figure 3A), NOP2, which is like yeast Nop2 in direct contact with the L1 stalk and can be visualized in close proximity of RPL10A on early to late nucleolar human pre-60S particles (103,194) (for the Rpl1-proximal location of Nop2 on the late nucleolar state E2 yeast pre-60S particle, see Supplementary Figure S10B), was also enriched. Contrary to the proximity labelling with the Rpl1-TurboID bait where Rpl13, but not the similarly proximal Rpl36 (eL36) (see PDB 8AGX; (185)), was found to be strongly enriched (Figure 3A), only RPL36, which is like RPL13 in immediate proximity of the C-terminal end of RPL10A in the human 80S ribosome (see PDB 6QZP; (195)), but not RPL13 was enriched in the RPL10A miniTurbo assay (Figure 7A). Moreover, a strong enrichment of the ribosome preservation factor SERBP1 (yeast Stm1), which is required for the activation of dormant 80S ribosomes (196), could be observed. Interestingly, while a human Acl1-like protein could not be revealed by this approach, the most enriched protein in the miniTurbo assay with the RPL10A bait was WDR89 (Figure 7A), the predicted human orthologue of Bcl1. In line with our proximity labelling data, WDR89 had previously been identified in affinity purifications of C-terminally HA-tagged RPL10A from two different human cell lines in large-scale interactome studies (see BioPlex Explorer website;

(197)), and AlphaFold3 predicted with high confidence the formation of a WDR89-RPL10A complex (Figure 7C). Notably, Bcl1 and Rpl1 are predicted to form a binary complex that shares remarkable similarity with the WDR89-RPL10A complex (Figure 7B and C), strongly suggesting that Bcl1 is the sought-after conserved binding partner of Rpl1. According to the structure models, the negatively charged top and side surface of the seven-bladed WD-repeat β-propeller (formed by residues 4-322 of Bcl1) accommodate conserved positively charged residues of the D1 domain, the D1-D2 linker segments, and, respectively, the D2 domain (Figure 7B and D). In line with a direct interaction, Y2H assays, performed with all possible combinations of N- and C-terminally G4BD- and G4AD-tagged Rpl1b and Bcl1, revealed a robust interaction for half of the combinations, especially when both proteins are tagged at their C-terminal end (Figure 7E). Moreover, and as predicted, the WD-repeat β-propeller domain (see Bcl1.N325 deletion variant) was sufficient to mediate an equally strong Y2H interaction as full-length Bcl1, whereas the largely unstructured C-terminal extension (residues 323-389) did not have the capacity to interact with Rpl1 (Figure 7F). Focusing on predicted interactions that occur at the top surface of the WD-repeat β-propeller, we simultaneously mutated neighbouring positively charged Rpl1 residues of the D1 domain (K195 and K196) or the D1-D2 linker segment (R45, K47, and R48), representing two of the three main Rpl1 sites that are in contact with the top surface, either to alanine or glutamate and assessed their effects on the Y2H interaction. Notably, the introduction of alanines was in both cases already sufficient to eliminate the interaction with Bcl1, while the interaction with Acl1 remained unaffected even by the charge reversal exchanges (Figure 7G), highlighting that these positively charged Rpl1 residues are relevant constituents of the Rpl1-Bcl1 interaction interface. In further support for their direct interaction, Rpl1 could be co-purified by Ni-NTA affinity purification with the C-terminally $(His)_6$-tagged Bcl1.N366 variant, which lacks the highly basic last third of the C-terminal extension (theoretical pI of 11.26 of the last 23 residues) and exhibits greater solubility than full-length Bcl1 (data not shown), upon co-expression of the two proteins in *E. coli* (Figure 7H). We conclude that Bcl1 is an evolutionarily conserved binding partner of Rpl1 that, in contrast to the relatively simple binding mode underlying the recognition of Rpl1 by the fungi-specific Acl1, appears to contact multiple positively charged sites within different structural regions (D1, D2, and interdomain linker segments) of Rpl1 in a rather sophisticated manner via two negatively charged surfaces of its WD-repeat β-propeller domain.

Acl1 and Bcl1 functionally cooperate and may form a trimeric complex with Rpl1

Next, we examined the functional relevance of the direct interaction between Bcl1 and Rpl1. As haploid Δ*bcl1* null mutant strains, generated *de novo* by deletion disruption of one *BCL1* copy in diploid W303 cells, did not exhibit a discernible growth phenotype (Figure 8A), we assessed whether absence of Bcl1 would, similar to the one of Acl1 (Figure 4C), have an impact on growth when Rpl1 is present in reduced amounts. While the simultaneous absence of Bcl1 and Rpl1a (Δ*bcl1*/Δ*rpl1a* double mutant) did not affect growth (Figure 8A), a weak, but clearly discernible enhancement of the slow-growth phenotype

of Δ*rpl1b* mutant cells could be observed in the absence of Bcl1 (Δ*bcl1*/Δ*rpl1b* double mutant) at 30ºC and, especially, at 37ºC (Figure 8B). Accordingly, the polysome profile of Δ*bcl1* cells was almost indistinguishable from the one of wild-type cells, and only a faintly perceptible formation of half-mers could be observed in Δ*bcl1*/Δ*rpl1a* double mutant cells (Supplementary Figure S14A). Polysome profile analysis with Δ*bcl1*/Δ*rpl1b* double mutant cells revealed an accumulation of free 40S subunits without a concomitant reduction in free 60S subunits, the appearance of half-mers, and an overall decrease in polysome content, these alterations were, however, not perceptibly more pronounced than in Δ*rpl1b* single mutant cells (Supplementary Figure S14B). We conclude that Bcl1 has some functional relevance when Rpl1 is present in lower amounts, especially at elevated growth temperatures, but its absence has clearly a lesser impact than the one of Acl1.

To gain insight into the functional environment of Bcl1, we next performed proximity labelling with C-terminally TurboID-tagged Bcl1. In agreement with the substantial enrichment of Bcl1 in the Acl1 TurboID assays (Figure 3B), Acl1 was prominently enriched in the reciprocal proximity labelling with the Bcl1-TurboID bait (Figure 8C). Despite being a direct interaction partner of Bcl1 (Figure 7E and H), and in contrast to the Acl1 TurboID assays, Rpl1 was, however, not enriched in the Bcl1 TurboID assay (Figure 8C). The reason for this is not clear, but the long length (67 residues) and/or a preferential orientation of Bcl1's C-terminal extension, combined with the predicted shielding of multiple surface-exposed lysine residues when Rpl1 is bound by Bcl1 and, even more so, when it could be simultaneously bound by both Bcl1 and Acl1 (Figure 7D and Supplementary Figure S15), might preclude an efficient biotinylation of Rpl1. Interestingly, the proximity labelling assay with C-terminally TurboID-tagged Bcl1 revealed that several pre-60S AFs, particularly Ebp2, Erb1, Loc1, Noc2, Nog1, Nug1, and Spb1, were among the abundantly present and discernibly enriched proteins (Figure 8C). Notably, when superposing the predicted Bcl1-Rpl1 complex onto Rpl1 in the structure of the late nucleolar state E2 pre-60S intermediate (103), the visualized parts of all the above-mentioned AFs cluster around Bcl1 (Figure 8D and Supplementary Figure S14D). Moreover, and consistent with all Rpl1 residues, except maybe Lys130, predicted to interact with Bcl1 not being in direct contact with the L1 stalk (Supplementary Figure S13B and C), an interaction of Bcl1 with Rpl1 does not appear to be precluded, at least at this late nucleolar pre-60S maturation stage, by the association of Rpl1 with its rRNA-binding site (Figure 8E). However, the superposition indicates that β-propeller blades 1 to 3 of Bcl1 would clash with Nop2 (Figure 8E), suggesting that Bcl1 must dissociate from Rpl1 prior to the incorporation of Nop2 into late nucleolar pre-60S particles. In line with the rather moderate enrichment of the above-mentioned proximal pre-60S AFs and, thus, a potentially transient association of Bcl1 with nucleolar pre-60S particles, sucrose gradient fractionation of total extracts from cells genomically expressing C-terminally TAP-tagged Bcl1 revealed that Bcl1 was strongly enriched in the soluble fractions (Figure 8F). Finally, fluorescence microscopy revealed that C-terminally ymNeonGreen-tagged Bcl1, expressed from a centromeric plasmid under the control of its cognate promoter in Δ*bcl1* cells, localized to the nucleus, where it was enriched, as indicated by its prevalent co-localization with the nucleolar

marker protein Nop58-yEmCherry, in the nucleolus (Figure 8G). Thus, the steady-state localization of Bcl1 is fully consistent with the observed enrichment of nucleolar pre-60S AFs in the proximity labelling assay, altogether strongly suggesting a functional role of Bcl1 in the nucleolus. Moreover, our data indicate that Bcl1, like most of the known DCs (Supplementary Figure S8), very likely transiently interacts with pre-ribosomal particles and that, besides directly interacting with Rpl1, it could also interact with Acl1 or form a trimeric complex with Rpl1 and Acl1.

To explore these possibilities, we next investigated whether these dimeric or trimeric complexes can be reconstituted in vitro. In line with AlphaFold not predicting the formation of a binary Bcl1-Acl1 complex (data not shown, see also below), C-terminally Flag-tagged Acl1 could, unlike Rpl1 (Figure 7H), not be co-purified by Ni-NTA affinity purification with C-terminally $(His)_6$-tagged Bcl1.N366 when the two proteins were co-expressed in *E. coli* (Figure 9A). However, upon inclusion of Rpl1 by co-expressing all three proteins together in *E. coli* (Rpl1 and Acl1-Flag from the same plasmid and Bcl1.N366-$(His)_6$ from a separate plasmid), the trimeric Bcl1.N366-Rpl1-Acl1 complex could be purified by consecutive Ni-NTA and anti-Flag affinity purification (Figure 9B). In support of this biochemical evidence, AlphaFold3 also predicted the formation of a trimeric complex (Figure 9C), with the two dimeric modules (Bcl1-Rpl1 and Rpl1-Acl1) exhibiting a mostly identical overall structure and interaction mode when compared to their individually predicted co-structures (Supplementary Figure S15A). Moreover, no direct contacts between Bcl1 and Acl1 could be observed in the predicted structure of the trimeric complex. Notably, the AlphaFold3 predictions of the trimeric complex as well as of the dimeric Acl1-Rpl1 complex also revealed a potential second Acl1-Rpl1 interaction interface. In addition to the N-terminal ankyrin repeat domain, which according to our Y2H, biochemical, and structural data is a fully sufficient and essential Rpl1-binding determinant (see Figures 5 and 6), residues of the three-helix fold (starting at residue 145 and ending approximately at residue 205) within Acl1's C-terminal half (residues 127-222) would also engage in predicted interactions with Rpl1 (Supplementary Figure S16A and B). In line with this possibility, Y2H assays revealed a weak interaction between the C-terminal half of Acl1 and full-length Rpl1 (Supplementary Figure S16C). Interestingly, while the ankyrin repeat domain recognizes a short Rpl1 segment that partially overlaps with the equally short rRNA-binding segment of the D2 domain (Figure 6A, C, and Supplementary Figure S13B and C), the predicted interaction-mediating surface of the three-helix fold would get into contact with the rRNA-binding surface of the D1 domain, which almost exclusively forms interactions with helix H77 of the L1 stalk (103,185) (Supplementary Figure S13B and C). Thus, by interacting with Rpl1 in this manner, Acl1 would effectively occlude both rRNA-binding surfaces of Rpl1 (Supplementary Figure S16A). Additionally, by embedding Rpl1 in the trimeric complex, the majority of its positively charged surfaces would be efficiently shielded by Acl1 and Bcl1 (Figure 9D and Supplementary Figure S15B and C). Taken together, the so far presented data, including the above biochemical experiments and AlphaFold predictions, provide strong evidence that Rpl1, by employing distinct surfaces to independently interact with its two binding partners, can form a trimeric complex

with Acl1 and Bcl1. Accordingly, the reciprocal enrichment of Bcl1 and Acl1 in the proximity labelling assays with the Acl1 and Bcl1 baits can only be interpreted in such a way that the trimeric complex must also occur in vivo (Figures 3B and 8C). Nevertheless, we wished to obtain additional evidence for the in vivo formation of the trimeric complex. To this end, we performed Y2H assays between Bcl1 and Acl1, as we hypothesised that endogenously expressed Rpl1 might be able to bridge an interaction of the two proteins at the promoters of the reporter genes. Consistent with this assumption, a Y2H interaction between Bcl1 and Acl1 could be observed (Figure 9E), albeit for only two of the eight combinations, i.e., when both proteins were tagged at their C-terminal end, and somewhat weaker than in the case of their respective interaction with Rpl1 (Figures 4A and 7E). In support of their Y2H interaction indeed being bridged by Rpl1, Bcl1 no longer interacted with Acl1 variants exhibiting a visibly reduced (Y47A, D70A, and D72A) or no (D34A and D68A) Rpl1-binding capacity, and, moreover, showed a strongly reduced interaction with Acl1 variants being only mildly (E79A) or barely (N4A) affected in their ability to interact with Rpl1 (Figure 9F and Supplementary Figure S16D). Moreover, Bcl1 still interacted to a largely unchanged extent with Rpl1 variants that showed no or a much weaker Y2H interaction with Acl1 (Figure 9G and Supplementary Figure S16E), indicating that the in vivo interaction between Bcl1 and Rpl1 is not necessarily dependent on Acl1 and, thus, could in principle also occur outside the trimeric complex in the normal cellular context. We conclude that Rpl1, Acl1, and Bcl1 can form, both upon their co-overexpression in bacteria and according to AlphaFold predictions, a trimeric complex that, based on several lines of evidence, also occurs in yeast cells, at least for a certain duration along Rpl1's journey to its assembly site on nucleolar pre-60S particles. Moreover, the Y2H interaction between Bcl1 and Rpl1 variants deficient in Acl1 binding raises the possibility that not only Acl1, as strongly suggested by its prominent enrichment in the Rpl1 TurboIDs and its Y2H interaction with Rpl1 variants deficient in Bcl1 binding (Figures 3A and 7G), but also Bcl1 could possibly form a binary complex with Rpl1 in vivo.

Among the r-proteins associated with DCs, Rpl1 is a special case in that it transiently interacts, most likely for a certain duration simultaneously, with two distinct binding partners. To explore the functional relevance of this particular setting, we next assessed the effects of the simultaneous absence of Acl1 and Bcl1 on growth, synthesis of 60S subunits, and the assembly of Rpl1. Consistent with a functional synergism, Δ*acl1*/Δ*bcl1* double mutant cells showed a clearly discernible growth defect at all tested temperatures compared to the virtually normal growth of Δ*acl1* and Δ*bcl1* single mutant cells (Figure 10A). In line with the observed growth defect, polysome profile analysis revealed a clear decrease in polysome content in Δ*acl1*/Δ*bcl1* double mutant cells; moreover, the accumulation of free 40S subunits and half-mer polysomes was more pronounced than in Δ*acl1* single mutant cells (Figure 10B). However, as in the case of Δ*acl1*/Δ*rpl1a* double mutant cells (Figure 4D), the size of the 60S peak was not reduced in Δ*acl1*/Δ*bcl1* double mutant cells, indicating that the formation and stability of pre-60S particles is not substantially reduced and, hence, that a fraction of the produced 60S subunits must rather be altered in a manner that renders subunit joining less efficient. Considering that the absence of Rpl1a already

negatively affected the growth of Δ*acl1* single mutant cells (Figure 4C), we next asked whether this slight reduction in Rpl1 levels would also have an additional impact on the growth of Δ*acl1*/Δ*bcl1* double mutant cells. As expected, Δ*acl1*/Δ*bcl1*/Δ*rpl1a* triple mutant cells grew substantially slower than Δ*acl1*/Δ*bcl1* and Δ*acl1*/Δ*rpl1a* double mutant cells (Figure 10C). Moreover, this further decline in growth rate was accompanied by an additional decrease in polysome content (Figure 10D). As a previous study had shown that 60S subunits lacking Rpl1 can be observed in Δ*rpl1b* mutant cells (181), i.e., when Rpl1 production is substantially reduced (72,98), we next assessed whether simultaneous absence of Acl1 and Bcl1 would also result in the formation of 60S subunits that do not contain Rpl1. To this end, we fractionated total extracts, prepared under polysome-preserving conditions by inhibiting translation elongation with cycloheximide, from wild-type, Δ*rpl1b*, and Δ*acl1*/Δ*bcl1* cells by sucrose gradient centrifugation and assessed the gradient localization and abundance of Rpl1 and the LSU and SSU control r-proteins Rpl4 and Rps3 by Western blotting (Figure 10E and Supplementary Figure S17). Upon quantification of the signal intensities of Rpl1 and Rpl4 in each fraction, we first separately calculated the relative abundance of Rpl1 and Rpl4 in the individual fractions by dividing their signal intensity in these fractions by their average signal intensity in two polysomal fractions (fraction 13 and 14), assuming that 60S subunits within translating 80S ribosomes not only obligatorily contain Rpl4, whose incorporation is essential for the formation of 60S subunits (34,198), but should also be equipped with Rpl1 in all three strains, as previously indicated by the similar relative levels of Rpl1 in the polysome fractions of wild-type and Δ*rpl1b* mutant cells (181). Then, we formed the ratio between the above-determined normalized abundance values of Rpl1 and Rpl4 in the individual fractions to assess the proportion of 60S subunits lacking Rpl1 in the different fractions of our two experimental replicates. Surprisingly, by applying this quantification strategy, we observed that only around 75% of the 60S subunits contained Rpl1 in the wild-type strain (Figure 10E, F, and Supplementary Figure S17). In the Δ*rpl1b* mutant strain, the proportion of 60S subunits containing Rpl1 decreased to below 20%, which, after normalization against the above wild-type value, agrees well with the previously reported reduction in Rpl1 presence on 60S subunits to around 30% of wild-type levels (181). Notably, cells simultaneously lacking Acl1 and Bcl1 (Δ*acl1*/Δ*bcl1* double mutant) exhibited a similar decrease in the proportion of 60S subunits containing Rpl1 as Δ*rpl1b* mutant cells, indicating that the two binding partners of Rpl1 cooperatively ensure that Rpl1 is provided in sufficient amounts and/or gets efficiently incorporated into pre-60S particles. Taken together, we conclude that the joint function of Acl1 and Bcl1, which together, by embedding Rpl1 within a trimeric complex, are predicted to efficiently shield almost all positively charged surfaces of Rpl1, is related to the provisioning of assembly-competent Rpl1.

Acl1 and Bcl1 contain functional NLSs that may target the trimeric complex to the nucleus

The nuclear import of highly basic proteins, such as histones and r-proteins, has been shown to rely, despite their small size, on active, importin-mediated transport processes (9,28,199,200). However, as

none of the different importins was particularly enriched in the Rpl1 TurboID assays and as a cytoplasmically formed trimeric complex, owing to its size (calculated molecular mass of 93 kDa) exceeding the limit for efficient passive diffusion across the selective phase of the NPC (201,202), would probably be precluded from efficiently entering the nucleus, we wondered whether Acl1 and/or Bcl1 might be involved in mediating the nuclear import of Rpl1. Consistent with this possibility, inspection of the primary sequence of Acl1 and Bcl1, which are both predominantly located in the nucleus in exponentially growing yeast cells (Figures 4E and 8G), revealed that both proteins harbour a potential NLS sequence. Acl1 contains at its C-terminal extremity four consecutive basic residues (KRRK) (Figure 11A), which, as also predicted by PSORT II (203), correspond to a classical monopartite NLS bearing the loose K-K/R-x-K/R consensus sequence that is expected to be recognized by the importin-α Kap60 (204). In line with this, AlphaFold3 predictions of the putative pentameric Kap95-Kap60-Acl1-Rpl1-Bcl1 import complex indicated that these positively charged residues would interact in a canonical manner with the major NLS-binding site of Kap60 (131) (Supplementary Figure S18A), suggesting that the transport adaptor Kap60, in conjunction with the importin-β Kap95, could be responsible for the nuclear import of Acl1 as well as of the dimeric Acl1-Rpl1 and the trimeric Acl1-Rpl1-Bcl1 complex. Bcl1 contains, like the validated Kap104 import cargo Hrp1 (205-207), a basic PY-NLS (bPY-NLS) at its C-terminal extremity (Figure 11B). Consistent with matching well the consensus sequence (basic-enriched stretch that is followed by a C-terminal R/K/H-$x_{(2-5)}$-P-Y/ϕ signature, with ϕ denoting a hydrophobic residue) (151,163), AlphaFold3 predicted with good confidence that the bPY-NLS of Bcl1 (residues 371-389) would be accommodated by the importin-β Kap104 in a similar manner as bPY-NLSs in co-structures with the human Kap104 equivalent Kapβ2/TNPO1 (208,209) (Supplementary Figure S18C). Moreover, AlphaFold3 also predicted the formation of the putative tetrameric Kap104-Bcl1-Rpl1-Acl1 import complex (Supplementary Figure S18B), in which the two modules, i.e., the dimeric Kap104-Bcl1 complex and the trimeric Bcl1-Rpl1-Acl1 complex, retained their overall structure and interaction mode when compared to their individually predicted co-structures. In further support of Kap104 being a strong candidate importin for mediating the nuclear import of Bcl1 and, thus, possibly also of the dimeric Bcl1-Rpl1 and the trimeric Bcl1-Rpl1-Acl1 complex, Bcl1 was, like the known bPY-NLS-containing Kap104 cargos Hrp1, Nab2, Syo1, and Tfg2 (46,206,207,210,211), previously detected by LC-MS/MS in a one-step affinity purification of Flag-tagged Kap104 (212).

To experimentally address whether the C-terminal segments of Acl1 and Bcl1 carrying the supposed NLS sequences would indeed correspond to functional NLSs in vivo, we assessed their capacity to target an N-terminally fused triple yEGFP reporter (3xyEGFP) to the nucleus by fluorescence microscopy. In line with the four basic residues at the C-terminal extremity of Acl1 being able to mediate nuclear import, the 3xyEGFP reporter fused to residues 205-222 (Acl1.205C) or 209-222 (Acl1.209C) was exclusively or, respectively, predominantly present in the nucleus (Figure 11A).

Similarly, both the entire C-terminal extension (residues 323-389, Bcl1.323C) of Bcl1 and a shorter, 26-residue-long segment (residues 364-389, Bcl1.364C), essentially consisting of the predicted bPY-NLS (residues 371-389), were sufficient to confer exclusive nuclear localization to the 3xyEGFP reporter, whereas the C-terminal extension lacking the bPY-NLS did not exhibit nuclear targeting activity (Figure 11B).

To obtain experimental evidence for a direct interaction between the predicted bPY-NLS of Bcl1 and Kap104, we intended to employ, as already before for the validation of interactions between importin-βs and r-proteins (see Figure 2), the Y2H method. To this end, we generated the Kap104.305C variant, which, akin to the previously successfully used Kap121.302C variant (Figure 2A), lacks HEAT repeats 1 to 7 and, thus, the majority of the RanGTP-interacting residues of Kapβ2/TNPO1 (141,153), but retains all Kap104 residues predicted to interact with Bcl1 (Supplementary Figure S18C). As hoped, Y2H assays between the N-terminally G4BD-tagged bPY-NLS-containing segment of Hrp1 (residues 504-534, Hrp1.504C) and the full-length Kap104 and Kap104.305C prey proteins, fused at their C-terminal end to the G4AD, permitted to recapitulate the previously reported RanGTP-sensitive in vitro interaction between Kap104 and a C-terminal Hrp1 segment starting at residue 494 (207) (Figure 11C). Consistent with Bcl1 being an import cargo of Kap104, the short bPY-NLS-containing segment of Bcl1 (Bcl1.364C) exhibited an equally strong Y2H interaction with the Kap104.305C variant as Hrp1.504C but did no longer interact with full-length Kap104 (Figure 11C). Similarly, also full-length Bcl1 interacted strongly with the Kap104.305C variant, while still showing a weak residual interaction with full-length Kap104. Intriguingly, however, the entire C-terminal extension of Bcl1 (Bcl1.323C), while, as expected, robustly interacting with the Kap104.305C variant, still displayed a moderately strong Y2H interaction with full-length Kap104. The reason for this is unclear, but we speculate that the residues preceding the bPY-NLS might somehow reduce, potentially by introducing a steric constraint, the efficiency by which the Y2H interaction between Kap104 and the complete C-terminal extension of Bcl1 is disrupted by endogenous GTP-loaded Gsp1 once this complex has been installed at the promoters of the reporter genes. To examine the relevance of the characteristic R-$x_{(2)}$-P-Y signature for the interaction, we evaluated the effects of the individual or combined alanine substitution of these residues on the Y2H interaction. While the R385A substitution in the context of the complete C-terminal extension or the short bPY-NLS-containing segment did not or, respectively, only marginally affect the Y2H interaction with the Kap104.305C variant, it abolished the interaction between the complete C-terminal extension and full-length Kap104 (Figure 11C and Supplementary Figure S18D). Strikingly, the single Y389A exchange, disrupting the predicted hydrogen bond between the tyrosyl of the C-terminal Tyr389 residue and the carboxyl group of residue Asp408 of Kap104 (Supplementary Figure S18C), was already sufficient to abrogate, both in the context of the entire and short C-terminal region, the Y2H interaction with the Kap104.305C variant (Figure 11C and Supplementary Figure S18D); accordingly, also the simultaneous P388A/Y389A double and R385A/P388A/Y389A triple

substitutions abolished the interaction. These Y2H results are reminiscent of previously reported binding affinity measurements between mutant bPY-NLS variants of Hrp1 and full-length Kap104, which showed that the introduction of the Y532A and P531A/Y532A substitutions resulted in no detectable in vitro binding, whereas the R525A exchange did not affect the binding capacity of Hrp1's bPY-NLS (207); thus, further substantiating the relevance of the tyrosine residue within the PY motif for the interaction with Kap104 in the case of C-terminally located bPY-NLSs.

Next, we determined whether these amino acid substitutions would also affect the nuclear targeting activity of the complete C-terminal extension or the short bPY-NLS-containing segment. In line with the Y2H interaction data, the R385A substitution did not alter the exclusive nuclear accumulation of the N-terminally fused 3xyEGFP reporter (Figure 11B and Supplementary Figure S18E). Surprisingly, however, the Y389A, P388A/Y389A, and R385A/P388A/Y389A exchanges, both in the Bcl1.323C and Bcl1.364C context, only resulted in a similar, partial relocalization of the 3xyEGFP reporter to the cytoplasm, showing that the nuclear targeting activity of the bPY-NLS-containing segment is not abolished by mutations that abrogate its Y2H interaction with the Kap104.305C variant. This observation either implies that this 26-residue-long segment, which is rich in positively charged amino acids (eight lysines and three arginines), can also be recognized and get imported by another importin than Kap104 or could indicate that the introduced amino acid substitutions do not completely prevent the formation of a productive import complex with full-length Kap104. A promising alternative importin was Kap121, as it was the only importin that was noteworthily enriched in the proximity labelling assay with C-terminally TurboID-tagged Bcl1 (Supplementary Figure S18F). Consistent with their suggested physical proximity, the complete C-terminal extension of Bcl1, when fused at its N-terminal end to the G4BD, interacted quite well with the C-terminally G4AD-tagged Kap121.302C variant, but, and in line with Bcl1 being a potential import cargo of Kap121, it did not show a Y2H interaction with full-length Kap121 (Supplementary Figure S18G). To our surprise, the shorter, 26-residue-long Bcl1.364C segment did, however, not interact with the Kap121.302C variant, indicating that Kap121 might not be the second importin contributing to its nuclear targeting when N-terminally fused to the 3xyEGFP reporter and, thus, that at least one further importin could potentially be involved in the import of Bcl1. However, it cannot be excluded that a steric constraint might selectively prevent the formation of the Y2H complex between Bcl1.364C and the N-terminally truncated Kap121.302C variant at the promoters of the reporter genes, while formation of the import complex with full-length Kap121 might still be possible. We conclude that Bcl1 harbours an NLS region at its C-terminal extremity that not only contains a bPY-NLS for Kap104-mediated import but also very likely features at least one or possibly even two additional, yet-to-be-defined determinants that enable nuclear import, with one possibly being recognized by Kap121.

Considering that Acl1 and Bcl1 can form a trimeric complex with Rpl1 in vitro and in vivo, we examined whether their nuclear import would show some interdependence. To this end, we expressed combinations of Acl1, Bcl1, and their C-terminally truncated variants lacking the NLS region (i.e.,

Acl1.N208 and Bcl1.N366), with one of the two being C-terminally tagged with ymNeonGreen, under the control of their cognate promoters from separate plasmids in Δ*acl1*/Δ*bcl1* cells. As expected, Acl1-ymNeonGreen and Bcl1-ymNeonGreen showed almost exclusive nuclear accumulation when co-expressed with either the full-length or NLS-lacking variant of Bcl1 and Acl1 (Figure 11D and E), indicating that their efficient import is not dependent on the presence of the NLS region on the other DC. Notably, also ymNeonGreen-tagged Acl1.N208 and Bcl1.N366 exhibited, when co-expressed with full-length Bcl1 or Acl1, a predominant nuclear localization, suggesting that these NLS-lacking variants get, albeit slightly less efficiently, imported as part of the trimeric Acl1-Rpl1-Bcl1 complex. In line with this conjecture, no nuclear accumulation of ymNeonGreen-tagged Acl1.N208 and Bcl1.N366 could be observed when they were co-expressed together with Bcl1.N366 or Acl1.N208. These results strongly suggest that Acl1 and Bcl1, besides being imported alone or in a dimeric complex with Rpl1, could also form a trimeric import complex in the cytoplasm of wild-type cells. As a cytoplasmic recognition of Rpl1 by Acl1 and Bcl1 could already occur during its synthesis, we assessed the capacity of C-terminally TAP-tagged Acl1 and Bcl1 to co-translationally capture nascent Rpl1 by IgG-Sepharose pull-down and real-time qRT-PCR (see Materials and Methods). While purification of TAP-tagged Rrb1 and Acl4, as previously shown (34,41), specifically enriched the *RPL3* or *RPL4* mRNA, an enrichment of the mRNA encoding Rpl1 could neither be observed in the Acl1 nor the Bcl1 purification (Supplementary Figure S19). Likewise, the experiment with both N- and C-terminally TAP-tagged Bcp1 did not reveal an enrichment of the *RPL23* mRNA. We conclude that both Acl1 and Bcl1 most likely only interact with newly synthesized Rpl1 once it has been released from the ribosome.

DISCUSSION

In this study, with the aim of expanding the inventory of DCs of r-proteins, we have performed a TurboID-based proximity labelling screen with all LSU r-proteins in the yeast *S. cerevisiae* (Figure 1A and Supplementary Figure S1). Despite certain potential limitations that are inherent to this proximity-dependent biotinylation approach, such as the availability of surface-exposed proximal lysine residues as biotinylation acceptor sites on the overall acidic DCs, the distance between the attached TurboID biotin ligase and the bound DC, and the productive complex formation between the tagged r-protein and its DC being hindered or prevented by the fused TurboID moiety, the majority (six out of eight) of the known DCs as well as one novel candidate DC were successfully identified as prominently and selectively enriched proteins in the proximity labelling assays of their respective N- and/or C-terminally TurboID-tagged r-protein client (Supplementary Figure S6; see also below). Importantly, analysis of multiple experimental replicates of the TurboID assays performed with the Rpl3-TurboID and the TurboID-Rpl1b baits revealed high reproducibility (Figure 1C and Supplementary Figure S10A), indicating that the single replicate screen generated a robust and reliable data set. In further support of the suitability of the chosen approach and its experimental design (induced expression of the plasmid-encoded TurboID-tagged r-protein for 1 h with simultaneous induction of biotinylation by addition of exogenous biotin) for the identification of transient interaction partners of unassembled r-proteins, the TurboID-based proximity labelling screen also unveiled potential interactions between LSU r-proteins and importins, which we confirmed in the case of four r-proteins by Y2H assays (Figure 2 and Supplementary Figure S1). Remarkably, even though designed to preferentially capture transient interactions of r-proteins prior to their assembly into pre-ribosomal particles, our approach also permitted to illuminate r-protein neighbourhoods on successive pre-ribosomal particles at spatiotemporal resolution, as exemplarily illustrated for the AFs and r-proteins that were reproducibly enriched in the proximity labelling assays with the Rpl3-TurboID and the TurboID-Rpl1b baits (Figure 1D-G and Supplementary Figure S10B-H). Finally, the reciprocal proximity labelling experiments with the already known, N- and C-terminally TurboID-tagged DCs not only prominently enriched in each case the respective r-protein client but also revealed in several cases an enrichment of distinct AFs (Supplementary Figure S8), which are notably either in proximity of their r-protein client on pre-ribosomal particles or have previously been functionally connected to their r-protein client (see for example neighbourhood of Rpl23 in Figure 1D), indicating that most DCs appear to be transiently associated with pre-ribosomal particles in order to promote the coordinated incorporation of their r-protein clients.

Notably, our proximity labelling screen enabled the identification of the fungi-specific ankyrin repeat-containing Acl1 as a transient interaction partner of Rpl1, which is the universally conserved r-protein associated with the flexible L1 stalk of the 60S subunit. Strikingly, and unlike the hitherto known DC-bound r-proteins, Rpl1 is also transiently associated with a second interaction partner, Bcl1,

a predicted WD-repeat β-propeller protein that is conserved throughout eukaryotes. While Acl1 and Bcl1 are individually dispensable for optimal growth (Figure 10A), several lines of evidence strongly suggest that they functionally cooperate to ensure that yeast cells are supplied with sufficient amounts of assembly-competent Rpl1. First, their simultaneous absence results in a clearly discernible growth defect, which is further amplified in cells concurrently lacking Rpl1a, and the synthesis of 60S subunits that can be devoid of Rpl1 (Figure 10). Second, Acl1 and Bcl1, although not directly interacting with each other, can form a trimeric complex with Rpl1 in vitro (Figure 9A and B), which, based on the prominent enrichment of Acl1 and Bcl1 in the reciprocal TurboID assays (Figures 3B and 8C), must also occur in vivo, at least for some duration during Rpl1's journey from the cytoplasm to its assembly site on nucleolar pre-60S particles. Third, the experimentally solved co-structure of Acl1's ankyrin repeat domain in complex with the second Rpl1 domain as well as AlphaFold3 predictions of the trimeric complex revealed that the suggested mode of Rpl1 accommodation would efficiently shield almost all of its positively charged surfaces (Figure 9D), which could prevent the aggregation of Rpl1 and/or facilitate its transport through the selective phase of the NPC. Based on the here presented data and the current state of knowledge, we propose the following model for how Rpl1, at least in the yeast *S. cerevisiae*, might be chaperoned by Acl1 and Bcl1 on its voyage to its rRNA-binding site on the L1 stalk within nucleolar pre-60S particles (Figure 12). Considering the prominent reciprocal enrichment of Acl1 and Rpl1 in their TurboID assays, the efficient formation of a soluble dimeric Acl1-Rpl1 complex upon co-expression of the two proteins in *E. coli*, and their simple mode of interaction (Figures 3, 4B, and 6A), we believe that Acl1 binds very early on to newly synthesized Rpl1; however, most likely not in a co-translational manner (Supplementary Figure S19). As nuclear accumulation of Acl1 and Bcl1 is only abrogated when both proteins simultaneously lack their C-terminal NLS region (Figure 11D and E), one can infer that Acl1 and Bcl1 can get co-imported in association with Rpl1 in a trimeric complex. We have shown that the C-terminal extremities of both Acl1 and Bcl1 exhibit nuclear targeting activity (Figure 11A and B). While the very C-terminal KRRK sequence of Acl1 is predicted to be recognized in a canonical manner by the major NLS-binding site of Kap60 and, thus, most likely enables classical import via the Kap60-Kap95 importin-α/β heterodimer (131,204) (Supplementary Figure S18A), the NLS region of Bcl1 appears to be more complex as it not only contains a C-terminally located bPY-NLS that interacts with the importin-β Kap104 in Y2H assays (151,163) (Figure 11B, C, and Supplementary Figure S18B and C), but likely also features a binding site for the importin-β Kap121 (Supplementary Figure S18G), which is the only discernibly enriched importin in the proximity labelling assay with the Bcl1-TurboID bait (Figure 8C and Supplementary Figure S18F), and presumably also for at least one additional, yet-to-be-assigned importin. These observations suggest that import of the trimeric complex could be independently mediated by at least three different importins; hence, further experiments are required to first corroborate an actual contribution of the above-mentioned importins and second to reveal the favoured import pathway of the trimeric complex.

However, considering the minor phenotypic consequences of the individual absence of Acl1 or Bcl1 (Figure 10A and B), their capacity to independently interact with Rpl1 in vitro (Figures 4B and 7H), and the finding that Rpl1 variants deficient in Acl1 or Bcl1 binding can still engage in a Y2H interaction with Bcl1 or, respectively, Acl1 (Figures 7G and 9G)**Error! Reference source not found.**, it can be assumed that import of Rpl1 does not obligatorily require prior formation of the trimeric complex but could also occur in the context of the dimeric Acl1-Rpl1 and, presumably to a lesser degree, the dimeric Bcl1-Rpl1 complex. Moreover, as yeast cells lacking both Acl1 and Bcl1 are viable, while Rpl1 is an essential LSU r-protein that could be visualized in the cryo-EM structures of late nucleolar state E pre-60S intermediates (103), nuclear import of 'free' Rpl1 would have to occur, either by passive diffusion or by its direct association with an importin. Alternatively, it cannot be formally excluded that Rpl1, when not imported in complex with Acl1 and/or Bcl1, could also get incorporated into cytoplasmic pre-60S intermediates that do not yet contain Rpl1. In line with this speculative scenario being potentially possible, it has been shown that pre-60S particles lacking Rpl1 can get exported, albeit less efficiently, from the nucleus to the cytoplasm (175,181). However, we assume that newly synthesized Rpl1 is efficiently captured by Acl1 and presumably also by Bcl1, but likely not in a co-translation manner (Supplementary Figure S19), and, thus, would get rapidly imported into the nucleus under normal conditions, primarily in the context of the trimeric Acl1-Rpl1-Bcl1 and, to a lesser extent, the dimeric Acl1-Rpl1 complex. Once in the nucleus, these Rpl1-containing cargo complexes are expected to be released from the respective transport-mediating importin by the binding of RanGTP, enabling the recycling and export of the importin. In case that the dimeric Acl1-Rpl1 complex was imported, the trimeric complex could potentially still be formed in the nucleus upon recruitment of Bcl1, which exhibits both a nucleolar and nucleoplasmic steady-state localization (Figure 8G), from its free nuclear pool. Based on the observed and predicted interactions of Rpl1 with the L1 stalk rRNA and within the trimeric complex as well as the revealed in vivo neighbourhoods of Acl1 and Bcl1, we envisage the following scenario for the transfer of Rpl1 from the trimeric complex onto its pre-ribosomal binding site. As the robust interaction between the ankyrin repeat domain of Acl1 and the short segment within the second structural domain of Rpl1 occludes the rRNA-binding surface of the D2 domain (103) (Figures 5C, D, 6A, and Supplementary Figure S13B and C), the initial interaction of Rpl1 with the L1 stalk rRNA is most likely mediated by the composite rRNA-binding surface of the D1 domain. This surface might, however, also be partially masked by predicted contacts with the predicted three-helix fold within Acl1's C-terminal part (Supplementary Figure S16B). But, as the C-terminal domain of Acl1 is only very weakly interacting with Rpl1 in Y2H assays (Supplementary Figure S16C), it can be assumed that the D1 domain will preferentially bind to its cognate rRNA-binding site and, thus, disengage from the loosely bound C-terminal domain of Acl1. Once docked via the D1 domain on helix H77 of the L1 stalk, the presumed higher affinity of the second rRNA-binding site, consisting of rRNA residues that are part of the bulge connecting 25S rRNA helices H78 and H77 (103) (Supplementary Figure S13B), is expected to enable the rapid release of Acl1 from its binding site on the D2 domain

and the full binding of Rpl1. In line with a highly transient association of Acl1 with pre-60S particles during the process of Rpl1 incorporation, no Rpl1-surrounding pre-60S AFs were enriched in the Acl1 TurboID assays (Figure 3B). In contrast, Bcl1 appears to remain associated with Rpl1 upon Acl1 release, as indicated by the moderate enrichment of several nucleolar pre-60S AFs, which notably all cluster around Bcl1 when the predicted Bcl1-Rpl1 complex is superposed onto Rpl1 in the cryo-EM structure of the late nucleolar state E2 pre-60S intermediate (103) (Figure 8D), in the proximity labelling assay with the Bcl1-TurboID bait (Figure 8C). According to this superposition, an interaction of Bcl1 with rRNA-bound Rpl1 is possible, but would most likely be precluded by a clash of β-propeller blades 1 to 3 of Bcl1 with Nop2 (Figure 8E), which binds to the concave surface of the L1 stalk rRNA on late nucleolar state E pre-60S intermediates (103). This raises the possibility that Bcl1 could get displaced from Rpl1 by Nop2 and would imply that incorporation of Rpl1, when transferred from the trimeric complex, very likely occurs prior to the full integration of Nop2 into late nucleolar pre-60S particles. How Acl1 and Bcl1 get back to the cytoplasm for another round of recognition and import of newly synthesized Rpl1 remains to be determined, but their relatively small sizes (calculated molecular weights of 24.67 kDa and 43.83 kDa, respectively) would be compatible with a passive diffusion mechanism (202). Clearly, future experiments will be required to fully appreciate the exact functional roles of Acl1 and Bcl1 as binding partners of Rpl1. Moreover, it will be of interest to learn how the protection, transport, and incorporation of uL1 is achieved in more advanced eukaryotic organisms, which notably appear to lack an Acl1-like binding partner of uL1. The identification of WDR89, the putative human orthologue of Bcl1, in the proximity labelling assay with human uL1 in HeLa cells (Figure 7A), as well as the remarkable similarity of the predicted structure models of the human WDR89-RPL10A and the yeast Bcl1-Rpl1 complex (Figure 7B and C), indicate that Bcl1-like proteins may play a prominent, potentially conserved role in this process in all eukaryotic organisms.

Surprisingly, Acl1 was the only novel selective r-protein binding partner that could be readily uncovered by our TurboID-based proximity labelling screen, raising the possibility that there might be no further DCs of LSU r-proteins in the yeast *S. cerevisiae* than the already discovered ones. Considering, however, that only six of the eight known DCs, as well as Acl1, were prominently enriched in the proximity labelling assays of their respective N- and/or C-terminally TurboID-tagged r-protein client (Figure 3A and Supplementary Figure S6), while the reciprocal TurboID assays with the DC baits, except in the case of Bcl1, effortlessly identified each respective r-protein client (Figure 3B and Supplementary Figure S8), it is possible that our proximity labelling screen may not have revealed all previously undiscovered DCs of LSU r-proteins. Moreover, we deem it likely that some selective r-protein interactors, as observed for Bcl1 in the assays with the TurboID-Rpl1b bait (Figure 3A), could still be hidden among the numerous, less prominently enriched proteins, indicating that the comprehensive identification of further candidate DCs would require a more detailed analysis of the data set. Alternatively, more general binding partners of free basic proteins such as the histone chaperone Nap1, which has previously been shown to not only interact with the SSU r-protein Rps6

(eS6) but also, at least in Y2H assays, with the LSU r-proteins Rpl39 (eL39) and Rpl42 (44), could take over a protective function for several r-proteins. In line with this conjecture, Nap1 was discernibly, albeit to different extents, enriched in the TurboID assays of Rpl39 and Rpl42 as well as in the ones of additional LSU r-proteins, including Rpl8, Rpl15 (eL15), Rpl24, and Rpl37 (eL37) (Supplementary Figure S1). Not unexpectedly, importins emerged as another class of transient interaction partners of LSU r-proteins in our TurboID-based proximity labelling screen. Here, we provide first evidence, by employing Y2H assays, for a direct interaction between four importin/r-protein pairs that were highlighted by the TurboID assays (Figure 2). While Rpl6, Rpl30, and Rpl38 likely correspond to bona fide import cargo of Kap114, Kap119, and, respectively, Kap121, the finding that Rpl40, which gets incorporated during the cytoplasmic stage of pre-60S maturation (100,101,116), only interacts with full-length Kap114 but not with variants lacking partially or completely the N-terminal RanGTP-binding site in the Y2H assays suggests that Kap114 could mediate the export of Rpl40. A bidirectional transport activity has been previously assigned to Kap122 (153,162); thus, Kap114, if indeed exporting Rpl40, would be the second *S. cerevisiae* biportin (151). Notably, these four r-proteins are predicted to be almost entirely accommodated by the respective importin in the AlphaFold3 models of the binary complexes (Figure 2). Compared to the prevailing recognition of short linear NLS sequences for nuclear targeting, the predicted entrapment of these r-proteins by the inner concave surface of the importins would efficiently shield their positively charged surfaces. Thus, our study reinforces the notion that importins, as already postulated by the Görlich laboratory more than 20 years ago (9), combine the protection of basic domains with their nucleocytoplasmic transport.

Taken together, this study has highlighted the suitability of the TurboID-based proximity labelling approach for the identification of transient interaction partners of r-proteins. We believe that this data set will not only fuel our exciting journey towards a comprehensive overview of all transient interactors of unassembled r-proteins but may also serve as an inspiring resource for illuminating interactions on pre-ribosomal particles that have escaped structural analyses and for exploring the unknOME side of the LSU r-protein proxiOMEs.

ACKNOWLEDGEMENTS

We gratefully acknowledge the Bioimage Core Facility of the University of Fribourg as well as Michael Stumpe of the Proteomics Unit of the Metabolomics and Proteomics Platform (MAPP) of the Department of Biology of the University of Fribourg for their support and assistance. We thank Jesús de la Cruz for providing the anti-Rpl1 antibody.

FUNDING

This work was supported by the Swiss National Science Foundation (SNSF project grants 31003A_175547 and 310030_204801 to D.K. and 310030_212187 to J.D.; SNSF R'Equip grant 316030_177088 to J.D.), the Max Planck Society (G.B.), and the Canton of Fribourg (D.K. and J.D.). Funding for open access charge: Swiss National Science Foundation.

CONFLICT OF INTEREST

None declared

REFERENCES

1. Melnikov, S., Ben-Shem, A., Garreau de Loubresse, N., Jenner, L., Yusupova, G. and Yusupov, M. (2012) One core, two shells: bacterial and eukaryotic ribosomes. *Nat Struct Mol Biol*, **19**, 560-567.
2. Woolford, J.L., Jr. and Baserga, S.J. (2013) Ribosome biogenesis in the yeast Saccharomyces cerevisiae. *Genetics*, **195**, 643-681.
3. Warner, J.R. (1999) The economics of ribosome biosynthesis in yeast. *Trends Biochem Sci*, **24**, 437-440.
4. Fernandez-Pevida, A., Kressler, D. and de la Cruz, J. (2015) Processing of preribosomal RNA in Saccharomyces cerevisiae. *Wiley Interdiscip Rev RNA*, **6**, 191-209.
5. Mitterer, V. and Pertschy, B. (2022) RNA folding and functions of RNA helicases in ribosome biogenesis. *RNA Biol*, **19**, 781-810.
6. Klinge, S. and Woolford, J.L., Jr. (2019) Ribosome assembly coming into focus. *Nat Rev Mol Cell Biol*, **20**, 116-131.
7. Bassler, J. and Hurt, E. (2019) Eukaryotic Ribosome Assembly. *Annu Rev Biochem*, **88**, 281-306.
8. Kressler, D., Hurt, E. and Bassler, J. (2017) A Puzzle of Life: Crafting Ribosomal Subunits. *Trends Biochem Sci*, **42**, 640-654.
9. Jäkel, S., Mingot, J.M., Schwarzmaier, P., Hartmann, E. and Gorlich, D. (2002) Importins fulfil a dual function as nuclear import receptors and cytoplasmic chaperones for exposed basic domains. *EMBO J*, **21**, 377-386.
10. Sung, M.K., Porras-Yakushi, T.R., Reitsma, J.M., Huber, F.M., Sweredoski, M.J., Hoelz, A., Hess, S. and Deshaies, R.J. (2016) A conserved quality-control pathway that mediates degradation of unassembled ribosomal proteins. *Elife*, **5**.
11. Sung, M.K., Reitsma, J.M., Sweredoski, M.J., Hess, S. and Deshaies, R.J. (2016) Ribosomal proteins produced in excess are degraded by the ubiquitin-proteasome system. *Mol Biol Cell*, **27**, 2642-2652.
12. Tye, B.W., Commins, N., Ryazanova, L.V., Wuhr, M., Springer, M., Pincus, D. and Churchman, L.S. (2019) Proteotoxicity from aberrant ribosome biogenesis compromises cell fitness. *Elife*, **8**.
13. Albert, B., Kos-Braun, I.C., Henras, A.K., Dez, C., Rueda, M.P., Zhang, X., Gadal, O., Kos, M. and Shore, D. (2019) A ribosome assembly stress response regulates transcription to maintain proteome homeostasis. *Elife*, **8**.
14. Pillet, B., Mendez-Godoy, A., Murat, G., Favre, S., Stumpe, M., Falquet, L. and Kressler, D. (2022) Dedicated chaperones coordinate co-translational regulation of ribosomal protein production with ribosome assembly to preserve proteostasis. *Elife*, **11**.
15. de la Cruz, J., Gomez-Herreros, F., Rodriguez-Galan, O., Begley, V., de la Cruz Munoz-Centeno, M. and Chavez, S. (2018) Feedback regulation of ribosome assembly. *Curr Genet*, **64**, 393-404.
16. Shore, D., Zencir, S. and Albert, B. (2021) Transcriptional control of ribosome biogenesis in yeast: links to growth and stress signals. *Biochem Soc Trans*, **49**, 1589-1599.
17. Albert, B., Knight, B., Merwin, J., Martin, V., Ottoz, D., Gloor, Y., Bruzzone, M.J., Rudner, A. and Shore, D. (2016) A Molecular Titration System Coordinates Ribosomal Protein Gene Transcription with Ribosomal RNA Synthesis. *Mol Cell*, **64**, 720-733.
18. Zencir, S., Dilg, D., Rueda, M.P., Shore, D. and Albert, B. (2020) Mechanisms coordinating ribosomal protein gene transcription in response to stress. *Nucleic Acids Res*, **48**, 11408-11420.
19. Knight, B., Kubik, S., Ghosh, B., Bruzzone, M.J., Geertz, M., Martin, V., Denervaud, N., Jacquet, P., Ozkan, B., Rougemont, J. *et al.* (2014) Two distinct promoter architectures centered on dynamic nucleosomes control ribosomal protein gene transcription. *Genes Dev*, **28**, 1695-1709.
20. Huber, F.M. and Hoelz, A. (2017) Molecular basis for protection of ribosomal protein L4 from cellular degradation. *Nat Commun*, **8**, 14354.

21. Zhang, Y., Sinning, I. and Rospert, S. (2017) Two chaperones locked in an embrace: structure and function of the ribosome-associated complex RAC. *Nat Struct Mol Biol*, **24**, 611-619.
22. Kramer, G., Shiber, A. and Bukau, B. (2019) Mechanisms of Cotranslational Maturation of Newly Synthesized Proteins. *Annu Rev Biochem*, **88**, 337-364.
23. Deuerling, E., Gamerdinger, M. and Kreft, S.G. (2019) Chaperone Interactions at the Ribosome. *Cold Spring Harb Perspect Biol*, **11**.
24. Gamerdinger, M. and Deuerling, E. (2024) Cotranslational sorting and processing of newly synthesized proteins in eukaryotes. *Trends Biochem Sci*, **49**, 105-118.
25. Koplin, A., Preissler, S., Ilina, Y., Koch, M., Scior, A., Erhardt, M. and Deuerling, E. (2010) A dual function for chaperones SSB-RAC and the NAC nascent polypeptide-associated complex on ribosomes. *J Cell Biol*, **189**, 57-68.
26. de la Cruz, J., Karbstein, K. and Woolford, J.L., Jr. (2015) Functions of ribosomal proteins in assembly of eukaryotic ribosomes in vivo. *Annu Rev Biochem*, **84**, 93-129.
27. Lam, Y.W., Lamond, A.I., Mann, M. and Andersen, J.S. (2007) Analysis of nucleolar protein dynamics reveals the nuclear degradation of ribosomal proteins. *Curr Biol*, **17**, 749-760.
28. Jäkel, S. and Görlich, D. (1998) Importin beta, transportin, RanBP5 and RanBP7 mediate nuclear import of ribosomal proteins in mammalian cells. *EMBO J*, **17**, 4491-4502.
29. Melnikov, S., Ben-Shem, A., Yusupova, G. and Yusupov, M. (2015) Insights into the origin of the nuclear localization signals in conserved ribosomal proteins. *Nat Commun*, **6**, 7382.
30. Rout, M.P., Blobel, G. and Aitchison, J.D. (1997) A distinct nuclear import pathway used by ribosomal proteins. *Cell*, **89**, 715-725.
31. Seidel, M., Romanov, N., Obarska-Kosinska, A., Becker, A., Trevisan Doimo de Azevedo, N., Provaznik, J., Nagaraja, S.R., Landry, J.J.M., Benes, V. and Beck, M. (2023) Co-translational binding of importins to nascent proteins. *Nat Commun*, **14**, 3418.
32. Mitterer, V., Gantenbein, N., Birner-Gruenberger, R., Murat, G., Bergler, H., Kressler, D. and Pertschy, B. (2016) Nuclear import of dimerized ribosomal protein Rps3 in complex with its chaperone Yar1. *Sci Rep*, **6**, 36714.
33. Steiner, A., Favre, S., Mack, M., Hausharter, A., Pillet, B., Hafner, J., Mitterer, V., Kressler, D., Pertschy, B. and Zierler, I. (2023) Dissecting the Nuclear Import of the Ribosomal Protein Rps2 (uS5). *Biomolecules*, **13**.
34. Pillet, B., Garcia-Gomez, J.J., Pausch, P., Falquet, L., Bange, G., de la Cruz, J. and Kressler, D. (2015) The Dedicated Chaperone Acl4 Escorts Ribosomal Protein Rpl4 to Its Nuclear Pre-60S Assembly Site. *PLoS Genet*, **11**, e1005565.
35. Pena, C., Schutz, S., Fischer, U., Chang, Y. and Panse, V.G. (2016) Prefabrication of a ribosomal protein subcomplex essential for eukaryotic ribosome formation. *Elife*, **5**.
36. Finley, D., Bartel, B. and Varshavsky, A. (1989) The tails of ubiquitin precursors are ribosomal proteins whose fusion to ubiquitin facilitates ribosome biogenesis. *Nature*, **338**, 394-401.
37. Lacombe, T., Garcia-Gomez, J.J., de la Cruz, J., Roser, D., Hurt, E., Linder, P. and Kressler, D. (2009) Linear ubiquitin fusion to Rps31 and its subsequent cleavage are required for the efficient production and functional integrity of 40S ribosomal subunits. *Mol Microbiol*, **72**, 69-84.
38. Martin-Villanueva, S., Fernandez-Pevida, A., Kressler, D. and de la Cruz, J. (2019) The Ubiquitin Moiety of Ubi1 Is Required for Productive Expression of Ribosomal Protein eL40 in Saccharomyces cerevisiae. *Cells*, **8**.
39. Martin-Villanueva, S., Fernandez-Pevida, A., Fernandez-Fernandez, J., Kressler, D. and de la Cruz, J. (2020) Ubiquitin release from eL40 is required for cytoplasmic maturation and function of 60S ribosomal subunits in Saccharomyces cerevisiae. *FEBS J*, **287**, 345-360.
40. Martin-Villanueva, S., Gutierrez, G., Kressler, D. and de la Cruz, J. (2021) Ubiquitin and Ubiquitin-Like Proteins and Domains in Ribosome Production and Function: Chance or Necessity? *Int J Mol Sci*, **22**.
41. Pausch, P., Singh, U., Ahmed, Y.L., Pillet, B., Murat, G., Altegoer, F., Stier, G., Thoms, M., Hurt, E., Sinning, I. *et al.* (2015) Co-translational capturing of nascent ribosomal proteins by their dedicated chaperones. *Nat Commun*, **6**, 7494.

42. Pillet, B., Mitterer, V., Kressler, D. and Pertschy, B. (2017) Hold on to your friends: Dedicated chaperones of ribosomal proteins: Dedicated chaperones mediate the safe transfer of ribosomal proteins to their site of pre-ribosome incorporation. *Bioessays*, **39**, 1-12.
43. Ting, Y.H., Lu, T.J., Johnson, A.W., Shie, J.T., Chen, B.R., Kumar, S.S. and Lo, K.Y. (2017) Bcp1 Is the Nuclear Chaperone of Rpl23 in Saccharomyces cerevisiae. *J Biol Chem*, **292**, 585-596.
44. Rössler, I., Embacher, J., Pillet, B., Murat, G., Liesinger, L., Hafner, J., Unterluggauer, J.J., Birner-Gruenberger, R., Kressler, D. and Pertschy, B. (2019) Tsr4 and Nap1, two novel members of the ribosomal protein chaperOME. *Nucleic Acids Res*, **47**, 6984-7002.
45. Black, J.J., Musalgaonkar, S. and Johnson, A.W. (2019) Tsr4 Is a Cytoplasmic Chaperone for the Ribosomal Protein Rps2 in Saccharomyces cerevisiae. *Mol Cell Biol*, **39**.
46. Kressler, D., Bange, G., Ogawa, Y., Stjepanovic, G., Bradatsch, B., Pratte, D., Amlacher, S., Strauss, D., Yoneda, Y., Katahira, J. *et al.* (2012) Synchronizing nuclear import of ribosomal proteins with ribosome assembly. *Science*, **338**, 666-671.
47. Calvino, F.R., Kharde, S., Ori, A., Hendricks, A., Wild, K., Kressler, D., Bange, G., Hurt, E., Beck, M. and Sinning, I. (2015) Symportin 1 chaperones 5S RNP assembly during ribosome biogenesis by occupying an essential rRNA-binding site. *Nat Commun*, **6**, 6510.
48. Castillo Duque de Estrada, N.M., Thoms, M., Flemming, D., Hammaren, H.M., Buschauer, R., Ameismeier, M., Bassler, J., Beck, M., Beckmann, R. and Hurt, E. (2023) Structure of nascent 5S RNPs at the crossroad between ribosome assembly and MDM2-p53 pathways. *Nat Struct Mol Biol*, **30**, 1119-1131.
49. Schütz, S., Fischer, U., Altvater, M., Nerurkar, P., Pena, C., Gerber, M., Chang, Y., Caesar, S., Schubert, O.T., Schlenstedt, G. *et al.* (2014) A RanGTP-independent mechanism allows ribosomal protein nuclear import for ribosome assembly. *Elife*, **3**, e03473.
50. Fewell, S.W. and Woolford, J.L., Jr. (1999) Ribosomal protein S14 of Saccharomyces cerevisiae regulates its expression by binding to RPS14B pre-mRNA and to 18S rRNA. *Mol Cell Biol*, **19**, 826-834.
51. Gudipati, R.K., Neil, H., Feuerbach, F., Malabat, C. and Jacquier, A. (2012) The yeast RPL9B gene is regulated by modulation between two modes of transcription termination. *EMBO J*, **31**, 2427-2437.
52. Johnson, T.L. and Vilardell, J. (2012) Regulated pre-mRNA splicing: the ghostwriter of the eukaryotic genome. *Biochim Biophys Acta*, **1819**, 538-545.
53. He, F., Li, C., Roy, B. and Jacobson, A. (2014) Yeast Edc3 targets RPS28B mRNA for decapping by binding to a 3' untranslated region decay-inducing regulatory element. *Mol Cell Biol*, **34**, 1438-1451.
54. Gabunilas, J. and Chanfreau, G. (2016) Splicing-Mediated Autoregulation Modulates Rpl22p Expression in Saccharomyces cerevisiae. *PLoS Genet*, **12**, e1005999.
55. Petibon, C., Parenteau, J., Catala, M. and Elela, S.A. (2016) Introns regulate the production of ribosomal proteins by modulating splicing of duplicated ribosomal protein genes. *Nucleic Acids Res*, **44**, 3878-3891.
56. Roy, B., Granas, D., Bragg, F., Jr., Cher, J.A.Y., White, M.A. and Stormo, G.D. (2020) Autoregulation of yeast ribosomal proteins discovered by efficient search for feedback regulation. *Commun Biol*, **3**, 761.
57. Thomas, B.J. and Rothstein, R. (1989) Elevated recombination rates in transcriptionally active DNA. *Cell*, **56**, 619-630.
58. Janke, C., Magiera, M.M., Rathfelder, N., Taxis, C., Reber, S., Maekawa, H., Moreno-Borchart, A., Doenges, G., Schwob, E., Schiebel, E. *et al.* (2004) A versatile toolbox for PCR-based tagging of yeast genes: new fluorescent proteins, more markers and promoter substitution cassettes. *Yeast*, **21**, 947-962.
59. Longtine, M.S., McKenzie, A., 3rd, Demarini, D.J., Shah, N.G., Wach, A., Brachat, A., Philippsen, P. and Pringle, J.R. (1998) Additional modules for versatile and economical PCR-based gene deletion and modification in Saccharomyces cerevisiae. *Yeast*, **14**, 953-961.
60. Kressler, D., Doere, M., Rojo, M. and Linder, P. (1999) Synthetic lethality with conditional dbp6 alleles identifies rsa1p, a nucleoplasmic protein involved in the assembly of 60S ribosomal subunits. *Mol Cell Biol*, **19**, 8633-8645.

61. Rappsilber, J., Mann, M. and Ishihama, Y. (2007) Protocol for micro-purification, enrichment, pre-fractionation and storage of peptides for proteomics using StageTips. *Nat Protoc*, **2**, 1896-1906.
62. Tyanova, S., Temu, T. and Cox, J. (2016) The MaxQuant computational platform for mass spectrometry-based shotgun proteomics. *Nat Protoc*, **11**, 2301-2319.
63. Tyanova, S., Temu, T., Sinitcyn, P., Carlson, A., Hein, M.Y., Geiger, T., Mann, M. and Cox, J. (2016) The Perseus computational platform for comprehensive analysis of (prote)omics data. *Nat Methods*, **13**, 731-740.
64. Kaeser-Pebernard, S., Vionnet, C., Mari, M., Sankar, D.S., Hu, Z., Roubaty, C., Martinez-Martinez, E., Zhao, H., Spuch-Calvar, M., Petri-Fink, A. *et al.* (2022) mTORC1 controls Golgi architecture and vesicle secretion by phosphorylation of SCYL1. *Nat Commun*, **13**, 4685.
65. Siva Sankar, D., Kaeser-Pebernard, S., Vionnet, C., Favre, S., de Oliveira Marchioro, L., Pillet, B., Zhou, J., Stumpe, M., Kovacs, W.J., Kressler, D. *et al.* (2024) The ULK1 effector BAG2 regulates autophagy initiation by modulating AMBRA1 localization. *Cell Rep*, **43**, 114689.
66. Wisniewski, J.R., Zougman, A., Nagaraj, N. and Mann, M. (2009) Universal sample preparation method for proteome analysis. *Nat Methods*, **6**, 359-362.
67. James, P., Halladay, J. and Craig, E.A. (1996) Genomic libraries and a host strain designed for highly efficient two-hybrid selection in yeast. *Genetics*, **144**, 1425-1436.
68. Shaner, N.C., Lambert, G.G., Chammas, A., Ni, Y., Cranfill, P.J., Baird, M.A., Sell, B.R., Allen, J.R., Day, R.N., Israelsson, M. *et al.* (2013) A bright monomeric green fluorescent protein derived from Branchiostoma lanceolatum. *Nat Methods*, **10**, 407-409.
69. Cormack, B.P., Bertram, G., Egerton, M., Gow, N.A.R., Falkow, S. and Brown, A.J.P. (1997) Yeast-enhanced green fluorescent protein (yEGFP): a reporter of gene expression in Candida albicans. *Microbiology (Reading)*, **143 (Pt 2)**, 303-311.
70. Kressler, D., de la Cruz, J., Rojo, M. and Linder, P. (1997) Fal1p is an essential DEAD-box protein involved in 40S-ribosomal-subunit biogenesis in Saccharomyces cerevisiae. *Mol Cell Biol*, **17**, 7283-7294.
71. Yaffe, M.P. and Schatz, G. (1984) Two nuclear mutations that block mitochondrial protein import in yeast. *Proc Natl Acad Sci U S A*, **81**, 4819-4823.
72. Petitjean, A., Bonneaud, N. and Lacroute, F. (1995) The duplicated Saccharomyces cerevisiae gene SSM1 encodes a eucaryotic homolog of the eubacterial and archaebacterial L1 ribosomal proteins. *Mol Cell Biol*, **15**, 5071-5081.
73. Frey, S., Pool, M. and Seedorf, M. (2001) Scp160p, an RNA-binding, polysome-associated protein, localizes to the endoplasmic reticulum of Saccharomyces cerevisiae in a microtubule-dependent manner. *J Biol Chem*, **276**, 15905-15912.
74. Schneider, C.A., Rasband, W.S. and Eliceiri, K.W. (2012) NIH Image to ImageJ: 25 years of image analysis. *Nat Methods*, **9**, 671-675.
75. Kabsch, W. (2010) Xds. *Acta Crystallogr D Biol Crystallogr*, **66**, 125-132.
76. McCoy, A.J., Grosse-Kunstleve, R.W., Adams, P.D., Winn, M.D., Storoni, L.C. and Read, R.J. (2007) Phaser crystallographic software. *J Appl Crystallogr*, **40**, 658-674.
77. Emsley, P. and Cowtan, K. (2004) Coot: model-building tools for molecular graphics. *Acta Crystallogr D Biol Crystallogr*, **60**, 2126-2132.
78. Adams, P.D., Afonine, P.V., Bunkoczi, G., Chen, V.B., Davis, I.W., Echols, N., Headd, J.J., Hung, L.W., Kapral, G.J., Grosse-Kunstleve, R.W. *et al.* (2010) PHENIX: a comprehensive Python-based system for macromolecular structure solution. *Acta Crystallogr D Biol Crystallogr*, **66**, 213-221.
79. Seeger, M.A., Zbinden, R., Flutsch, A., Gutte, P.G., Engeler, S., Roschitzki-Voser, H. and Grutter, M.G. (2013) Design, construction, and characterization of a second-generation DARP in library with reduced hydrophobicity. *Protein Sci*, **22**, 1239-1257.
80. Jumper, J., Evans, R., Pritzel, A., Green, T., Figurnov, M., Ronneberger, O., Tunyasuvunakool, K., Bates, R., Zidek, A., Potapenko, A. *et al.* (2021) Highly accurate protein structure prediction with AlphaFold. *Nature*, **596**, 583-589.
81. Varadi, M., Anyango, S., Deshpande, M., Nair, S., Natassia, C., Yordanova, G., Yuan, D., Stroe, O., Wood, G., Laydon, A. *et al.* (2022) AlphaFold Protein Structure Database: massively

expanding the structural coverage of protein-sequence space with high-accuracy models. *Nucleic Acids Res*, **50**, D439-D444.
82. Varadi, M., Bertoni, D., Magana, P., Paramval, U., Pidruchna, I., Radhakrishnan, M., Tsenkov, M., Nair, S., Mirdita, M., Yeo, J. *et al.* (2024) AlphaFold Protein Structure Database in 2024: providing structure coverage for over 214 million protein sequences. *Nucleic Acids Res*, **52**, D368-D375.
83. Abramson, J., Adler, J., Dunger, J., Evans, R., Green, T., Pritzel, A., Ronneberger, O., Willmore, L., Ballard, A.J., Bambrick, J. *et al.* (2024) Accurate structure prediction of biomolecular interactions with AlphaFold 3. *Nature*, **630**, 493-500.
84. Pettersen, E.F., Goddard, T.D., Huang, C.C., Meng, E.C., Couch, G.S., Croll, T.I., Morris, J.H. and Ferrin, T.E. (2021) UCSF ChimeraX: Structure visualization for researchers, educators, and developers. *Protein Sci*, **30**, 70-82.
85. Meng, E.C., Goddard, T.D., Pettersen, E.F., Couch, G.S., Pearson, Z.J., Morris, J.H. and Ferrin, T.E. (2023) UCSF ChimeraX: Tools for structure building and analysis. *Protein Sci*, **32**, e4792.
86. UniProt, C. (2023) UniProt: the Universal Protein Knowledgebase in 2023. *Nucleic Acids Res*, **51**, D523-D531.
87. Notredame, C., Higgins, D.G. and Heringa, J. (2000) T-Coffee: A novel method for fast and accurate multiple sequence alignment. *J Mol Biol*, **302**, 205-217.
88. Stelter, P., Huber, F.M., Kunze, R., Flemming, D., Hoelz, A. and Hurt, E. (2015) Coordinated Ribosomal L4 Protein Assembly into the Pre-Ribosome Is Regulated by Its Eukaryote-Specific Extension. *Mol Cell*, **58**, 854-862.
89. Branon, T.C., Bosch, J.A., Sanchez, A.D., Udeshi, N.D., Svinkina, T., Carr, S.A., Feldman, J.L., Perrimon, N. and Ting, A.Y. (2018) Efficient proximity labeling in living cells and organisms with TurboID. *Nat Biotechnol*, **36**, 880-887.
90. Kwon, K. and Beckett, D. (2000) Function of a conserved sequence motif in biotin holoenzyme synthetases. *Protein Sci*, **9**, 1530-1539.
91. Roux, K.J., Kim, D.I., Raida, M. and Burke, B. (2012) A promiscuous biotin ligase fusion protein identifies proximal and interacting proteins in mammalian cells. *J Cell Biol*, **196**, 801-810.
92. Samavarchi-Tehrani, P., Samson, R. and Gingras, A.C. (2020) Proximity Dependent Biotinylation: Key Enzymes and Adaptation to Proteomics Approaches. *Mol Cell Proteomics*, **19**, 757-773.
93. Kim, D.I., Birendra, K.C., Zhu, W., Motamedchaboki, K., Doye, V. and Roux, K.J. (2014) Probing nuclear pore complex architecture with proximity-dependent biotinylation. *Proc Natl Acad Sci U S A*, **111**, E2453-2461.
94. Larochelle, M., Bergeron, D., Arcand, B. and Bachand, F. (2019) Proximity-dependent biotinylation mediated by TurboID to identify protein-protein interaction networks in yeast. *J Cell Sci*, **132**.
95. Bhutada, P., Favre, S., Jaafar, M., Hafner, J., Liesinger, L., Unterweger, S., Bischof, K., Darnhofer, B., Siva Sankar, D., Rechberger, G. *et al.* (2022) Rbp95 binds to 25S rRNA helix H95 and cooperates with the Npa1 complex during early pre-60S particle maturation. *Nucleic Acids Res*, **50**, 10053-10077.
96. Fenech, E.J., Cohen, N., Kupervaser, M., Gazi, Z. and Schuldiner, M. (2023) A toolbox for systematic discovery of stable and transient protein interactors in baker's yeast. *Mol Syst Biol*, **19**, e11084.
97. Steffen, K.K., McCormick, M.A., Pham, K.M., MacKay, V.L., Delaney, J.R., Murakami, C.J., Kaeberlein, M. and Kennedy, B.K. (2012) Ribosome deficiency protects against ER stress in Saccharomyces cerevisiae. *Genetics*, **191**, 107-118.
98. Ho, B., Baryshnikova, A. and Brown, G.W. (2018) Unification of Protein Abundance Datasets Yields a Quantitative Saccharomyces cerevisiae Proteome. *Cell Syst*, **6**, 192-205 e193.
99. Holzer, S., Ban, N. and Klinge, S. (2013) Crystal structure of the yeast ribosomal protein rpS3 in complex with its chaperone Yar1. *J Mol Biol*, **425**, 4154-4160.
100. Fernandez-Pevida, A., Rodriguez-Galan, O., Diaz-Quintana, A., Kressler, D. and de la Cruz, J. (2012) Yeast ribosomal protein L40 assembles late into precursor 60 S ribosomes and is required for their cytoplasmic maturation. *J Biol Chem*, **287**, 38390-38407.

101. Kargas, V., Castro-Hartmann, P., Escudero-Urquijo, N., Dent, K., Hilcenko, C., Sailer, C., Zisser, G., Marques-Carvalho, M.J., Pellegrino, S., Wawiorka, L. *et al.* (2019) Mechanism of completion of peptidyltransferase centre assembly in eukaryotes. *Elife*, **8**.
102. Sanghai, Z.A., Miller, L., Molloy, K.R., Barandun, J., Hunziker, M., Chaker-Margot, M., Wang, J., Chait, B.T. and Klinge, S. (2018) Modular assembly of the nucleolar pre-60S ribosomal subunit. *Nature*, **556**, 126-129.
103. Cruz, V.E., Sekulski, K., Peddada, N., Sailer, C., Balasubramanian, S., Weirich, C.S., Stengel, F. and Erzberger, J.P. (2022) Sequence-specific remodeling of a topologically complex RNP substrate by Spb4. *Nat Struct Mol Biol*, **29**, 1228-1238.
104. Kater, L., Thoms, M., Barrio-Garcia, C., Cheng, J., Ismail, S., Ahmed, Y.L., Bange, G., Kressler, D., Berninghausen, O., Sinning, I. *et al.* (2017) Visualizing the Assembly Pathway of Nucleolar Pre-60S Ribosomes. *Cell*, **171**, 1599-1610 e1514.
105. Mitterer, V., Thoms, M., Buschauer, R., Berninghausen, O., Hurt, E. and Beckmann, R. (2023) Concurrent remodelling of nucleolar 60S subunit precursors by the Rea1 ATPase and Spb4 RNA helicase. *Elife*, **12**.
106. Pertschy, B., Saveanu, C., Zisser, G., Lebreton, A., Tengg, M., Jacquier, A., Liebminger, E., Nobis, B., Kappel, L., van der Klei, I. *et al.* (2007) Cytoplasmic recycling of 60S preribosomal factors depends on the AAA protein Drg1. *Mol Cell Biol*, **27**, 6581-6592.
107. Kappel, L., Loibl, M., Zisser, G., Klein, I., Fruhmann, G., Gruber, C., Unterweger, S., Rechberger, G., Pertschy, B. and Bergler, H. (2012) Rlp24 activates the AAA-ATPase Drg1 to initiate cytoplasmic pre-60S maturation. *J Cell Biol*, **199**, 771-782.
108. Prattes, M., Grishkovskaya, I., Hodirnau, V.V., Hetzmannseder, C., Zisser, G., Sailer, C., Kargas, V., Loibl, M., Gerhalter, M., Kofler, L. *et al.* (2022) Visualizing maturation factor extraction from the nascent ribosome by the AAA-ATPase Drg1. *Nat Struct Mol Biol*, **29**, 942-953.
109. Kressler, D., Roser, D., Pertschy, B. and Hurt, E. (2008) The AAA ATPase Rix7 powers progression of ribosome biogenesis by stripping Nsa1 from pre-60S particles. *J Cell Biol*, **181**, 935-944.
110. Ismail, S., Flemming, D., Thoms, M., Gomes-Filho, J.V., Randau, L., Beckmann, R. and Hurt, E. (2022) Emergence of the primordial pre-60S from the 90S pre-ribosome. *Cell Rep*, **39**, 110640.
111. de la Cruz, J., Lacombe, T., Deloche, O., Linder, P. and Kressler, D. (2004) The putative RNA helicase Dbp6p functionally interacts with Rpl3p, Nop8p and the novel trans-acting Factor Rsa3p during biogenesis of 60S ribosomal subunits in Saccharomyces cerevisiae. *Genetics*, **166**, 1687-1699.
112. Sailer, C., Jansen, J., Sekulski, K., Cruz, V.E., Erzberger, J.P. and Stengel, F. (2022) A comprehensive landscape of 60S ribosome biogenesis factors. *Cell Rep*, **38**, 110353.
113. Kater, L., Mitterer, V., Thoms, M., Cheng, J., Berninghausen, O., Beckmann, R. and Hurt, E. (2020) Construction of the Central Protuberance and L1 Stalk during 60S Subunit Biogenesis. *Mol Cell*, **79**, 615-628 e615.
114. Ben-Shem, A., Garreau de Loubresse, N., Melnikov, S., Jenner, L., Yusupova, G. and Yusupov, M. (2011) The structure of the eukaryotic ribosome at 3.0 A resolution. *Science*, **334**, 1524-1529.
115. Sanghai, Z.A., Piwowarczyk, R., Broeck, A.V. and Klinge, S. (2023) A co-transcriptional ribosome assembly checkpoint controls nascent large ribosomal subunit maturation. *Nat Struct Mol Biol*, **30**, 594-599.
116. Zhou, Y., Musalgaonkar, S., Johnson, A.W. and Taylor, D.W. (2019) Tightly-orchestrated rearrangements govern catalytic center assembly of the ribosome. *Nat Commun*, **10**, 958.
117. Rosado, I.V., Dez, C., Lebaron, S., Caizergues-Ferrer, M., Henry, Y. and de la Cruz, J. (2007) Characterization of Saccharomyces cerevisiae Npa2p (Urb2p) reveals a low-molecular-mass complex containing Dbp6p, Npa1p (Urb1p), Nop8p, and Rsa3p involved in early steps of 60S ribosomal subunit biogenesis. *Mol Cell Biol*, **27**, 1207-1221.
118. Joret, C., Capeyrou, R., Belhabich-Baumas, K., Plisson-Chastang, C., Ghandour, R., Humbert, O., Fribourg, S., Leulliot, N., Lebaron, S., Henras, A.K. *et al.* (2018) The Npa1p complex

chaperones the assembly of the earliest eukaryotic large ribosomal subunit precursor. *PLoS Genet*, **14**, e1007597.
119. Dez, C., Froment, C., Noaillac-Depeyre, J., Monsarrat, B., Caizergues-Ferrer, M. and Henry, Y. (2004) Npa1p, a component of very early pre-60S ribosomal particles, associates with a subset of small nucleolar RNPs required for peptidyl transferase center modification. *Mol Cell Biol*, **24**, 6324-6337.
120. Rosado, I.V. and de la Cruz, J. (2004) Npa1p is an essential trans-acting factor required for an early step in the assembly of 60S ribosomal subunits in Saccharomyces cerevisiae. *RNA*, **10**, 1073-1083.
121. Zhang, J., Harnpicharnchai, P., Jakovljevic, J., Tang, L., Guo, Y., Oeffinger, M., Rout, M.P., Hiley, S.L., Hughes, T. and Woolford, J.L., Jr. (2007) Assembly factors Rpf2 and Rrs1 recruit 5S rRNA and ribosomal proteins rpL5 and rpL11 into nascent ribosomes. *Genes Dev*, **21**, 2580-2592.
122. Madru, C., Lebaron, S., Blaud, M., Delbos, L., Pipoli, J., Pasmant, E., Rety, S. and Leulliot, N. (2015) Chaperoning 5S RNA assembly. *Genes Dev*, **29**, 1432-1446.
123. Kharde, S., Calvino, F.R., Gumiero, A., Wild, K. and Sinning, I. (2015) The structure of Rpf2-Rrs1 explains its role in ribosome biogenesis. *Nucleic Acids Res*, **43**, 7083-7095.
124. Wu, S., Tutuncuoglu, B., Yan, K., Brown, H., Zhang, Y., Tan, D., Gamalinda, M., Yuan, Y., Li, Z., Jakovljevic, J. *et al.* (2016) Diverse roles of assembly factors revealed by structures of late nuclear pre-60S ribosomes. *Nature*, **534**, 133-137.
125. West, M., Hedges, J.B., Chen, A. and Johnson, A.W. (2005) Defining the order in which Nmd3p and Rpl10p load onto nascent 60S ribosomal subunits. *Mol Cell Biol*, **25**, 3802-3813.
126. Hedges, J., West, M. and Johnson, A.W. (2005) Release of the export adapter, Nmd3p, from the 60S ribosomal subunit requires Rpl10p and the cytoplasmic GTPase Lsg1p. *EMBO J*, **24**, 567-579.
127. Porras-Yakushi, T.R., Whitelegge, J.P., Miranda, T.B. and Clarke, S. (2005) A novel SET domain methyltransferase modifies ribosomal protein Rpl23ab in yeast. *J Biol Chem*, **280**, 34590-34598.
128. Porras-Yakushi, T.R., Whitelegge, J.P. and Clarke, S. (2007) Yeast ribosomal/cytochrome c SET domain methyltransferase subfamily: identification of Rpl23ab methylation sites and recognition motifs. *J Biol Chem*, **282**, 12368-12376.
129. Yeh, M.C., Hsu, N.H., Chu, H.Y., Yang, C.H., Hsu, P.H., Chou, C.C., Shie, J.T., Lee, W.M., Ho, M.C. and Lo, K.Y. (2024) Dual protection by Bcp1 and Rkm1 ensures incorporation of uL14 into pre-60S ribosomal subunits. *J Cell Biol*, **223**.
130. Kosugi, S., Hasebe, M., Tomita, M. and Yanagawa, H. (2009) Systematic identification of cell cycle-dependent yeast nucleocytoplasmic shuttling proteins by prediction of composite motifs. *Proc Natl Acad Sci U S A*, **106**, 10171-10176.
131. Stewart, M. (2007) Molecular mechanism of the nuclear protein import cycle. *Nat Rev Mol Cell Biol*, **8**, 195-208.
132. Homma, K., Terui, S., Minemura, M., Qadota, H., Anraku, Y., Kanaho, Y. and Ohya, Y. (1998) Phosphatidylinositol-4-phosphate 5-kinase localized on the plasma membrane is essential for yeast cell morphogenesis. *J Biol Chem*, **273**, 15779-15786.
133. Audhya, A. and Emr, S.D. (2003) Regulation of PI4,5P2 synthesis by nuclear-cytoplasmic shuttling of the Mss4 lipid kinase. *EMBO J*, **22**, 4223-4236.
134. Evans, R., O'Neill, M., Pritzel, A., Antropova, N., Senior, A., Green, T., Žídek, A., Bates, R., Blackwell, S., Yim, J. *et al.* (2021) Protein complex prediction with AlphaFold-Multimer. *bioRxiv*, 2021.2010.2004.463034.
135. Bischoff, F.R. and Ponstingl, H. (1991) Mitotic regulator protein RCC1 is complexed with a nuclear ras-related polypeptide. *Proc Natl Acad Sci U S A*, **88**, 10830-10834.
136. Kadowaki, T., Goldfarb, D., Spitz, L.M., Tartakoff, A.M. and Ohno, M. (1993) Regulation of RNA processing and transport by a nuclear guanine nucleotide release protein and members of the Ras superfamily. *EMBO J*, **12**, 2929-2937.
137. Belhumeur, P., Lee, A., Tam, R., DiPaolo, T., Fortin, N. and Clark, M.W. (1993) GSP1 and GSP2, genetic suppressors of the prp20-1 mutant in Saccharomyces cerevisiae: GTP-binding proteins involved in the maintenance of nuclear organization. *Mol Cell Biol*, **13**, 2152-2161.

138. Schlenstedt, G., Saavedra, C., Loeb, J.D., Cole, C.N. and Silver, P.A. (1995) The GTP-bound form of the yeast Ran/TC4 homologue blocks nuclear protein import and appearance of poly(A)+ RNA in the cytoplasm. *Proc Natl Acad Sci U S A*, **92**, 225-229.
139. Rexach, M. and Blobel, G. (1995) Protein import into nuclei: association and dissociation reactions involving transport substrate, transport factors, and nucleoporins. *Cell*, **83**, 683-692.
140. Görlich, D., Pante, N., Kutay, U., Aebi, U. and Bischoff, F.R. (1996) Identification of different roles for RanGDP and RanGTP in nuclear protein import. *EMBO J*, **15**, 5584-5594.
141. Chook, Y.M. and Blobel, G. (1999) Structure of the nuclear transport complex karyopherin-beta2-Ran x GppNHp. *Nature*, **399**, 230-237.
142. Lee, S.J., Matsuura, Y., Liu, S.M. and Stewart, M. (2005) Structural basis for nuclear import complex dissociation by RanGTP. *Nature*, **435**, 693-696.
143. Kobayashi, J. and Matsuura, Y. (2013) Structural basis for cell-cycle-dependent nuclear import mediated by the karyopherin Kap121p. *J Mol Biol*, **425**, 1852-1868.
144. Albertini, M., Pemberton, L.F., Rosenblum, J.S. and Blobel, G. (1998) A novel nuclear import pathway for the transcription factor TFIIS. *J Cell Biol*, **143**, 1447-1455.
145. Pemberton, L.F., Rosenblum, J.S. and Blobel, G. (1999) Nuclear import of the TATA-binding protein: mediation by the karyopherin Kap114p and a possible mechanism for intranuclear targeting. *J Cell Biol*, **145**, 1407-1417.
146. Polizotto, R.S. and Cyert, M.S. (2001) Calcineurin-dependent nuclear import of the transcription factor Crz1p requires Nmd5p. *J Cell Biol*, **154**, 951-960.
147. Hodges, J.L., Leslie, J.H., Mosammaparast, N., Guo, Y., Shabanowitz, J., Hunt, D.F. and Pemberton, L.F. (2005) Nuclear import of TFIIB is mediated by Kap114p, a karyopherin with multiple cargo-binding domains. *Mol Biol Cell*, **16**, 3200-3210.
148. Caesar, S., Greiner, M. and Schlenstedt, G. (2006) Kap120 functions as a nuclear import receptor for ribosome assembly factor Rpf1 in yeast. *Mol Cell Biol*, **26**, 3170-3180.
149. Jiou, J., Shaffer, J.M., Bernades, N.E., Fung, H.Y.J., Kikumoto Dias, J., D'Arcy, S. and Chook, Y.M. (2023) Mechanism of RanGTP priming H2A-H2B release from Kap114 in an atypical RanGTP*Kap114*H2A-H2B complex. *Proc Natl Acad Sci U S A*, **120**, e2301199120.
150. Fung, H.Y.J., Jiou, J., Niesman, A.B., Bernardes, N.E. and Chook, Y.M. (2025) Nap1 and Kap114 co-chaperone H2A-H2B and facilitate targeted histone release in the nucleus. *J Cell Biol*, **224**.
151. Wing, C.E., Fung, H.Y.J. and Chook, Y.M. (2022) Karyopherin-mediated nucleocytoplasmic transport. *Nat Rev Mol Cell Biol*, **23**, 307-328.
152. Hahn, S. and Schlenstedt, G. (2011) Importin beta-type nuclear transport receptors have distinct binding affinities for Ran-GTP. *Biochem Biophys Res Commun*, **406**, 383-388.
153. Aksu, M., Trakhanov, S., Vera Rodriguez, A. and Gorlich, D. (2019) Structural basis for the nuclear import and export functions of the biportin Pdr6/Kap122. *J Cell Biol*, **218**, 1839-1852.
154. Cingolani, G., Petosa, C., Weis, K. and Muller, C.W. (1999) Structure of importin-beta bound to the IBB domain of importin-alpha. *Nature*, **399**, 221-229.
155. Lee, B.J., Cansizoglu, A.E., Suel, K.E., Louis, T.H., Zhang, Z. and Chook, Y.M. (2006) Rules for nuclear localization sequence recognition by karyopherin beta 2. *Cell*, **126**, 543-558.
156. Maertens, G.N., Cook, N.J., Wang, W., Hare, S., Gupta, S.S., Oztop, I., Lee, K., Pye, V.E., Cosnefroy, O., Snijders, A.P. *et al.* (2014) Structural basis for nuclear import of splicing factors by human Transportin 3. *Proc Natl Acad Sci U S A*, **111**, 2728-2733.
157. An, S., Yoon, J., Kim, H., Song, J.J. and Cho, U.S. (2017) Structure-based nuclear import mechanism of histones H3 and H4 mediated by Kap123. *Elife*, **6**.
158. Bernardes, N.E., Fung, H.Y.J., Li, Y., Chen, Z. and Chook, Y.M. (2022) Structure of IMPORTIN-4 bound to the H3-H4-ASF1 histone-histone chaperone complex. *Proc Natl Acad Sci U S A*, **119**, e2207177119.
159. Liao, C.C., Wang, Y.S., Pi, W.C., Wang, C.H., Wu, Y.M., Chen, W.Y. and Hsia, K.C. (2023) Structural convergence endows nuclear transport receptor Kap114p with a transcriptional repressor function toward TATA-binding protein. *Nat Commun*, **14**, 5518.
160. Bischoff, F.R., Klebe, C., Kretschmer, J., Wittinghofer, A. and Ponstingl, H. (1994) RanGAP1 induces GTPase activity of nuclear Ras-related Ran. *Proc Natl Acad Sci U S A*, **91**, 2587-2591.

161. Maurer, P., Redd, M., Solsbacher, J., Bischoff, F.R., Greiner, M., Podtelejnikov, A.V., Mann, M., Stade, K., Weis, K. and Schlenstedt, G. (2001) The nuclear export receptor Xpo1p forms distinct complexes with NES transport substrates and the yeast Ran binding protein 1 (Yrb1p). *Mol Biol Cell*, **12**, 539-549.
162. Vera Rodriguez, A., Frey, S. and Gorlich, D. (2019) Engineered SUMO/protease system identifies Pdr6 as a bidirectional nuclear transport receptor. *J Cell Biol*, **218**, 2006-2020.
163. Chook, Y.M. and Süel, K.E. (2011) Nuclear import by karyopherin-betas: recognition and inhibition. *Biochim Biophys Acta*, **1813**, 1593-1606.
164. Kobayashi, J., Hirano, H. and Matsuura, Y. (2015) Crystal structure of the karyopherin Kap121p bound to the extreme C-terminus of the protein phosphatase Cdc14p. *Biochem Biophys Res Commun*, **463**, 309-314.
165. Sekulski, K., Cruz, V.E., Weirich, C.S. and Erzberger, J.P. (2023) rRNA methylation by Spb1 regulates the GTPase activity of Nog2 during 60S ribosomal subunit assembly. *Nat Commun*, **14**, 1207.
166. Yelland, J.N., Bravo, J.P.K., Black, J.J., Taylor, D.W. and Johnson, A.W. (2023) A single 2'-O-methylation of ribosomal RNA gates assembly of a functional ribosome. *Nat Struct Mol Biol*, **30**, 91-98.
167. Ben-Shem, A., Jenner, L., Yusupova, G. and Yusupov, M. (2010) Crystal structure of the eukaryotic ribosome. *Science*, **330**, 1203-1209.
168. Li, Z., Chen, S., Zhao, L., Huang, G., Xu, H., Yang, X., Wang, P., Gao, N. and Sui, S.F. (2023) Nuclear export of pre-60S particles through the nuclear pore complex. *Nature*, **618**, 411-418.
169. Li, J., Mahajan, A. and Tsai, M.D. (2006) Ankyrin repeat: a unique motif mediating protein-protein interactions. *Biochemistry*, **45**, 15168-15178.
170. Koch, B., Mitterer, V., Niederhauser, J., Stanborough, T., Murat, G., Rechberger, G., Bergler, H., Kressler, D. and Pertschy, B. (2012) Yar1 protects the ribosomal protein Rps3 from aggregation. *J Biol Chem*, **287**, 21806-21815.
171. Hibbs, M.A., Hess, D.C., Myers, C.L., Huttenhower, C., Li, K. and Troyanskaya, O.G. (2007) Exploring the functional landscape of gene expression: directed search of large microarray compendia. *Bioinformatics*, **23**, 2692-2699.
172. Engel, S.R., Aleksander, S., Nash, R.S., Wong, E.D., Weng, S., Miyasato, S.R., Sherlock, G. and Cherry, J.M. (2025) Saccharomyces Genome Database: advances in genome annotation, expanded biochemical pathways, and other key enhancements. *Genetics*, **229**.
173. Jorgensen, P., Rupes, I., Sharom, J.R., Schneper, L., Broach, J.R. and Tyers, M. (2004) A dynamic transcriptional network communicates growth potential to ribosome synthesis and critical cell size. *Genes Dev*, **18**, 2491-2505.
174. Wade, C.H., Umbarger, M.A. and McAlear, M.A. (2006) The budding yeast rRNA and ribosome biosynthesis (RRB) regulon contains over 200 genes. *Yeast*, **23**, 293-306.
175. Musalgaonkar, S., Black, J.J. and Johnson, A.W. (2019) The L1 stalk is required for efficient export of nascent large ribosomal subunits in yeast. *RNA*, **25**, 1549-1560.
176. Huh, W.K., Falvo, J.V., Gerke, L.C., Carroll, A.S., Howson, R.W., Weissman, J.S. and O'Shea, E.K. (2003) Global analysis of protein localization in budding yeast. *Nature*, **425**, 686-691.
177. Giaever, G., Chu, A.M., Ni, L., Connelly, C., Riles, L., Veronneau, S., Dow, S., Lucau-Danila, A., Anderson, K., Andre, B. *et al.* (2002) Functional profiling of the Saccharomyces cerevisiae genome. *Nature*, **418**, 387-391.
178. Costanzo, M., VanderSluis, B., Koch, E.N., Baryshnikova, A., Pons, C., Tan, G., Wang, W., Usaj, M., Hanchard, J., Lee, S.D. *et al.* (2016) A global genetic interaction network maps a wiring diagram of cellular function. *Science*, **353**.
179. Stirnimann, C.U., Petsalaki, E., Russell, R.B. and Muller, C.W. (2010) WD40 proteins propel cellular networks. *Trends Biochem Sci*, **35**, 565-574.
180. Kuznetsov, D., Tegenfeldt, F., Manni, M., Seppey, M., Berkeley, M., Kriventseva, E.V. and Zdobnov, E.M. (2023) OrthoDB v11: annotation of orthologs in the widest sampling of organismal diversity. *Nucleic Acids Res*, **51**, D445-D451.
181. McIntosh, K.B., Bhattacharya, A., Willis, I.M. and Warner, J.R. (2011) Eukaryotic cells producing ribosomes deficient in Rpl1 are hypersensitive to defects in the ubiquitin-proteasome system. *PLoS One*, **6**, e23579.

182. Rotenberg, M.O., Moritz, M. and Woolford, J.L., Jr. (1988) Depletion of Saccharomyces cerevisiae ribosomal protein L16 causes a decrease in 60S ribosomal subunits and formation of half-mer polyribosomes. *Genes Dev*, **2**, 160-172.
183. Liang, X., Zuo, M.Q., Zhang, Y., Li, N., Ma, C., Dong, M.Q. and Gao, N. (2020) Structural snapshots of human pre-60S ribosomal particles before and after nuclear export. *Nat Commun*, **11**, 3542.
184. Jones, D.T. (1999) Protein secondary structure prediction based on position-specific scoring matrices. *J Mol Biol*, **292**, 195-202.
185. Tesina, P., Ebine, S., Buschauer, R., Thoms, M., Matsuo, Y., Inada, T. and Beckmann, R. (2023) Molecular basis of eIF5A-dependent CAT tailing in eukaryotic ribosome-associated quality control. *Mol Cell*, **83**, 607-621 e604.
186. Wyler, E., Wandrey, F., Badertscher, L., Montellese, C., Alper, D. and Kutay, U. (2014) The beta-isoform of the BRCA2 and CDKN1A(p21)-interacting protein (BCCIP) stabilizes nuclear RPL23/uL14. *FEBS Lett*, **588**, 3685-3691.
187. Lafontaine, D.L.J., Riback, J.A., Bascetin, R. and Brangwynne, C.P. (2021) The nucleolus as a multiphase liquid condensate. *Nat Rev Mol Cell Biol*, **22**, 165-182.
188. King, M.R., Ruff, K.M. and Pappu, R.V. (2024) Emergent microenvironments of nucleoli. *Nucleus*, **15**, 2319957.
189. Sekiguchi, T., Todaka, Y., Wang, Y., Hirose, E., Nakashima, N. and Nishimoto, T. (2004) A novel human nucleolar protein, Nop132, binds to the G proteins, RRAG A/C/D. *J Biol Chem*, **279**, 8343-8350.
190. Sekiguchi, T., Hayano, T., Yanagida, M., Takahashi, N. and Nishimoto, T. (2006) NOP132 is required for proper nucleolus localization of DEAD-box RNA helicase DDX47. *Nucleic Acids Res*, **34**, 4593-4608.
191. Chamousset, D., De Wever, V., Moorhead, G.B., Chen, Y., Boisvert, F.M., Lamond, A.I. and Trinkle-Mulcahy, L. (2010) RRP1B targets PP1 to mammalian cell nucleoli and is associated with Pre-60S ribosomal subunits. *Mol Biol Cell*, **21**, 4212-4226.
192. Dörner, K., Ruggeri, C., Zemp, I. and Kutay, U. (2023) Ribosome biogenesis factors-from names to functions. *EMBO J*, **42**, e112699.
193. Vanden Broeck, A. and Klinge, S. (2024) Eukaryotic Ribosome Assembly. *Annu Rev Biochem*, **93**, 189-210.
194. Vanden Broeck, A. and Klinge, S. (2023) Principles of human pre-60S biogenesis. *Science*, **381**, eadh3892.
195. Natchiar, S.K., Myasnikov, A.G., Kratzat, H., Hazemann, I. and Klaholz, B.P. (2017) Visualization of chemical modifications in the human 80S ribosome structure. *Nature*, **551**, 472-477.
196. Shetty, S., Hofstetter, J., Battaglioni, S., Ritz, D. and Hall, M.N. (2023) TORC1 phosphorylates and inhibits the ribosome preservation factor Stm1 to activate dormant ribosomes. *EMBO J*, **42**, e112344.
197. Huttlin, E.L., Bruckner, R.J., Navarrete-Perea, J., Cannon, J.R., Baltier, K., Gebreab, F., Gygi, M.P., Thornock, A., Zarraga, G., Tam, S. *et al.* (2021) Dual proteome-scale networks reveal cell-specific remodeling of the human interactome. *Cell*, **184**, 3022-3040 e3028.
198. Pöll, G., Braun, T., Jakovljevic, J., Neueder, A., Jakob, S., Woolford, J.L., Jr., Tschochner, H. and Milkereit, P. (2009) rRNA maturation in yeast cells depleted of large ribosomal subunit proteins. *PLoS One*, **4**, e8249.
199. Jäkel, S., Albig, W., Kutay, U., Bischoff, F.R., Schwamborn, K., Doenecke, D. and Gorlich, D. (1999) The importin beta/importin 7 heterodimer is a functional nuclear import receptor for histone H1. *EMBO J*, **18**, 2411-2423.
200. Bernardes, N.E. and Chook, Y.M. (2020) Nuclear import of histones. *Biochem Soc Trans*, **48**, 2753-2767.
201. Schmidt, H.B. and Gorlich, D. (2016) Transport Selectivity of Nuclear Pores, Phase Separation, and Membraneless Organelles. *Trends Biochem Sci*, **41**, 46-61.
202. Timney, B.L., Raveh, B., Mironska, R., Trivedi, J.M., Kim, S.J., Russel, D., Wente, S.R., Sali, A. and Rout, M.P. (2016) Simple rules for passive diffusion through the nuclear pore complex. *J Cell Biol*, **215**, 57-76.

203. Nakai, K. and Horton, P. (1999) PSORT: a program for detecting sorting signals in proteins and predicting their subcellular localization. *Trends Biochem Sci*, **24**, 34-36.
204. Lange, A., Mills, R.E., Lange, C.J., Stewart, M., Devine, S.E. and Corbett, A.H. (2007) Classical nuclear localization signals: definition, function, and interaction with importin alpha. *J Biol Chem*, **282**, 5101-5105.
205. Lee, D.C. and Aitchison, J.D. (1999) Kap104p-mediated nuclear import. Nuclear localization signals in mRNA-binding proteins and the role of Ran and Rna. *J Biol Chem*, **274**, 29031-29037.
206. Lange, A., Mills, R.E., Devine, S.E. and Corbett, A.H. (2008) A PY-NLS nuclear targeting signal is required for nuclear localization and function of the Saccharomyces cerevisiae mRNA-binding protein Hrp1. *J Biol Chem*, **283**, 12926-12934.
207. Süel, K.E., Gu, H. and Chook, Y.M. (2008) Modular organization and combinatorial energetics of proline-tyrosine nuclear localization signals. *PLoS Biol*, **6**, e137.
208. Cansizoglu, A.E., Lee, B.J., Zhang, Z.C., Fontoura, B.M. and Chook, Y.M. (2007) Structure-based design of a pathway-specific nuclear import inhibitor. *Nat Struct Mol Biol*, **14**, 452-454.
209. Imasaki, T., Shimizu, T., Hashimoto, H., Hidaka, Y., Kose, S., Imamoto, N., Yamada, M. and Sato, M. (2007) Structural basis for substrate recognition and dissociation by human transportin 1. *Mol Cell*, **28**, 57-67.
210. Aitchison, J.D., Blobel, G. and Rout, M.P. (1996) Kap104p: a karyopherin involved in the nuclear transport of messenger RNA binding proteins. *Science*, **274**, 624-627.
211. Süel, K.E. and Chook, Y.M. (2009) Kap104p imports the PY-NLS-containing transcription factor Tfg2p into the nucleus. *J Biol Chem*, **284**, 15416-15424.
212. Ho, Y., Gruhler, A., Heilbut, A., Bader, G.D., Moore, L., Adams, S.L., Millar, A., Taylor, P., Bennett, K., Boutilier, K. *et al.* (2002) Systematic identification of protein complexes in Saccharomyces cerevisiae by mass spectrometry. *Nature*, **415**, 180-183.

FIGURE LEGENDS

Figure 1. **Establishing the proxiOME of LSU r-proteins by TurboID-based proximity labelling.** **(A)** Schematic overview of our TurboID-based proximity labelling approach. Wild-type yeast cells (*S. cerevisiae*) are transformed with a centromeric plasmid (*LEU2* marker) containing an r-protein gene (*RPG*, coloured in orange) fused in frame to the DNA sequence encoding the TurboID protein biotin ligase (TurboID, green), which is expressed under the transcriptional control of the copper-inducible *CUP1* promoter (P*CUP1*, red). The C-terminal TurboID tag is separated from the r-protein by inclusion of a (Gly-Ala)5 linker (black) and additionally contains a 2xHA tag (blue) at its C-terminal end. For transcription termination, the coding sequence is followed by the *ADH1* terminator (T*ADH1*, dark blue). Expression of the TurboID-tagged r-protein and biotinylation are induced for 1 h by the simultaneous addition of copper and biotin to exponentially growing cultures. TurboID catalyses the conversion of biotin into a reactive biotinoyl-5'-AMP (bioAMP) intermediate, which can covalently modify surface-exposed lysine (K) residues of the TurboID moiety and the bait r-protein as well as of proximal proteins, such as direct (red) and indirect (blue) interaction partners of the TurboID-tagged bait r-protein (orange). Biotinylated proteins are purified from total cell extracts by affinity purification with streptavidin-coupled beads. Purified proteins are then identified and quantified by bottom-up label-free mass spectrometry. **(B)** TurboID results obtained with C-terminally TurboID-tagged Rpl3 (Rpl3-TurboID). The abundance of each detected protein is displayed as its normalized intensity-based absolute quantification (iBAQ) value on the vertical axis, and its relative enrichment (fold change) on the horizontal axis as the log2 fold change of its normalized iBAQ abundance between the bait sample and the average of the GFP-TurboID and NLS-GFP-TurboID controls, from which missing values were imputed according to the normal distribution of the intensities within a sample. The bait r-protein, its known DC, and selected enriched proteins are written in bold. **(C)** Representation of the variation of the enrichment of the Rpl3 bait, its DC Rrb1, proximal AFs, and abundantly detected r-proteins between the experimental replicates (n=8); r-proteins that are close to or far away from Rpl3, as indicated by available structures of pre-60S particles, mature 60S subunits, and 80S ribosomes, are referred to as proximal or non-proximal RPs. The variation of the enrichment is represented by boxes highlighting the upper and lower quartiles of each data set, while the whiskers indicate the minimal and maximal limits of the distribution; outliers are shown as dots, the average by a line, and the median by a cross. **(D-G)** Location of Rpl3 and its neighbouring proteins on different pre-60S intermediates: **(D)** early nucleolar pre-60S (state 2) (PDB: 6C0F (102)), **(E)** late nucleolar pre-60S (state E1) (PDB: 7R7A (103)), **(F)** nucleoplasmic pre-60S (Rix1-Rea1) (PDB: 6YLH (113)), **(G)** cytoplasmic pre-60S (Lsg1-TAP, state I) (PDB: 6RZZ (101)). The indicated proteins have been highlighted in different colours; other r-proteins and AFs are coloured in light cyan and (pre-)rRNAs in light grey.

Figure 2. The r-protein proxiOMEs also unveil potential interactions with importins. (A-D, left panels) TurboID results obtained with the Rpl38-TurboID **(A)**, Rpl30-TurboID **(B)**, TurboID-Rpl6a **(C)**, and Ubi1-TurboID **(D)** r-protein baits. The bait r-proteins, the enriched importins, and, in the case of the Ubi1-TurboID, the proximal AFs Nmd3, Lsg1, and Yvh1 are written in bold. **(A-D, middle panels)** AlphaFold3 models of the Kap121-Rpl38 **(A)**, Kap119-Rpl30 **(B)**, Kap114-Rpl6 **(C)**, and Kap114-Rpl40-Gsp1-GTP **(D)** complexes. The respective ipTM scores are indicated. **(A-D, right panels)** Y2H interaction assays between Rpl38 **(A)**, Rpl30 **(B)**, Rpl6 **(C)**, or Ubi1 **(D)** and the indicated importins or their N-terminally truncated variants **(upper right panels)**, and between these importins or their N-terminally truncated variants and the Gsp1.Q71L mutant variant **(lower right panels)**. Plasmids expressing the indicated G4BD-tagged bait and G4AD-tagged prey proteins were co-

transformed into the Y2H reporter strain PJ69-4A. Transformed cells were spotted in 10-fold serial dilution steps onto SC-Leu-Trp (SC-LT), SC-His-Leu-Trp (SC-HLT), and SC-Ade-Leu-Trp (SC-ALT) plates, which were incubated for 3 days at 30°C.

Figure 3. ProxiOMEs of Rpl1 and Acl1 as established by TurboID-based proximity labelling. (A) TurboID results obtained with the C- and N-terminally TurboID-tagged Rpl1b-TurboID (left panel) and TurboID-Rpl1b (right panel) bait proteins. **(B)** TurboID results obtained with Acl1-TurboID (left panel) and TurboID-Acl1 (right panel). The bait proteins and selected enriched proteins are written in bold.

Figure 4. Acl1 is a direct interaction partner of Rpl1 and is involved in LSU biogenesis. (A) Y2H interaction assays between Rpl1 and Acl1. **(B)** In vitro binding assay between Rpl1 and Acl1. Untagged Rpl1b (Rpl1b) or C-terminally $(His)_6$-tagged Rpl1b (Rpl1b-$(His)_6$) and C-terminally Flag-tagged Acl1 (Acl1-Flag) were co-expressed in *E. coli* and purified by Ni-NTA affinity purification. Proteins were revealed by SDS-PAGE and Coomassie staining (top) or by Western blotting using anti-Rpl1 and anti-Flag antibodies (bottom). Bands corresponding to C-terminally $(His)_6$-tagged and untagged Rpl1 or to Acl1-Flag are indicated by blue or black arrowheads. M: molecular weight standard, T: total extract, P: pellet fraction (insoluble proteins), S: soluble extract, E: imidazole eluate. **(C)** Negative genetic interactions between Δ*acl1* and Δ*rpl1a* (left panel) or Δ*rpl1b* (right panel). Strains with the indicated genotypes, derived from tetratype tetrads, were spotted in 10-fold serial dilution steps onto YPD plates, which were incubated for the indicated times at 30, 37, 23, and 16°C. **(D)** Polysome profiles of wild-type (*ACL1*, *RPL1A*), Δ*acl1*, Δ*rpl1a*, and Δ*acl1*/Δ*rpl1a* cells grown at 30ºC in YPD medium. Whole cell lysates were prepared under polysome-preserving conditions in the presence of cycloheximide. Eight A_{260} units of clarified lysate were separated in 10-50% sucrose gradients by ultracentrifugation, and the A_{254} absorption profiles were recorded by continuous monitoring. Sedimentation is from left to right. Free 40S and 60S subunits, free 80S couples/monosomes (80S), and polysomes are labelled. Half-mer peaks are indicated by arrowheads. **(E)** The subcellular localization of genomically expressed Acl1-ymNeonGreen was assessed by fluorescence microscopy in cells grown at 30ºC in SC-Ade medium. The subcellular position of the nucleolus was revealed by the nucleolar marker protein Nop58-yEmCherry, which was expressed from plasmid under the control of its cognate promoter. **(F)** The *ACL1*-TAP strain, expressing C-terminally TAP-tagged Acl1 from its genomic locus under the transcriptional control of its cognate promoter, was grown at 30ºC in YPD medium and the whole cell lysate was prepared under polysome-preserving conditions and analysed by sucrose gradient centrifugation and fractionation. Five A_{260} units of clarified lysate were separated in a 10-50% sucrose gradient by ultracentrifugation and the absorption profile was recorded by continuous monitoring at A_{254} (upper panel). 20 gradient fractions were collected from the top to the bottom at equidistant time intervals, and proteins were concentrated by TCA precipitation. An input (I) control (0.05 A_{260} units of the clarified lysate) and the gradient fractions (1-20) were analysed by Western blotting using anti-protA, anti-Rpl4, anti-Rps3, and anti-Rpl1 antibodies (lower panel).

Figure 5. Acl1 interacts via its ankyrin repeat domain with the second domain of Rpl1. (A, B) Mapping of the respective interaction-mediating regions on Rpl1 **(A, upper panel)** and Acl1 **(B, upper panel)** by Y2H assays. **(A, B, lower panels)** Cartoon representation of the Rpl1 structure (PDB: 6YLH (113)) and the AlphaFold model of Acl1 (AF-P25631-F1-v4). The two structural domains of Rpl1 (D1

and D2) and the ankyrin repeat domain of Acl1 are indicated. **(C)** Y2H interaction between minimal internal Rpl1 fragments and the ankyrin repeat domain of Acl1 (Acl1.N127). **(D)** In vitro binding assay between Rpl1b(63-158) and Acl1.N127. Untagged Rpl1b(63-158) or Rpl1b(63-158)-$(His)_6$ and Acl1.N127-Flag were co-expressed in *E. coli* and purified by Ni-NTA affinity purification. Proteins were revealed by SDS-PAGE and Coomassie staining (top) or by Western blotting using anti-Rpl1 and anti-Flag antibodies (bottom). Bands corresponding to C-terminally $(His)_6$-tagged and untagged Rpl1(63-158) or to Acl1.N127-Flag are indicated by blue or black arrowheads. M: molecular weight standard, T: total extract, P: pellet fraction, S: soluble extract, E: imidazole eluate.

Figure 6. Crystal structure of Acl1's ankyrin domain in complex with the second Rpl1 domain. (A) Cartoon representation of the X-ray co-structure of the second structural domain of Rpl1 (blue; resolved residues 64-151) and the ankyrin repeat domain Acl1 (red; resolved residues 2-127). In the lower part, the interacting residues are highlighted and labelled. The observed H-bonds are depicted as dotted lines. **(B)** Representation of the electrostatic surface potential of the Acl1-Rpl1 complex; red indicates negative potential and blue positive potential. **(C)** Schematic representation of the interaction mode. The backbone and side chains of Rpl1 residues 94-101 are shown as an elongated polypeptide and the side chains of the interacting Acl1 residues are indicated. H-bonds are depicted as dotted lines. **(D)** Distribution of the interaction-mediating Acl1 residues (highlighted by red dots) on the ankyrin repeat domain. **(E, F)** Mutational analysis of the Acl1-Rpl1 interaction interface. Y2H assays between the indicated Rpl1 mutant variants and Acl1 **(E)** and between the indicated Acl1 mutant variants and Rpl1 **(F)**. Single-letter abbreviations for the amino acid residues are as follows: A, Ala; D, Asp; E, Glu; K, Lys; N, Asn; Y, Tyr.

Figure 7. The conserved Bcl1 interacts via its WD40 β-propeller with Rpl1. (A) Proximity labelling assay with C-terminally miniTurbo-tagged RPL10A (HsRPL10A-miniTurbo), the orthologous human protein of yeast Rpl1, in HeLa cells. The assay was carried out in three experimental replicates, with miniTurbo-EGFP and EGFP-miniTurbo-NLS serving as cytoplasmic and nuclear background controls. The RPL10A bait r-protein and selected enriched proteins are written in bold, the red dot highlights the highly enriched WDR89. **(B)** AlphaFold3 model of the Bcl1-Rpl1 complex in two different orientations. The seven-bladed β-propeller domain of Bcl1 is coloured in green and the C-terminal extension in light green; the position of residue Asn322 (N322) is indicated to better visualize from where the C-terminal extension emanates. **(C)** AlphaFold3 model of the WDR89-RPL10A complex (left) and its structural superposition with the AlphaFold3 model of the Bcl1-Rpl1 complex (right). **(D)** Predicted electrostatic surface potential of Bcl1 (left) and close-up view of two of the three Rpl1 sites, indicating residues predicted to form H-bonds with Bcl1, that are in contact with the negatively charged top surface of the β-propeller (right). **(E-G)** Y2H interaction assays between the full-length Rpl1 and Bcl1 proteins **(E)**, between full-length Rpl1 and the C-terminally truncated Bcl1.N366 and Bcl1.N325 variants or the C-terminal extension of Bcl1 (323C) **(F)**, and between the indicated Rpl1 mutant variants and either Bcl1 or Acl1 **(G)**. Single-letter abbreviations for the amino acid residues are as follows: A, Ala; E, Glu; K, Lys; R, Arg. **(H)** In vitro binding assay between Bcl1.N366 and Rpl1. Bcl1.N366-$(His)_6$ or Bcl1.N366 and Rpl1b were co-expressed in *E. coli* and purified by Ni-NTA affinity purification. Proteins were revealed by SDS-PAGE and Coomassie staining (top) or by Western blotting using anti-Rpl1 and anti-His antibodies (bottom). Bands corresponding to Bcl1.N366-$(His)_6$ and Bcl1.N366 or to Rpl1b are indicated by blue or black arrowheads. M: molecular weight standard, T: total extract, P: pellet fraction, S: soluble extract, E: imidazole eluate.

Figure 8. Bcl1 may transiently interact with nucleolar pre-60S particles. (A, B) Genetic interactions between Δ*bcl1* and Δ*rpl1a* **(A)** or Δ*rpl1b* **(B)**. Strains with the indicated genotypes, derived from tetratype tetrads, were spotted in 10-fold serial dilution steps onto YPD plates, which were incubated for the indicated times at 30, 37, 23, and 16°C. **(C)** TurboID results obtained with Bcl1-TurboID. The bait protein and selected enriched proteins are written in bold. **(D, E)** Superposition of the AlphaFold3 model of the Bcl1-Rpl1 complex onto Rpl1 within the late nucleolar state E2 pre-60S particle (PDB: 7NAC (103)). Bcl1-proximal proteins in the neighbourhood of the superimposed Bcl1-Rpl1 complex are indicated and highlighted in different colours, other r-proteins and AFs are coloured in cyan and (pre-)rRNAs in light grey **(D)**. Close-up view of the L1 stalk rRNA and the superimposed Bcl1-Rpl1 complex without (left) or with (right) showing Nop2 **(E)**. **(F)** A *BCL1*-TAP strain, expressing C-terminally TAP-tagged Bcl1 from its genomic locus, was grown at 30ºC in YPD medium. The whole cell lysate was prepared under polysome-preserving conditions and analysed by sucrose gradient centrifugation and fractionation as described in the legend of Figure 4F. **(G)** The subcellular localization of Bcl1-ymNeonGreen, expressed from plasmid under the control of its cognate promotor in a Δ*bcl1* null mutant strain, was assessed by fluorescence microscopy in cells grown at 30ºC in SC-Ade-Leu medium. The subcellular position of the nucleolus was revealed by the nucleolar marker protein Nop58-yEmCherry, which was expressed from a plasmid under the control of its cognate promoter.

Figure 9. Acl1, Bcl1, and Rpl1 can form a trimeric complex. (A) In vitro binding assay between Bcl1.N366 and Acl1. Bcl1.N366-$(His)_6$ or Bcl1.N366 and Acl1-Flag were co-expressed in *E. coli* and purified by Ni-NTA affinity purification. Proteins were revealed by SDS-PAGE and Coomassie staining (top) or by Western blotting using anti-His and anti-Flag antibodies (bottom). Bands corresponding to Bcl1.N366-$(His)_6$ and Bcl1.N366 or to Acl1-Flag are indicated by blue or black arrowheads. M: molecular weight standard, T: total extract, P: pellet fraction, S: soluble extract, E: imidazole eluate. **(B)** Purification of the trimeric Acl1-Rpl1-Bcl1 complex. Bcl1.N366-$(His)_6$, Rpl1, and either Acl1-Flag (left) or untagged Acl1 (right) were co-expressed in *E. coli* and purified by consecutive Ni-NTA and anti-Flag affinity purification. Proteins were revealed by SDS-PAGE and Coomassie staining (top) or by Western blotting using anti-His, anti-Flag, and anti-Rpl1 antibodies (bottom). Bands corresponding to Bcl1.N366-$(His)_6$, Rpl1, and Acl1-Flag or Acl1 are indicated by blue, black, or red arrowheads. M: molecular weight standard, T: total extract, P: pellet fraction, S: soluble extract, E1: imidazole eluate, E2: Flag eluate. **(C, D)** Cartoon representation **(C)** and predicted electrostatic surface potential with the protected positively charged surface of Rpl1 being highlighted **(D)** of the AlphaFold3 model of the Acl1-Rpl1-Bcl1 trimeric complex. The ipTM scores of the respective binary interactions are indicated. **(E-G)** Y2H interaction assays between the full-length Acl1 and Bcl1 proteins **(E)**, between the indicated Acl1 mutant variants and either Bcl1 or Rpl1 **(F)**, and between the indicated Rpl1 mutant variants and either Bcl1 or Acl1 **(G)**. Single-letter abbreviations for the amino acid residues are as follows: A, Ala; D, Asp; E, Glu; K, Lys; N, Asn; Y, Tyr.

Figure 10. Acl1 and Bcl1 functionally cooperate to ensure efficient incorporation of Rpl1. (A, C) Negative genetic interactions between Δ*acl1* and Δ*bcl1* **(A)** or between Δ*acl1*, Δ*bcl1*, and Δ*rpl1a* **(C)**. Strains with the indicated genotypes, derived from tetratype tetrads, were spotted in 10-fold serial dilution steps onto YPD plates, which were incubated for the indicated times at 30, 37, 23, and 16°C. **(B, D)** Polysome profiles of wild-type (*ACL1*, *BCL1*), Δ*acl1*, Δ*bcl1*, and Δ*acl1*/Δ*bcl1* cells **(B)**, and of

Δ*acl1*, Δ*acl1*/Δ*bcl1*, Δ*acl1*/Δ*rpl1a*, and Δ*acl1*/Δ*bcl1*/Δ*rpl1a* cells **(D)** grown at 30ºC in YPD medium. **(E)** Whole cell lysates of wild-type (WT), Δ*rpl1b*, and Δ*acl1*/Δ*bcl1* strains, grown at 30ºC in YPD medium, were prepared under polysome-preserving conditions and analysed by sucrose gradient centrifugation and fractionation as described in the legend of Figure 4F. An input (I) control (0.05 A_{260} units of the clarified lysate) and the gradient fractions (1-20) were analysed by Western blotting using anti-Rps3, anti-Rpl4, and anti-Rpl1 antibodies. **(F)** Bar graph showing the average and standard deviation (n=2) of the normalized Rpl1/Rpl4 ratios in the 60S (9), 80S (10, 11), and polysomal (13-15) fractions of the indicated strains.

Figure 11. Acl1 and Bcl1 contain functional NLSs that may target the trimeric complex to the nucleus. (A, B) The C-terminal extremity of Acl1 contains a predicted cNLS **(A, upper panel)**, and the C-terminal extremity of Bcl1 resembles a bPY-NLS, as illustrated by its comparison with the known bPY-NLSs of Hrp1 and Syo1 **(B, upper panel)**. Basic residues are coloured in blue and residues of the characteristic C-terminal signature of PY-NLSs in red. **(A, B, lower panels)** The nuclear targeting activity, as inferred from the capacity to confer nuclear localization to an N-terminally fused 3xyEGFP reporter, of C-terminal Acl1 segments (205C, residues 205-222; 209C, residues 209-222) **(A, lower panels)**, and of the entire C-terminal extension of Bcl1 (323C, residues 323-389), the extension lacking the terminal bPY-NLS region (residues 323-366), and the bPY-NLS-containing C-terminal extremity of Bcl1 (364C, residues 364-389) as well as the indicated mutant variants thereof **(B, lower panels)** was assessed by fluorescence microscopy in cells grown at 30ºC in SC-Leu medium. The 3xyEGFP control protein and the N-terminally 3xyEGFP-tagged fusion proteins were expressed from plasmid under the control of the *ADH1* promoter in cells expressing the nucleolar marker protein Nop58-yEmCherry from the genomic locus. **(C)** Y2H interaction assays between the N-terminally G4BD-tagged (G4BDN) bPY-NLS-containing C-terminal extremity of Hrp1 (Hrp1.504C), full-length Bcl1, Bcl1.323C, and Bcl1.364C, as well as the indicated mutant variants thereof, and C-terminally G4AD-tagged full-length Kap104 (right) or the N-terminally truncated Kap104.305C variant (left). Single-letter abbreviations for the amino acid residues are as follows: A, Ala; P, Pro; R, Arg; Y, Tyr. **(D, E)** The subcellular localization of C-terminally ymNeonGreen-tagged Acl1 (Acl1-ymNG) or its C-terminally truncated, NLS-lacking variant (Acl1.N208-ymNG) **(D)** and of C-terminally ymNeonGreen-tagged Bcl1 (Bcl1-ymNG) or its C-terminally truncated, NLS-lacking variant (Bcl1.N366-ymNG) **(E)** was assessed by fluorescence microscopy in Δ*acl1*/Δ*bcl1* cells, grown at 30ºC in SC-Ade-Leu-Trp medium, that simultaneously expressed Bcl1 or Bcl1.N366 **(D)** and, respectively, Acl1 or Acl1.N208 **(E)**. The ymNeonGreen-tagged and untagged proteins were expressed from plasmid under the control of the cognate *ACL1* or *BCL1* promoter. The subcellular position of the nucleolus was revealed by the nucleolar marker protein Nop58-yEmCherry, which was expressed from plasmid under the control of its cognate promoter.

Figure 12. Simplified model showing how Acl1 and Bcl1 functionally cooperate to mediate the safe transfer of newly synthesized Rpl1 to its rRNA-binding site on the L1 stalk within nucleolar pre-60S particles. Upon its release from translating 80S ribosomes, newly synthesized Rpl1 is captured by Acl1 and/or Bcl1 and imported either as a dimeric Acl1-Rpl1 and trimeric Acl1-Rpl1-Bcl1 complex (main pathways) or a dimeric Bcl1-Rpl1 complex (minor pathway). Nuclear import of these complexes is mediated by importins, most likely the importin-α/β heterodimer Kap60/Kap95 (Acl1-Rpl1 and Acl1-Rpl1-Bcl1) or the importin-β Kap104 (Bcl1-Rpl1 and Acl1-Rpl1-Bcl1), upon recognition of the respective NLSs that are located at the C-terminal extremity of both Acl1 and Bcl1. Once in the nucleus,

these cargo complexes are dissociated form the importins by the binding of RanGTP. As Acl1 protects one of the two rRNA-binding surfaces of Rpl1, it will get efficiently dissociated by the full integration of Rpl1 into nucleolar pre-60S particles, whereas Bcl1, as suggested by the identification of Rpl1-proximal AFs in its proxiOME, may remain transiently associated until a certain maturation stage with pre-60S particles. The question marks indicate the possibilities that Rpl1 may also enter the nucleus, albeit inefficiently, on its own or, alternatively, may get incorporated into cytoplasmic pre-60S subunits. For simplicity, the anticipated return of Acl1 and Bcl1 to the cytoplasm (for another round of Rpl1 binding, import, and delivery), the RanGTP-mediated cargo release in the nucleus, the export of exportin-bound importin-α and RanGTP-bound importin-βs, and the cytoplasmic recycling of importins (dissociation of RanGTP upon its conversion to RanGDP) for another round of cargo binding are not depicted. For more details, see Discussion.

SUPPLEMENTARY FIGURE LEGENDS

Supplementary Figure S1. The proxiOME of LSU r-proteins. Graphical representation of the TurboID results obtained with all N- and C-terminally TurboID-tagged LSU r-proteins as well as with the ribosomal-like AFs Rlp7 and Rlp24. The employed bait protein is indicated above each graph. The bait proteins, enriched DCs and importins, and selected enriched r-proteins and AFs are written in bold.

Supplementary Figure S2. (A) Localization of the four TurboID-tagged GFP control proteins, expressed for 1 h in the presence of 0.1 mM $CuSO_4$ under the control of the *CUP1* promoter from plasmid, was assessed by fluorescence microscopy in cells expressing the nucleolar marker protein Nop58-yEmCherry from the genomic locus that were grown in SC-Leu medium at 30ºC. **(B)** Evaluation of the functionality of C-terminally TurboID-tagged Rpl3. Empty vector (YCplac111) and plasmids harbouring *RPL3*, *RPL3*-yEGFP, or *RPL3*-TurboID, expressed under the transcriptional control of the *RPL3* promoter, were transformed into an *RPL3* shuffle strain. Transformants were restreaked on SC-Leu plates and cells were then spotted in10-fold serial dilution steps onto SC-Leu plates and SC plates containing 5-fluoroorotic acid (5-FOA), which were incubated for 3 days at 30°C. After plasmid shuffling, cells were restreaked on SC-Leu plates and then spotted in 10-fold serial dilution steps onto SC-Leu and YPD plates. **(C)** Y2H interaction assays between the r-proteins Rpl3, Rpl5, and Rpl10 (tagged at their N- or C-termini with the G4BD) and their respective G4AD-tagged DC Rrb1, Syo1, and Sqt1. **(D)** AlphaFold3 model of the Rrb1-Rpl3 complex. The prediction was done with full-length Rrb1 and Rpl3 lacking its N-terminal methionine as input, but, for clarity, only residues 90-511 of Rrb1 (red) and residues 2-14 of Rpl3 (blue) are shown in the cartoon representation (left) and the representation depicting the electrostatic surface potential of Rrb1 (right).

Supplementary Figure S3. Bar graphs showing the log2 fold enrichment of AFs, which were enriched in the TurboID assays with the Rpl3-TurboID bait (see Figure 1B), in the TurboID assays of all N- (red bars) and C-terminally (blue bars) TurboID-tagged LSU r-proteins as well as the ones of Rlp7 and Rlp24. In the case of the Rpl3-TurboID bait (dark blue bars) and the TurboID-Rpl1 bait, their log2 fold enrichment corresponds to the average of the eight or, respectively six experimental replicates. Dashed lines indicate the median log2 fold enrichment of an AF across all shown TurboID assays. The order of the LSU r-proteins (from left to right) is according to their first visualization in structures of early nucleolar to cytoplasmic pre-60S particles.

Supplementary Figure S4. (A-C) Location of Rpl3 and its neighbouring proteins on: **(A)** the late nucleolar state E2 pre-60S particle (PDB: 7NAC (103)), **(B)** the early nucleoplasmic state NE1 pre-60S particle (PDB: 7U0H (103)), and **(C)** the 80S ribosome (PDB 4V88 (114)). The indicated proteins have been highlighted in different colours; other r-proteins and AFs are coloured in light cyan and (pre-)rRNAs in light grey. **(D)** Superposition of the AlphaFold3 model of the Tif6-Rei1.N66 (left) and Tif6-Reh1.N62 (right) complex onto Tif6 (shown in cartoon representation) within the cytoplasmic Lsg1-TAP state II (left; PDB: 6S05) or Lsg1-TAP state III (right; PDB: 6QIK) pre-60S particles (101)) , in which either parts of Rei1 or Reh1 can be visualized. Rei1 is coloured in orange and Reh1 in dark blue. **(E)** Y2H interaction assays between Tif6 and Reh1.N62 (residues 1-62) or Rei1.N66 (residues 1-66). Note that multicopy plasmids were used for these Y2H assays.

Supplementary Figure S5. (A-D) Bar graphs showing the log2 fold enrichment of Nsa1 **(A)**, Nmd3 and Lsg1 **(B)**, Rrp1 **(C)**, and Yvh1 **(D)** in the TurboID assays of all N- (red bars) and C-terminally (blue bars) TurboID-tagged LSU r-proteins as well as the ones of Rlp7 and Rlp24. In the case of the Rpl3-TurboID bait (dark blue bars) and the TurboID-Rpl1 bait, their log2 fold enrichment corresponds to the average of the eight or, respectively six experimental replicates. Dashed lines indicate the median log2 fold enrichment of an AF across all shown TurboID assays. The order of the LSU r-proteins (from left to right) is according to their first visualization in structures of early nucleolar to cytoplasmic pre-60S particles. The right or lower panels show the location and neighbouring proteins of: **(A)** Nsa1 on the early nucleolar state C pre-60S particle (PDB: 6EM1 (104)), **(B)** Nmd3 and Lsg1 on a cytoplasmic pre-60S intermediate (Lsg1-TAP, state V; PDB: 6RI5 (101)), **(C)** Rrp1 on the early nucleolar state 2 pre-60S particle (PDB: 6C0F (102)), **(D)** Yvh1 on the cytoplasmic Rpl10-inserted pre-60S particle (PDB: 6N8O (116)). The indicated proteins have been highlighted in different colours; other r-proteins and AFs are coloured in light cyan and (pre-)rRNAs in light grey.

Supplementary Figure S6. Identification of the known DCs in the proxiOMEs of their r-protein clients. (A-I) Graphical representation of the TurboID results obtained with N- and C-terminally TurboID-tagged Rpl3 **(A)**, Rpl4a **(B)**, Rpl5 **(C)**, Rpl10 **(D)**, Rpl11b **(E)**, Rpl23b **(F)**, Rps2 **(G)**, Rps3 **(H)**, and Rps26a **(I)**. **(J)** TurboID result obtained with the C-terminally TurboID-tagged Rpl4 variant lacking its C-terminal extension (Rpl4a.N264). The employed bait r-protein is indicated above each graph, and the bait r-protein, its known DC, and selected enriched proteins are written in bold.

Supplementary Figure S7. The DCs Rrb1, Acl4, Syo1, and Bcp1 are specifically enriched in the TurboID assays of their r-protein client. Bar graphs showing the log2 fold enrichment of Rrb1, Acl4, Syo1, and Bcp1 in the TurboID assays of all N- (red bars) and C-terminally (blue bars) TurboID-tagged LSU r-proteins as well as the ones of Rlp7 and Rlp24. In the case of the Rpl3-TurboID bait and the TurboID-Rpl1 bait, their log2 fold enrichment corresponds to the average of the eight or, respectively six experimental replicates. Dashed lines indicate the median log2 fold enrichment of an AF across all shown TurboID assays. The order of the LSU r-proteins (from left to right) is according to their first visualization in structures of early nucleolar to cytoplasmic pre-60S particles.

Supplementary Figure S8. Identification of the known r-protein clients in the proxiOMEs of their DCs. (A-H) Graphical representation of the TurboID results obtained with N- and C-terminally TurboID-tagged Rrb1 **(A)**, Acl4 **(B)**, Syo1 **(C)**, Sqt1 **(D)**, Bcp1 **(E)**, Tsr4 **(F)**, Yar1 **(G)**, and Tsr2 **(H)**. The abundance of each detected protein is displayed as its normalized intensity-based absolute quantification (iBAQ) value on the vertical axis, and its relative enrichment (fold change) on the horizontal axis as the log2 fold change of its normalized iBAQ abundance between the bait sample and the median of the remaining DC TurboIDs and the two respective control TurboIDs with prior imputation of missing values. The bait DC, its related r-protein and the relevant enriched proteins are written in bold. The employed bait DC is indicated above each graph, and the bait DC, its known r-protein client(s), and selected enriched proteins are written in bold.

Supplementary Figure S9. Bcp1 shields all prominent positively charged surfaces of Mss4. (A) Cartoon representation of the AlphaFold3 model of the Bcp1-Kap60-Kap95 complex (upper left) and the Bcp1-Mss4 complex (upper right; for clarity of the representation, residues 1-331 of Mss4 have been hidden). The ipTM scores of the individual binary interactions are indicated. Close-up view highlighting the Kap60-interacting residues (14-16 and 221-227; dark red) of Bcp1 in contact with Kap60 (lower right) or in the Bcp1-Mss4 complex (lower right). The location of the functional NLS region of Mss4 (residues 347-364; (133)) within the predicted Bcp1-Mss4 complex is highlighted in dark green. **(B)** Y2H interaction assays between Bcp1 and Rpl23 (positive control) or the indicated Mss4 segments. **(C)** Predicted electrostatic surface potential of the Bcp1-Mss4 complex (AlphaFold3 model; left), the Bcp1-interacting surface of Mss4 with residues 200-231 of Bcp1 in cartoon representation (middle), and the Mss4-interacting surface of Bcp1 with residues 347-364 of Mss4 in cartoon representation, revealing the respective negatively (Bcp1) or positively (Mss4) interaction interfaces.

Supplementary Figure S10. ProxiOME of Rpl1. (A) Representation of the variation of the enrichment of the Rpl1 bait, its DC Acl1, proximal AFs, and abundantly detected r-proteins between the experimental replicates (n=6); r-proteins that are close to or far away from Rpl1, as indicated by available structures of pre-60S particles, mature 60S subunits, and 80S ribosomes, are referred to as proximal or non-proximal RPs. The variation of the enrichment is represented by boxes highlighting the upper and lower quartiles of each data set, while the whiskers indicate the minimal and maximal limits of the distribution; outliers are shown as dots, the average by a line, and the median by a cross. **(B-H)** Location of Rpl1 or the L1 stalk rRNA and their neighbouring proteins on: **(B)** the late nucleolar state E2 pre-60S particle (PDB: 7NAC (103)), **(C)** the early nucleoplasmic state NE2 pre-60S particle (PDB: 6YLY (113)), **(D)** the nucleoplasmic pre-60S intermediate of the Nog2-containing pre-rotation state (PDB: 7UOO (165)), **(E)** the nucleoplasmic Rix1-Rea1 pre-60S particle (PDB: 6YLH (113)), **(F)** the NPC-trapped pre-60S particle (PDB: 8HFR (168)), **(G)** the cytoplasmic Lsg1-TAP state I pre-60S particle (PDB: 6RZZ (101)), and **(H)** the 80S ribosome (with the Rpl1-bound L1 stalk rRNA added from the PDB 4V7R 80S structure (167) and superposed on the PDB 4V88 80S structure (114)). The indicated proteins have been highlighted in different colours; other r-proteins and AFs are coloured in light cyan and (pre-)rRNAs in light grey.

Supplementary Figure S11. Acl1 and its identified Rpl1-interacting residues are conserved within the Fungi kingdom. The amino acid sequence of *S. cerevisiae* Acl1 (*S.cer*., UniProt: P25631) was aligned with the amino acid sequences of selected potential orthologous proteins, identified with the BLAST function of the UniProtKB (86), belonging to a specific subkingdom, phylum, or subphylum of the Fungi kingdom (see Materials and Methods). For clarity, only the alignment parts covering most of the N-terminal ankyrin repeat domain (residues 3-80 and 113-115 of *S. cerevisiae* Acl1) are shown, and interaction-mediating residues of *S. cerevisiae* Acl1 (indicated on top) that are conserved or semi-conserved are coloured in red or orange. Kingdom, subkingdom, phylum, and subphylum names are indicated. Species names are abbreviated as follows (with the UniProtKB or UniParc number of the respective protein referenced between parentheses): *Kazachstania africana*, *K.afr.* (H2B114); *Naumovozyma dairenensis*, *N.dai*. (G0WFQ9); *Candida glabrata*, *C.gla.* (Q6FWT6); *Tetrapisispora phaffii*, *T.pha.* (G8BT41); *Vanderwaltozyma polyspora*, *V.pol.* (A7TG26); *Zygosaccharomyces rouxii*, *Z.rou.* (C5DVQ9); *Zygotorulaspora mrakii*, *Z.mra*. (A0A7H9AWJ3); *Torulaspora delbrueckii*, *T.del.* (G8ZN72); *Lachancea thermotolerans*, *L.the.* (C5DBY1); *Kluyveromyces lactis*, *K.lac.* (Q6CTY4); *Eremothecium cymbalariae*, *E.cym.* (G8JPK3); *Komagataella phaffii*, *K.pha.* (C4R8E0); *Debaryomyces hansenii*, *D.han.* (Q6BK78); *Candida albicans*, *C.alb.* (A0A1D8PHS4); *Yarrowia lipolytica*, *Y.lip.* (Q6C254); *Aspergillus nidulans*, *A.nid.* (Q5BDT5); *Penicillium rubens*, *P.rub.* (B6H7C4); *Neurospora crassa*, *N.cra.* (Q7RZ65); *Chaetomium thermophilum*, *C.the.* (G0S6G3); *Chaetomium globosum*, *C.glo.* (Q2H182), *Schizosaccharomyces pombe*, *S.pom.* (Q9UU77); *Schizosaccharomyces japonicus*, *S.jap.* (B6JYY9); *Cryptococcus neoformans*, *C.neo.* (Q5KM81); *Ustilago maydis*, *U.may.* (A0A0D1E9K4); *Puccinia striiformis*, *P.str.* (A0A2S4WKI7); *Hesseltinella vesiculosa*, *H.ves.* (A0A1X2GXH0); *Linnemannia elongata*, *L.elo.* (A0A197K2N3); *Rhizophagus irregularis*, *R.irr.* (U9U5S0); *Neoconidiobolus thromboides*, *N.thr.* (UPI002211511C); *Coemansia biformis*, *C.bif.* (A0A9W8CY32); *Tieghemiomyces parasiticus*, *T.par.* (A0A9W8ADQ8); *Syncephalis pseudoplumigaleata*, *S.pse.* (A0A4P9YSW2); *Thamnocephalis sphaerospora*, *T.sph.* (A0A4P9XN32); *Allomyces macrogynus*, *A.mac.* (A0A0L0S8J9); *Catenaria anguillulae*, *C.ang.* (A0A1Y2HCN5); *Batrachochytrium dendrobatidis*, *B.den.* (A0A177W6V9); *Spizellomyces punctatus*, *S.pun.* (A0A0L0HTG5); *Rozella allomycis*, *R.all.* (A0A075AZK2).

Supplementary Figure S12. Acl1 interacts via its ankyrin repeat domain with the second domain of Rpl1. (A, B) Complete data set for the mapping of the minimal respective interaction-mediating regions on Rpl1 **(A)** and Acl1 **(B)** by Y2H assays. **(C)** Negative control Y2Hs showing that the indicated, C-terminally G4BD-tagged Rpl1 variants do not self-activate the reporter genes when assayed together with the non-fused G4AD. Related to the data shown in Figure 5A and 5B.

Supplementary Figure S13. (A) Representation of the electrostatic surface potential of the X-ray co-structure of the ankyrin repeat domain of Acl1 (residues 2-127) in complex with the second structural domain of Rpl1 (residues 64-151) with either Acl1 (in red) or Rpl1 (in blue) in cartoon representation to reveal the respective negatively (Acl1) or positively (Rpl1) charged interaction interfaces. **(B, C)** Representation of the interactions of Rpl1 with the L1 stalk rRNA as observed in the cryo-EM structure of: **(B)** the late nucleolar state E2 pre-60S particle (PDB: 7R7C (103)) and **(C)** the RQC-associated 60S subunit **(C)** (PDB: 8AGX, (185)). **(D)** The Acl1-interacting residues of Rpl1 are conserved in Rpl1 orthologues in metazoans, plants, and other fungi, as shown here for Rpl1 of *Chaetomium thermophilum* (UniProt: G0S4Z9), *Schizosaccharomyces pombe* (O74836), *Homo sapiens* (P62906), *Mus musculus* (P53026), *Gallus gallus* (F6SU35), *Xenopus laevis* (Q7ZYS8), *Danio rerio* (Q6PC69), *Caenorhabditis*

elegans (Q9N4I4), *Drosophila melanogaster* (Q9VTP4), and *Arabidopsis thaliana* (P59230). **(E)** Cartoon representation of the ankyrin repeat domain of Acl1 (residues 2-127) in complex with the second structural domain of Rpl1 (residues 64-151) as observed in our experimental X-ray co-structure or the AlphaFold3 model (ipTM score 0.86). The superposition of the two structures reveals their high similarity.

Supplementary Figure S14. (A, B) Polysome profiles of wild-type (*BCL1*, *RPL1A*), Δ*rpl1a*, Δ*bcl1*, and Δ*bcl1*/Δ*rpl1a* cells **(A)**, and of wild-type (*BCL1*, *RPL1B*), Δ*rpl1b*, Δ*bcl1*, and Δ*bcl1*/Δ*rpl1b* cells **(B)** grown at 30ºC in YPD medium. **(C)** Cartoon representation of the superposed predicted (extracted from the AlphaFold3 model of the Bcl1-Rpl1 complex) and observed (extracted from the late nucleolar state E2 pre-60S particle (PDB: 7NAC (103)) Rpl1 structures. **(D)** Close-up view of the superposition (shown in Figure 8D) of the AlphaFold3 model of the Bcl1-Rpl1 complex onto Rpl1 within the late nucleolar state E2 pre-60S particle (PDB: 7NAC (103)), highlighting the first resolved residue of Erb1 and the last resolved residues of Ebp2, Nug1, and Loc1.

Supplementary Figure S15. (A) AlphaFold3 models of the Bcl1-Rpl1 (upper left), the Acl1-Rpl1-Bcl1 (upper middle), and the Acl1-Rpl1 (upper right) complexes. The lower panels show the superposition of the predicted Bcl1-Rpl1 or Acl1-Rpl1 complex with the predicted trimeric complex. The ipTM scores of the individual binary interactions are indicated.**(B, C)** Representation of the predicted electrostatic surface potential of the trimeric Acl1-Rpl1-Bcl1 complex (AlphaFold3 model) **(B)** with either Bcl1 and Rpl1, Acl1 and Rpl1, or Acl1 and Bcl1 in cartoon representation to reveal the respective negatively (Acl1 and Bcl1) or positively (Rpl1) charged interaction interfaces **(C)**.

Supplementary Figure S16. (A) Interaction between Rpl1 (light blue) and the L1 stalk rRNA (grey) as observed on the late nucleolar state E2 pre-60S particle (left panel; PDB: 7R7C (103)). AlphaFold3 model of the Acl1-Rpl1 complex (right panel). Superposition of the AlphaFold3 model of the Acl1-Rpl1 complex and the Rpl1-bound L1 stalk rRNA (middle panel), revealing that Acl1 shields the rRNA-binding surfaces of Rpl1. **(B)** Y2H interaction assays between Rpl1 and full-length Acl1 or the indicated C-terminal segments of Acl1 (127C, residues 127-222; 143C, residues 143-222). The right panel shows the negative control Y2Hs with the non-fused G4AD, revealing that the indicated, C-terminally G4BD-tagged Acl1 variants do not self-activate the reporter genes. **(C)** Close-up view of the predicted interaction between residues of the predicted three-helix fold within Acl1's C-terminal part and the first structural domain (D1) of Rpl1. **(D, E)** Y2H interaction assays between Bcl1 and the indicated Rpl1 **(D)** or Acl1 **(E)** mutant variants. Complete data set related to the data shown in Figure 9G and 9F. Single-letter abbreviations for the amino acid residues are as follows: A, Ala; D, Asp; E, Glu; K, Lys; N, Asn; Y, Tyr.

Supplementary Figure S17. Second experimental replicate of the sucrose gradient centrifugation and fractionation experiment shown in Figure 10E that was used for the bar graph showing the average and standard deviation (n=2) of the normalized Rpl1/Rpl4 ratios in the 60S, 80S, and polysomal fractions of wild-type, Δ*rpl1b*, and Δ*acl1*/Δ*bcl1* cells in Figure 10F.

Supplementary Figure S18. **Acl1 and Bcl1 contain functional NLSs that may target the trimeric complex to the nucleus. (A, B)** Surface representation of the AlphaFold3 model of the pentameric Kap95-Kap60-Acl1-Rpl1-Bcl1 complex **(A)** and the tetrameric Kap104-Bcl1-Rpl1-Acl1 complex **(B)**. **(C)** AlphaFold3 model of the binary Kap104-Bcl1 complex in cartoon representation with Bcl1 in semi-transparent surface representation (left). Close-up view showing the molecular details of the predicted interaction between Kap104 and the C-terminal bPY-NLS of Bcl1, with interacting residues being labelled and the observed H-bonds being depicted as dotted lines (right). **(D)** Y2H interaction assays between N-terminally G4BD-tagged (G4BDN) Bcl1, Bcl1.323C, and the indicated mutant variants of Bcl1.323C and C-terminally G4AD-tagged full-length Kap104 (right) or the N-terminally truncated Kap104.305C variant (left). Single-letter abbreviations for the amino acid residues are as follows: A, Ala; P, Pro; R, Arg; Y, Tyr. **(E)** The nuclear targeting activity of Bcl1.323C and the indicated mutant variants thereof was assessed by fluorescence microscopy in cells grown at 30ºC in SC-Leu medium. The 3xyEGFP and 3xyEGFP-SV40NLS control proteins and the N-terminally 3xyEGFP-tagged Bcl1.323C fusion proteins were expressed from plasmid under the control of the *ADH1* promoter in cells expressing the nucleolar marker protein Nop58-yEmCherry from the genomic locus. **(F)** Graphical representation of the TurboID result obtained with C-terminally TurboID-tagged Bcl1 (Bcl1-TurboID). The Bcl1 bait protein, Acl1, and the enriched importin Kap121 are written in bold; orange dots highlight the location of importins on the graph. **(G)** Y2H interaction assays between full-length Bcl1, Bcl1.323C, and Bcl1.364C and C-terminally G4AD-tagged full-length Kap121 (right) or the N-terminally truncated Kap121.302C variant (left).

Supplementary Figure S19. Co-translational capturing assay. The DCs Acl1 (Acl1-TAP), Bcl1 (Bcl1-TAP), Bcp1 (TAP-Bcp1 and Bcp1-TAP), and, as positive controls, Acl4 (Acl4-TAP) and Rrb1 (TAP-Rrb1) were affinity purified (IgG-Sepharose pull-down) from extracts of cycloheximide-treated cells and the associated RNA was isolated from the TEV eluates. Each of the six DC purifications was assessed for their content of the four RPG mRNAs (*RPL1*, *RPL3*, *RPL4*, and *RPL23*) by real-time qRT-PCR. For each cDNA, real-time qPCRs were performed in triplicates. The bar graph shows the relative enrichment of the four RPG mRNAs in the six DC purifications.

SUPPLEMENTARY TABLE

Supplementary Table S1: Data collection and refinement statistics

	Rpl1(63-158)-Acl1.N127
Data collection	
X-ray source	ESRF, Grenoble ID30A-3 (MASSIF-3)
Detector	Eiger1 X 4M
Wavelength (Å)	0.967697
Space group	$P6_522$
Cell dimensions (*a*, *b*, *c* (Å))	101.65, 101.65, 108.13
Resolution (Å)*	46.07-2.55 (2.70-2.55)
Total reflections	445071
Multiplicity	39.52
Unique reflections	11261
Completeness (%)	100.0 (100.0)
R_{meas} (%)	29.5 (222.0)
$CC_{1/2}$	99.8 (52.3)
$I/\sigma(I)$	17.87 (2.78)
Mosaicity (°)	0.221
Wilson *B*-factor (Å^2)	57.24
Refinement	
Resolution (Å)	46.07-2.55
Rwork, Rfree	0.195, 0.242
Reflections (working, test set)	10698, 563
Completeness for range (%)	100.0
r.m.s.d. from ideal	
Bond lengths (Å)	0.011
Bond angles (°)	1.190
Total number of atoms	1663
Mean B value (Å^2)	63.94

*Values in parentheses are for highest-resolution shell

Figure 1

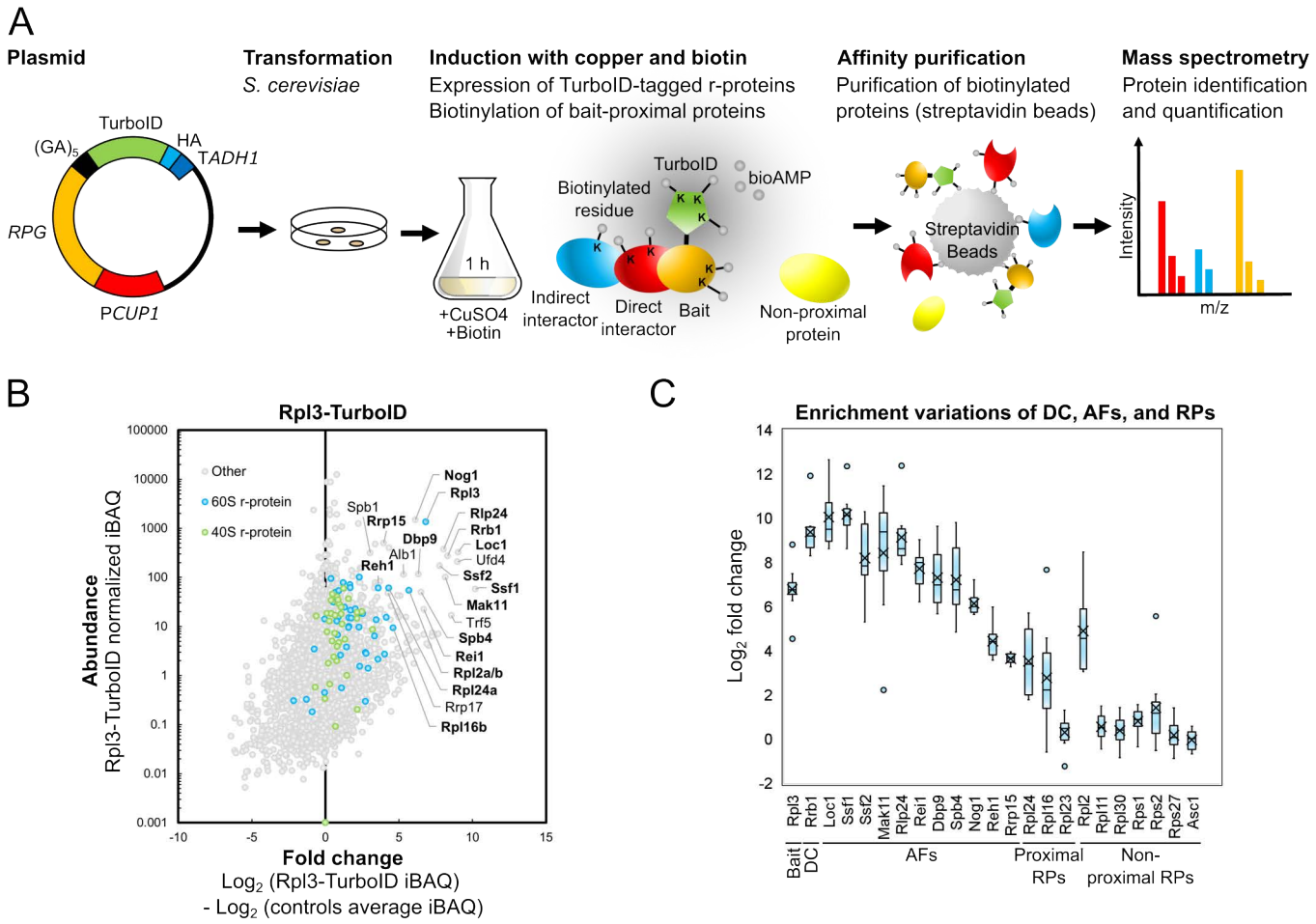
A
Plasmid
Transformation
S. cerevisiae
Induction with copper and biotin
Expression of TurboID-tagged r-proteins
Biotinylation of bait-proximal proteins
Affinity purification
Purification of biotinylated proteins (streptavidin beads)
Mass spectrometry
Protein identification and quantification
TurboID
(GA)5
HA
TADH1
RPG
PCUP1
1 h
+CuSO4
+Biotin
Biotinylated residue
TurboID
bioAMP
Indirect interactor
Direct interactor
Bait
Non-proximal protein
Streptavidin Beads
Intensity
m/z
B
Rpl3-TurboID
Abundance
Rpl3-TurboID normalized iBAQ
Other
60S r-protein
40S r-protein
Fold change
Log2 (Rpl3-TurboID iBAQ)
- Log2 (controls average iBAQ)
C
Enrichment variations of DC, AFs, and RPs
Log2 fold change
Bait DC
AFs
Proximal RPs
Non-proximal RPs
D
Early nucleolar pre-60S (state 2)
Mak11
Rlp24
Nog1
Rpl3
C
Ssf1
Rrp15
Rpl16
180°
Tif6
Rpl23
E
Late nucleolar pre-60S (state E1)
Spb4
Spb1
Rlp24
Nog1
Ile560
Rpl16
C
Rpl3
180°
Tif6
Rpl23
Spb1
Spb4
F
Nucleoplasmic pre-60S (Rix1-Rea1)
Rlp24
Tif6
Nog1
C
Rpl3
Rpl16
Alb1
G
Cytoplasmic pre-60S (Lsg1-TAP, state I)
Tif6
Rpl24
Rpl3
Rei1
Rpl16
C

Figure 2

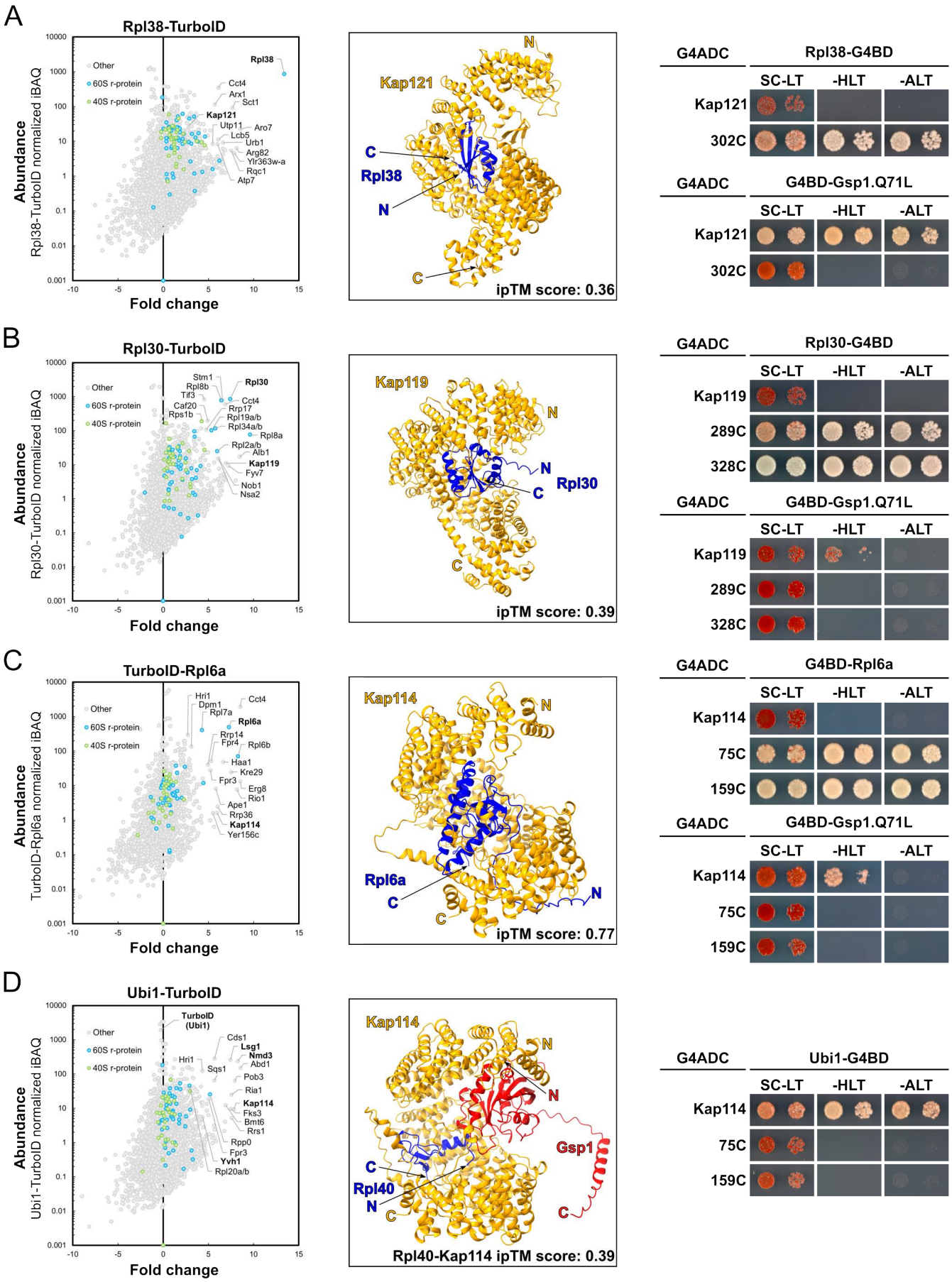
A
Rpl38-TurboID
Abundance
Rpl38-TurboID normalized iBAQ
Fold change
Other
60S r-protein
40S r-protein
Rpl38
Cct4
Arx1
Sct1
Kap121
Utp11
Aro7
Lcb5
Urb1
Arg82
Ylr363w-a
Rqc1
Atp7
Kap121
N
C
Rpl38
N
C
ipTM score: 0.36
G4ADC
Rpl38-G4BD
SC-LT
-HLT
-ALT
Kap121
302C
G4ADC
G4BD-Gsp1.Q71L
SC-LT
-HLT
-ALT
Kap121
302C
B
Rpl30-TurboID
Abundance
Rpl30-TurboID normalized iBAQ
Fold change
Other
60S r-protein
40S r-protein
Stm1
Rpl8b
Tif3
Caf20
Rps1b
Rpl30
Cct4
Rrp17
Rpl19a/b
Rpl34a/b
Rpl8a
Rpl2a/b
Alb1
Kap119
Fyv7
Nob1
Nsa2
Kap119
N
N
Rpl30
C
C
ipTM score: 0.39
G4ADC
Rpl30-G4BD
SC-LT
-HLT
-ALT
Kap119
289C
328C
G4ADC
G4BD-Gsp1.Q71L
SC-LT
-HLT
-ALT
Kap119
289C
328C
C
TurboID-Rpl6a
Abundance
TurboID-Rpl6a normalized iBAQ
Fold change
Other
60S r-protein
40S r-protein
Hri1
Dpm1
Rpl7a
Cct4
Rpl6a
Rrp14
Fpr4
Rpl6b
Haa1
Kre29
Fpr3
Erg8
Rio1
Ape1
Rrp36
Kap114
Yer156c
Kap114
N
Rpl6a
C
N
C
ipTM score: 0.77
G4ADC
G4BD-Rpl6a
SC-LT
-HLT
-ALT
Kap114
75C
159C
G4ADC
G4BD-Gsp1.Q71L
SC-LT
-HLT
-ALT
Kap114
75C
159C
D
Ubi1-TurboID
Abundance
Ubi1-TurboID normalized iBAQ
Fold change
Other
60S r-protein
40S r-protein
TurboID
(Ubi1)
Cds1
Lsg1
Nmd3
Abd1
Hri1
Sqs1
Pob3
Ria1
Kap114
Fks3
Bmt6
Rrs1
Rpp0
Fpr3
Yvh1
Rpl20a/b
Kap114
N
N
Gsp1
C
Rpl40
N
C
C
Rpl40-Kap114 ipTM score: 0.39
G4ADC
Ubi1-G4BD
SC-LT
-HLT
-ALT
Kap114
75C
159C

Figure 3

A

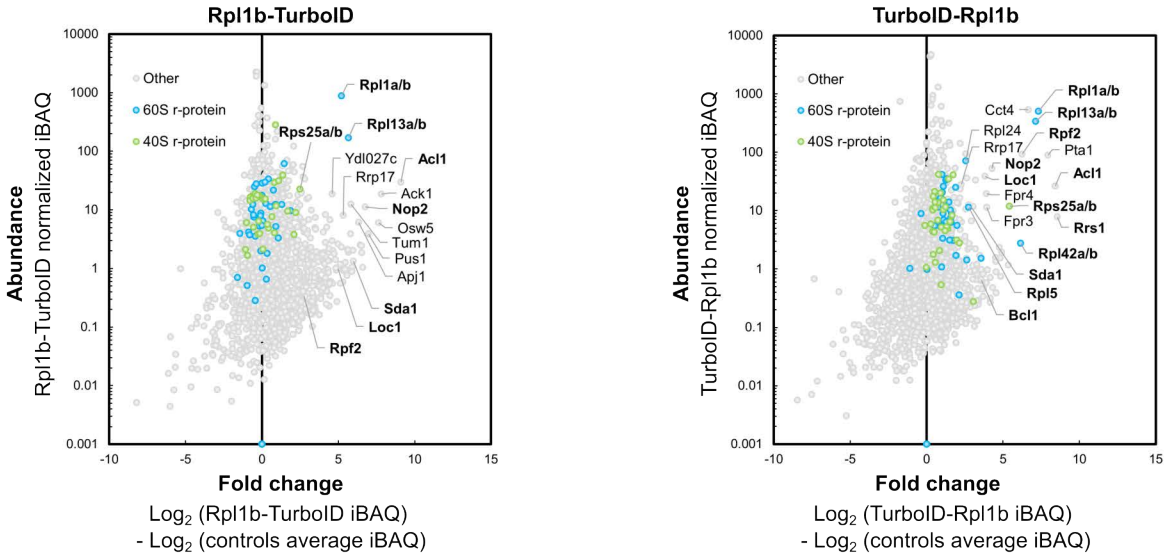
Rpl1b-TurboID
Other
60S r-protein
40S r-protein
Rpl1a/b
Rpl13a/b
Rps25a/b
Ydl027c
Acl1
Rrp17
Ack1
Nop2
Osw5
Tum1
Pus1
Apj1
Sda1
Loc1
Rpf2
Abundance
Rpl1b-TurboID normalized iBAQ
Fold change
Log2 (Rpl1b-TurboID iBAQ)
- Log2 (controls average iBAQ)
TurboID-Rpl1b
Other
60S r-protein
40S r-protein
Rpl1a/b
Cct4
Rpl13a/b
Rpl24
Rpf2
Rrp17
Pta1
Nop2
Acl1
Loc1
Fpr4
Rps25a/b
Fpr3
Rrs1
Rpl42a/b
Sda1
Rpl5
Bcl1
Abundance
TurboID-Rpl1b normalized iBAQ
Fold change
Log2 (TurboID-Rpl1b iBAQ)
- Log2 (controls average iBAQ)

B

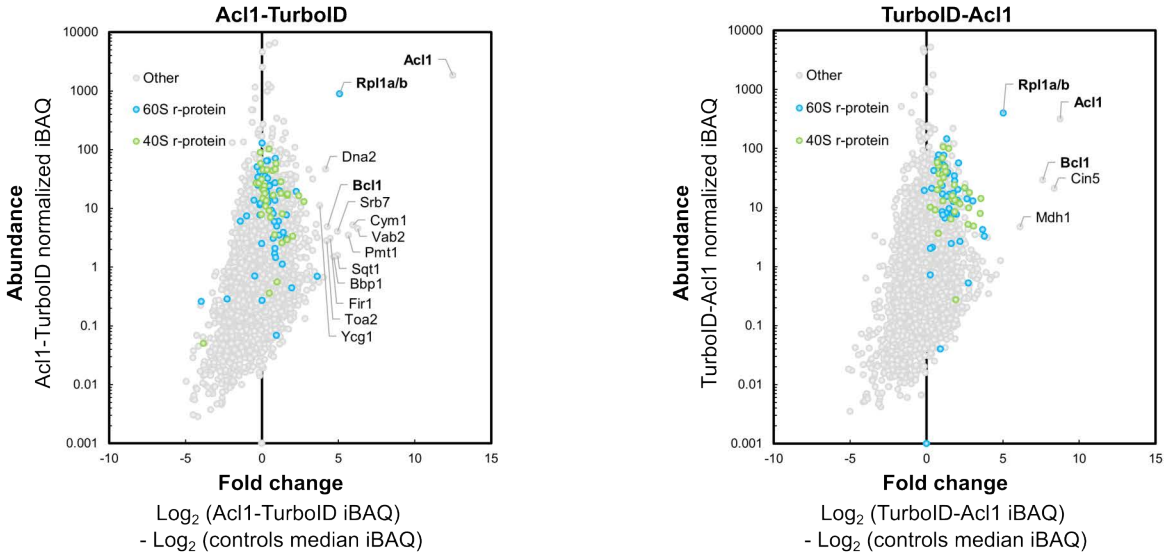
Acl1-TurboID
Other
60S r-protein
40S r-protein
Acl1
Rpl1a/b
Dna2
Bcl1
Srb7
Cym1
Vab2
Pmt1
Sqt1
Bbp1
Fir1
Toa2
Ycg1
Abundance
Acl1-TurboID normalized iBAQ
Fold change
Log2 (Acl1-TurboID iBAQ)
- Log2 (controls median iBAQ)
TurboID-Acl1
Other
60S r-protein
40S r-protein
Rpl1a/b
Acl1
Bcl1
Cin5
Mdh1
Abundance
TurboID-Acl1 normalized iBAQ
Fold change
Log2 (TurboID-Acl1 iBAQ)
- Log2 (controls median iBAQ)

Figure 4

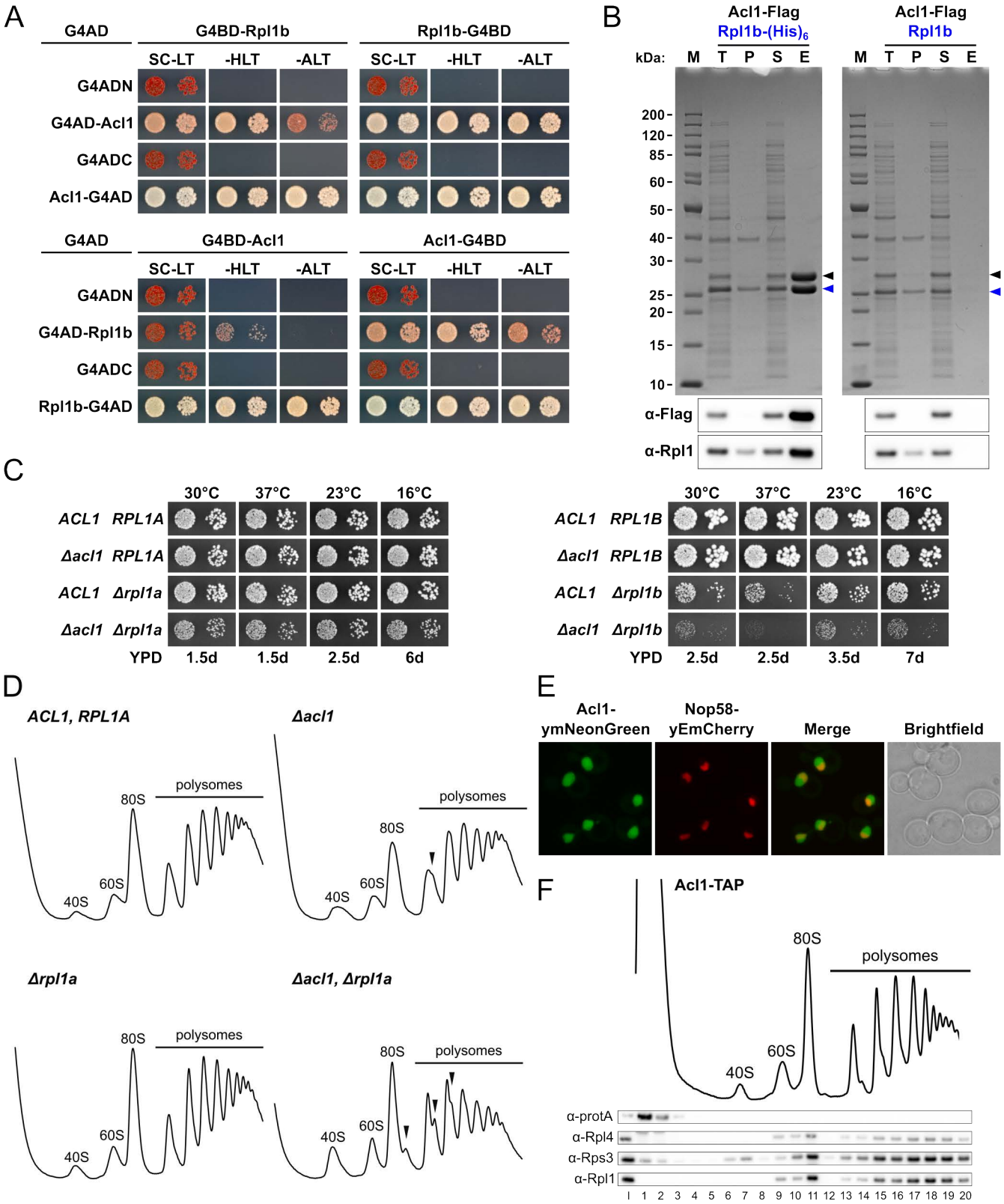
A
G4AD
G4BD-Rpl1b
Rpl1b-G4BD
SC-LT
-HLT
-ALT
G4ADN
G4AD-Acl1
G4ADC
Acl1-G4AD
G4AD
G4BD-Acl1
Acl1-G4BD
G4AD-Rpl1b
Rpl1b-G4AD
B
Acl1-Flag
Rpl1b-(His)6
Rpl1b
kDa:
M T P S E
200
120
85
60
50
40
30
25
20
15
10
α-Flag
α-Rpl1
C
30°C
37°C
23°C
16°C
ACL1 RPL1A
Δacl1 RPL1A
ACL1 Δrpl1a
Δacl1 Δrpl1a
YPD 1.5d 1.5d 2.5d 6d
ACL1 RPL1B
Δacl1 RPL1B
ACL1 Δrpl1b
Δacl1 Δrpl1b
YPD 2.5d 2.5d 3.5d 7d
D
ACL1, RPL1A
Δacl1
Δrpl1a
Δacl1, Δrpl1a
polysomes
80S
60S
40S
E
Acl1-ymNeonGreen
Nop58-yEmCherry
Merge
Brightfield
F
Acl1-TAP
80S
polysomes
60S
40S
α-protA
α-Rpl4
α-Rps3
α-Rpl1
I 1 2 3 4 5 6 7 8 9 10 11 12 13 14 15 16 17 18 19 20

Figure 5

A

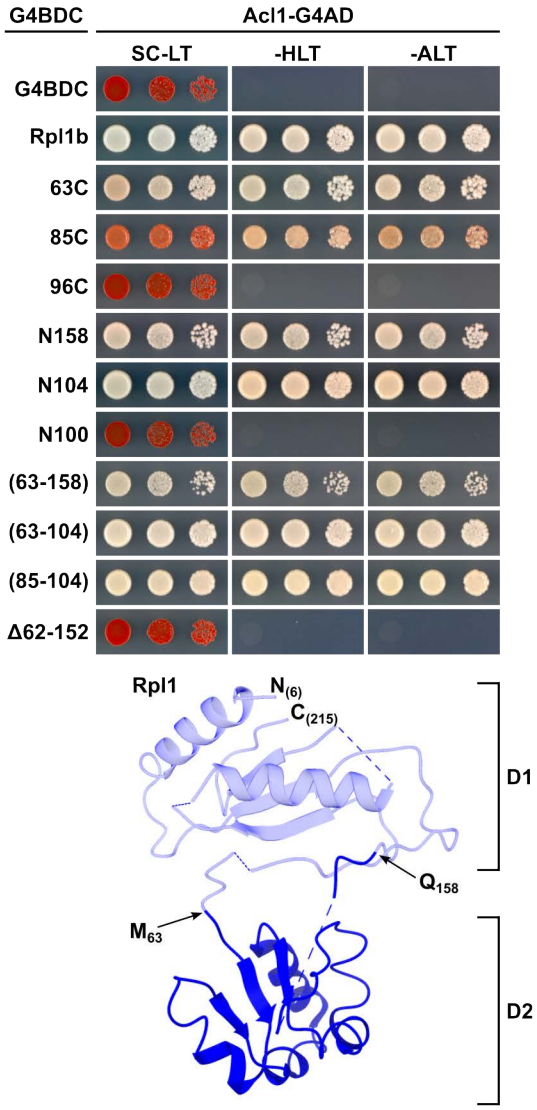

B

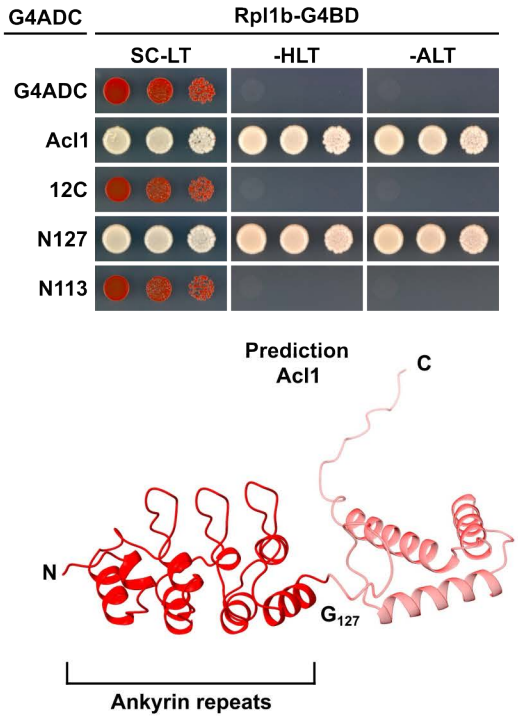

C

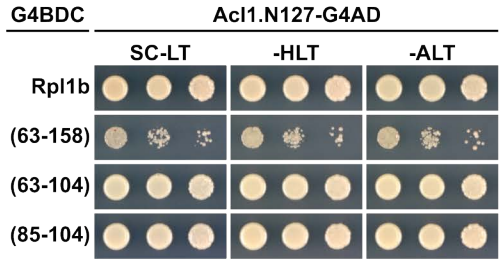

D

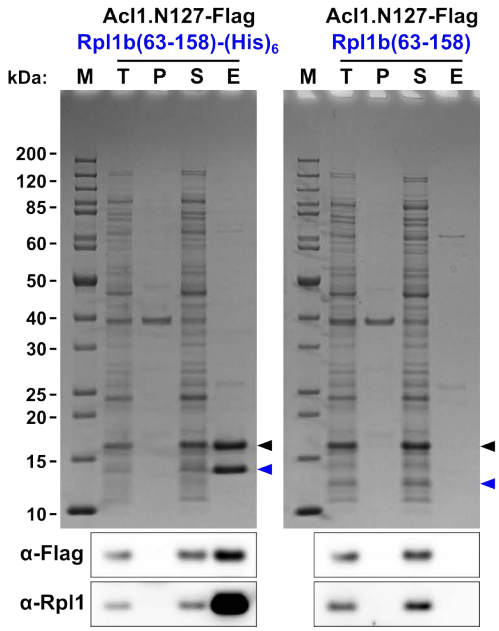

Figure 6

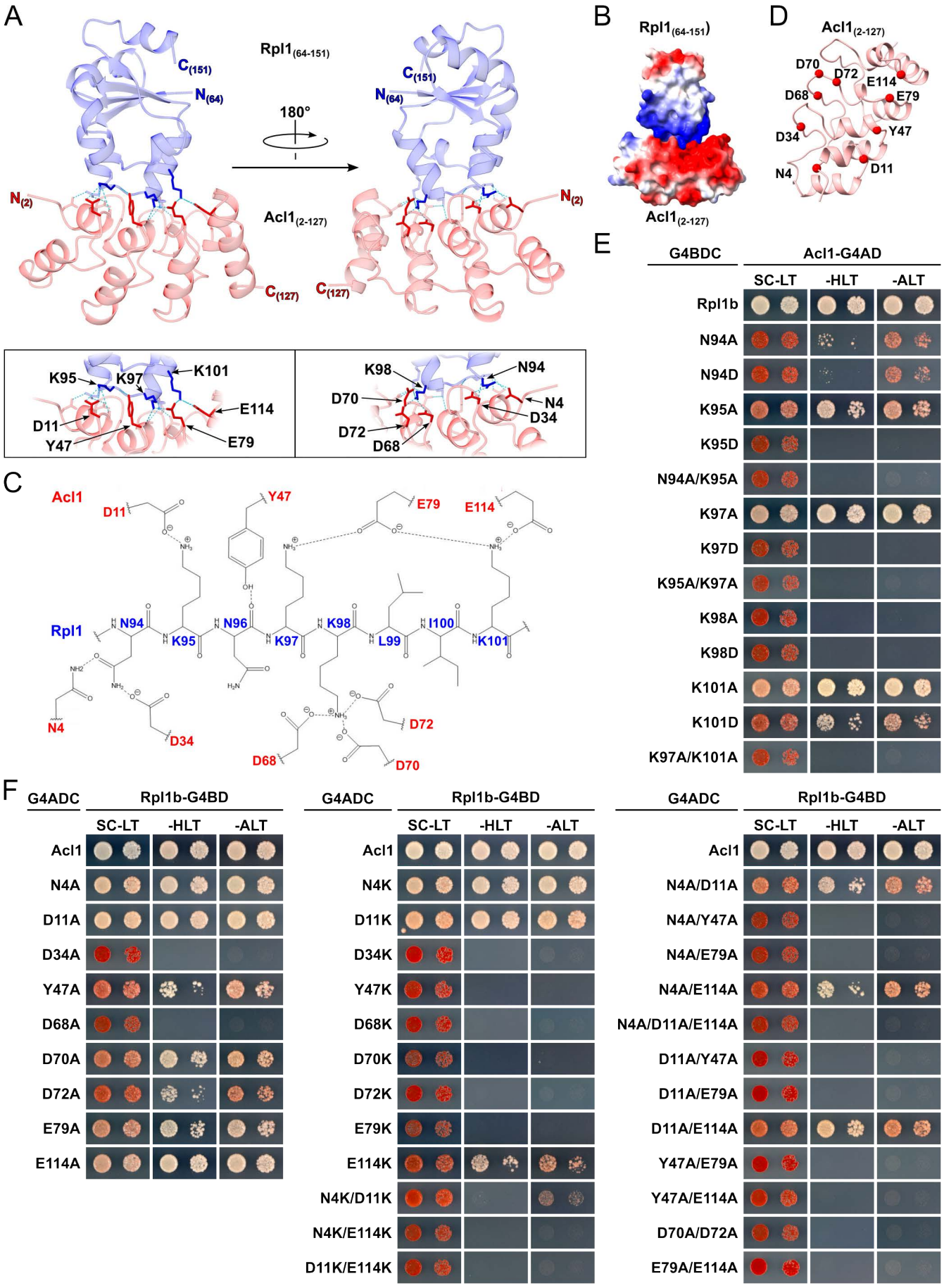
A
Rpl1(64-151)
C(151)
N(64)
180°
N(2)
Acl1(2-127)
C(127)
K95
K97
K101
E114
D11
Y47
E79
K98
N94
D70
N4
D34
D72
D68
B
Rpl1(64-151)
Acl1(2-127)
D
Acl1(2-127)
D70
D72
E114
D68
E79
D34
Y47
N4
D11
C
Acl1
D11
Y47
E79
E114
Rpl1
N94
K95
N96
K97
K98
L99
I100
K101
N4
D34
D68
D72
D70
E
G4BDC
Acl1-G4AD
SC-LT
-HLT
-ALT
Rpl1b
N94A
N94D
K95A
K95D
N94A/K95A
K97A
K97D
K95A/K97A
K98A
K98D
K101A
K101D
K97A/K101A
F
G4ADC
Rpl1b-G4BD
SC-LT
-HLT
-ALT
Acl1
N4A
D11A
D34A
Y47A
D68A
D70A
D72A
E79A
E114A
N4K
D11K
D34K
Y47K
D68K
D70K
D72K
E79K
E114K
N4K/D11K
N4K/E114K
D11K/E114K
N4A/D11A
N4A/Y47A
N4A/E79A
N4A/E114A
N4A/D11A/E114A
D11A/Y47A
D11A/E79A
D11A/E114A
Y47A/E79A
Y47A/E114A
D70A/D72A
E79A/E114A

Figure 7

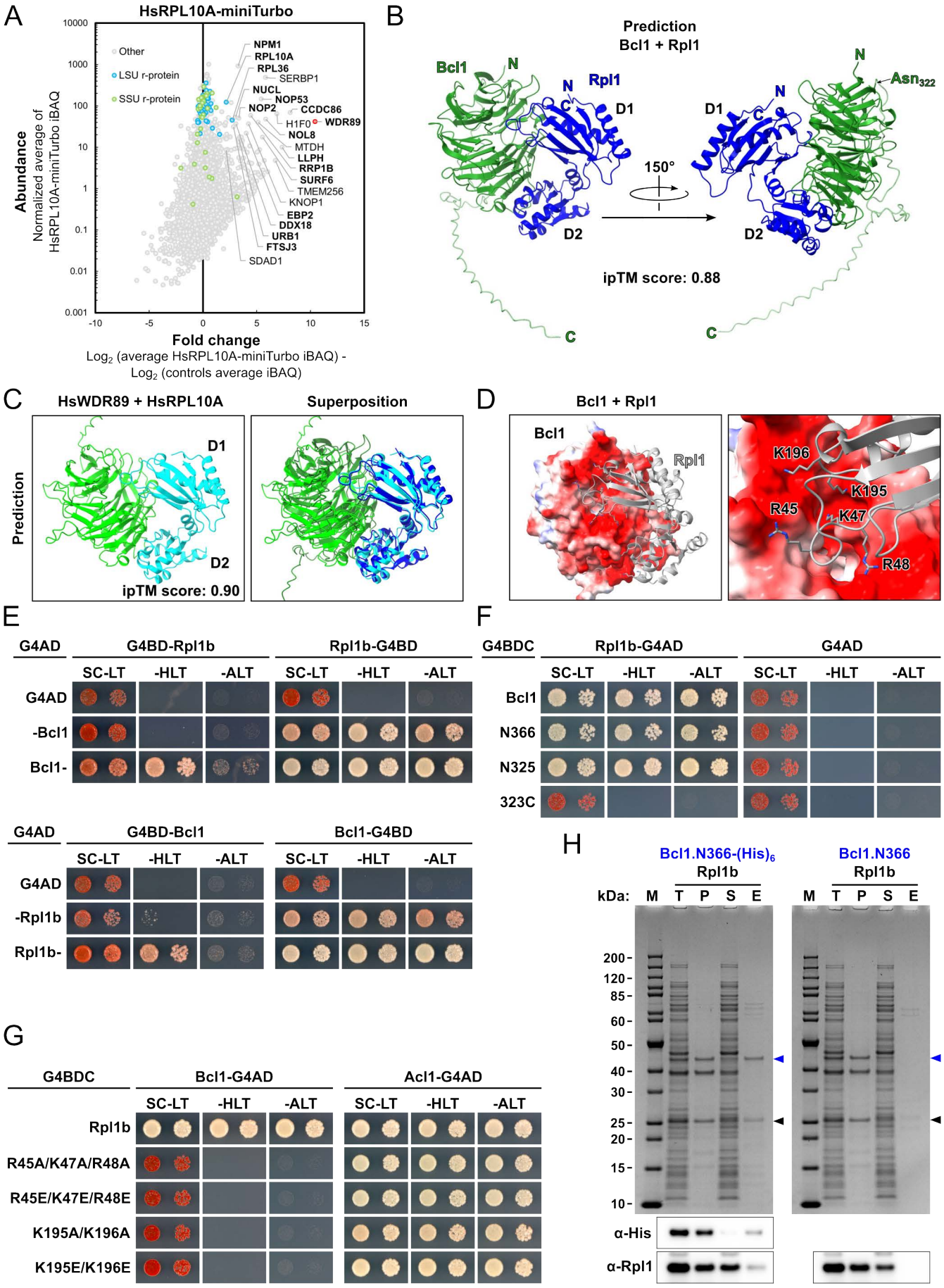
A
HsRPL10A-miniTurbo
Other
LSU r-protein
SSU r-protein
NPM1
RPL10A
RPL36
SERBP1
NUCL
NOP53
NOP2
CCDC86
H1F0
WDR89
NOL8
MTDH
LLPH
RRP1B
SURF6
TMEM256
KNOP1
EBP2
DDX18
URB1
FTSJ3
SDAD1
Abundance
Normalized average of HsRPL10A-miniTurbo iBAQ
Fold change
Log2 (average HsRPL10A-miniTurbo iBAQ) - Log2 (controls average iBAQ)
B
Prediction
Bcl1 + Rpl1
Bcl1
Rpl1
N
C
D1
D2
150°
Asn322
ipTM score: 0.88
C
HsWDR89 + HsRPL10A
Superposition
Prediction
D1
D2
ipTM score: 0.90
D
Bcl1 + Rpl1
Bcl1
Rpl1
K196
K195
R45
K47
R48
E
G4AD
G4BD-Rpl1b
Rpl1b-G4BD
SC-LT
-HLT
-ALT
G4AD
-Bcl1
Bcl1-
G4AD
G4BD-Bcl1
Bcl1-G4BD
-Rpl1b
Rpl1b-
F
G4BDC
Rpl1b-G4AD
G4AD
Bcl1
N366
N325
323C
H
Bcl1.N366-(His)6
Rpl1b
Bcl1.N366
kDa:
M
T
P
S
E
200
120
85
60
50
40
30
25
20
15
10
α-His
α-Rpl1
G
G4BDC
Bcl1-G4AD
Acl1-G4AD
Rpl1b
R45A/K47A/R48A
R45E/K47E/R48E
K195A/K196A
K195E/K196E

Figure 8

A

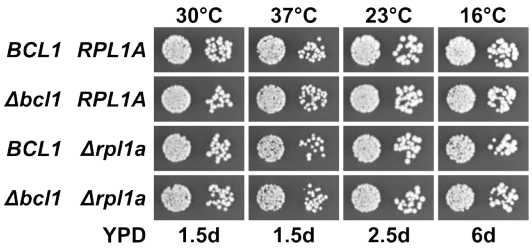

B

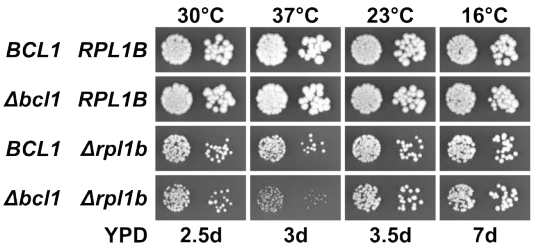

C

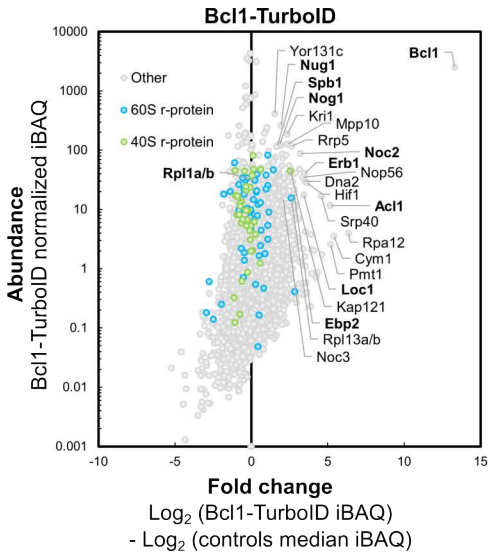

D

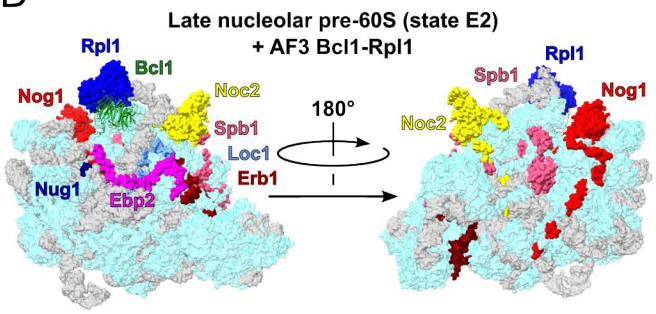

E

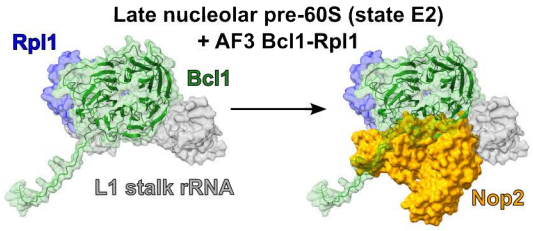

F

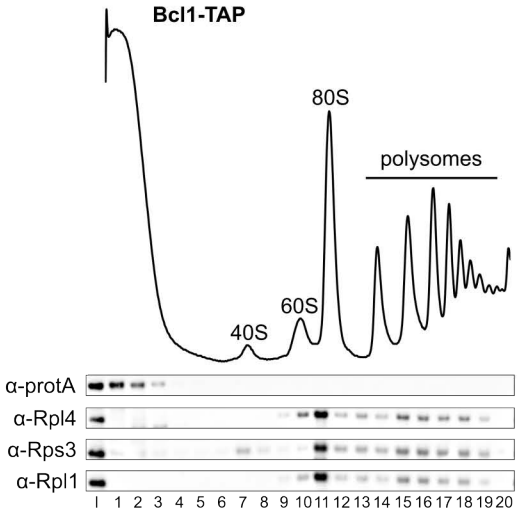

G

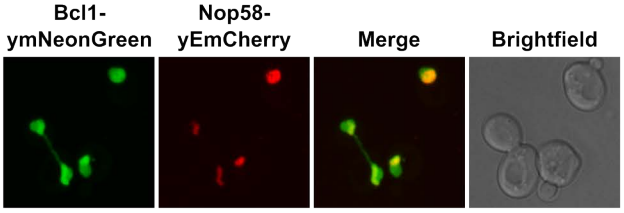

Figure 9

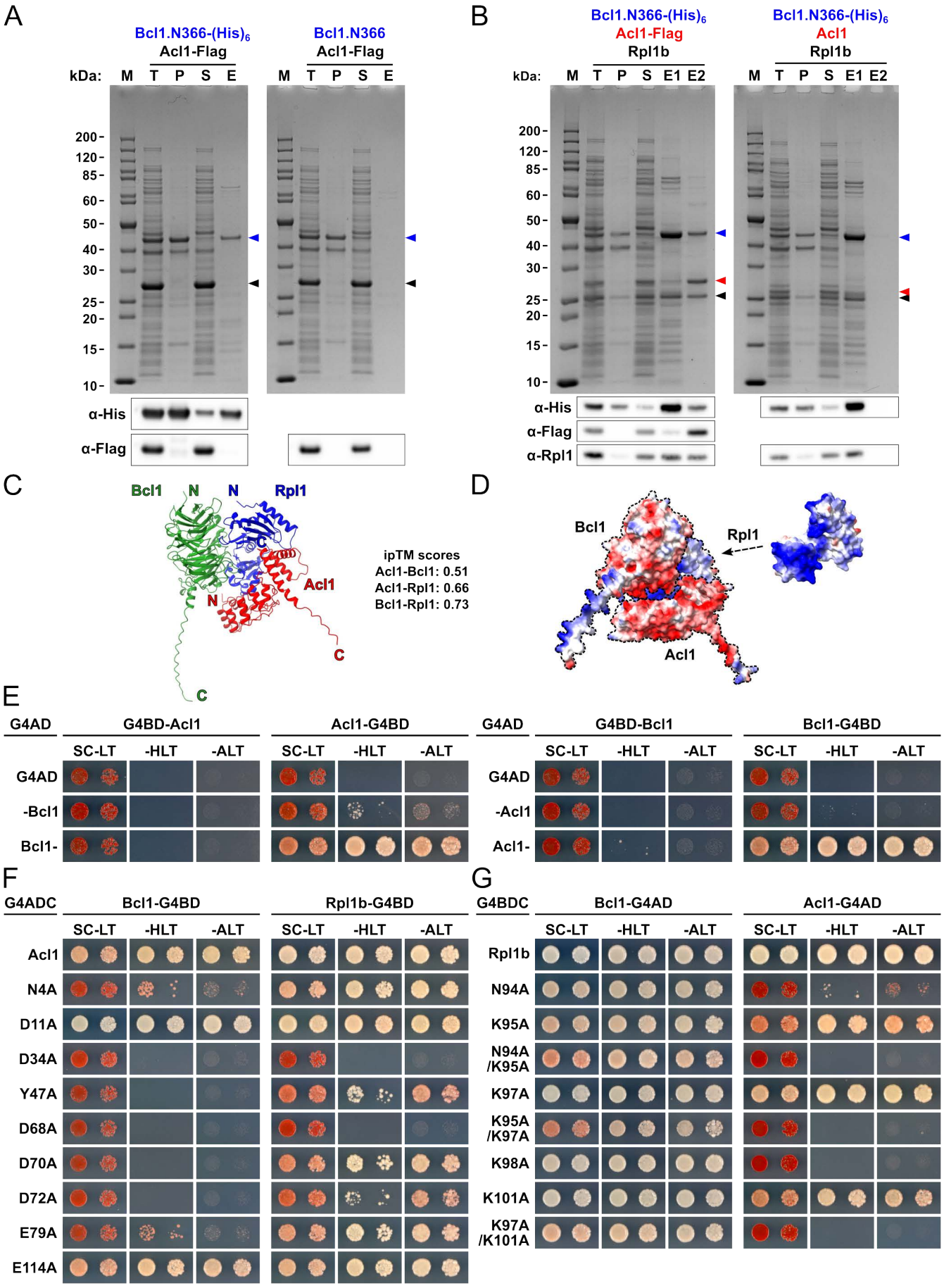
A
Bcl1.N366-(His)6
Acl1-Flag
Bcl1.N366
Acl1-Flag
kDa:
M T P S E
200
120
85
60
50
40
30
25
20
15
10
α-His
α-Flag
B
Bcl1.N366-(His)6
Acl1-Flag
Rpl1b
Bcl1.N366-(His)6
Acl1
Rpl1b
M T P S E1 E2
α-His
α-Flag
α-Rpl1
C
Bcl1
N
N
Rpl1
C
Acl1
N
C
ipTM scores
Acl1-Bcl1: 0.51
Acl1-Rpl1: 0.66
Bcl1-Rpl1: 0.73
D
Bcl1
Rpl1
Acl1
E
G4AD
G4BD-Acl1
Acl1-G4BD
G4AD
G4BD-Bcl1
Bcl1-G4BD
SC-LT
-HLT
-ALT
G4AD
-Bcl1
Bcl1-
-Acl1
Acl1-
F
G4ADC
Bcl1-G4BD
Rpl1b-G4BD
Acl1
N4A
D11A
D34A
Y47A
D68A
D70A
D72A
E79A
E114A
G
G4BDC
Bcl1-G4AD
Acl1-G4AD
Rpl1b
N94A
K95A
N94A /K95A
K97A
K95A /K97A
K98A
K101A
K97A /K101A

Figure 10

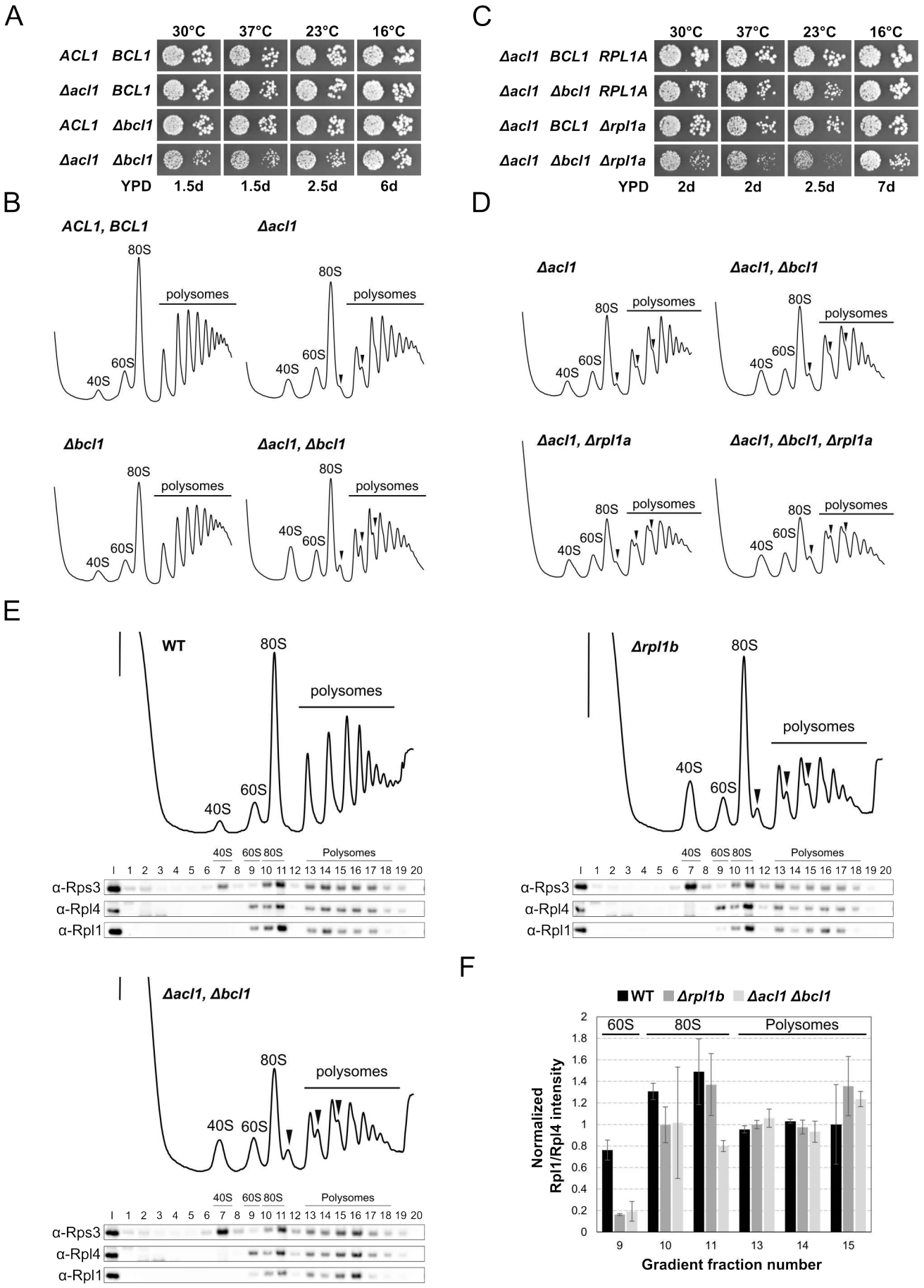
A
30°C
37°C
23°C
16°C
ACL1 BCL1
Δacl1 BCL1
ACL1 Δbcl1
Δacl1 Δbcl1
YPD 1.5d 1.5d 2.5d 6d
C
Δacl1 BCL1 RPL1A
Δacl1 Δbcl1 RPL1A
Δacl1 BCL1 Δrpl1a
Δacl1 Δbcl1 Δrpl1a
YPD 2d 2d 2.5d 7d
B
ACL1, BCL1
Δacl1
Δbcl1
Δacl1, Δbcl1
80S
60S
40S
polysomes
D
Δacl1
Δacl1, Δbcl1
Δacl1, Δrpl1a
Δacl1, Δbcl1, Δrpl1a
E
WT
Δrpl1b
Δacl1, Δbcl1
40S 60S 80S Polysomes
I 1 2 3 4 5 6 7 8 9 10 11 12 13 14 15 16 17 18 19 20
α-Rps3
α-Rpl4
α-Rpl1
F
WT Δrpl1b Δacl1 Δbcl1
60S 80S Polysomes
Normalized Rpl1/Rpl4 intensity
Gradient fraction number

Figure 11

A

Acl1 205 GQGSMAGSGDEPDSKRRK 222

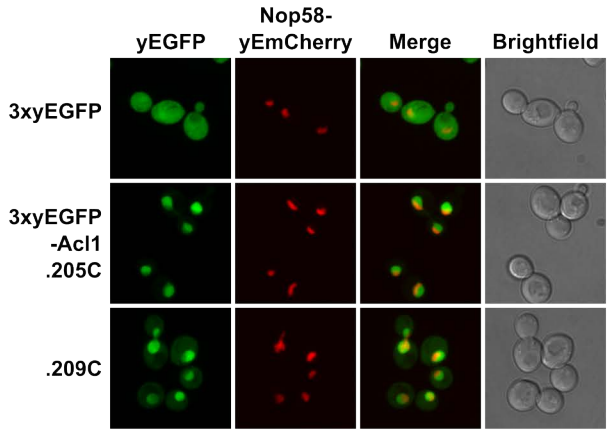

B

```
Bcl1 364    SVSTRPRKEKHKKAKKHSMKSRFKPY    389
Hrp1 504 NHRSGGNHRRNGRGGRGGYNRRNNGYHPYNR  534
Syo1   1            MGRSKKRSRASSSRLNPLRKA  21
```

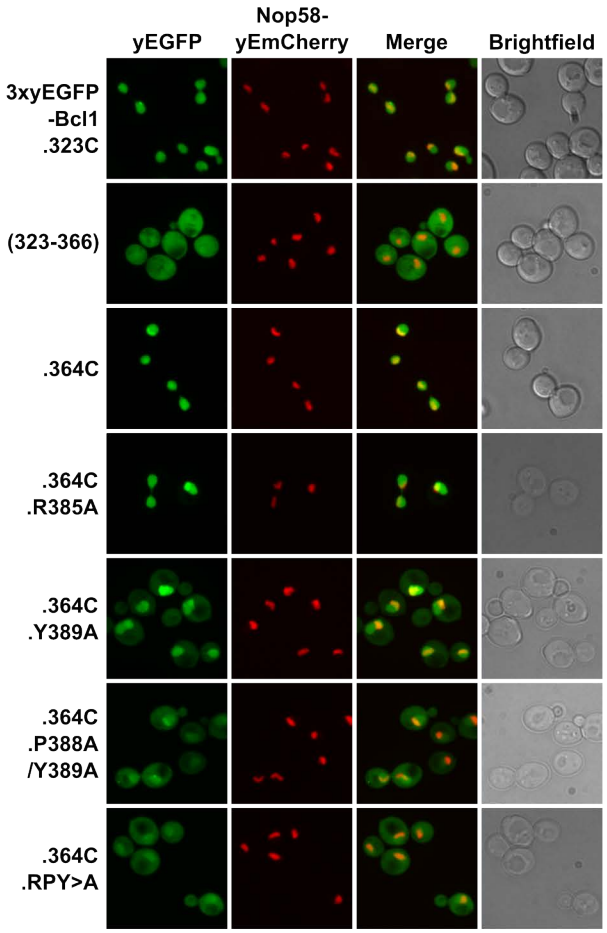

C

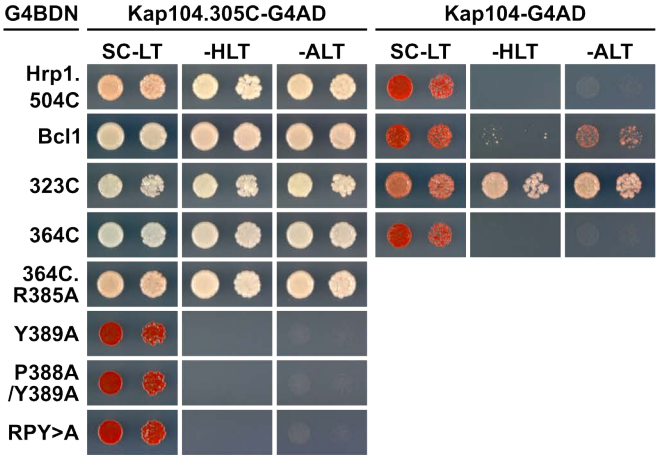

D

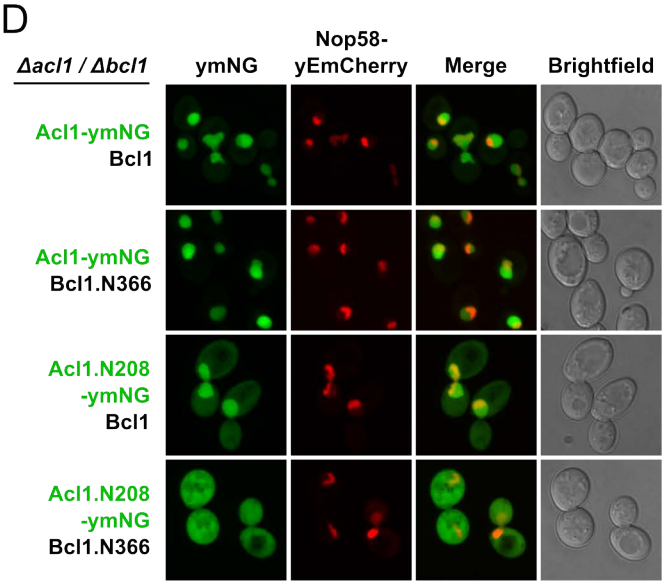

E

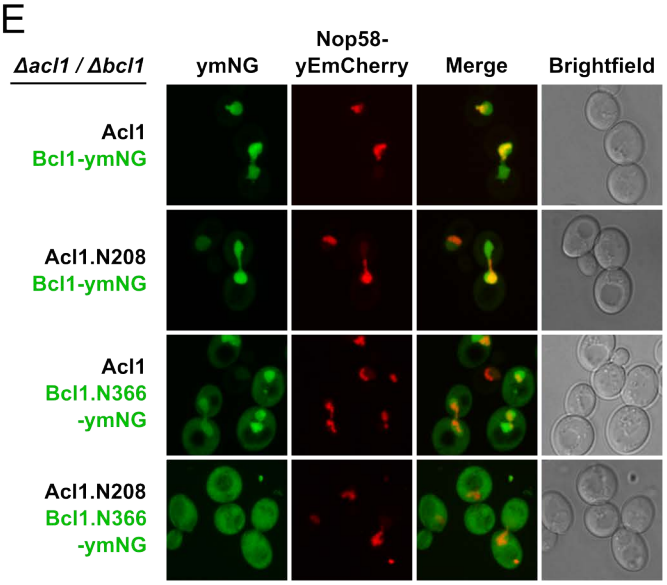

Figure 12

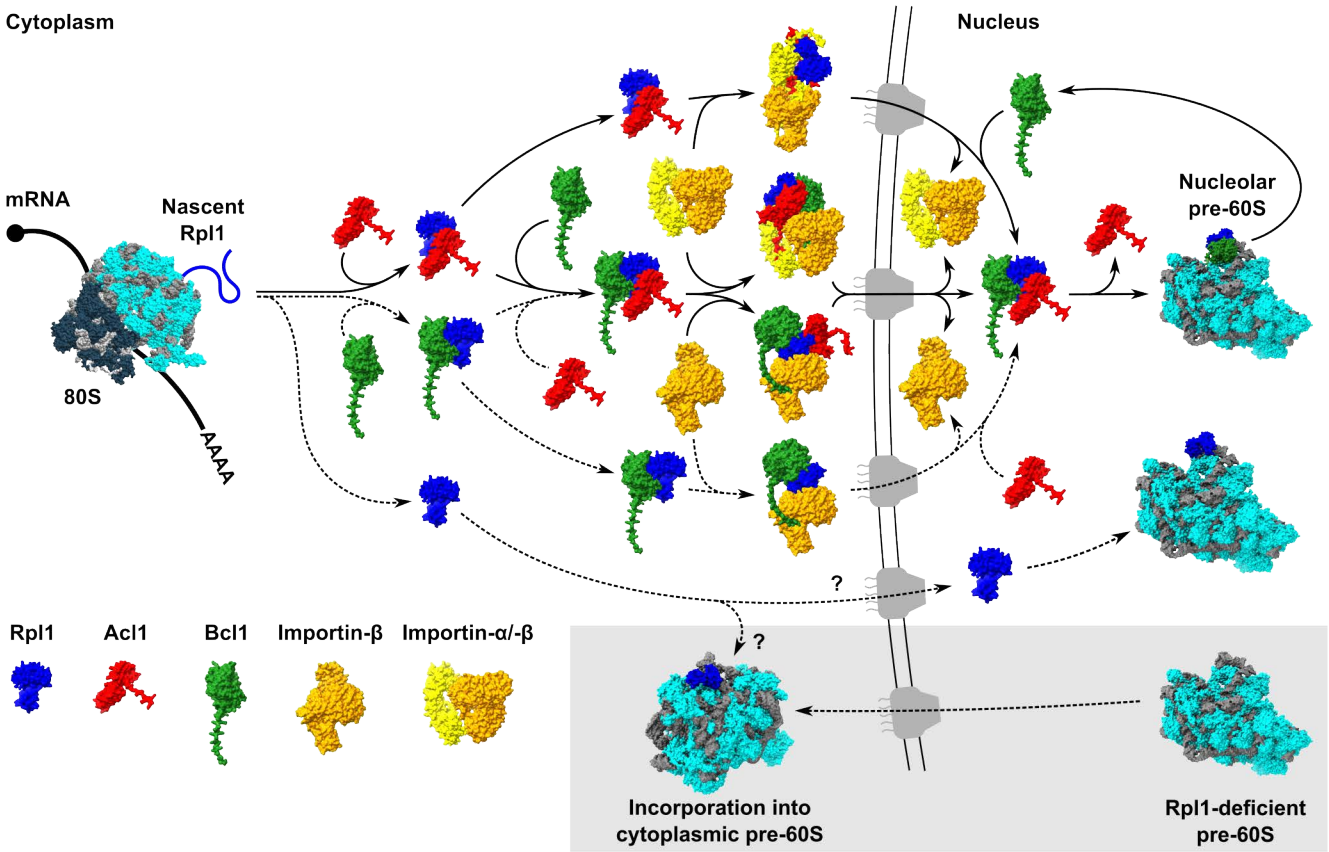
Cytoplasm
Nucleus
mRNA
Nascent
Rpl1
80S
AAAA
Nucleolar
pre-60S
?
?
Rpl1
Acl1
Bcl1
Importin-β
Importin-α/-β
Incorporation into
cytoplasmic pre-60S
Rpl1-deficient
pre-60S

Supplementary Figure S1 - Page 1/5

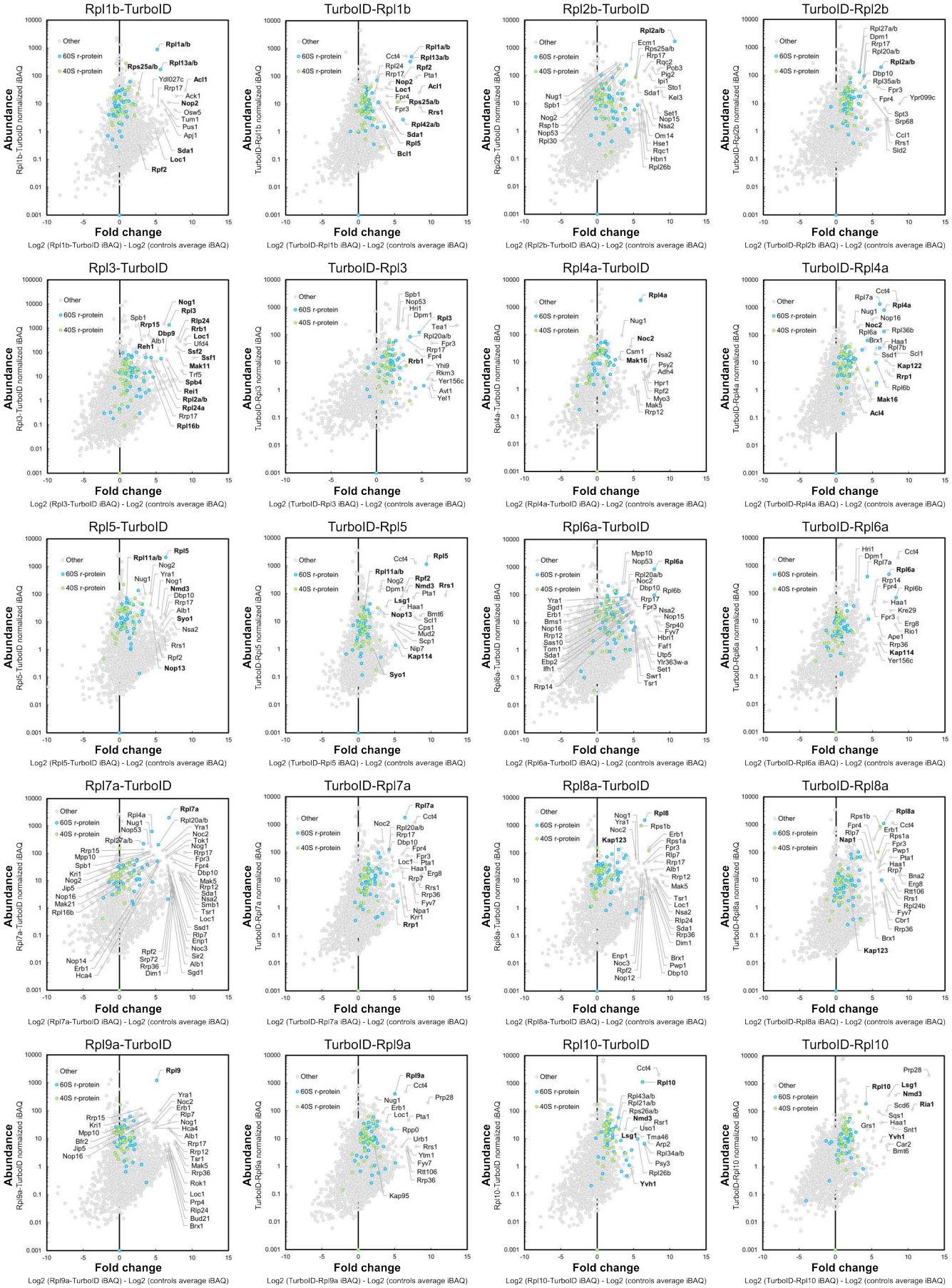

Supplementary Figure S1 - Page 2/5

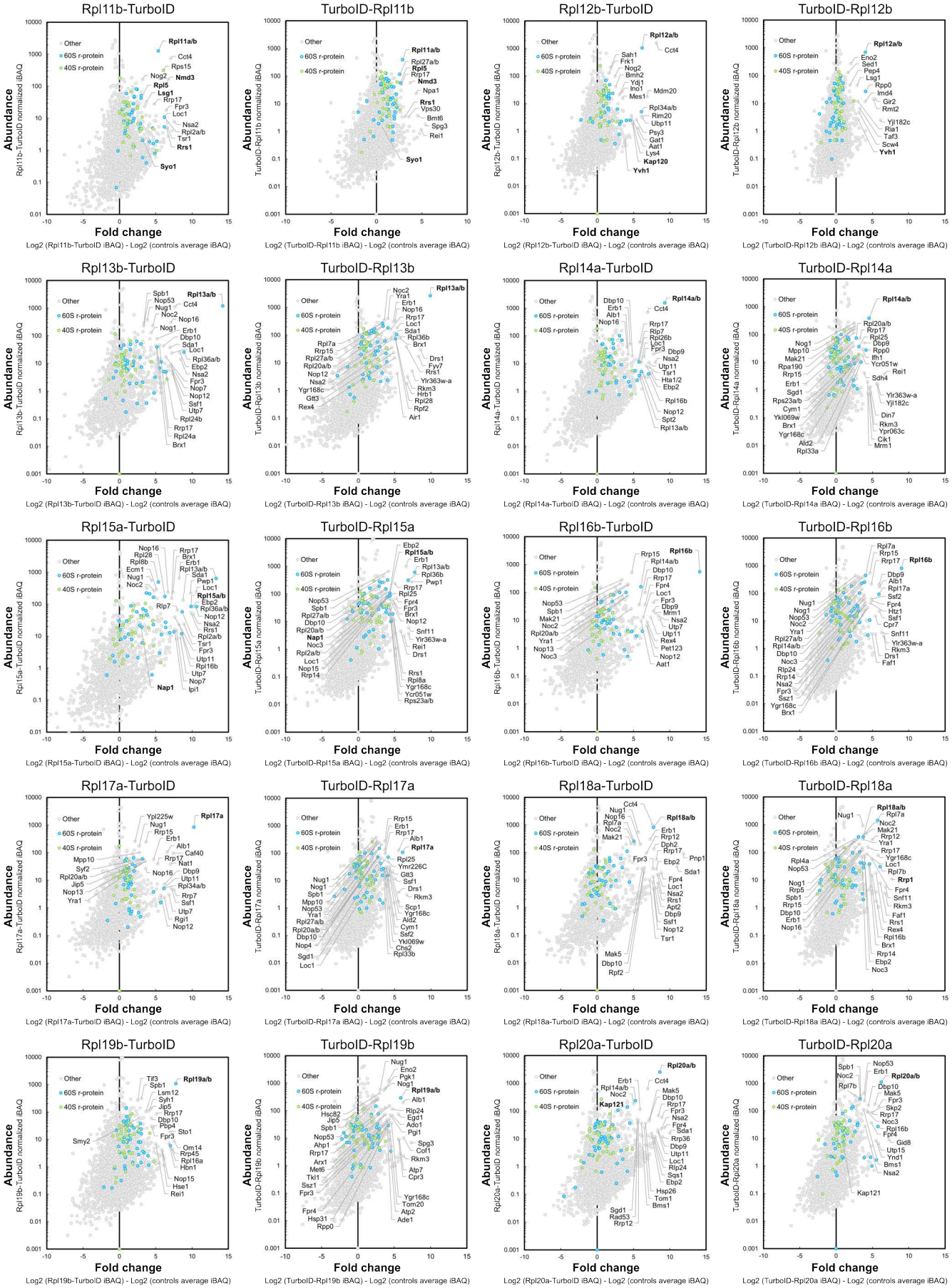

Supplementary Figure S1 - Page 3/5

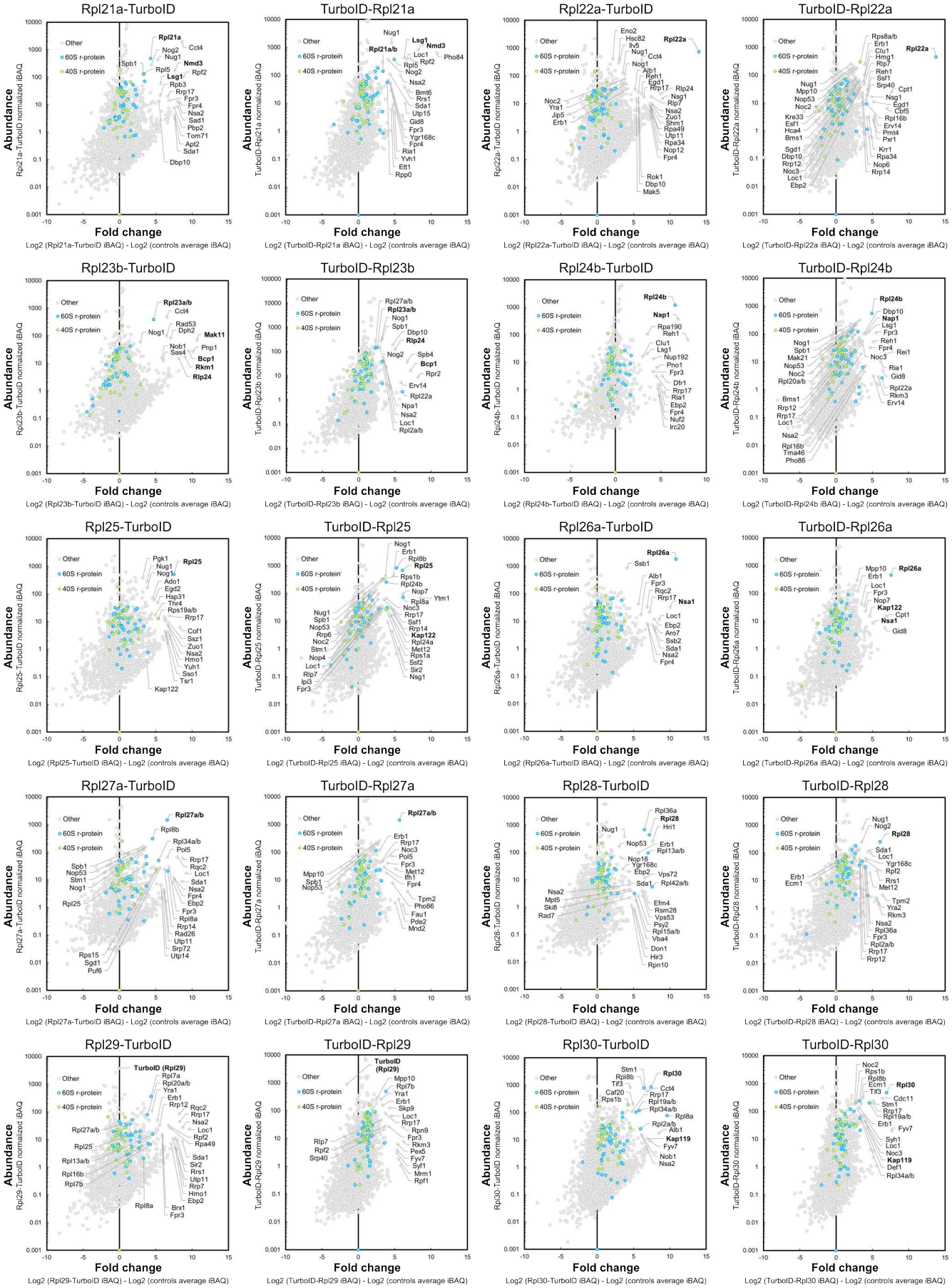

Supplementary Figure S1 - Page 4/5

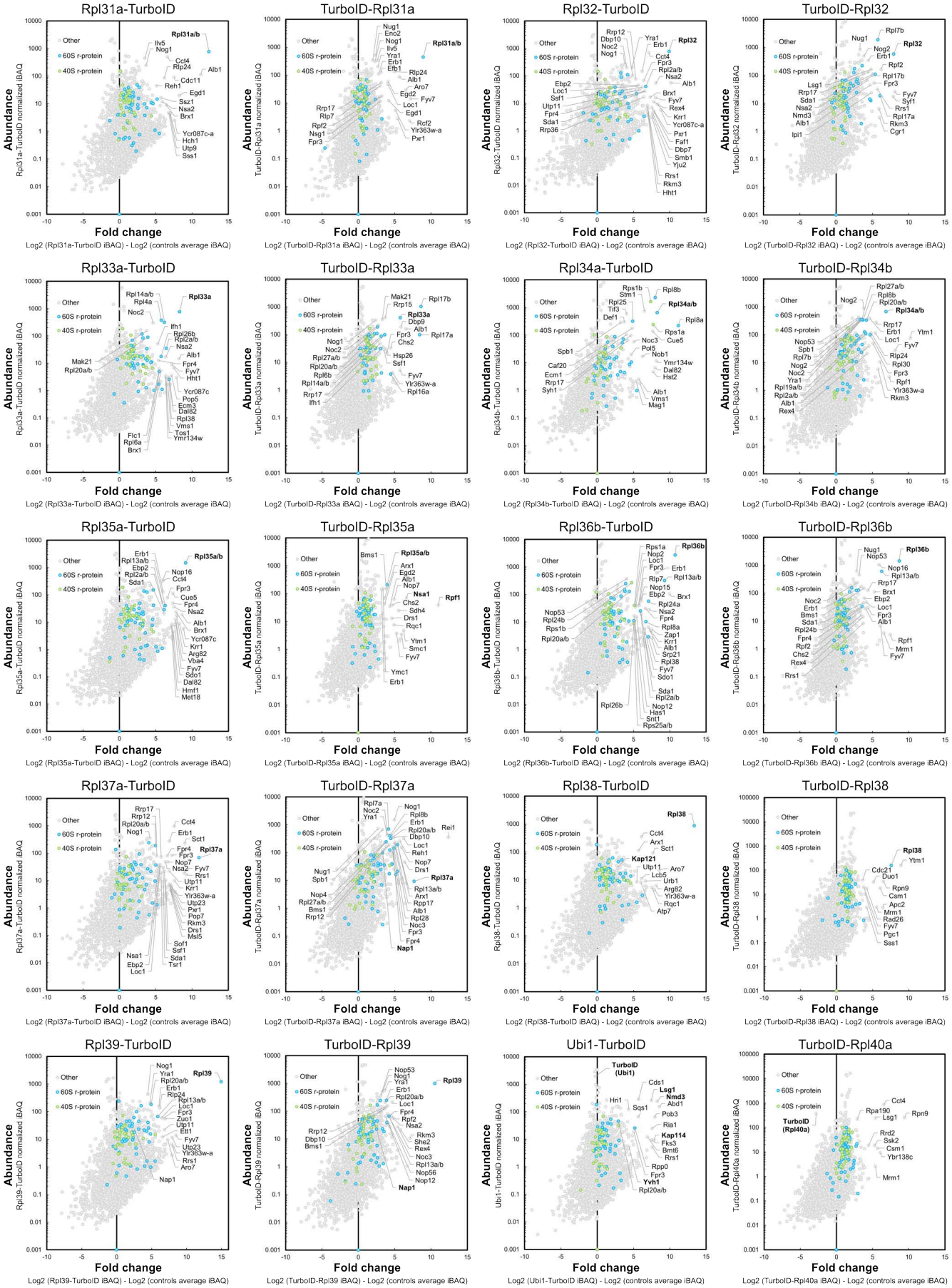

Supplementary Figure S1 - Page 5/5

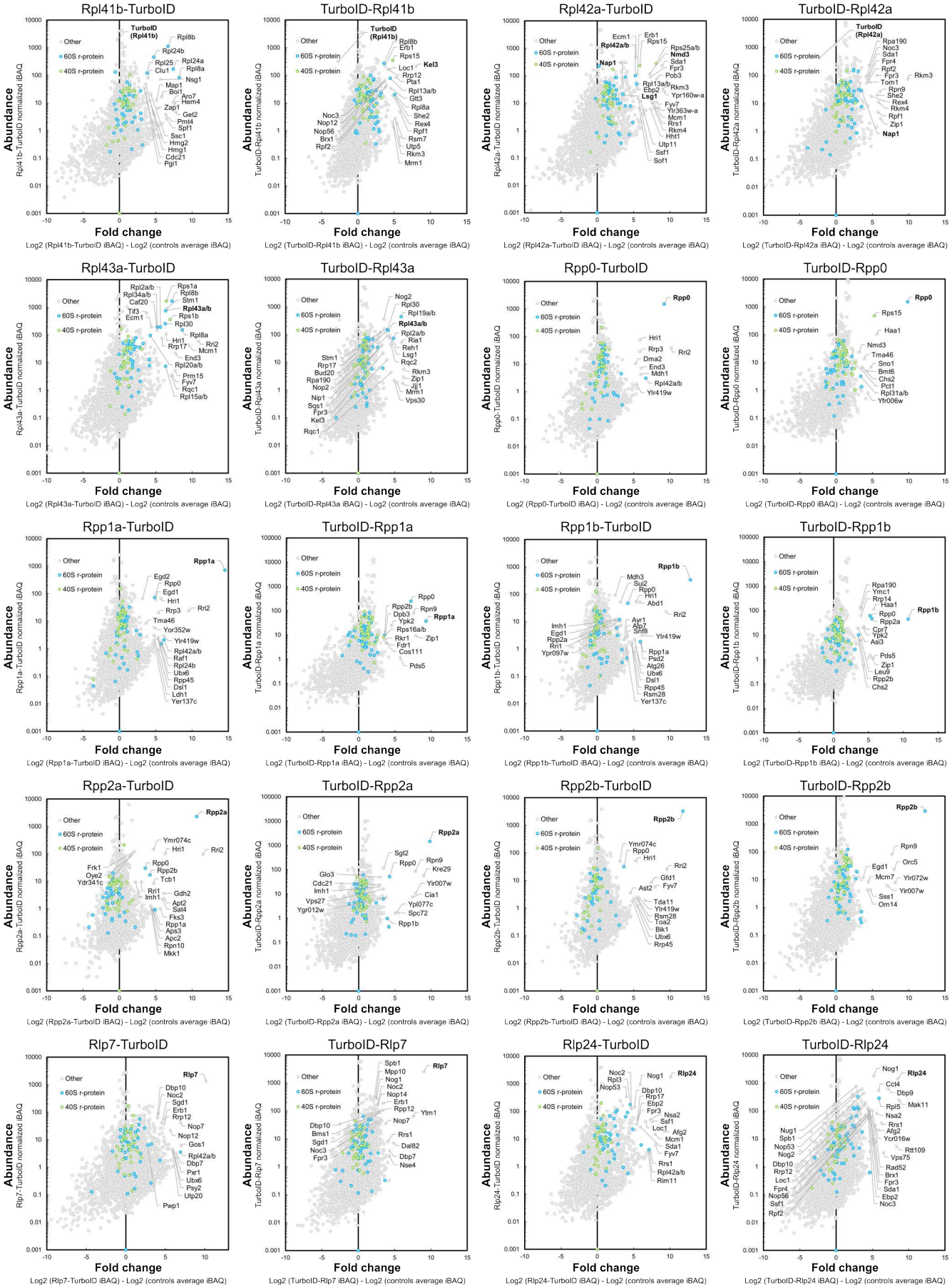

Supplementary Figure S2

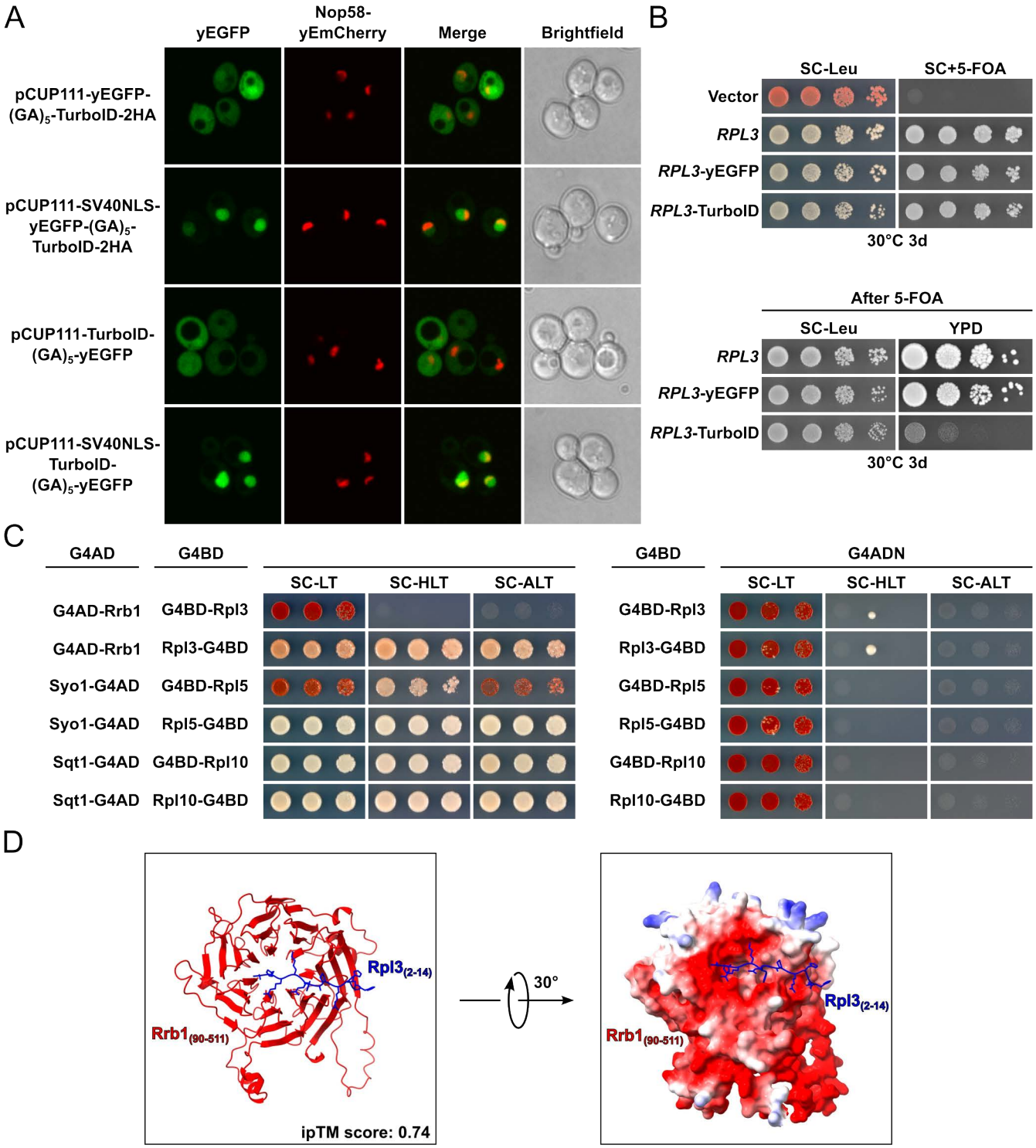

Supplementary Figure S3 - Page 1/2

Supplementary Figure S3 - Page 2/2

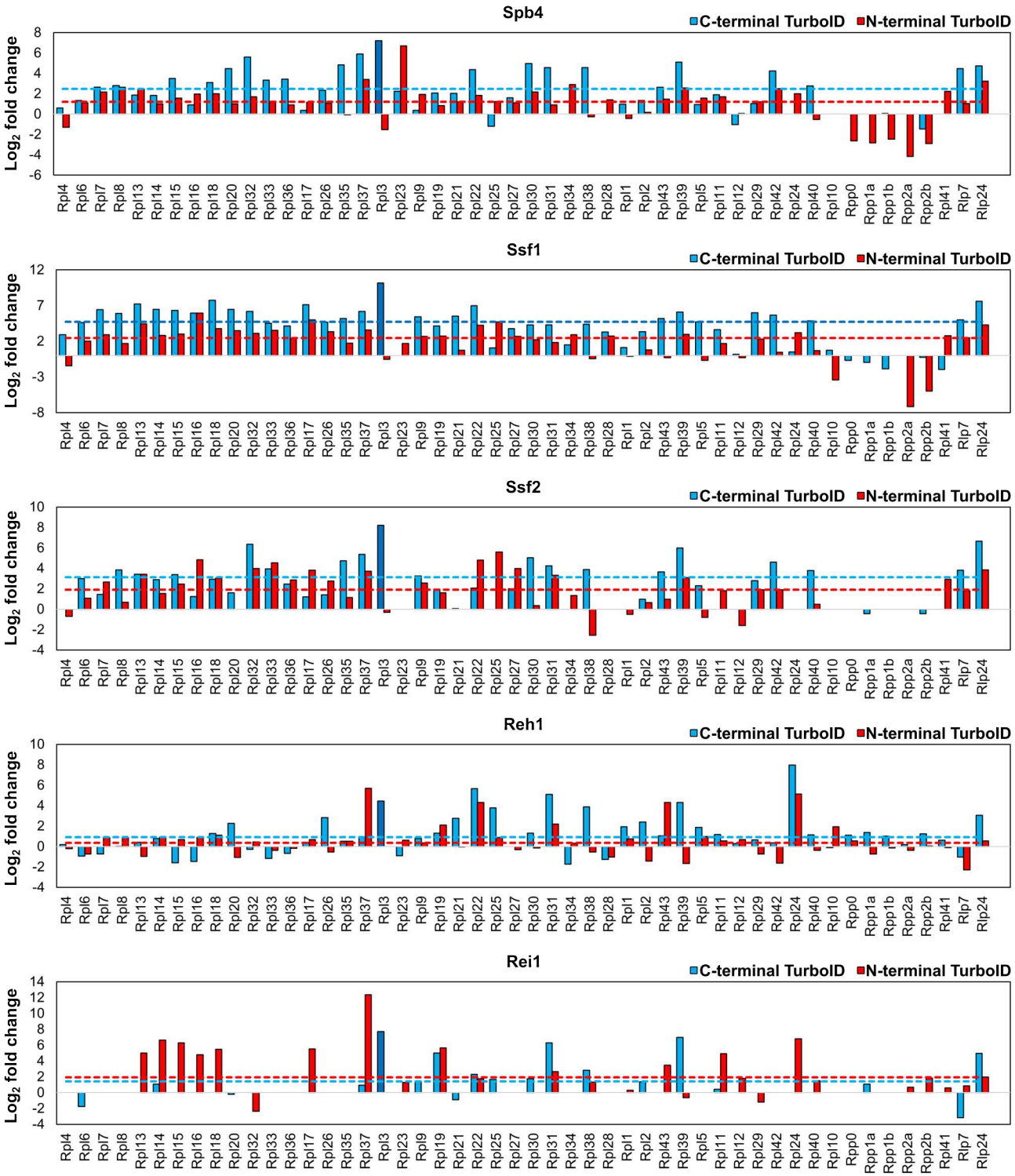

Supplementary Figure S4

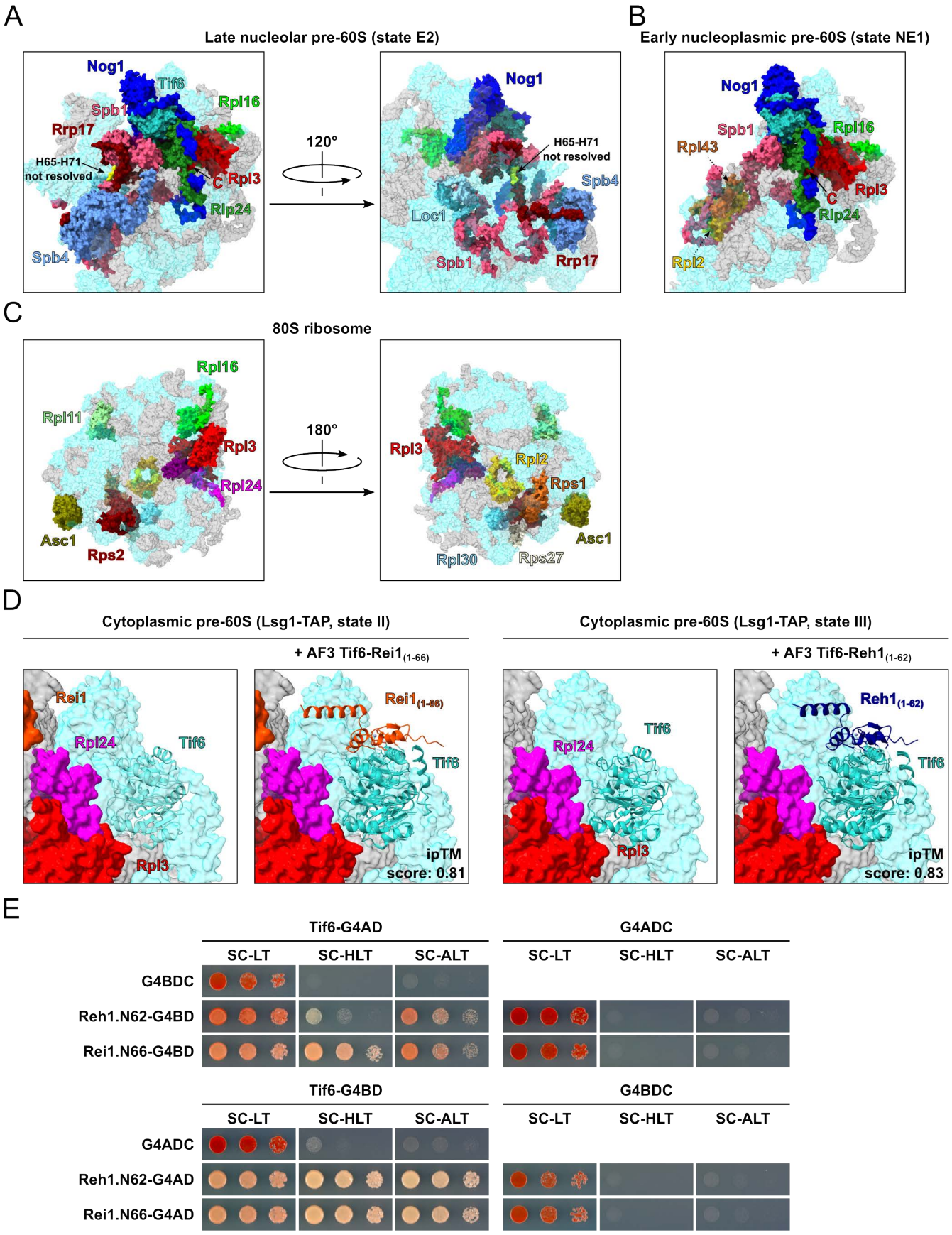

Supplementary Figure S5

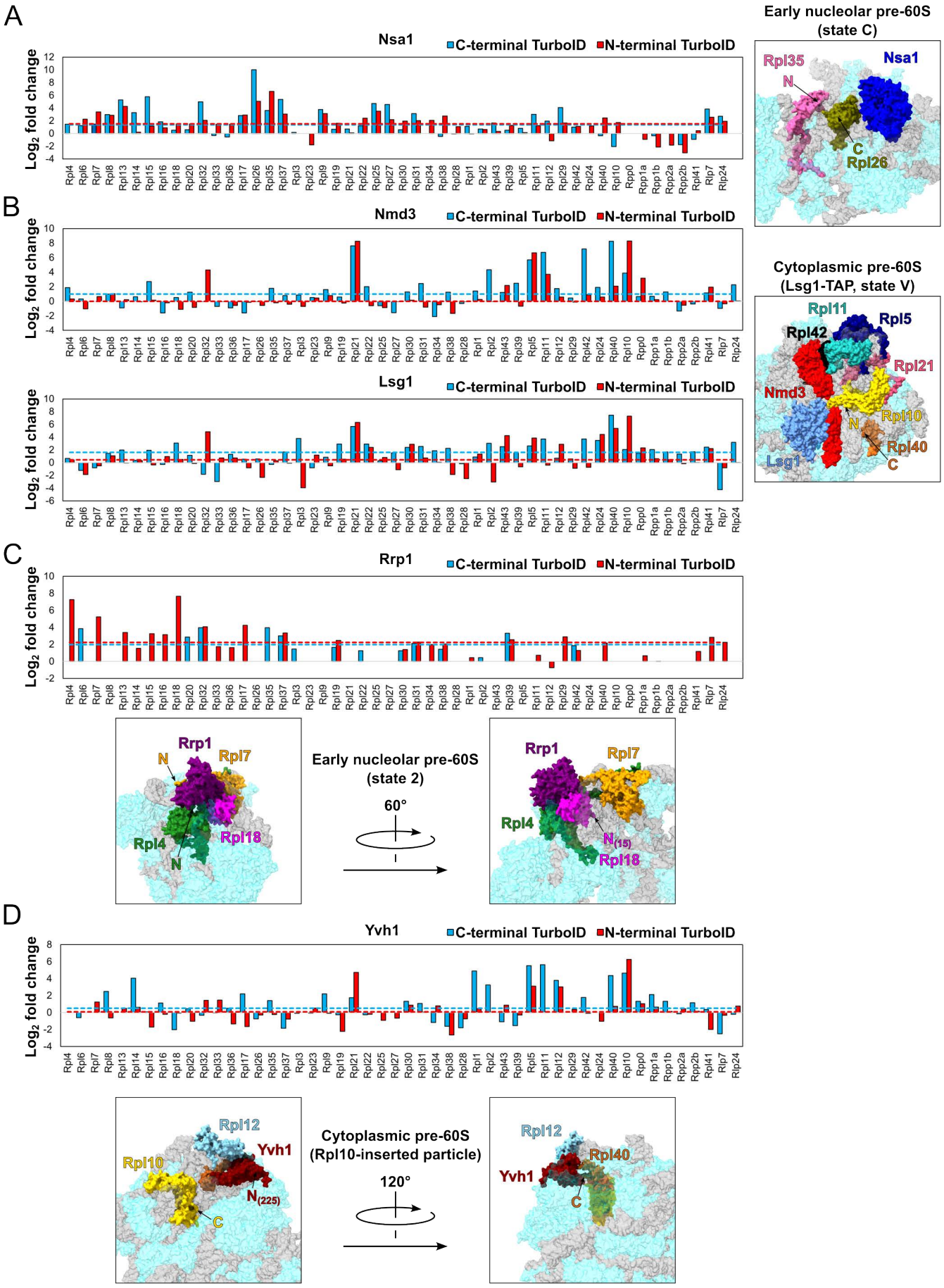

Supplementary Figure S6

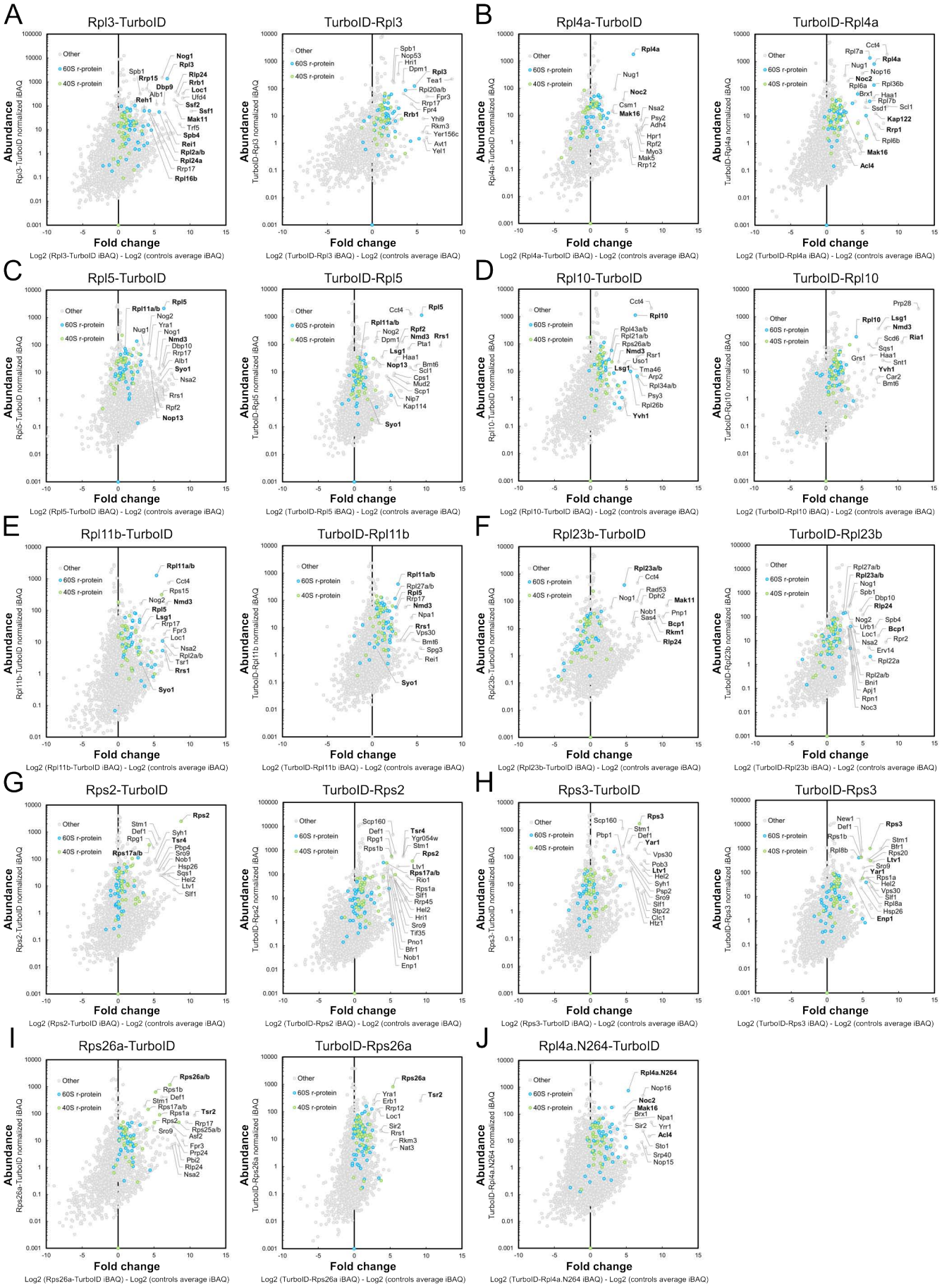

Supplementary Figure S7

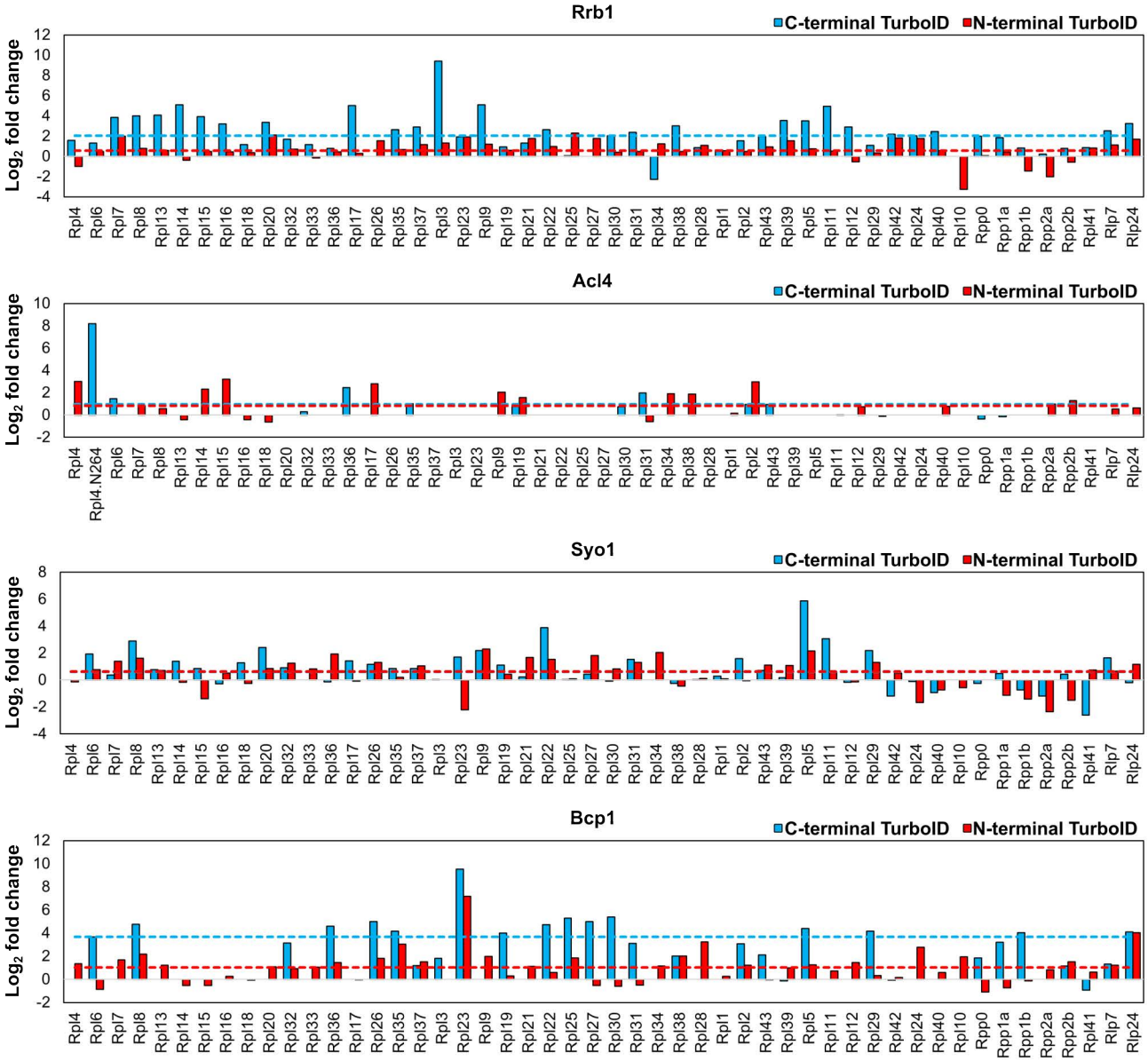

Supplementary Figure S8

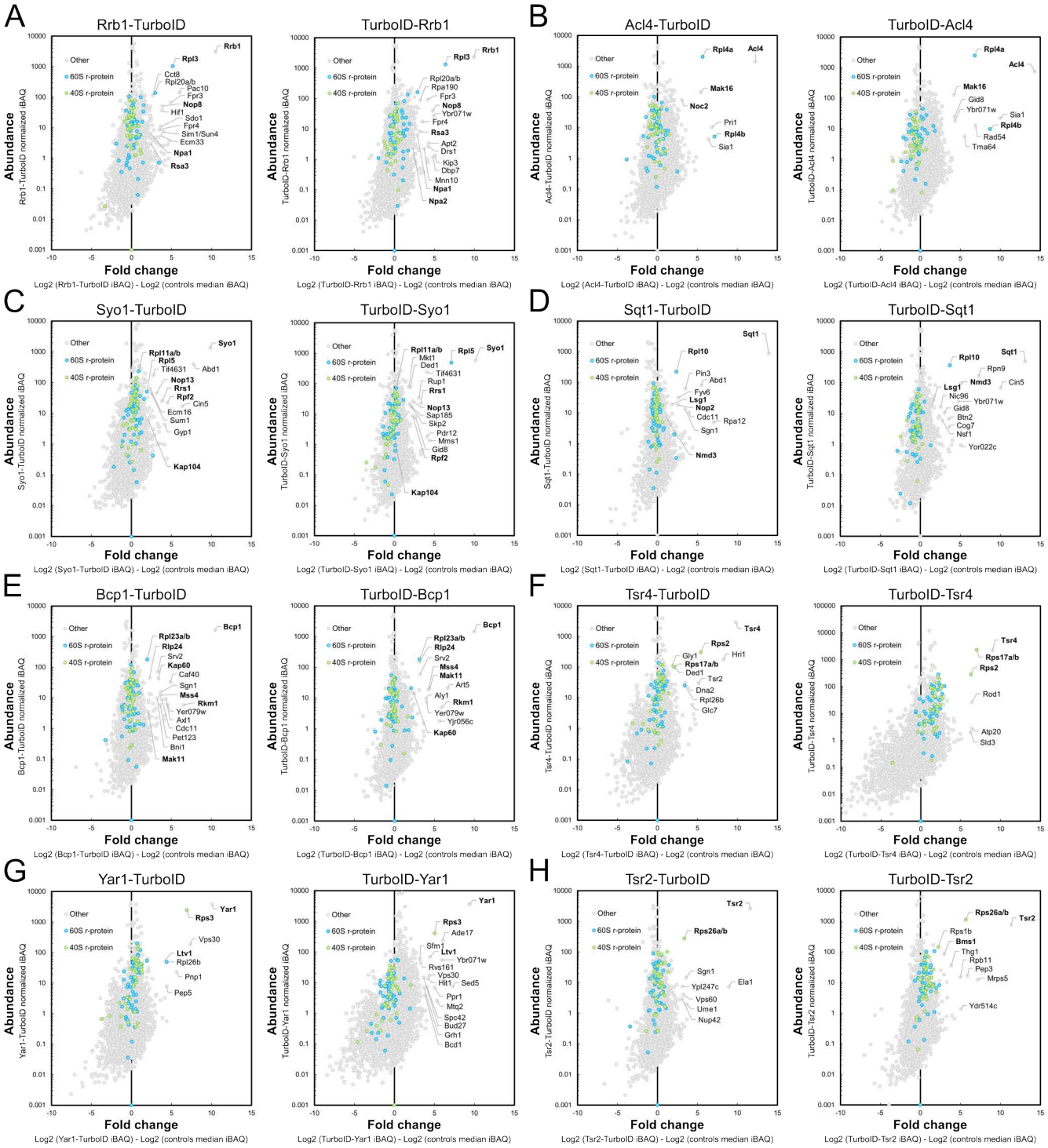

Supplementary Figure S9

A

Prediction of the Bcp1-Kap60-Kap95 interaction

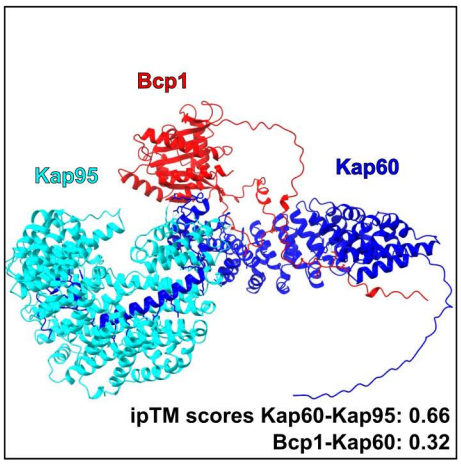

Prediction of the Bcp1-Mss4 interaction

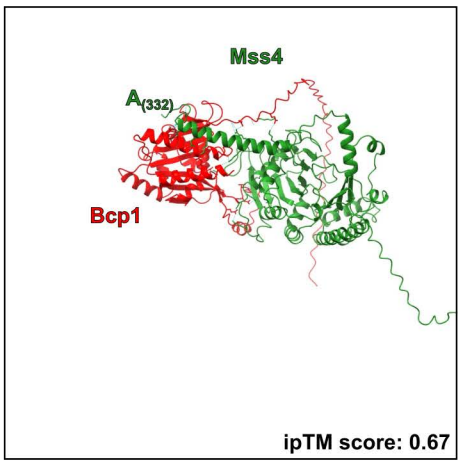

Kap60-interacting regions of Bcp1

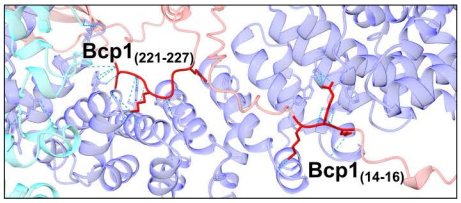

Kap60-interacting regions of Bcp1 and Mss4 NLS region

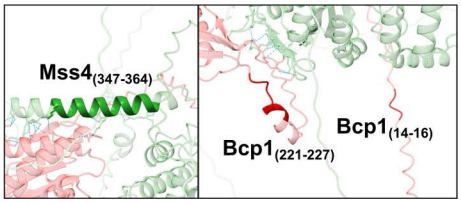

B

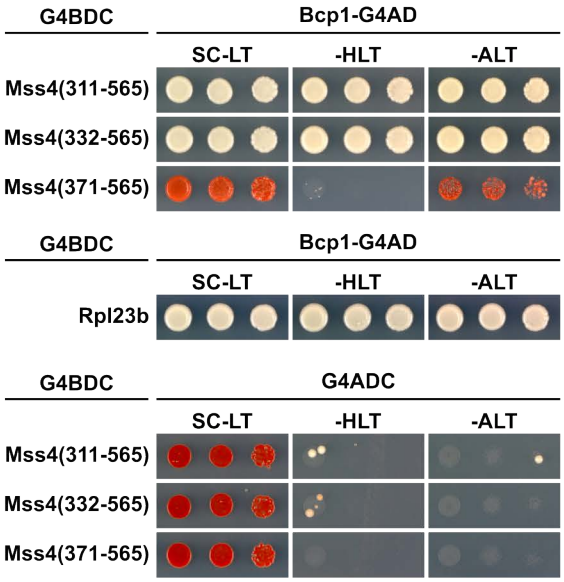

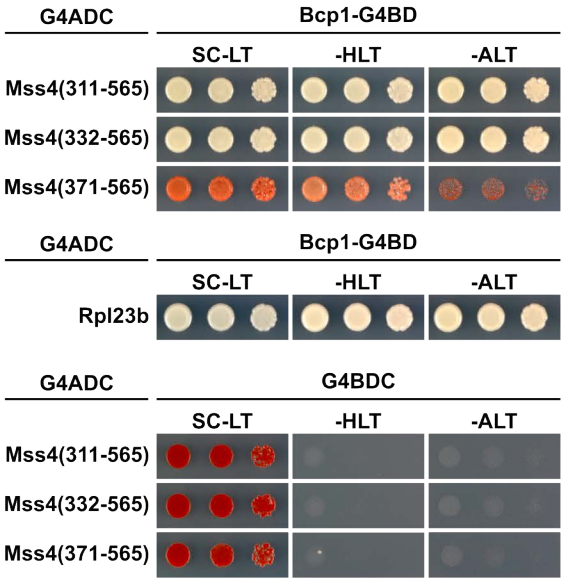

C

Bcp1-Mss4 complex

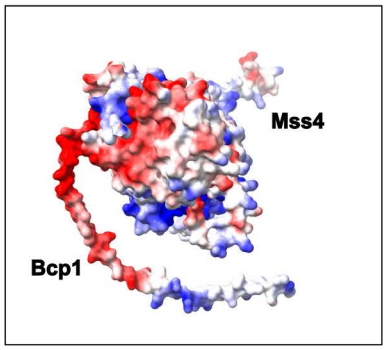

Bcp1-interacting Mss4 surface

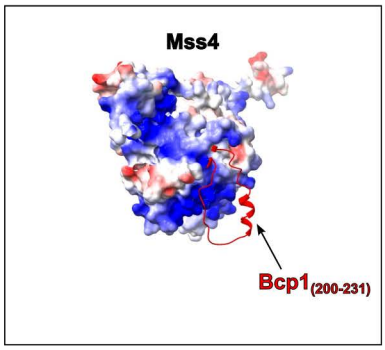

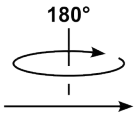

Mss4-interacting Bcp1 surface

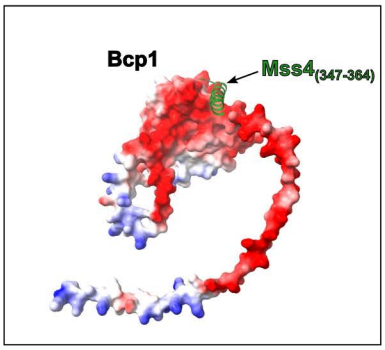

Supplementary Figure S10

A

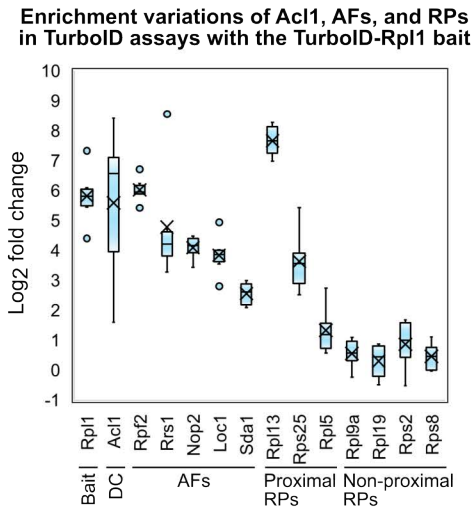

B

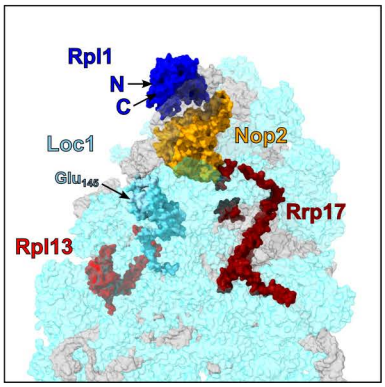

C

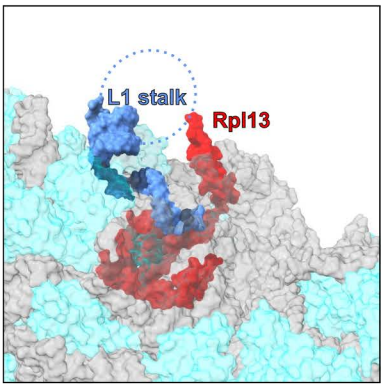

D

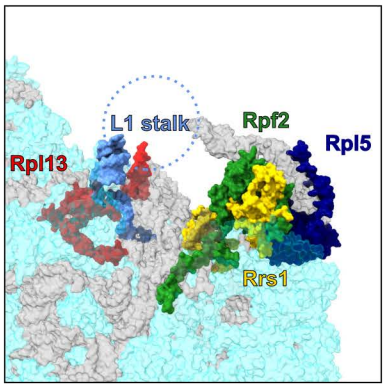

E

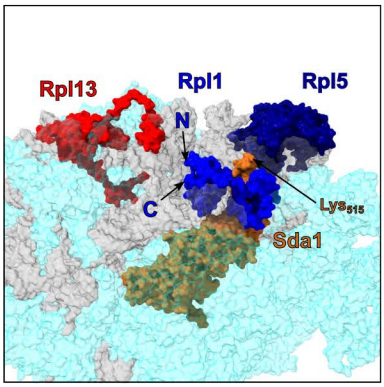

F

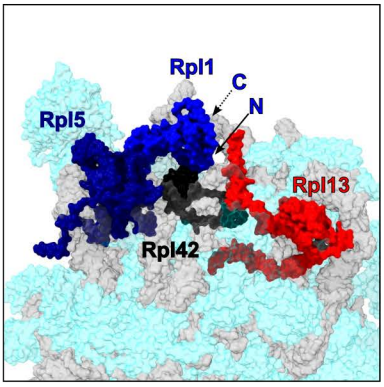

G

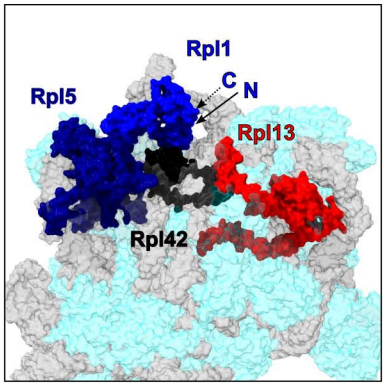

H

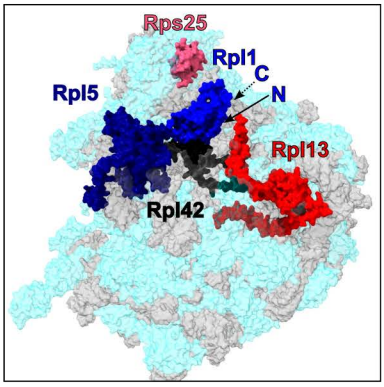

Supplementary Figure S11

```
                                                                                                                D70
                                N4     D11                         D34          Y47                        D68 D72    E79       E114
Fungi
  Dikarya
    Ascomycota
      Saccharo-mycotina
        S.cer.   3 ANIWVAASDGNLDRVEHILRE-SK---GAMTPQSKDINGYTPMHAAAAYGHLDLLKKMCN-EYN----GDINVLDNDGDTPLHHVED-[x]32-GED 115
        K.afr.   1 MNIWVAASDGRQELVEKFLNE-NP----SLSANTKDPNGYTPVHAAAAYGHHDLLRKLCS-EYN----GDVNIRDADGDTPLHHCED-[x]32-GEF 112
        N.dai.   1 MNIWIAASDGKTGIVRQILTTPNT----TFTANSKDPNGYTPIHAAAAYGHIDLLRSLCS-EFG----GDINIRDNDGDTPLHHCED-[x]32-GES 113
        C.gla.   1 MNIWIAASDGRGDIVEKFLAD-------GLSANSKDPNGYTPVHAAAAYGHLDLLRKLCQ-EHG----GDINVRDSDGDTPLHHCED-[x]32-AEF 110
        T.pha.   1 MNIWIAASDGRIDLVEKFLNS-NT----GVTVNSKDENGYTPVHAAAAYGHNDLLRKLCN-EYN----GDINIRDFDGDTPLHHVED-[x]32-SEF 112
        V.pol.   1 MNIWVAASDGDVAVVEKYLNS-GN----GLTANSKDPNGYTPVHAAAAYGHIGLLEKLCK-EYG----GDINVRDSDGDTPLHHVED-[x]32-SEF 112
        Z.rou.   1 MNVWIAASDGRTSVVEKLLQE-NY----QRDGNVKDPNGYTPVHAAAAYGHIELLRKLCQ-EYG----GNINVKDSDGDTPLHHCED-[x]32-GEF 112
        Z.mra.   1 MNIWIAASDGKQEVVEQLLAQ-GS----GIDSNVKDPNGYTPVHAAAAYGHIELLKKLCK-DYN----GDINVRDGDGDTPLHHCED-[x]32-GEF 112
        T.del.   1 MNIWTAASDGREDVVEQLLAQ-NN----GLNANSKDPNGYTSVHAAAAYGHIELLKKLCK-QYN----GDINIRDNDGDTPLHHCED-[x]32-AEF 112
        L.the.   1 MNIWIAASDGRAELVEKFLSE-------GFTAESKDPNGYTPIHAAASYGHIDLLRELCSAPYS----GSVNVRDNDGDTPLHHCED-[x]32-GEF 111
        K.lac.   1 MNIWIAASNGETELVEKFIKQ-------GQTANDKDENGYTPIHAAAAYGHIDLLKKLVQ-EHN----GDVNIKDSDNDTPLHHCED-[x]32-CDD 110
        E.cym.   1 MNIWVAASDGLTETVEKLLQQ-QP----GLTANSKDPNGYTAVHGAASYGHVDLLRLLVN-KYH----GDINVRDNDGDTPLHHTED-[x]32-QES 112
        K.pha.   4 ANIWVAASDGELAKVQNWVEK--H----GLSPNEKDPNGYTPIHAAAAYGHKELIRYLI--EKG----ADINIQDQDGDTPLHHVES-[x]32-DEF 113
        D.han.   3 SNIWVAAADNQVKIVESYLDG--G----DFTPNSKDPNGYTPIHAAASYGHIGLLKLLI--KRG----GDINVQDSEGDAPLHHVED-[x]32-DEF 112
        C.alb.   3 SNIWIAAADNQRQIVEQYINS--N----EYTPNSKDPNGYTAIHAAASYGHLNLLQYLI--EKG----GDINIQDNEGDTPLHHVED-[x]32-DEF 112
        Y.lip.   1 MNIWVAASDGQLDVVKNFIEN--D----GLSPNAKDENGYTPVHAAASYGHMDLLRYLI--DKG----GDINVTDEDGDTALHTVEE-[x]32-DEF 110
                     *:* **::.    *.  :             : ** ****.:*.**:***  *:. :          ..:*: * :.*:.**  *.        :
      Pezizomycotina
        A.nid.   4 PNPYILAADNPSA-VLALLRS-NP---SI--ASNQDEHGYSLLHAAASYGHIDLLRALVK-EFN----VDVNLLDEDGETCLFVTEN-[x]32-GSF 113
        P.rub.   3 QNPYLLACDNPKA-LLDLLRS-NP---AI--ASSQDESGYSLLHAAASYGHADLLRALVK-EFN----VDVNLLDEDGETCLFVVED-[x]32-NEF 112
        N.cra.   3 NNPYLLAADNPEA-CIALLRE-NP---SL--ASGQDEHGYSLIHAAASYNHLDLLRTLVG-EFK----VPVDLKDEDGETALFVVET-[x]32-EDY 112
        C.the.   3 PNPYLLAADNPQA-LISLLRE-QP---QL--ASGQDEHGYSLVHAAASYNHLDLLRQLIR-EFK----VPVDLKDEDGETALFVVET-[x]32-GDF 112
        C.glo.   3 PNPYLLAADNPAA-LLALLHE-DP---AL--ASGQDEHGYSLVHAAASYNHLSLLRSLAR-EFK----VPIDLKDEDGETALFVVES-[x]32-GDW 112
      Taphrinomycotina
        S.pom.   6 PNIWIAASDGKTD-VV-LKHL-DS---GI-SPNAADENGYTPIHAAVSYGHSDLLKILV--ERG----GDINIRDQDGETPLFVCEK-[x]32-GEF 114
        S.jap.   6 PNVWVAASDGKID-VV-LKHL-EA---GV-SPNVLDENGYTPMHAAASYGHKELLKLLV--ERG----GNVNVCDNDGETPLFVCET-[x]32-GEF 114
                     * :: *.*.       : :  .        ..  *  **: :***.:*.* .**: :   *        ::: *:**:* *.  *        .
    Basidiomycota
        C.neo.   7 KNLWVAASDGDIERVKYLIEQ------ENCTANDKDANSYTPLHAAASYAHIDLLSYLLS--IG----GDPNLTDDDGETPLYVVEN-[x]30--DH 113
        U.may.  19 KNIWIAAGEGDLGRVKECVDG------EGISPVAADEFTYTPLHAAASYGHLDILRYLLN--HPSAPSDAVNTTDSDLDTPLFVCET-[x]32--EH 131
        P.str.  12 KNIWVAASDGDLERVKELIEA-------GLSPSVADENSYTPIHAAASWGRLEVLRYLKS--VG----GDMNTTDDEGDTPLFSVED-[x]30--DY 117
                     *:*:**.:*:: **:  :            :.   *   ***:****::.:::::*  : .         .  *  *.: :***.  *        :
  Fungi incertae sedis
    Mucoromycota
        H.ves.   8 DNIWVAAGDGQLERIKVLLE--EG-----VDPNGKDEFGYTPIHAAVSYAQKEVLECLLS--HG----GDINVEDADKDTPLYVCET-[x]31--GW 114
        L.elo.   3 HNIWLAASDGDLAAVKAFINE-KG-----VSINAQDEFGYSALHAAASYGHKELITYLLE--NG----ADVNIQDPEGDSPLFVCET-[x]31--EW 110
        R.irr.   2 SNIWVAAANGDIQRVTELIR--SG-----LSPNSKDSNGYTPLAAAASYNHFDLIEFLIS--EG----ADVNIRDNDNDTPLYVAEN-[x]31--EW 108
    Zoopagomycota
        N.thr.   5 KNIWIAASDGDLEVVKSYLE--SG-----ISVDAKDPYGYTPLSASVSYDHYDLATYLIE--QG----ANVNIVDFDNETPLHHCES-[x]31--EN 111
        C.bif.   4 KNIWVAASDGVMDRVKQLIEK-DN-----ISVDAKDQNGYTPLHAAVSYDHLDIVQYLLE--KK----ADVAIVDTDGDTPLHVCET-[x]31--EF 111
        T.par.   4 KNIWVAASDGVMDRVKQLIEK-DN-----ISVDAKDQNGYTPLHAAVSYDHLDIVQYLLE--KK----ADVAIVDTDGDTPLHVCET-[x]31--EF 111
        S.pse.   8 SNIWIAAGEGDNERVQTLLAN-G------INVNVADDHGYTALHAAASYDRLATIELLLQ--HG----ANVNCTDTDGDTPLFACET-[x]31-VDK 115
        T.sph.   2 KNIWIAASDGDIEGVKALLDA-G------QPVNAADDNGYTPLHAAASYDHLELIQLLLE--RG----ADANQADEDGDTPLFACET-[x]31-PDR 109
    Blastocladiomycota
        A.mac.  17 NNIWLECADGHVDRVAAFLDA-G------VDVNAQDDTGYSPLHAAASYNHVDLVRFLLS--KG----ADPNITDEDGDTPLHMAED-[x]31--DR 123
        C.ang.  26 NNIWLACADGDLATVKSLIES-GN-----VAPNAQDENGYSALHAAASYDHMDIVEYLLS--KD---ESLVHLTDEDGDTPLHAAET-[x]31--ER 134
    Chytridiomycota
        B.den.  14 DNIWIASGDGRVEDVEYFLKS-GGFGGAPMDANAKDSSGYTSLHAAASYNHLDLMRMLVK-EYG----ADPNVVDHDGYTPLHVIET-[x]31--CW 127
        S.pun.  12 TNIWLACSDGRMDLVEHFLKH-GGPGGTPLDPNVKDDTGYTPLHAAAAYAHIPLIHLLVT-TYH----AQIDIVDDDGDTPLHVCET-[x]31--ER 125
    Cryptomycota
        R.all.   8 LNIWIAA-N--VTMVKHYIEN-EG-----FSPNAKDDNGYFPLAAAVAYDHLDVIEYLLQ--RN----ADINLTDNEGGNCLFYCEN-[x]31--DY 112
                     ***: . :      :   :              :  *  ** .: *:.:* :       :           .     * :  . *.  *
```

Supplementary Figure S12

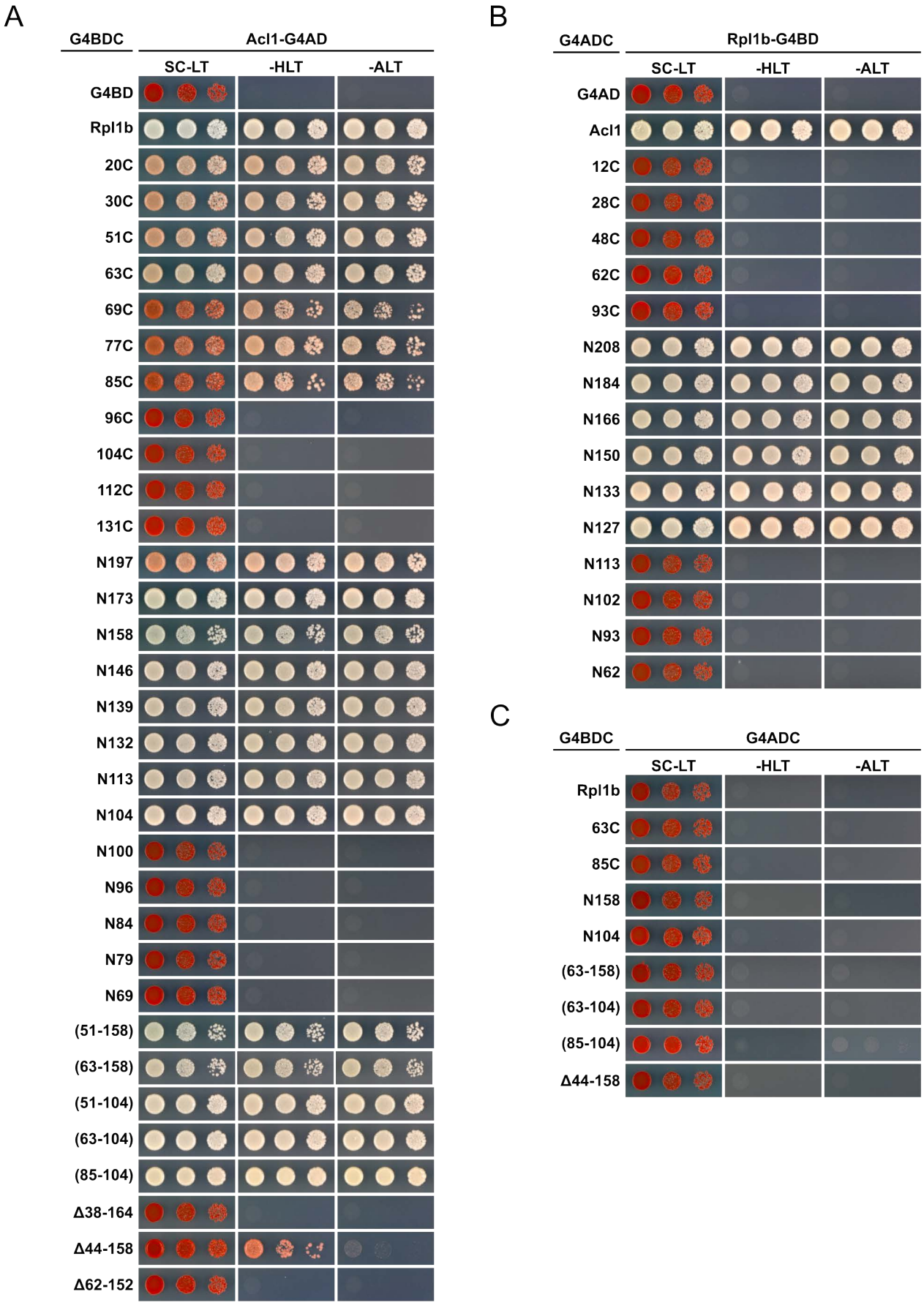

Supplementary Figure S13

A

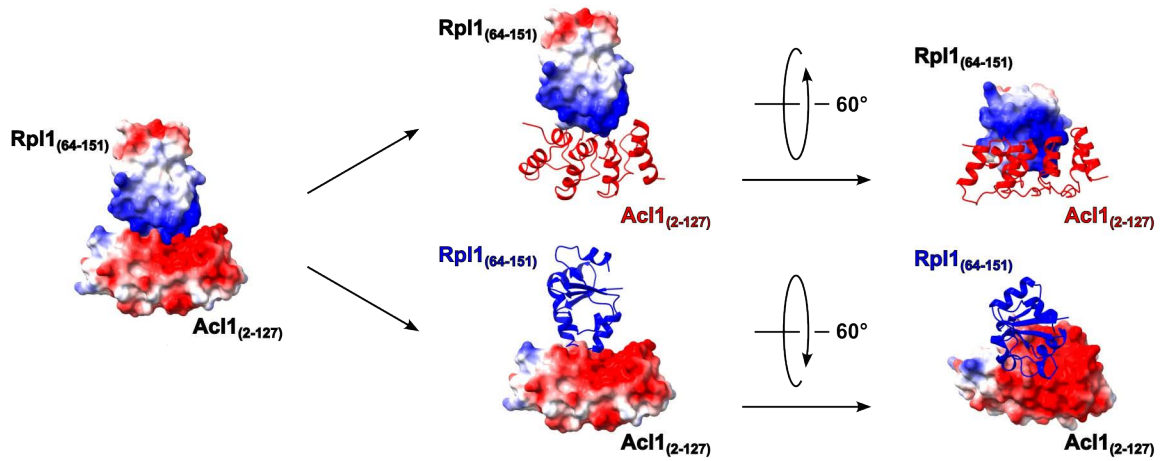

B

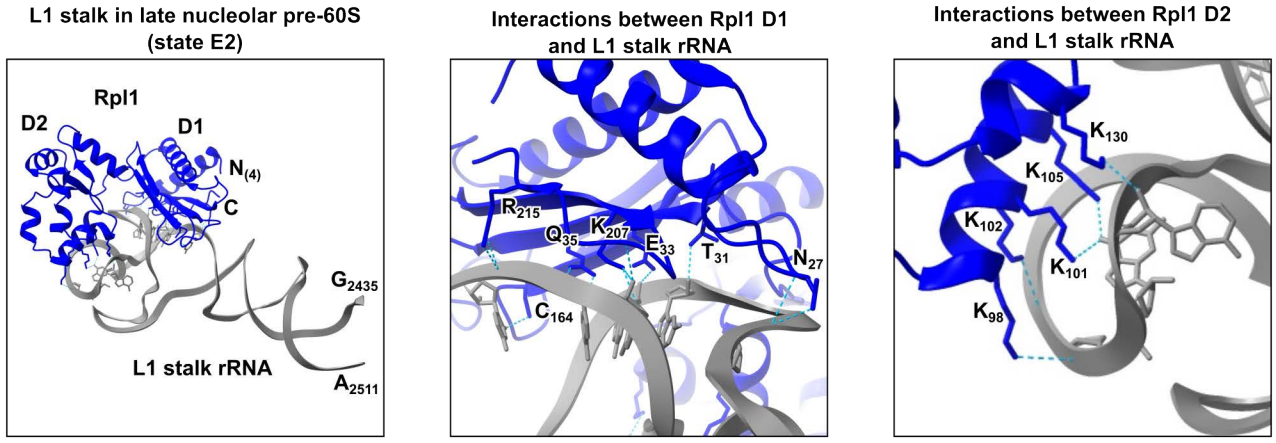

C

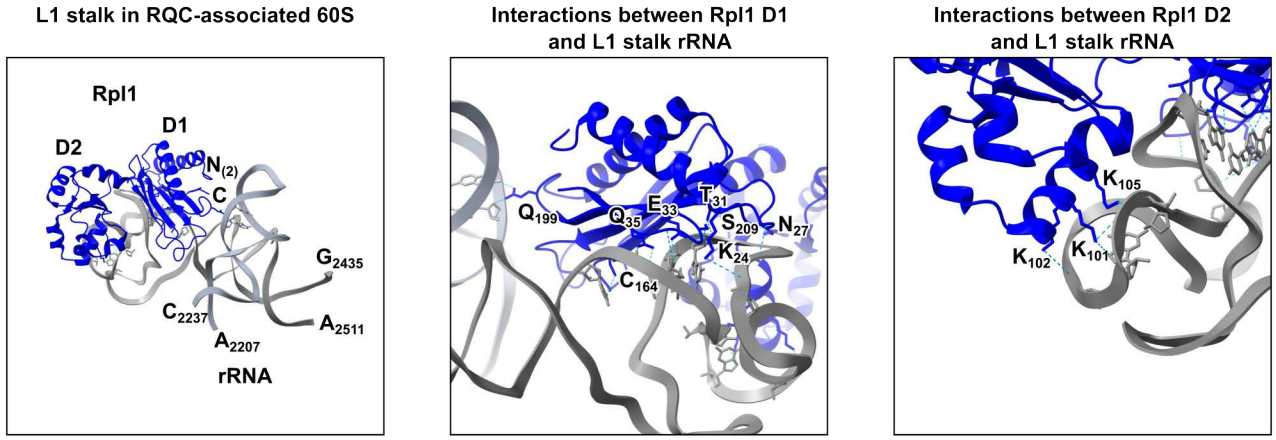

D

Saccharomyces cerevisiae	94	NKNKKLIK	101
Chaetomium thermophilum	94	NKNKKLIK	101
Schizosaccharomyces pombe	93	NKNKKLVK	100
Homo sapiens	94	NKNKKLVK	101
Mus musculus	94	NKNKKLVK	101
Gallus gallus	94	NKNKKLVK	101
Xenopus laevis	94	NKNKKLVK	101
Danio rerio	93	NKNKKLVK	100
Caenorhabditis elegans	93	NKQKKLIK	100
Drosophila melanogaster	94	NKNKKLVK	101
Arabidopsis thaliana	93	NKNKKLVK	100
		:*:*	

E

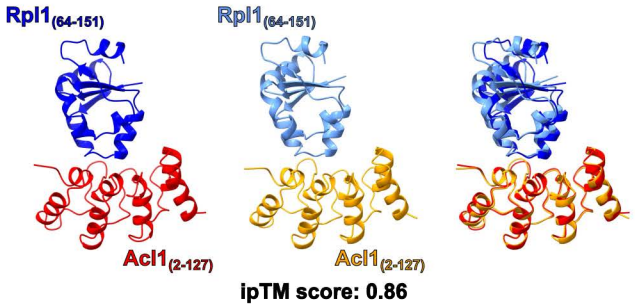

Supplementary Figure S14

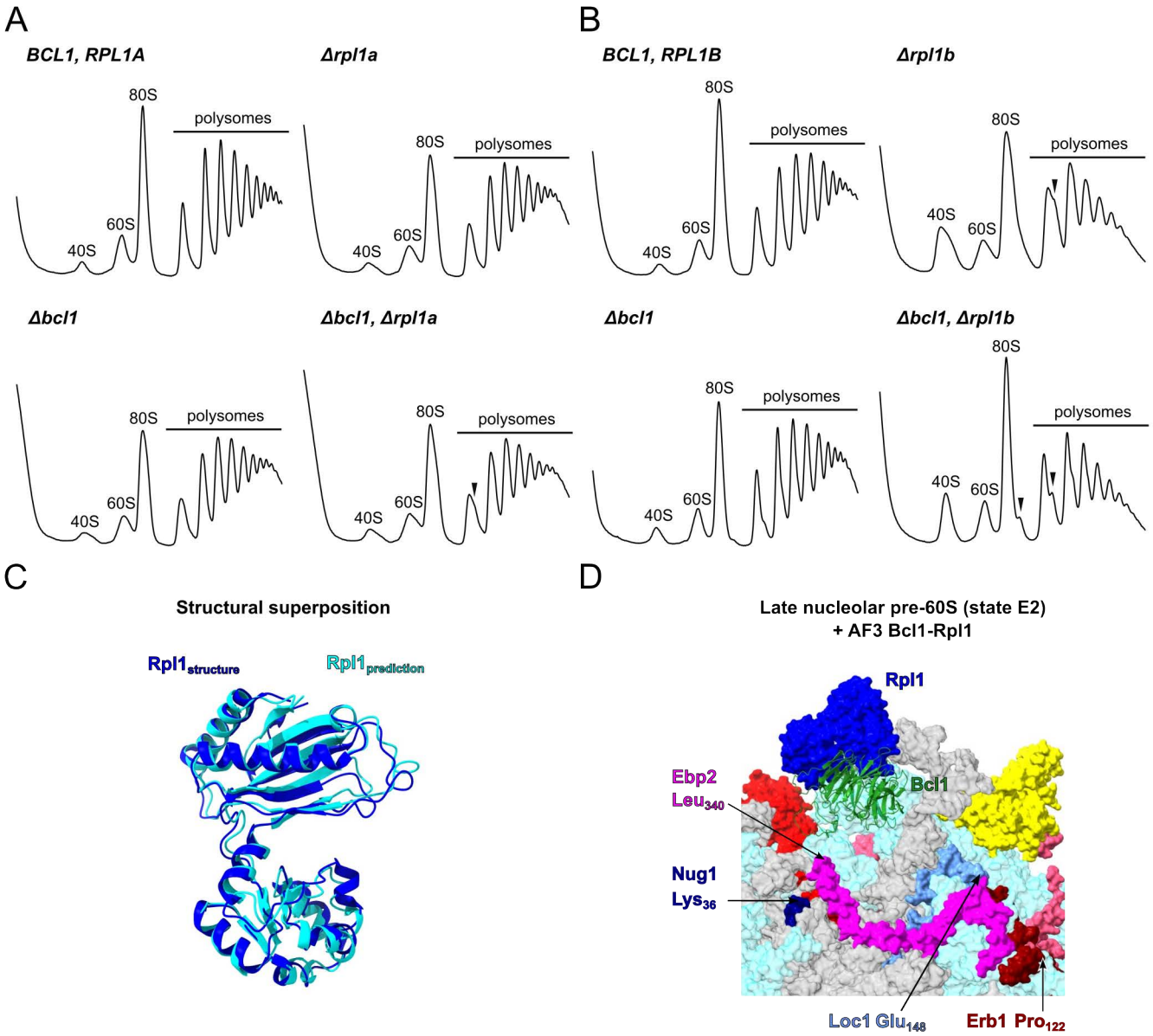

Supplementary Figure S15

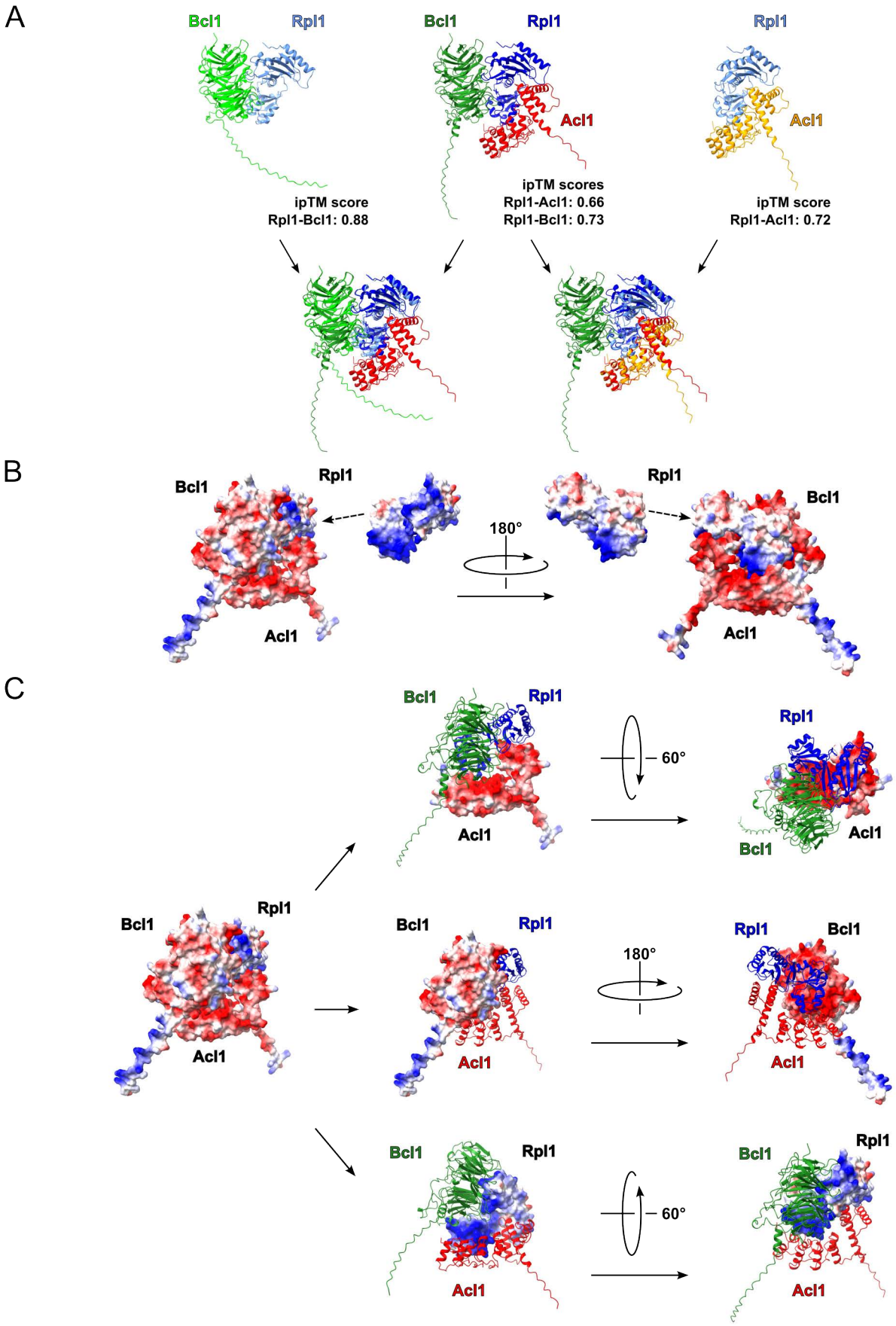

Supplementary Figure S16

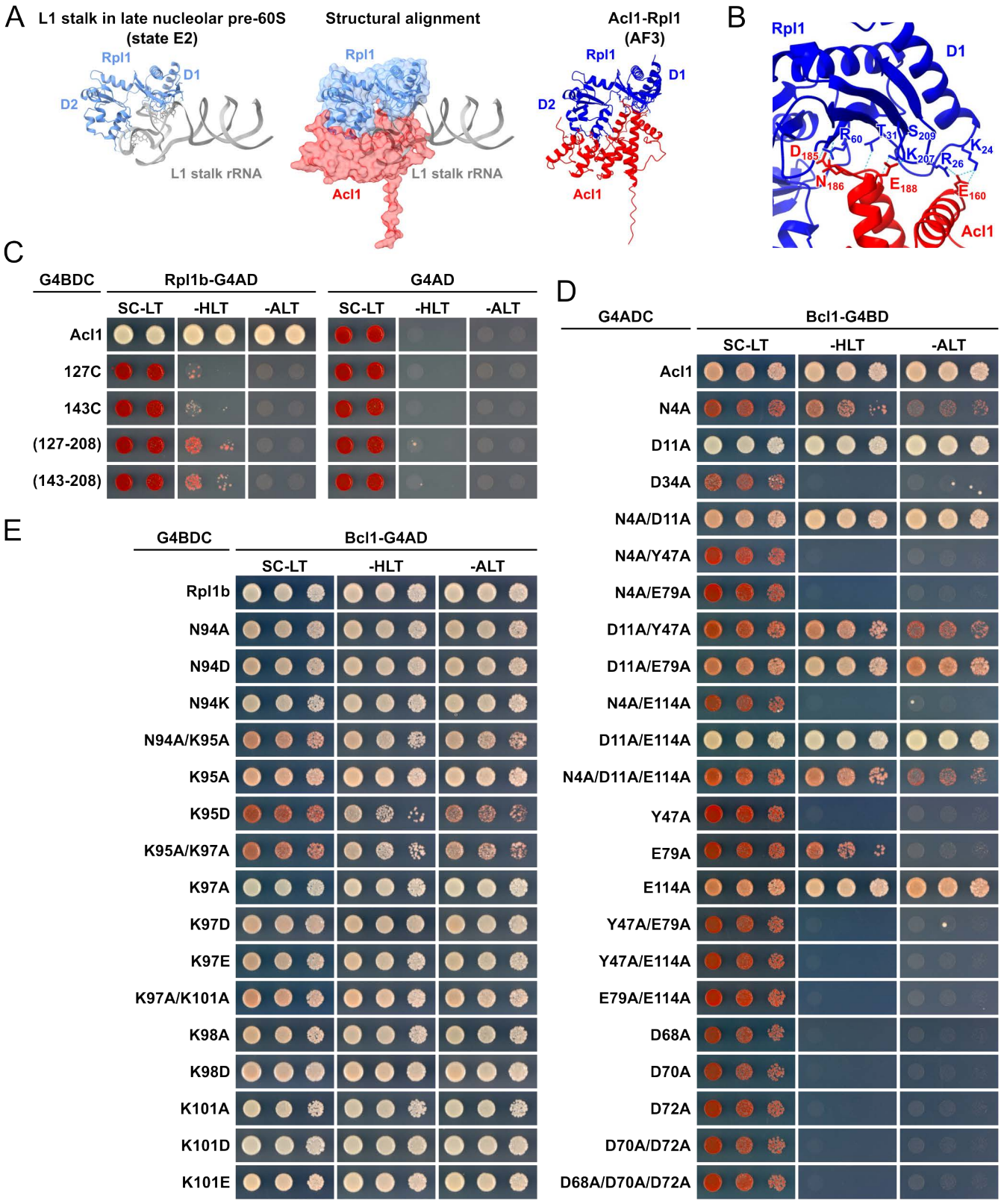

Supplementary Figure S17

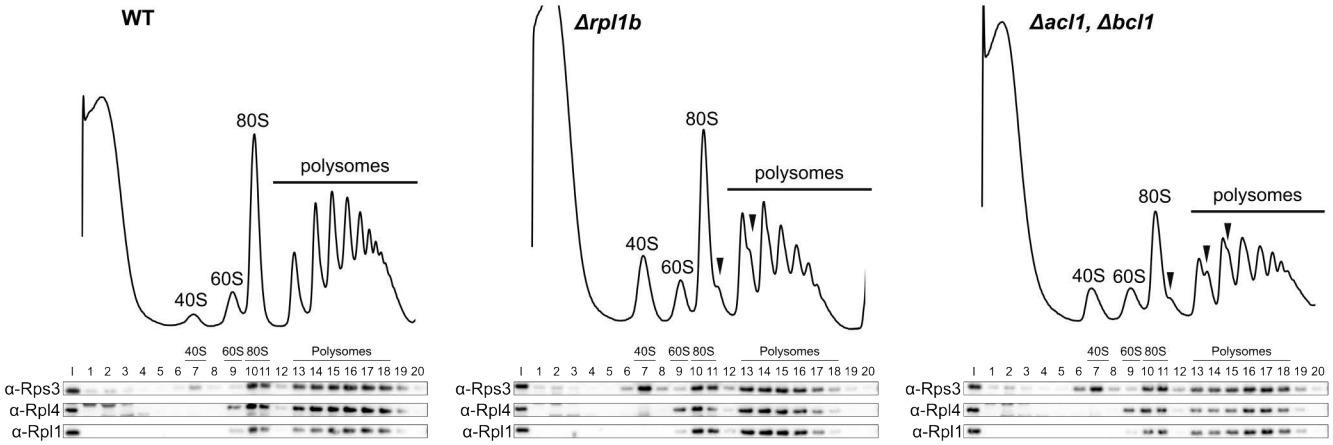

Supplementary Figure S18

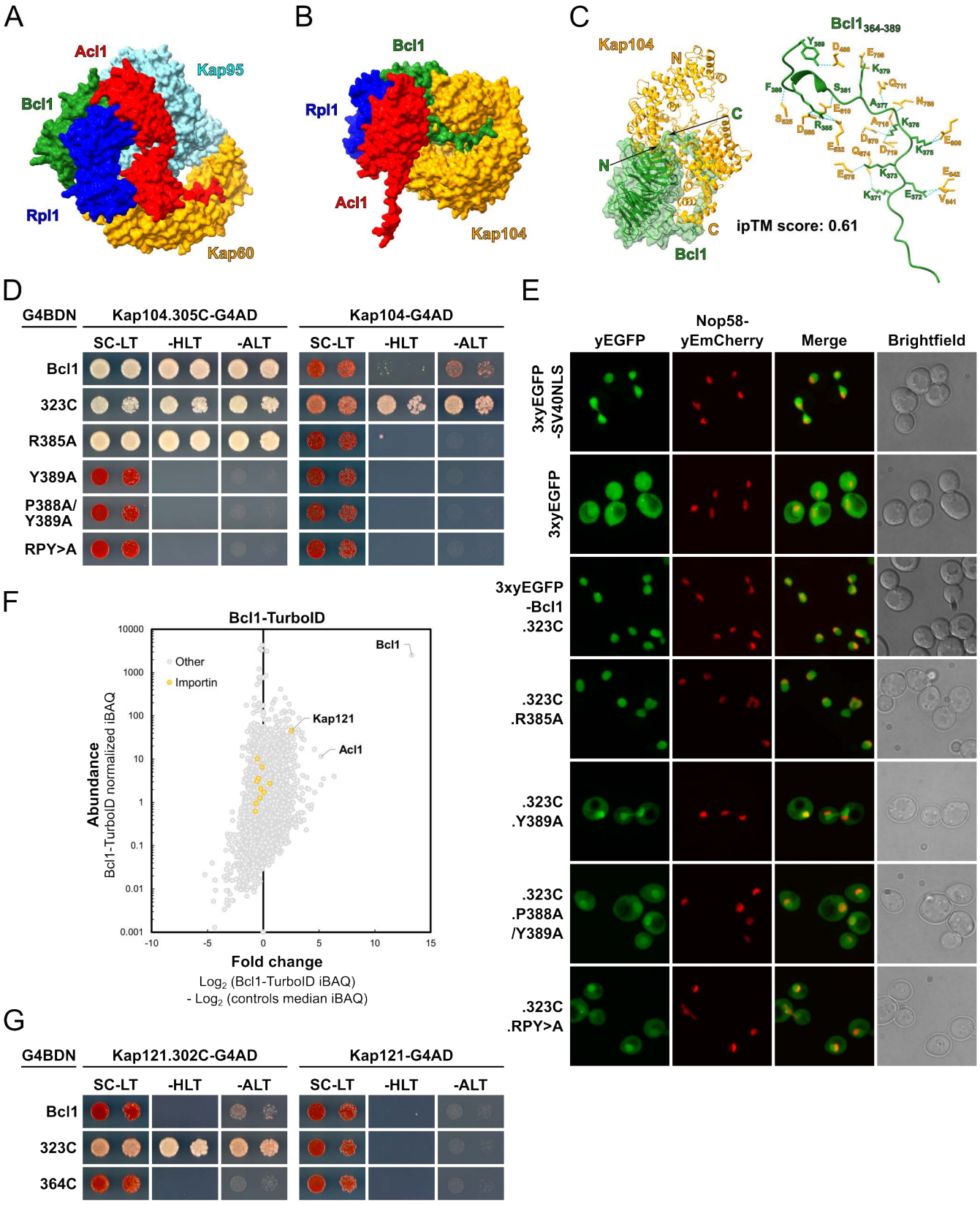
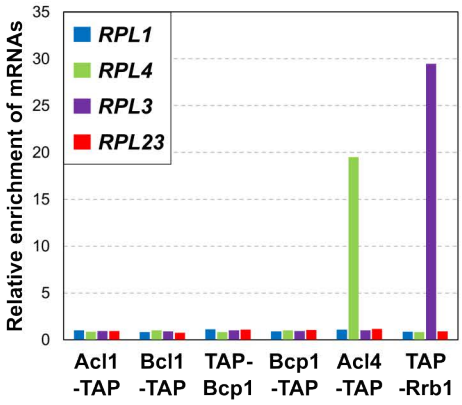
Supplementary Figure S19